KATHOLIEKE UNIVERSITEIT LEUVEN
FACULTEIT TOEGEPASTE WETENSCHAPPEN
DEPARTEMENT ELEKTROTECHNIEK (ESAT)
AFDELING ESAT-TELEMIC
Kasteelpark Arenberg 10, B-3001 Leuven (Heverlee), België

FULL WAVE INTEGRAL EQUATION BASED ELECTROMAGNETIC MODELLING OF 3D METALLIC STRUCTURES IN PLANAR STRATIFIED MEDIA

Promotor :
Prof. Dr. Ir. G. VANDENBOSCH

Proefschrift voorgedragen tot
het behalen van het doctoraat
in de toegepaste wetenschappen

door

Ir. Mark VRANCKEN

December 2002

KATHOLIEKE UNIVERSITEIT LEUVEN
FACULTEIT TOEGEPASTE WETENSCHAPPEN
DEPARTEMENT ELEKTROTECHNIEK (ESAT)
AFDELING ESAT-TELEMIC
Kasteelpark Arenberg 10, B-3001 Leuven (Heverlee), België

FULL WAVE INTEGRAL EQUATION BASED ELECTROMAGNETIC MODELLING OF 3D METALLIC STRUCTURES IN PLANAR STRATIFIED MEDIA

Jury :
Voorzitter :
Prof. Dr. Ir. G. Vandenbosch, promotor
Prof. Dr. Ir. B. Nauwelaers
Prof. Dr. Ir. R. Mertens (IMEC)
Prof. Dr. P.-S. Kildal
(Chalmers Univerity of Technology,
Gothenburg, Sweden)
Prof. Dr. Ir. S. Vandewalle
Prof. Dr. E. Michielssen
(University of Illinois
at Urbana-Champaign, United States)

Proefschrift voorgedragen tot
het behalen van het doctoraat
in de toegepaste wetenschappen

door

Ir. Mark VRANCKEN

U.D.C.
Wet. Depot :
ISBN

December 2002

D/
ISBN

Contents

List of Publications

International Journals

- M. Vrancken and G.A.E. Vandenbosch, "Characteristic aperture modes for the mutual coupling analysis in finite arrays of aperture-coupled antennas," *Arch. Elek. Ubertragungstech. (AEU)*, vol. 56, pp. 19-26, Jan. 2002.
- M. Vrancken and G.A.E. Vandenbosch, "Integral equation analysis of vertical current sheets in planar circuits and antennas," *Electron. Lett.*, vol. 38, pp. 3-5, Jan. 2002.
- M. Vrancken and G.A.E. Vandenbosch, "Characteristic modes for the multiple stacked aperture problem with application to the finite array analysis of flat plate slot array antennas," *Arch. Elek. Ubertragungstech. (AEU)*, vol. 56, pp. 411-415, Jun. 2002.
- M. Vrancken and G.A.E. Vandenbosch, "Hybrid dyadic-mixed potential integral equation analysis of 3D planar circuits and antennas," *IEE Proc. Pt. H., Microwaves Antennas Propagat.*, accepted for publication.
- M. Vrancken and G.A.E. Vandenbosch, "Hybrid dyadic-mixed potential and combined spectral-space domain integral equation analysis of quasi 3D structures in stratified media," *IEEE Trans. Microwave Theory Tech.*, accepted for publication.
- M. Vrancken and G.A.E. Vandenbosch, "Factorisation of transmission line type Green's functions," *J. Electromagn. Waves Appl.*, vol. 16, No. 12, pp. 1733-1751, 2002.
- M. Vrancken and G.A.E. Vandenbosch, "Integral equation formulation and solution for extended vertical current sheets in multilayered planar structures," *Radio Sci.*, **Invited Paper**, accepted for publication.
- M. Vrancken and G.A.E. Vandenbosch, "Semantics of dyadic and mixed potential field representation for 3D current distributions in planar stratified media," *IEEE Trans. Antennas Propagat.*, accepted for publication.

National Journals

- M. Vrancken and G.A.E. Vandenbosch, "Integral equation analysis of 3D structures in planar stratified media,"" *HF Revue, Begian Journal of Electronics and communications*, no. 2, pp. 74-76, 2002.

- G.A.E. Vandenbosch, M. Vrancken and B.L.A. Van Thielen, "Planar antennas at K.U. Leuven: a modelling point of view," *HF Revue, Belgian Journal of Electronics and communications*, no. 1, pp. 3-10, 2002.

International Conferences

- M. Vrancken, G.A.E. Vandenbosch and A.R. Van de Capelle, "Using special aperture field eigenmodes to simplify mutual coupling calculations in finite arrays of aperture coupled antennas", *Proc. of the COST260 Workshop on Smart Antenna Design and Technology*, Dubrovnik, Croatia, Dec. 11-12, 1997, pp.1.32-1.36.

- M. Vrancken and G.A.E. Vandenbosch, "Aperture reduction : a new technique for finite arrays of aperture coupled antennas," *Progress in Electromagnetics Symposium (PIERS 98)*, Nantes, France, Jul. 13-17, 1998.

- M. Vrancken and G.A.E. Vandenbosch, "Full wave analysis of flat plate slot array antennas for satellite TV reception", *Proc. of* 7^{th} *International Conference on Advances in Communications and Control (COMCON7)*, Athens, Greece, Jun. 28 - Jul. 2, 1999, pp. 67-75.

- M. Vrancken and G.A.E. Vandenbosch, "Integral equation modelling of vertical current sheets in planar media with a mixed spectral-spatial computation of the coupling matrix", *Proc. of the* 8^{th} *COST 260 Meeting on Smart Antennas : C.A.D. and Technology*, Rennes, France, Oct. 1-3, 2000, pp 1.16-1.19.

- M. Vrancken and G.A.E. Vandenbosch, "Progress in integral equation analysis of vertical current sheets in arbitrarily multi-layered media", *Proc. of the* 9^{th} *COST 260 Meeting and Workshop on Smart Antennas*, Gothenburg, Sweden, May 2-5, 2001, pp. 1.1-1.4.

- M. Vrancken and G.A.E. Vandenbosch, "Integral equation modelling of vertical conducting shields in planar circuits and antennas", *Proc. of* 4^{th} *European Symposium on Electromagnetic Compatibility (EMC Europe 2000)*, Brugges, Belgium, Sep. 11-15, 2000, vol 1., pp. 275-279.

- M. Vrancken and G.A.E. Vandenbosch, "Alternative formulation of the electric field in a stratified medium applied with a mixed spectral-spatial coupling calculation for integral equation modelling of vertical current sheets", *Proc. of*

IEEE APS Conference on Antennas and Propagation for Wireless Communication (APWC 2000), Waltham, Boston, Massachusetts, United States, Nov. 6-8, 2000, pp 51-54.

- M. Vrancken and G.A.E. Vandenbosch, "A mixed spectral-spatial approach to the integral equation modelling of vertical current sheets in the arbitrarily layered medium," *Proc. of the 2001 URSI International Symposium on Electromagnetic Theory*, Victoria, Canada, May 13-17, 2001, pp. 672-674.

- M. Vrancken and G.A.E. Vandenbosch, "Integral equation modelling of 2.5D structures with alternative Green's functions in arbitrary layered media", *Proc. of International Conference on Electromagnetics in Advanced Applications (ICEAA '01)*, Torino, Italy, Sep. 10-14, 2001, pp. 493-496.

- M. Vrancken and G.A.E. Vandenbosch, "Hybrid dyadic - mixed potential integral equation analysis of passive microwave devices in layered media", 31^{th} *European Microwave Conference (EuMC 2001)*, London, United Kingdom, Sep. 24-28, 2001.

- M. Vrancken and G.A.E. Vandenbosch, "Progress in the integral equation analysis of vertical current sheets in arbitrarily multi-layered media", **Invited Paper**, *Proc. of* 16^{th} *International Conference on Applied Electromagnetics and Communications (ICECOM '01)*, Dubrovnik, Croatia, Sep. 24-26, 2001, pp. 224-227.

- M. Vrancken and G.A.E. Vandenbosch, "Integral equation analysis of 3D structures in planar stratified media," *Proc. of* 9^{th} *URSI forum*, Louvain-la-Neuve, Belgium, Dec. 13, 2001, pp. 22-24.

- M. Vrancken and G.A.E. Vandenbosch, "Full wave electromagnetic modelling of complicated 3D packages and interconnections," $XXVII^{th}$ *General Assembly of the International Union of Radio Science (URSI GA2002)*, Maastricht, The Netherlands, Aug. 17-24, 2002.

- G.A.E. Vandenbosch, M. Vrancken and B.L.A. Van Thielen, "Multilevel modeling frameworks for planar antennas," $XXVII^{th}$ *General Assembly of the International Union of Radio Science (URSI GA2002)*, Maastricht, The Netherlands, Aug. 17-24, 2002.

- G.A.E. Vandenbosch, M. Vrancken and B.L.A. Van Thielen, "The use of hierarchy in modeling tools for planar structures," 9^{th} *International Conference on Mathematical Methods in Electromagnetic Theory (MMET '02)*, Kiev, Ukraine, Sep. 10-13, 2002, pp. 61-66.

Chapter 1

Introduction

1.1 Historical Perspective on Electromagnetic Modelling

All electrodynamic phenomena at a macroscopic level are described by Maxwell's set of partial differential equations already established in the 19^{th} century. Although this set of equations in principle provides the whole field of electrical engineering with a concise and complete mathematical foundation, their solution for most practical problems has long remained elusive. Complete analytical solutions can in general only be obtained for a limited number of standard problems with very simple geometry and material composition. These can be studied to improve our physical understanding but their applicability to solve realistic engineering problems remains very limited.

"Low Frequency" Circuit Theory

Important progress in the field of electrical engineering could however be made without being able to solve the intricate boundary value problems associated with even the simplest electrical circuits. The laws of circuit theory were largely established experimentally, prior to the formulation of Maxwell's equations, and succeed in describing simple low frequency electronic circuits by considering them as an interconnection of wires and discrete lumped elements as resistors, inductors and capacitors. With the benefit of hindsight, it is now clear that circuit theory is an extreme simplification of electromagnetic field theory valid when the dimensions of the circuit are very small compared to the wavelength or equivalently when the retardation effects due to the finite propagation speed of electromagnetic phenomena can be neglected.

Antennas and Microwave Circuits

In two particular domains however, the simplifications underlying ordinary circuit theory were not valid at all : the antenna and microwave circuit disciplines.

Hertz originally demonstrated generation of radio waves at microwave frequencies in 1890. However, wireless communications became based on lower frequencies after Marconi demonstrated long distance communication with low frequency waves in 1901. The generation of radio waves by antennas and speculations on their subsequent propagation mechanisms were generally studied throughout the 1920's and 30's with approximate analytical solutions from electromagnetic wave theory [1], [2].

The real development of microwave circuits occurred during World War II, when the wavelength of the signals involved diminished as a consequence of the need to improve the resolution of radar systems. In such circuits, many of the functions are performed in spatially distributed systems of which the operation is thus fundamentally based on electromagnetic wave phenomena. These new circuits were successfully analysed with microwave network theory [1], [2]. In this approach, the waveguiding structures (initially metallic bulky waveguides) are represented as transmission lines, while passive components and discontinuities are modeled with equivalent lumped networks, extracted from the field theoretical problem with highly ingenious analytical methods. Microwave circuits continued to develop in the postwar period with the development of printed planar wave guiding structures in the 1950's and the integration of active solid state devices in the 1960's [3].

Up to this point however, the use of electromagnetic field theory to analyse and design antennas and microwave circuits has remained a specialized backwater niche, with a strong emphasis on heavy analytical work to obtain approximate solutions which could be evaluated with a minimum of computational effort.

The Appearance of Computational Electromagnetics

Perhaps the most important development in electromagnetic modelling occurred with the appearance of digital computers in the late 1960's. The availability of ever increasing amounts of computational power, speed and memory at ever decreasing cost shifted the balance from analytical to primarily computational techniques. Further analytical work became devoted to developing new numerical algorithms and rendering the computations easier, faster and more accurate. It became possible to obtain numerical solutions for boundary value problems of such complexity that even the attempt to solve them was deemed ludicrous and impossible before the era of the computer. Initial development and use of these techniques were driven from a defense point of view with applications in the design of antennas and sophisticated microwave and millimeter wave integrated circuits for radar systems, and the computation of Radar scattering Cross Sections (RCS) of aerospace vehicles [4]. Real full wave solutions were already possible for the simpler antenna and RCS boundary value problems, with the more complicated full wave circuit analysis slowly coming within

reach.

The Spread of EM Simulation

In the late 1980's, computational power became available to the design engineer as high end work stations and became even more accessible with the spread of cheaper desktop Personal Computers (PC's). Full wave analysis of sections of circuits was now realised to such a degree that the first commercial electromagnetic field simulators (Ansoft HFSS, Sonnet *em*) could successfully be brought to the market [5], [6], [7].

The effects of this evolution have been twofold. On the positive side, the availability of numerical solutions for realistic problems and the visualisation of the resulting fields and currents can improve our physical understanding of the phenomena involved. Engineers no longer need to base their designs on lumped circuit models but can directly probe and manipulate the underlying electromagnetic nature of their products. In principle, it becomes possible to achieve "first pass" design success, optimizing the design in advance, and thus avoiding the iterative design cycle with costly experimental prototypes. On the negative side, the possibility now arises to consider the design process simply as a black box process, where input and output parameters are simply fed into and extracted from the numerical algorithm, with little physical understanding of what goes on in between. Such an approach will lead to too large a dependence on numerical techniques while the arcane design skills based on elementary physics and engineering principles will fade away [8].

The New Arising Trends

Since the 1990's, the new demands of the Information Age with its emphasis on high speed and large bandwidth requirements have been pushing the entire field of EM simulation towards the more commercial applications in communications, both wired and wireless, digital signal processing and high speed computer circuitry with spinoff into all consumer electronics devices.

Traditionally, high speed electronic circuits have been grouped into two classes : microwave circuits using analog waveforms typically at frequencies above 3 GHz and digital circuits typically processing logic pulses at clock rates below 1GHz. Digital logic circuits are composed of densely packed multiple metal planes, with metal signal and ground return traces horizontally between these planes. Interconnect devices like vias and pins connect the traces and regions between the metal planes in the vertical direction. The relatively low operating frequency of digital circuits has allowed designs still to be based on low frequency circuit approaches.

However, at present, a major evolution is going on which makes the distinction between the analog field-theoretical microwave circuits and the circuit-theoretical digital logic circuits fade away. The demand for higher processing speeds have pushed the clock rates of everyday digital circuits into the GHz range, which implies total bandwidths well into the microwave range. On the other hand, the pressure to achieve mass production of reliable and high yield systems at an affordable cost have forced

designers to integrate as many components and circuit functions on an as small an area as possible, combining digital and analog signal processing circuits on the same substrate, resulting in ever increasing component density, decreasing circuit size, higher levels of integration and overall system complexity.

Under these circumstances, the point has been reached where the operation of high speed digital circuits becomes limited by the electromagnetic coupling and wave effects in the digital interconnect circuits, creating a true on-chip interconnect bottleneck. Typical effects such as delay, distortion, cross talk, interference and integrity of the signals as they propagate through the interconnects can no longer be studied using classical circuit theory. The circumstances have been reached where the circuit theory approach simply breaks down. Circuit parameters are unknown and at times not even meaningful. It becomes necessary to take into account the full three dimensional environment with a complete solution of Maxwell's equations. The understanding of microwave phenomena becomes essential for the design and packaging of high speed digital circuits. Digital circuit designers with traditional VLSI (Very Large Scale Integration) and solid-state background will now have to enter the world of electromagnetic fields [4].

The design of contemporary circuits exhibits a degree of sophistication and complexity that can no longer be met by traditional design methods, but needs to be supported by powerful CAE-CAD (Computer Aided Engineering / Design) software. In such packages, full wave 3D EM simulators are used directly in automated iterative loops to optimise the design of the linear passive parts of the circuit [9] and are then coupled with nonlinear semiconductor device models [10]. The future will see their further interfacing with thermal, topological and mechanical modelling into complete global yield- and performance driven man-machine design environments [7], [10].

1.2 Relevance of Analytical Techniques in an Age of Simulation

An important feature of any numerical method is the amount of analytical work performed in its implementation.

Purely numerically oriented methods in general require very little analytical preprocessing. They generally consist of a mainly computational algorithm. They are very versatile in the type of structures they can handle since they make very little assumptions on geometry and material composition. However, the drawback of this approach is that they often suffer from low computational efficiency and consequently have to rely heavily on computational power. These methods risk of degenerating into brute force methods with low accuracy and robustness.

Analytical work on the other hand can only be done under some simplifying hypothe-

ses on the nature of the structure. The knowledge of the geometry combined with the physical knowledge and insight of the developer allows to extract relevant parts of the solution analytically in advance. The amount of analytical and programming expense on the side of the researcher is considerable. The result is a problem specific but more efficient, more accurate and often more robust approach.

A significant portion of research today is numerically oriented to the extent that one is led to believe that analytical techniques have become of secondary importance. However, it is equally clear that the desire to simulate realistic and complex large scale 3D problems such as complete circuit topologies will always be accompanied with the everlasting ailments of insufficient computational power both in terms of speed and memory and this demand will probably always be beyond the reach of whatever computational barriers future progress in computer hardware may be able to breach. Successful numerical work will therefore probably continue to consist of optimally combining the advantages of numerical and analytical techniques in hybrid wave structure interaction algorithms.

1.3 Fundamental Modelling at ESAT-TELEMIC

Fundamental full wave electromagnetic modelling at KU Leuven started with the development of a Boundary Integral Equation (BIE) (See Chapter 3) model by Vandenbosch [11]. This model was initially conceived to analyse microstrip patch antenna configurations in stratified dielectric media. Such antennas arose together with printed microwave transmission line structures such as microstrip. They typically consist of printed flat planar conductors located at the interface between the layers of a stacked dielectric medium. The effect of the background medium is incorporated rigorously in the Green's function kernel of the BIE (See Chapter 4). Vandenbosch also developed a special technique to rigorously model the coaxial probe feed of these antennas [12], [13].

Subsequent work remained concentrated on antenna configurations, as Demuynck developed the "expansion wave" concept to simplify the analysis of large antenna arrays [14], [15]. He also improved the computation of the Green's functions for multilayered media [16], [17]. In the mean time, magnetic currents were introduced to model aperture or slot (openings in infinitely large conducting ground planes) coupled antennas. A special de-embedding technique (See Chapter 2) was developed to excite structures with traveling waves on single conductor transmission lines.

Among the antenna topics, Volski [18] combined diffraction theory with integral equation techniques to model the finiteness of the layer structure in the lateral direction, while Svezhentsev [19] performed modelling work on conformal antennas.

Soliman [20] used the magnetic current modelling to design several planar antenna elements and arrays of the slot and aperture type [21]. He introduced an improved

de-embedding procedure for multimode combined multiconductor multislot transmission lines [22]. He also introduced the Discrete Complex Image Method (DCIM) to accelerate the computation of the Green's functions.

Although the emphasis has been put on antenna analysis, the nature of the solver allows it to be applied equally well for the analysis of printed planar microwave circuits. This topic was taken up by Van Thielen [23]. He introduced the capability to incorporate "black box" models of discrete circuit elements and active devices into the full wave analysis. He further improved the de-embedding procedure and introduced simplified models to compute the interaction between the transmission line structures, discontinuities and active devices.

1.4 Objective of this Research

The electromagnetic full wave solver MAGMAS (Model for Analysis of General Multilayered Antenna Structures) available at the outset of this work can be categorized in several manners. The electromagnetic boundary value problem is formulated and solved with a Boundary Integral Equation (BIE) method (See Chapter 3). It can analyse planar antennas and circuits embedded within a planar stratified medium (See Chapter 5). The numerical solution relies heavily on analytical work, such that it is a good example of the hybrid numerical analytical approach.

In the original field of application, planar antennas are evolving into more arbitrary almost completely three dimensional structures. In the field of microwave circuits, increasing complexity has equally well introduced geometries beyond the capabilities of planar solvers. In a new opening field, full wave electromagnetic field simulation will be increasingly engaged in the analysis and design of electronic circuits, where mixed digital and analog signals and waves propagate and interact in a complicated three dimensional environment.

The objective of this work is therefore to extend the modelling capabilities of the MAGMAS framework from planar to three dimensional structures, faithful to the underlying hybrid analytical numerical approach, and taking into account the technical background of the antenna, microwave and traditional circuit structures envisaged, many of which can be considered as embedded within a planar stratified medium.

A secondary objective is to demonstrate that full wave electromagnetic simulation is no longer the restricted playground of antenna design engineers, and thus make electrical engineers aware of what electromagnetic field simulation technology might be able to do in the field of traditional circuit design.

1.5 Outline of the Dissertation

The dissertation consists of two major parts.

The first part consists of Chapters 2 and 3. These introductory chapters provide the reader who might be less acquainted with the field of computational electromagnetics with the necessary physical and numerical background.

Chapter 2 starts directly from Maxwell's equations. These equations are the direct basis for the Finite Element Method (FEM) and Finite Difference Time Domain (FDTD) numerical techniques of Chapter 3. The solution of these equations in integral form allows to introduce the concept of the Green's function, and forms the basis for the derivation of the Boundary Integral Equation (BIE) method in Chapters 3 and worked out in the remainder of the text. The importance of the wave nature of the field and the reduction of a complete field theoretical solution to macroscopic measurable quantities is discussed.

Chapter 3 discusses the theoretical formulation, the basic algorithm, and limitations of the FDTD, the FEM and the BIE numerical techniques, which are the most important one used today.

The second and largest part comprises Chapters 4 through 8. This part covers the actual work performed in this thesis.

Chapter 4 derives the full spectral electric and magnetic dyadic Green's functions. These give the electric and magnetic fields in the spectral domain, generated by a three dimensional point like current source embedded within an arbitrary plane stratified medium. From the transmission line formalism used, a new factorised form for the Green's functions is developed, which is used in the remainder of the text for analytical as well as numerical purposes.

Chapter 5 considers the expressions for the electric field in the spatial domain. The physical interpretation is usually facilitated by casting the expression in the space domain in mixed potential form. Several distinct mixed potential formulations are possible and it is shown for the first time in this work that they are related by the standard theory of Gauge transformations, applied for the case of a multilayered medium. The relation of the field formulation to the geometry of the problem is discussed. Typical theoretical and numerical problems of "total" mixed potential formulations can be avoided by the newly developed hybrid dyadic mixed potential field formulation.

Chapter 6 discusses the evaluation of the reaction integrals to obtain the elements of the discrete matrix representation of the BIE. Traditional spectral and space domain approaches are further blended in a combined spectral space domain approach. In this approach, all transverse integrations are performed in the space domain with the mixed potential formalism, while all z, z' integrations involve the dyadic part of the

formulation and can be done fully analytically in the spectral domain.

Chapter 7 provides more details on the most important numerical and analytical techniques used. It is shown how in the inverse Fourier transform and in the remaining evaluation of the reaction integrals in the space domain, the use of physics based analytical extraction techniques can reduce the computationally expensive purely numerical work to a minimum.

Chapter 8 demonstrates the capabilities of the full wave BIE solver developed in this work. The examples are taken from the traditional antenna and microwave fields, as well as from the more traditional field of "low frequency" electronics. Accuracy and correctness of the software is verified by comparison with known analytical results, simulated and measured results from open literature, and by comparison with the results obtained from commercially available full wave solvers.

Chapter 2

Physical Aspects of Electromagnetic Theory

2.1 Introduction

All electrodynamic phenomena at a macroscopic scale are in principle described by Maxwell's equations. The solution of this set of equations under realistic and complicated circumstances in general requires numerical solution techniques, which are discussed in the next chapter. The underlying principles of these techniques, their application and the correct interpretation of the results remain based on physical principles some of which are highlighted in this chapter. The most important characteristic of the electromagnetic field is its inherent "wave" nature. This manifests itself not only in the radiation generated by antennas, but even affects the operation of ordinary electronic circuits. An accurate prediction of the macroscopic behaviour of these devices can be done by considering the complete underlying boundary value problem. In this chapter, these topics are considered for the case of a homogeneous medium, but the main derivations and principles remain valid for more complicated media.

2.2 Historical Perspective

The development of a mathematical theory of electric and magnetic phenomena has been brought about by the efforts of a large number of eminent men who now figure in our mental pantheon of scientific heroes, such as Coulomb and Laplace, Ampère and Biot, Weber and Faraday.

Originally, electrodynamic phenomena were described with an action-at-a-distance approach by finding mechanical force formulas for the instantaneous interaction between moving electric charges, such as the formulas of Ampère and Weber [24], [25], [26]. A contrasting approach was developed by Faraday, who sought the origin of these phenomena in real actions going on in an intervening "aether" medium. By means of elastic solid analogies and mechanical aether models, these ideas were put on a mathematical basis by James Clerk Maxwell into the Maxwell-Faraday field theory in 1864. Apart from unifying and describing all then known experimental and theoretical results [27], this theory also predicted the existence of electromagnetic waves [28], which were later demonstrated experimentally by Heinrich Hertz [29], [30]. As the atomic nature of electricity was gradually revealed, the original interpretation became superseded and the theory was refined and purified by the work of Hertz, Heaviside, Fitzgerald and Lorentz [31] into a framework in which the electromagnetic field is a more abstract carrier of far-action between moving electric charges, now propagated at the finite velocity of light.

This historical dichotomy has its counterpart in present day numerical techniques. The Finite Element Method (FEM) and Finite Difference Time Domain (FDTD) approaches are really "field based" techniques using directly Maxwell's Equations, which of course remain the fundamental basis of all formulations. However, the Boundary Integral Equation (BIE) derived from Maxwell's equations in Section 2.5 does exhibit all characteristics of an interaction at a distance formulation, although not a mechanical one, but an electromagnetic "reaction" as defined in Section 2.9.1 .

2.3 Maxwell's Equations

When a macroscopic scalar charge distribution $\rho(x, y, z, t)$ depends on time, the movement of its microscopic constituents produces a vector electric current distribution $\vec{J}(x, y, z, t)$ according to the charge conservation law

$$\nabla.\vec{J}(\vec{r}, t) = -\frac{\partial \rho(\vec{r}, t)}{\partial t}. \tag{2.1}$$

The interaction between the resulting electric currents $\vec{J}(x, y, z, t)$ can be described by the assumption of the existence of two coupled vector fields $\vec{E}(x, y, z, t)$ and $\vec{H}(x, y, z, t)$ in ordinary space-time x, y, x, t. The whole theory can now be condensed into the two independent [32] Maxwell equations

$$\nabla \times \vec{E}(\vec{r}, t) = -\frac{\partial \mu \vec{H}(\vec{r}, t)}{\partial t} \tag{2.2}$$

$$\nabla \times \vec{H}(\vec{r}, t) = +\frac{\partial \epsilon \vec{E}(\vec{r}, t)}{\partial t} + \vec{J}(\vec{r}, t). \tag{2.3}$$

In these equations, the dielectric permittivity ϵ and magnetic permeability μ characterise the material properties of the medium in which the interaction takes places. In

this work we consider them as constants in space and time and independent of the field strengths, either over the whole medium as in this chapter or in each layer of the planar stratified medium considered in the remainder of this work. For these cases, they can be consider as statistical averages of the underlying processes at the atomic level of the material which produce its electric and magnetic characteristics. This coupled set of first order partial differential equations is the appropriate expression of a theory of action exerted between contiguous parts of a "medium" or field, and forms the basis of the FEM and FDTD techniques of Chapter 3.

Taking the divergence $\nabla.$ of Equations (2.2) and (2.3), using the property $\nabla.\nabla\times\vec{F}=0$, and inserting the law of charge conservation Equation (2.1), we obtain the two remaining but dependent Maxwell equations

$$\nabla\ .\ \mu\vec{H}(\vec{r},t) = 0 \tag{2.4}$$
$$\nabla\ .\ \epsilon\vec{E}(\vec{r},t) = \rho(\vec{r},t). \tag{2.5}$$

A lot of the subsequent computations are simplified by working in the frequency domain, such that the time variable is transformed into a frequency parameter. When the field has a sinusoidal time dependence, it can be represented by a complex vector phasor $\vec{E}(x,y,z,\omega)$ from which the time dependence is recovered as

$$\vec{E}(x,y,z,t) = Re\left[\vec{E}(x,y,z,\omega)e^{j\omega t}\right]. \tag{2.6}$$

In this way, differentiation and integration in time are simply replaced by algebraic multiplication and division with the factor $j\omega$. The law of charge conservation (2.1) and the independent Maxwell equations (2.2), (2.3) thus become in the frequency domain

$$\nabla.\vec{J}(\vec{r},\omega) = -j\omega\ \rho(\vec{r},\omega) \tag{2.7}$$
$$\nabla\times\vec{E}(\vec{r},\omega) = -j\omega\ \mu\vec{H}(\vec{r},\omega) \tag{2.8}$$
$$\nabla\times\vec{H}(\vec{r},\omega) = +j\omega\ \epsilon\vec{E}(\vec{r},t)+\vec{J}(\vec{r},\omega). \tag{2.9}$$

2.4 The Wave Equations

Upon eliminating $\vec{H}$ and $\vec{E}$ from Equations (2.8), (2.9) we immediately obtain the vector Helmholtz wave equations

$$\nabla\times\nabla\times\vec{E}-k^2\vec{E} = -j\omega\mu\vec{J} \tag{2.10}$$
$$\nabla\times\nabla\times\vec{H}-k^2\vec{H} = \nabla\times\vec{J} \tag{2.11}$$

where $k=\omega\sqrt{\mu\epsilon}$ is the wavenumber of the medium. Although we now have more complicated second order differential equations, the equations are decoupled, each expressing one field type directly as a function of the current $\vec{J}$. A solution can now be

formulated with the help of Green's theorem in Section 2.5. These equations clearly describe the "waving" nature of the fields and their generation by the current distribution. The most prominent manifestation of this phenomenon is the "radiation" field discussed in Section 2.6. However, even if no radiation is present, the electromagnetic behaviour of practical antennas and electronic circuits is still determined by the "wave" nature as discussed in Section 2.8. These more subtle wave interactions can only be taken into account accurately by a complete solution of the underlying boundary value problem (Section 2.7) and ultimately affect the measurements performed at a macroscopic level (Section 2.9).

2.5 Solution in Integral Form

The above wave equations can now be solved formally with the Green's function technique. This method is a generalisation of the technique introduced in 1828 by George Green [33] to solve the electrostatic scalar Poisson equation for the potential generated by a given charge distribution. The result will be that the fields can be written as integrals over the currents multiplied with a Green's function. This Green's function is the solution of the simpler problem for a point source excitation of unit strength. The Green's function can be considered as the mathematical description of the electromagnetic interaction at a distance between macroscopic current distributions, propagated at a finite speed. The expressions also allow to study the radiation field (Section 2.6) and are the basis for the derivation of the Boundary Integral Equations of Chapter 3.

The geometry of our problem is depicted in Figure 2.1. We consider a certain region V' of space with "running" coordinate $\vec{r}'$. The source $\vec{J}_S(\vec{r}')$ is only present over a smaller and limited volume V_S of this region. The volume V' is delimited internally by S_c and S_δ and on the outside by S_∞. The inner surface S_c is introduced to facilitate the derivation of the boundary integral equations of Chapter 3. We want to determine the field at any position $\vec{r}$ outside of the source region. To do this, we will need to exclude this "observation" point from the volume V' with a principal volume V_δ with boundary S_δ of radius δ . Over the entire space V', Equations (2.10) and (2.11) are valid.

The problem can now be solved by first considering the simpler problem of a point-like current source of unit strength

$$\vec{J}_S(\vec{r}') = \delta(\vec{r}' - \vec{r}_S)\overline{I} \tag{2.12}$$

located at a single position $\vec{r}_S$ and unit dyadic $\overline{I}$. . The field excited by this simple source is the dyadic Green's function $\overline{G}(\vec{r}', \vec{r}_S)$ which is the solution of

$$\left[\nabla' \times \nabla' \times -k^2\right] \overline{G}(\vec{r}', \vec{r}_S) = 4\pi\delta(\vec{r}' - \vec{r}_S)\overline{I}. \tag{2.13}$$

It can be shown [34] that the dyadic Green's function can be obtained from an even

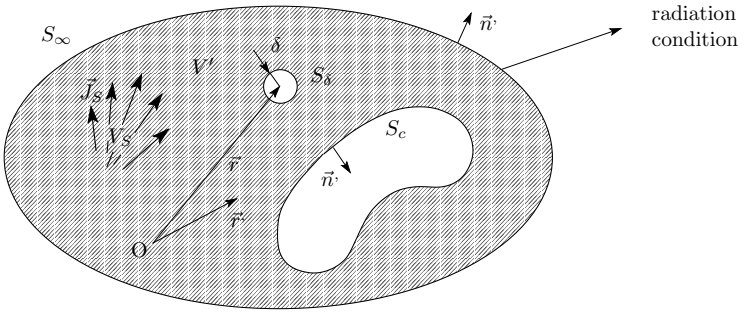

Figure 2.1: Generic volume V' and limiting surface $S' = S_\infty + S_\delta + S_c$ to solve the wave equations by application of Green's theorem. The excitation is provided by an imposed current distribution $\vec{J}_S$. On the outer limiting surface S_∞ receding to infinity the fields satisfy the radiation condition.

simpler scalar Green's function $g(\vec{r}', \vec{r}_S)$ which satisfies the scalar wave equation

$$\left(\nabla'^2 + k^2\right) g(\vec{r}', \vec{r}_S) = -4\pi\delta(\vec{r}' - \vec{r}_S). \tag{2.14}$$

The solution to this problem has long been known to be

$$g(\vec{r}', \vec{r}_S) = \frac{e^{-jkR}}{R} \tag{2.15}$$

with R the spatial distance $\sqrt{(x' - x_S)^2 + (y' - y_S)^2 + (z' - z_S)^2}$. The dyadic Green's function $\overline{G}(\vec{r}', \vec{r}_S)$ can now be written as

$$\overline{G}(\vec{r}', \vec{r}_S) = \left[\overline{I} + \frac{1}{k^2}\nabla'\nabla'\right] g(\vec{r}', \vec{r}_S). \tag{2.16}$$

Both the scalar and dyadic Green's function are singular when the points $\vec{r}'$ and $\vec{r}_S$ coincide, but are valid solutions of Equations (2.13) and (2.14) even at these points.

The field at the observation point $\vec{r}$ generated by a current distribution $\vec{J}_S(\vec{r}')$ (notice the switch of coordinates) which is distributed over a limited volume V_S of the space V' can now be obtained by using a generalisation of Green's theorem originally given in scalar form [33]. The fields can be expressed with the scalar Green's function $g(\vec{r}, \vec{r}')$ if we use Green's theorem in vector form [34], [35]

$$\int_{V'} \nabla' \times \nabla' \times \vec{A} \,.\, \vec{B} - \vec{A} \,.\, \nabla' \times \nabla' \times \vec{B} \quad \mathrm{d}V' =$$

$$\int_{S'} \vec{n}' \,.\, \left(\vec{A} \times \nabla' \times \vec{B} + \nabla' \times \vec{A} \times \vec{B}\right) \quad \mathrm{d}S' \tag{2.17}$$

or using the dyadic Green's function $\overline{G}(\vec{r},\vec{r}')$ if we use Green's theorem in vector-dyadic form [34], [35]

$$\int_{V'} \nabla' \times \nabla' \times \vec{A} \,.\, \overline{C} - \vec{A} \,.\, \nabla' \times \nabla' \times \overline{C} \quad \mathrm{d}V' = \int_{S'} \vec{n}' \,.\, \left(\vec{A} \times \nabla' \times \overline{C} + \nabla' \times \vec{A} \times \overline{C} \right) \quad \mathrm{d}S'. \quad (2.18)$$

These theorems are only valid for smooth functions $\vec{A}(\vec{r}')$, $\vec{B}(\vec{r}')$ and $\overline{C}(\vec{r}')$. We therefore have to exclude the observation point from the integration domain with the principal volume V_δ to avoid the singular point of the scalar and dyadic Green's functions when $\vec{r} = \vec{r}'$. Over the remaining integration domain, the right members of Equations (2.13), (2.14) are always 0.

We can now apply Green's theorem Equation (2.17) with $\vec{A} = \vec{E}(\vec{r}')$ and $\vec{B} = g(\vec{r},\vec{r}')\vec{i}$ with $\vec{i}$ an arbitrary constant vector. Inserting the Helmholtz equations (2.10) and (2.14) and simplifying the resulting expressions with Maxwell's equations we obtain

$$\int_{V'} j\omega\mu g(\vec{r},\vec{r}')\vec{J}\,\mathrm{d}V' - \int_{V'} \nabla'.\vec{E}\;\nabla' g(\vec{r},\vec{r}')\;\mathrm{d}V' = \int_{S'} j\omega\mu g(\vec{r},\vec{r}')\vec{n}' \times \vec{H}\;\mathrm{d}S' - \int_{S'} \vec{n}'.\vec{E}\;\nabla' g(\vec{r},\vec{r}')\;\mathrm{d}S' - \int_{S'} \vec{n}' \times \vec{E} \times \nabla' g(\vec{r},\vec{r}')\;\mathrm{d}S' \quad (2.19)$$

where the limiting surface $S'$is actually $S_\infty + S_\delta + S_c$

Two additional steps are required to obtain the field at the observation point $\vec{r}$. The first is to let the outer portion of the limiting surface S_∞ recede to infinity. If the Sommerfeld radiation conditions [36]

$$\lim_{R\to\infty} \vec{i}_r \times \nabla \times \vec{E} = -jk\vec{E} \quad (2.20)$$

$$\lim_{R\to\infty} \vec{i}_r \times \nabla \times \vec{H} = -jk\vec{H} \quad (2.21)$$

are satisfied, the fields decay fast enough for this contribution to the integral to vanish. The second is to let the size δ of the principal volume V_δ around the observation point $\vec{r}$ shrink to 0. In this case, the singular parts of the field become dominant and the field can then be integrated analytically over the shrinking surface S_δ. In [37], [38], it is shown in detail that the result of the limiting procedure is just 4π times the field value at the observation point. We thus obtain

$$\begin{aligned} 4\pi\vec{E}(\vec{r}) \;=\; & -\int_{V_S} j\omega\mu g(\vec{r},\vec{r}')\vec{J}_S\;\mathrm{d}V' + \int_{V_S} \frac{\nabla'.\vec{J}_S}{-j\omega\epsilon}\;\nabla' g(\vec{r},\vec{r}')\;\mathrm{d}V' \\ & - \int_{S_c} j\omega\mu g(\vec{r},\vec{r}')\vec{n}' \times \vec{H}\;\mathrm{d}S' + \int_{S_c} \vec{n}'.\vec{E}\;\nabla' g(\vec{r},\vec{r}')\;\mathrm{d}S' \end{aligned}$$

$$+\int_{S_c} \vec{n}' \times \vec{E} \times \nabla' g(\vec{r},\vec{r}') \, \mathrm{d}S' \quad . \tag{2.22}$$

This is an important result. The first term on the right is the field generated by the imposed current distribution $\vec{J}_S$ and can be considered as an imposed incident field. The remaining last three terms constitute the "scattered" field generated by the "induced" or "equivalent" electric and magnetic currents and charges $\vec{n}' \times \vec{H}$, $-\vec{n}' \times \vec{E}$, $\vec{n}'.\vec{E}$, $-\vec{n}'.\vec{H}$, flowing on the surface S_c. This contribution will allow to derive the boundary integral equations in Chapter 3. Notice that the field at the observation point $\vec{r}$ is obtained by integrating the contributions of all currents $\vec{J}_S$ at other distant positions $\vec{r}'$ after being multiplied with the Green's function $g(\vec{r},\vec{r}')$. This integral relation relationship is therefore the appropriate mathematical expression for the action or field at a distance of the generating current distribution, and the Green's function describes the propagation mechanism.

Similar results can be obtained for the magnetic field by combining Equations (2.17), (2.11), (2.14) as

$$\begin{aligned} 4\pi\vec{H}(\vec{r}) \;=\; & -\int_{V_S} g(\vec{r},\vec{r}') \, \nabla' \times \vec{J}_S \, \mathrm{d}V' \\ & -\int_{S_c} j\omega\epsilon g(\vec{r},\vec{r}')\vec{n}' \times \vec{E} \, \mathrm{d}S' - \int_{S_c} \vec{n}'.\vec{H} \, \nabla' g(\vec{r},\vec{r}') \, \mathrm{d}S' \\ & +\int_{S_c} \vec{n}' \times \vec{H} \times \nabla' g(\vec{r},\vec{r}') \, \mathrm{d}S' \quad . \end{aligned} \tag{2.23}$$

In some cases, it is preferable to have expressions available using the dyadic Green's function. By starting from the vector-dyadic Green's theorem Equation (2.18) and inserting (2.10), (2.11), (2.13) we obtain

$$\begin{aligned} 4\pi\vec{E}(\vec{r}) \;=\; & -\int_{V_S} j\omega\mu \, \overline{G}(\vec{r},\vec{r}') \, . \, \vec{J}_S \, \mathrm{d}V' \\ & +\int_{S_c} \vec{n}' \times \vec{E} \, . \, \nabla' \times \overline{G}(\vec{r},\vec{r}') \, \mathrm{d}S' - \int_{S_c} j\omega\mu \, \vec{n}' \times \vec{H} \, . \, \overline{G}(\vec{r},\vec{r}') \, \mathrm{d}S' \end{aligned} \tag{2.24}$$

$$\begin{aligned} 4\pi\vec{H}(\vec{r}) \;=\; & -\int_{V_S} \nabla' \times \vec{J}_S \, . \, \overline{G}(\vec{r},\vec{r}') \, \mathrm{d}V' \\ & +\int_{S_c} \vec{n}' \times \vec{H} \, . \, \nabla' \times \overline{G}(\vec{r},\vec{r}') \, \mathrm{d}S' + \int_{S_c} j\omega\epsilon \, \vec{n}' \times \vec{E} \, . \, \overline{G}(\vec{r},\vec{r}') \, \mathrm{d}S'. \end{aligned} \tag{2.25}$$

If the free space scalar and dyadic Green's functions are replaced with their equivalents that incorporate the multilayered medium as determined in Chapters 4 and 5, the

above derivations remain valid. This is so because the radiation conditions remain satisfied, and because the singular behaviour for $\vec{r} = \vec{r}'$ in any medium is the same as if the medium is a homogeneous one (see Chapter 5).

Retaining only the source term contributions from Equations (2.22) and (2.23), and using the properties $\nabla g = -\nabla' g$, $\nabla \times f\vec{F} = \nabla f \times \vec{F} + f\nabla \times \vec{F}$, we rewrite these expressions as

$$\vec{E}(\vec{r},\omega) = -j\omega\mu \int_{V_S} \vec{J}(\vec{r}',\omega)\frac{e^{-jkR}}{4\pi R}\,\mathrm{d}V' - \nabla \int_{V_S} \left(\frac{\nabla'.\vec{J}(\vec{r}',\omega)}{-j\omega}\right)\frac{e^{-jkR}}{4\pi\epsilon R}\,\mathrm{d}V' \quad (2.26)$$

$$\vec{H}(\vec{r},\omega) = \nabla \times \int_{V_S} \vec{J}(\vec{r}',\omega)\frac{e^{-jkR}}{4\pi R}\,\mathrm{d}V'. \quad (2.27)$$

The corresponding expressions in the time domain can be obtained by performing the inverse Fourier transform. From Equations (2.26), (2.27) we see that we will require the time domain counterpart of the frequency domain scalar Green's function

$$g(\vec{r},\vec{r}',\omega) = \frac{e^{-j\frac{\omega}{c}R}}{R} \quad (2.28)$$

which can be obtained analytically as

$$g(\vec{r},\vec{r}',t,t') = \frac{\delta(t-t'-R/c)}{R}. \quad (2.29)$$

This time domain scalar Green's function is the solution for the corresponding time domain scalar wave equation

$$\left(\nabla^2 - \frac{1}{c^2}\frac{\partial^2}{\partial t^2}\right) g(\vec{r},\vec{r}',t,t') = -4\pi\delta(\vec{r}-\vec{r}')\delta(t-t'). \quad (2.30)$$

It describes a spherical wavefront generated by the source at $\vec{r}', t'$ and traversing the distance $R = |\vec{r} - \vec{r}'|$ at a finite propagation speed c to be detected at $\vec{r}, t$. This time delay $t - t' = R/c$ was described in the frequency domain by the phase shift e^{-jkR}.

By the properties of the Fourier transform, the fields in the time domain are convolutions of the source distributions $\vec{J}(\vec{r}',t')$, $\rho(\vec{r}',t')$ with the spherical wavefronts of Equation (2.29) that can be evaluated in closed form as

$$\vec{E}(\vec{r},t) = -\frac{\partial}{\partial\tau}\frac{\mu}{4\pi}\int_{V_S}\frac{\vec{J}(\vec{r}',\tau)}{R}\,\mathrm{d}V' - \nabla\frac{1}{4\pi\epsilon}\int_{V_S}\frac{\rho(\vec{r}',\tau)}{R}\,\mathrm{d}V' \quad (2.31)$$

$$\vec{H}(\vec{r},t) = \nabla \times \frac{1}{4\pi}\int_{V_S}\frac{\vec{J}(\vec{r}',\tau)}{R}\,\mathrm{d}V' \quad (2.32)$$

where the retarded time τ is given by

$$\tau = t - |\vec{r} - \vec{r}'|/c. \quad (2.33)$$

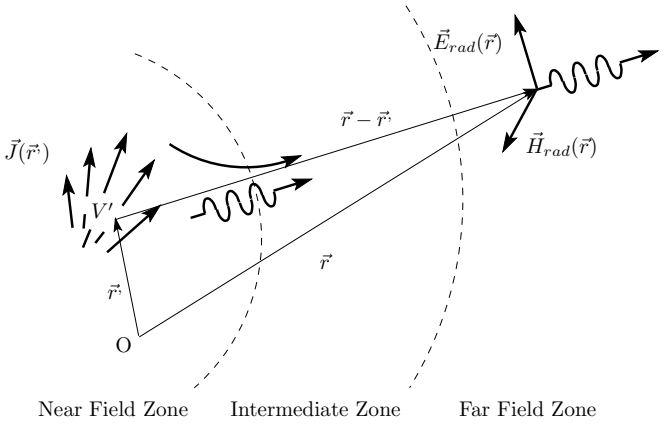

Figure 2.2: Radiation and evanescent fields generated by a source distribution $\vec{J}(\vec{r}')$.

2.6 Electromagnetic Radiation

One particularly important type of electromagnetic field is the radiation field. Its main characteristics are that it is the dominant field component at large distances from a localised source distribution, and that it is able to transfer energy generated by the source to very large distances. This phenomenon is thus the physical basis of all wireless communications devices.

2.6.1 The Macroscopic Point of View

From the frequency domain expressions Equations (2.26) and (2.27), the dominant field components at large distance R can be determined as

$$\vec{E}_{rad}(\vec{r},\omega) = j\omega\mu \int_{V'} \frac{(\vec{r}-\vec{r}')\times(\vec{r}-\vec{r}')\times\vec{J}(\vec{r}',\omega)}{R^3}\frac{e^{-jkR}}{4\pi}\,\mathrm{d}V' \tag{2.34}$$

$$\vec{H}_{rad}(\vec{r},\omega) = -\frac{j\omega}{c}\int_{V'} \frac{(\vec{r}-\vec{r}')\times\vec{J}(\vec{r}',\omega)}{R^2}\frac{e^{-jkR}}{4\pi}\,\mathrm{d}V'. \tag{2.35}$$

From these formulas, we obtain the main characteristics of the radiation field. The field decays only as $1/R$. Real power is carried away radially from the localised source distribution, while reactive energy is stored locally in the immediate surrounding of the source distribution. The amount of radiation is proportional to ω^2. Radiation is thus typically generated at very high frequencies. The situation is depicted in Figure 2.2. However, this macroscopic frequency domain point of view gives very little information about the mechanism and exact location at the source responsible

for the generation of the radiation field. A time domain approach can reveal more details on these topics.

From the time domain expressions Equations (2.31) and (2.32), the radiation field becomes

$$\vec{E}_{rad}(\vec{r},t) = \frac{\mu}{4\pi}\int\limits_{V'} \frac{(\vec{r}-\vec{r}')\times(\vec{r}-\vec{r}')\times\dfrac{\partial\vec{J}(\vec{r}',\tau)}{\partial\tau}}{R^3}\,\mathrm{d}V' \tag{2.36}$$

$$\vec{H}_{rad}(\vec{r},t) = -\frac{1}{4\pi c}\int\limits_{V'} \frac{(\vec{r}-\vec{r}')\times\dfrac{\partial\vec{J}(\vec{r}',\tau)}{\partial\tau}}{R^2}\,\mathrm{d}V'. \tag{2.37}$$

Radiation is thus generated by any current which varies sufficiently fast in time. The location at the source where the radiation is generated can now be traced accurately by relating the appearance of a radiation field to a strong variation of the current at a position determined by the appropriate time delay τ.

2.6.2 The Microscopic Point of View

A more detailed study at the microscopic level can be done by considering the current as the movement of elementary charge carriers q with a velocity $\vec{v}$.

$$\vec{J}(\vec{r},t) = q\vec{v}(\vec{r},t) \tag{2.38}$$

To obtain the generally valid expressions for the complete field of a point charge moving in an arbitrary fashion, we need to trace the exact trajectory of the moving charge, an analysis which was performed by Liénard and Wiechert [39], [40], [41], [42] already in 1898. Their expressions are valid for all velocities. For small velocities $v << c$, the radiation field is correctly given by inserting Equation (2.38) into Equations (2.36) and (2.37) such that one has to consider an integrated charge acceleration product

$$\int\limits_{V'} q\vec{a}(\vec{r}',\tau)\,\mathrm{d}V'. \tag{2.39}$$

This shows that a charge moving in a straight line with constant velocity $\vec{v}$ produces no radiation field. Only at the instant when the charge carrier undergoes acceleration a wavefront is generated capable of transferring energy to very large distances. Although completely rigorous, this microscopic point of view is exceedingly difficult to apply to macroscopic engineering problems. This is so because in such problems, the movement of the charges is almost impossible to trace and generally occurs at very small velocities ($v << c$). The radiation phenomenon is more generated by a wave traveling close

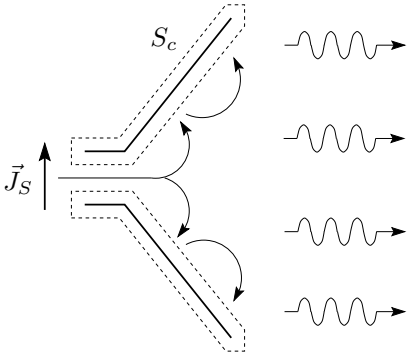

Figure 2.3: The boundary value problem for a generic antenna.

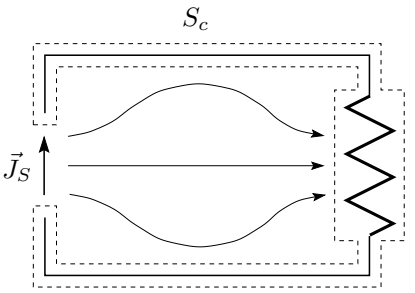

Figure 2.4: The boundary value problem for a generic circuit.

the speed of light c in a charge-sea of which the individual charges move hardly at all (similar to a sound wave in a material medium) . Due to the large number of charges involved, all fields have to be added together.

Detailed studies [43], [44], [45], [46], [47], [48] reveal that radiation is typically generated at the excitation points of the structure, open ends where reflection occurs and sharp corners where current flow is strongly curved. On long straight pieces of antennas or transmission lines in circuits, almost no radiation is generated.

2.7 The Boundary Value Problem

Numerical techniques in electromagnetics have typically been developed to deal with antenna and radiation problems. However, they are increasily being applied to rigorously analyse phenomena in electronic circuits which are not only radiation but also even more complicated near field interaction problems. The mathematical formulation of Section 2.5 is a rigorous description of all phenomena in both the antenna and circuit domain.

2.7.1 The Antenna Problem

Figure 2.3 depicts the boundary value problem for a generic antenna problem. The imposed current distribution $\vec{J}_S$ supplies energy to the metallic scatterer delimited by the surface S_c. As a consequence of the fields generated by the source, charges on the metallic surface will move and produce a current and this process generates an additional "scattered" electromagnetic field. Energy supplied by the source can be thought of as divided in two parts. One part can be thought of as being stored in the "potential" energy due to spatial separation and "kinetic" energy due to the

movement of the charges on the scatterer surface S_c. An equivalent point of view is that this energy is stored in the reactive electric and magnetic non-radiating near fields. The metallic surface thus acts as a guiding structure for near field energy propagation. The other part of the energy is "lost" by driving the acceleration of the charges on the surface. Equivalently, this energy is found in the radiation far field. The metallic surface thus also reflects real energy into the far field [43].

Generally, the geometry of the antenna is optimised to convert the energy of the source as efficiently as possible into radiation. This requires the dimensions of the antenna to be of the same size as the wavelength of the radiation. The antenna problem is typically a "high" frequency problem.

2.7.2 The Circuit Problem

On the other hand, typical electrical circuits operate at low enough frequencies such that one can (up to now) assume an almost static situation. The size of electrical circuits is typically much less than the wavelength. Such a problem is depicted in Figure 2.4

In this case, the field generated by the source induces an almost static electric charge distribution on the surface of the conducting wires of the circuit. This induced charge distribution produces a second "scattered" field. The total electrostatic field set up as a result drives the current on the wire surface, which is a magnetostatic DC current [49]. The DC power supplied by the source can be thought of as being carried by the current and converted into heat in the load resistor [50], [51]. Equivalently, the energy can be thought of as being carried by the electrostatic and magnetostatic fields outside of the wires which guide the energy through the surrounding space to enter the load resistor sideways [41], [42], [52] where it is dissipated.

As the frequency at which the source drives the circuit increases however, the charge distribution is no longer static, but has to be altered continuously to support the current. The current is no longer magnetostatic but changes in time also. The energy associated with these slow charge build up and movement is reactive and can also be thought of as being stored in the electric and magnetic near fields of the circuit. It is accounted for in a first order approximation by adding discrete capacitors and inductors to the circuit (or equivalently, these phenomena will manifest themself first in the parts of the circuits designed specifically for this purpose, the capacitors and inductors.)

As the frequency continues to increase however, this first order approximation will falter, as the operation of the circuit will be determined by the full details of the geometry of the circuit and its surrounding. Apart from energy transfer to the load, some energy is also converted into radiation. In such a case, a rigorous description can only be obtained by accurately determining the complete charge and current distribution everywhere.

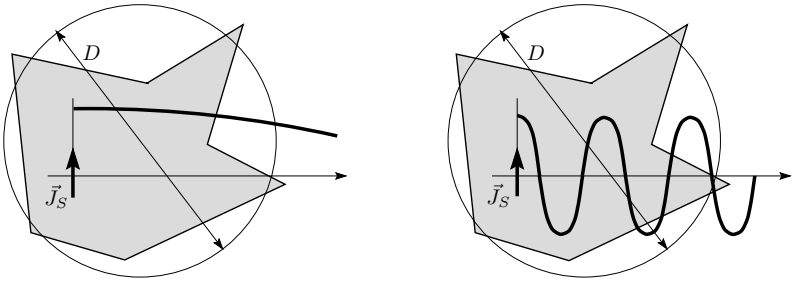

(a) A "low" frequency problem.

(b) A "high" frequency problem.

Figure 2.5: Whether or not the "wave" nature of the field has to be taken into account depends on the frequency applied by the source and the physical size of the problem domain.

Generally, an electric circuit is designed to transfer the energy generated by the source as efficiently as possible to the load, or to perform a desired operation on it by manipulating the electric and magnetic effects of the circuit. The production of radiation is considered to be an undesirable side effect.

2.8 The "Wave" Nature of the Field

The wave Equations (2.10),(2.11) explicitly demonstrate that the electromagnetic field is always a "waving" field. For real life applications, the question arises when this wave nature has to be taken into account [53].

Consider a geometrical structure, whether an antenna or a circuit, with a fixed characteristic dimension D as depicted in Figure 2.5. A source $\vec{J}_S$ generates a field with sinusoidal time dependence $\sin \omega t$ at a frequency $f = \omega/2\pi$ which spreads out over the object. The field observed at the edge of the object varies as $\sin \omega(t - D/c)$. The deviation of the field at the edge of the object with that at the source position is measured by the phase difference which can be written as

$$\frac{D/c}{1/f} = \frac{T_{travel}}{\Delta T_{source}} = \frac{D}{c/f} = \frac{D}{\lambda} \tag{2.40}$$

with T_{travel} the travel time over the object, ΔT_{source} the characteristic time interval over which the source changes, and λ the wavelength. To judge whether the wave nature of the field has to be taken into account, all time intervals have to be compared to ΔT_{source}, and all dimensions normalized to the wavelength λ.

If the excitation occurs at a very low frequency as in Figure 2.5(a), then $T_{travel} << \Delta T_{source}$, which means that the field at the edge assumes a value determined almost

instantaneously by the value imposed by the source, without any time delay. Alternatively, the size of the object becomes very small $D << \lambda$, such that the spatial variation of the field over the object due to wave effects can be neglected. The spatial resolution with which the field can detect geometrical and material details is very small. The structure can often be characterised by a single number, typically obtained from a "no wave" quasi-static analysis.

With a very high frequency excitation, we have $T_{travel} >> \Delta T_{source}$, such that when the field reaches the edge of the structure, the source has already changed considerably and this time delay has to be taken into account. Alternatively, the object becomes large $D >> \lambda$ compared to the wavelength. The field shows a strong spatial variation and its spatial resolution is now so high that all geometrical and material details affect the total solution. Only a "full wave" solution involving a large number of unknowns can accurately describe this situation.

2.9 Macroscopic Measurable Quantities

The complete solution of a boundary value problem provides three dimensional vector field and current distributions. However, from the point of view of an experimenter or an everyday electrical engineer, it is very difficult to measure such vector fields directly and to correlate them to his problem at hand. It is therefore required to reduce the complete solution to observable quantities which can be measured simpler and directly. This is achieved with the "reaction" concept [54], [55], [56] which links the complete vector field solutions to simple quantities familiar from classical circuit and network theory.

2.9.1 Impedance Z-parameters

In order to extract a measurable quantity from a complicated boundary value problem, an excitation current source $\vec{J}_S$ has to be imposed over small volume V_S as depicted in Figure 2.6. From the solution of the boundary value problem, the resulting field at the source distribution $\vec{E}(\vec{J}_S)$ is then measured by integrating it with the source distribution and this quantity characterises the "reaction" of the whole structure to the impressed source. The generalised impedance

$$Z = -\frac{1}{I_S^2} \int_{S'} \vec{E}(\vec{J}_S).\vec{J}_S \, \mathrm{d}S' \tag{2.41}$$

is just this "reaction" normalized by a factor $I_S = |\int_{S'} \vec{J}_S \, \mathrm{d}S'|$ to make it independent of the amplitude of the chosen excitation. It is a single complex number determined by the frequency, the complete geometry of the structure and its surrounding. If the

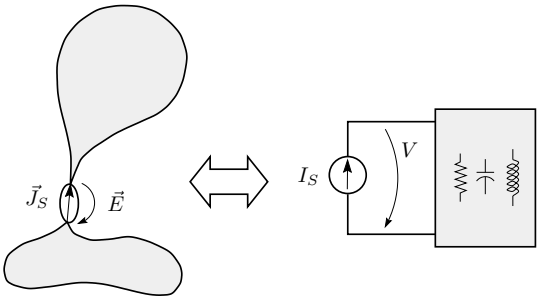

Figure 2.6: Generalised network parameters can be extracted from the total field solution of the boundary value problem.

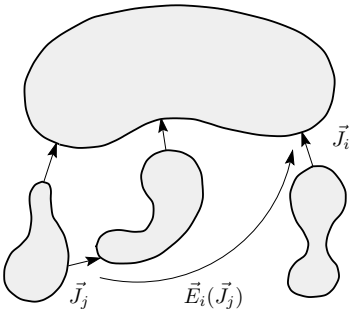

Figure 2.7: Multiport electromagnetic boundary value problem.

volume V_S is small compared to the wavelength, the generalised impedance is just the familiar impedance $Z = V/I_S$ as the ratio of the voltage V resulting from applying an imposed lumped current source I_S. The power generated by the source current becomes

$$P = -\int_{S'} \vec{E}.\vec{J}_S^* \, \mathrm{d}S' = V I_S^*. \tag{2.42}$$

The concept can be generalised for N ports [55] or volumes V_j as depicted in Figure 2.7. In this case the mutual impedance Z_{ij} measures the reaction at port i from the excitation at port j

$$Z_{ij} = -\frac{1}{I_i I_j} \int_{S_i} \vec{E}_i(\vec{J}_j).\vec{J}_i \, \mathrm{d}S_i \tag{2.43}$$

which by proper normalization is independent of the amplitude of the observation and source distributions $\vec{J}_i$, $\vec{J}_j$.

2.9.2 Scattering S-parameters

The impedance Z_{ij} is mostly used to characterise low frequency circuits and simple antennas. For more complicated microwave network problems, scattering or S-parameters are used. They are especially useful when the actual excitation for the experimental situation is done with a transmission line. A transmission line can be any structure specifically designed to transport electromagnetic energy from one point to another as depicted in Figure 2.8. Its longitudinal dimensions are typically much larger than its transverse dimensions. In a transverse cross section of the line, multiple conductors and/or material discontinuities are used to capture and confine the

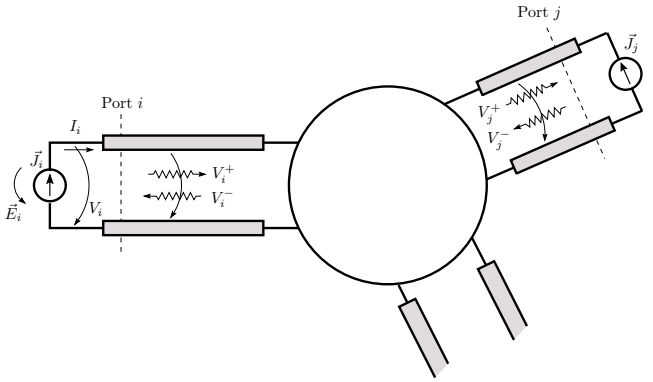

Figure 2.8: Extraction of scattering or S-parameters from the full wave solution of the boundary value problem.

energy and to force it to propagate along the length of the structure. The propagating field can be decomposed into a forward (incident) and backward (reflected) wave as depicted in Figure 2.8. The $\vec{E}$, $\vec{H}$ field patterns of the traveling waves can be translated into circuit theoretical voltage and current waves [57], [58] in terms of which the S-parameters can be defined as

$$S_{ij} = \frac{V_i^-}{V_j^+} \tag{2.44}$$

the ratio of the outgoing wave on port i to the incident wave on port j.

These S-parameters can be obtained from a full-wave electromagnetic simulation by inserting a physical piece of the transmission line as part of the boundary value problem. The excitation at the fundamental level remains a "small" current source located at the beginning of the line. The length of the transmission line between the excitation point and the central part of the scatterer or circuit has to be sufficiently long to allow the eigenmode field distribution to be built up naturally. It then becomes possible to relate the fields and currents at the actual excitation points to the traveling waves on the transmission line and thus convert the originally computed Z-parameters into the desired S-parameters. This is called a "de-embedding" procedure. The S-parameters can be measured directly as complex numbers by a vector network analyser.

2.10 Conclusions

In this chapter, we have repeated Maxwell's equations as the mathematical foundation to describe all electromagnetic phenomena at a macroscopic level. They directly

constitute the basis for the Finite Element Method (FEM) and FDTD (Finite Difference Time Domain) numerical methods discussed in the next chapter. The solution of the wave equations in integral form allowed to introduce the concept of the Green's function, which describes how the electromagnetic interaction is carried over larger distances with the finite velocity of light. This formulation will lead to the Boundary Integral Equation (BIE) approach derived further in Chapter 3. The integral solutions allowed to discuss the radiation field, typically occurring in high frequency antenna problems, but this is not the only important wave phenomenon. Whenever the size of the problem domain is large compared to the wavelength, or when the field varies so rapidly that the occurring time delay can no longer be neglected, a complete solution of the boundary value becomes necessary. This problems emerges at the moment in electronic circuits. Finally, it was shown how the total field solution for a given problem is reduced into quantities like impedance Z and scattering S parameters which can be measured directly at a macroscopic level.

Chapter 3

Numerical Methods for Electromagnetics

3.1 Introduction

In this chapter, we present a short overview of the most commonly used computational techniques that are based on Maxwell's equations to simulate circuit and antenna behaviour at the most fundamental electromagnetic level. These are the so called "full wave" techniques. This means that no fundamental approximations are made in the formulation stage of the problem although the subsequent numerical solution on a computer may require more subtle approximations.

A reason for exploring the underlying principles of numerical techniques is to provide a more general background which will enable one to fit the specific approach presented in this work into the overall scheme of computational electromagnetics. The present discussion gives a short overview of the theoretical basis, the solution algorithm used and some problems and limitations of the most common numerical techniques. Some of the validation presented in Chapter 8 will also include results obtained with commercial full wave solvers which are based on the numerical techniques presented here.

The available full wave numerical techniques can be classified at the highest level according to whether the problem is formulated in the time domain or frequency domain (Section 3.2) and whether the mathematical description of the electromagnetic problem is differential equation or integral equation based (Section 3.3).

A list of some available commercially full wave solvers is given in Section 3.6.

3.2 Frequency versus Time Domain

Historically, almost all theoretical work has been performed in the frequency domain [59]. This is because closed-form time domain solutions are almost impossible to obtain [43]. By assuming a sinusoidal time dependence, the time dimension can be eliminated as independent variable while its Fourier transformed counterpart frequency is just a parameter in the computation. The physical time delay is transformed into a phase shift. Only the spatial variation of the problem has to be sampled. Dispersive material characteristics are easily included in the frequency domain. The further analytical analysis often requires further simplifying assumptions on problem geometry, boundary conditions and material properties. Growing computational resources have transformed the evaluation of analytical formulas into problem specific and consequently highly efficient frequency domain field solvers [59]. Initially, time domain or transient data was generated by using frequency domain solvers to compute a pre-established range of frequencies and perform an inverse Fourier transform.

However, increasing speed and memory of computers made it possible to model the behaviour of 3D electromagnetic fields directly in the time domain. The independent time variable now also has to be sampled. The solution is formulated from the outset in algorithmic form, with a minimum of analytical preprocessing. The algorithm mimics the space-time behaviour of the field with a Marching on in Time (MoT) approach, making it very suited for parallel and vector computers. No matrix inversion is thus required. Less geometrical and material restrictions are imposed at the cost of larger computational requirements. A single computation with a smooth pulse excitation can provide wide-band frequency data, although the computation has to be redone for each new excitation. Non-linear effects are more easily modeled in the time domain. Perhaps the most attractive feature of direct time domain modelling is the opportunity for improving our insight into the physical behaviour of electromagnetic fields by studying them directly in space-time, the natural dimensions in which dynamic physical events take place.

3.3 Differential versus Integral Equation Methods

Differential equation methods are derived directly from Maxwell's curl equations or the Helmholtz wave equations with little analytical preprocessing. Consequently, arbitrary geometries and material inhomogeneities can be handled. The field has to be sampled and stored over a 3D space. Due to finite computer memory resources, the computational domain has to be truncated. These methods are thus inherently better suited for closed shielded problems. For open radiating structures, special absorbing or radiation boundary conditions have to be formulated. The differential equation describes local interactions between contiguous field samples, resulting in sparse matrix representations. However, for a given problem, the number of samples is considerably larger than for an integral equation description.

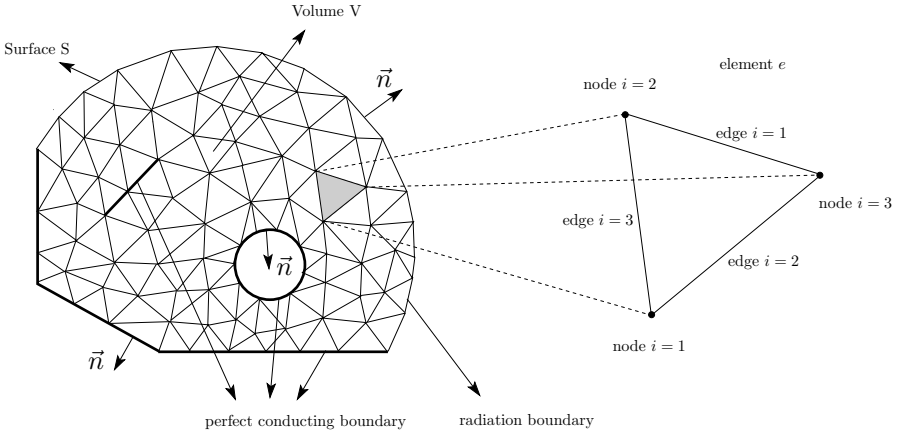

Figure 3.1: Typical FEM mesh with basisfunctions defined on small triangular (2D) or tetrahedral (3D) regions called elements. Location of nodes i and edges i associated with one of the elements e.

The formulation of an integral equation demands extensive analytical preprocessing. First, a Green's function that incorporates the geometry and material characteristics of the surrounding medium has to be determined, preferably in closed form. This makes the formulation problem specific but computationally more efficient and physically more robust. Secondly, application of Green's theorem as in Chapter 2 allows to express the field as an integral of the surface currents. Automatic inclusion of the radiation condition makes the method ideally suited for open radiation problems. The current has to be sampled over a 2D surface, reducing the number of unknowns. However, the Green's function makes all current samples interact with each other giving full matrix representations.

3.4 Differential Equation Based Methods

The most popular differential equation based methods are the Finite Element Method (FEM) described in Section 3.4.1, which is used almost exclusively in the frequency domain, and the Finite-Difference Time Domain (FDTD) technique described in Section 3.4.2.

3.4.1 Finite Element Method (FEM)

The finite element method is widely used in all branches of engineering [60]. It was first introduced into electrical engineering for solving waveguide problems [61]. The

defining feature of the finite element method lies in the choice of special expansion functions, defined over small triangular (2D) or tetrahedral (3D) regions of the computational domain as in Figure 3.1. These allow a practically unlimited capability to conform to complex geometries and material inhomogeneities. The discretisation of the problem typically gives very large but sparse matrix equations which can be solved efficiently with iterative techniques.

Basic Formulation

In literature, the FEM is often derived from a variational point of view where we seak minima and maxima of (energy) functionals. Since the energy interpretation is not readily available in electromagnetics and to stress the similarity of FEM with the solution of integral equations, a method of moments based formulation will be given. The Helmholtz wave equation for the electric field

$$\nabla \times \nabla \times \vec{E} - k^2 \vec{E} = -j\omega\mu\vec{J} \tag{3.1}$$

is enforced in an average sense by integrating it with certain weighting functions $\vec{W}_m$ over the entire domain

$$\int_V \vec{W}_m . \left(\nabla \times \nabla \times \vec{E} - k^2 \vec{E} + j\omega\mu\vec{J} \right) \, \mathrm{d}V = 0. \tag{3.2}$$

This equation is cast into a 'weak' form by using $\nabla.(\vec{A}\times\vec{B}) = \vec{B}.(\nabla\times\vec{A}) - \vec{A}.(\nabla\times\vec{B})$ to shift one derivative to the testing functions

$$\int_V \nabla \times \vec{W}_m . \nabla \times \vec{E} \, \mathrm{d}V - k^2 \int_V \vec{W}_m . \vec{E} \, \mathrm{d}V + \int_S \vec{W}_m . \vec{n} \times \nabla \times \vec{E} \, \mathrm{d}S = -j\omega\mu \int_V \vec{W}_m . \vec{J} \, \mathrm{d}V. \tag{3.3}$$

With $\nabla \times \vec{E} = -j\omega\mu\vec{H}$, the third term in the above equations now incorporates the boundary conditions on the tangential magnetic field over the limiting surface S into the basic equations and this is an essential aspect of a FEM formulation. Since these are not known a priori at the boundary radiation or absorbing boundary conditions must be applied. The last term is the forcing function with the known excitation $\vec{J}$.

Node and Edge Based elements, Spurious Solutions

To discretise Equation (3.3), the field is expanded using subdomain functions defined on the rectangular (or tetrahedral) domains of Figure 3.1 which are called elements.

$$f = \sum_{e=1}^{N_e} \sum_{n=1}^{nodes} F_n^e f_n^e, \qquad \vec{E} = \sum_{e=1}^{N_e} \sum_{n}^{edges} E_n^e \vec{E}_n^e \tag{3.4}$$

For a scalar function f, the edge based elements f_n^e of Figure 3.2 are used, while the vector field $\vec{E}$ is expanded with vectorial functions. The expansion function f_n^e is a

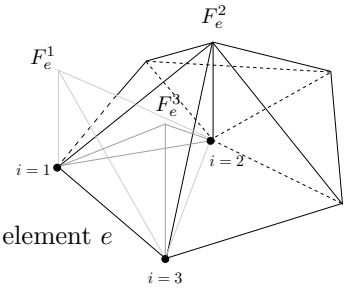

Figure 3.2: Node base elements to expand a scalar function f.

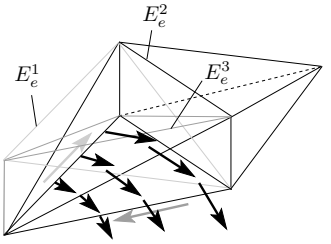

Figure 3.3: Edge based elements to expand a vector field $\vec{E}$.

typical hat function with unity value at node i of element e and F_n^e is its unknown amplitude as depicted in Figure 3.2. A scalar representation naturally enforces a continuous field representation. The use of node based elements to expand each component of a vector field has long hampered the breakthrough of FEM for vectorial field problems. Not only does it make the imposition of vector boundary conditions cumbersome, the solution is also corrupted by the appearance of non-physical spurious modes [62], [63]. These spurious modes are not just an accuracy problem (they do not go away by decreasing cell size) [64], but are a fundamental problem of the scalar continuous field representation. The physical vector field only requires continuity of the tangential field components, but allows for discontinuous normal components. It was found that the vector nature of the field is best incorporated already into the basis functions [65] by using an expansion such as the one depicted in Figure 3.3. The vectorial expansion function is now associated with an edge n (opposite to node n). Its tangential component along edge n is constant and unity while it is zero along the other edges. The normal component varies linearly along edge n. Its amplitude is given by E_n^e. These expansion functions are called "Whitney" elements [66], "curl conforming" elements [67], or "edge based" elements [68].

Element Equations

Equation (3.3) is now discretised into a matrix equation by inserting the expansion (3.4). The Galerkin method is obtained when the weight functions equal the expansion functions $\vec{W}_m = \vec{E}_m^e$. Instead of directly working this out, it is computationally more advantageous to compute all combinations for the elements separately, which amounts to leaving out the sum over the elements at this stage. This gives the element matrix equations for each rectangle/tetrahedron

$$\left\{[A^e] - k^2\,[B^e]\right\}[E^e] = [C^e] \tag{3.5}$$

where

$$A_{mn}^e \;=\; \int_{V_e} \nabla \times \vec{E}_m . \nabla \times \vec{E}_n \; \mathrm{d}V$$

$$\begin{aligned} B^e_{mn} &= \int_{V_e} \vec{E}_m.\vec{E}_n \, \mathrm{d}V \\ C^e_m &= -j\omega\mu \int_{V_e} \vec{E}_m.\vec{J} \, \mathrm{d}V. \end{aligned} \tag{3.6}$$

These integrals can usually be evaluated in closed form since the basis functions are polynomials over triangular domains. This is done conveniently by expressing the basis functions with simplex coordinates [64]. The surface integral in Equation (3.3) only gives a contribution when the element e is located at the boundary of the domain. In this cases it gives extra contributions to A^e and B^e when a radiation or absorbing boundary condition is used, and a contribution to C^e when it represents an incident field at the boundary.

Assembly of the Matrix Equation

Reintroducing the sum over the elements corresponds to consolidating the equations for adjacent elements into a single equation for each node or edge, such that it corresponds to the overlap of the actual basis functions. A global matrix equation

$$\left\{[A] - k^2 [B]\right\} [E] = [C] \tag{3.7}$$

which is very sparse is obtained.

Excitation and Boundary Conditions

The excitation of the field can be a volumetric source distribution represented by $\vec{J}$ in Equation (3.3). It can also be an incident field $\vec{E}_i$ at the boundary of the domain which can be incorporated through the surface integral of (3.3). In such a case, the total field formulation has to be converted into a scattered field problem by inserting $\vec{E} = \vec{E}^{in} + \vec{E}^{scat}$ and rearranging terms [63].

Perfect electric conductors in the computational domain or at the boundary are easily modeled when vector tangential elements are used to expand the electric field. Since this tangential component has to be zero on the conducting surface, the corresponding coefficients are simply put equal to zero and disappear from the matrix equation.

Radiation (RBC) and Absorbing (ABC) Boundary Conditions

For open radiation and scattering problems, the size of the computational domain has to be constrained. Special conditions have to be imposed on the boundaries of the domain to simulate an infinite domain without causing unphysical reflection of the field at the truncation.

Radiation Boundary Conditions (RBC's) can be expressed in the form of surface integral equations that relate tangential electric and magnetic fields over the boundary surface. This leads to hybrid finite element - boundary integral equations [69], [70]. Such a formulation is exact and can be enforced even very close in the "near field" of

the scatterer but unfortunately they express a global radiation condition that couples information around the entire boundary. The extra fill-in requires extra computation time and strongly reduces the sparse nature of the FEM matrix.

The sparse character of the FEM matrix can be conserved by using local Radiation Boundary Conditions (RBC's). They are only approximate in nature and this also requires that they be employed at a certain distance of the wave-structure interaction region thus enlarging the computational domain. They are incorporated in the FEM formulation through the surface integral of Equation (3.3)

$$\int_S \vec{E}.\vec{n} \times \nabla \times \vec{E} \; \mathrm{d}S = -j\omega\mu \int_S \vec{E}.\vec{n} \times \vec{H} \; \mathrm{d}S \approx \int_S \vec{E}.P(\vec{E}) \; \mathrm{d}S. \tag{3.8}$$

We have to find an expression $P(\vec{E})$ that expresses the tangential magnetic field or the tangential component of $\nabla \times \vec{E}$ as a function of the tangential $\vec{E}$-field and its higher order derivatives on the boundary, and simultaneously simulates the local outgoing wave nature of the field. The order of the derivatives in the expression $P(\vec{E})$ determines the order of the RBC. The higher the order, the better the accuracy of the RBC, allowing a nearer placement to the scatterer at the expense of increased complexity for its evaluation. The simplest 0^{th} order radiation boundary condition in cylindrical coordinates amounts to no more than the Sommerfeld radiation condition

$$\lim_{\rho \to \infty} \frac{\partial E}{\partial \rho} = -jkE. \tag{3.9}$$

Higher N^{th} order scalar RBC's for a 2D circular boundary were given by Bayliss-Turkel [71]

$$\prod_{n=1}^{N} \left(jk + \frac{\partial}{\partial \rho} + \frac{4n-3}{2\rho} \right) E = 0. \tag{3.10}$$

These conditions were extended to be applied with the vector Helmholtz equation on a 3D spherical surface [72], [73]. Vector absorbing boundary conditions for arbitrarily shaped boundary's can be worked out [74], [75], but still are only valid for near normal incidence far away from the scatterer.

The energy of a field incident on the boundary can also be dissipated by wrapping the computational domain with a layer of lossy absorbing material (ABC's), thus creating a numerical anechoic chamber. These absorbers usually consist of artificial non-physical materials of which the material parameters are tuned to obtain low reflection coefficients [76], [77]. An important artificial absorber with very low reflection and high absorption was developed by Bérenger [78] within the context of FDTD techniques and will be discussed there. Its application for FEM mesh truncation is still under investigation.

Accuracy : Higher Order and Parametric Elements, Numerical Dispersion

The discretisation error is the difference between the solution of the continuous problem and its discrete representation. While it is true that it is determined by the electrical size of the elements, more considerations have to be taken into account.

A great reduction of error and faster convergence can be obtained by using higher order polynomials within an element to give a smoother representation of the field on the cell [79]. The modelling flexibility of FEM can be improved further with the use of basis functions defined on cells with curved edges themselves, the so called "parametric" elements [80].

For a fixed spatial discretisation, overall accuracy tends to degrade with increasing size of the computational domain [81]. For these cases, numerical dispersion dominates the overall error. The speed of a wave in free space does not depend on frequency. The spatial discretisation procedure alone makes speed depend on frequency. Waves therefore propagate at the wrong velocity, yielding a progressive and cumulative phase error the farther the waves propagate [82]. The error also depends on the direction of propagation (grid anisotropy) [83]. For large domains, the use of highly complicated RBC's may therefore be of little effect. It also compromises the generally claimed superior scaling properties of FEM with problem size since to maintain a fixed accuracy we need to decrease element size on top of the already present increase of the number of cells with the extension of the domain.

3.4.2 Finite-Difference Time Domain (FDTD)

The Basic Algorithm

The FDTD method starts straight from Maxwell's source-free curl equations

$$-\mu \frac{\partial \vec{H}}{\partial t} = \nabla \times \vec{E} \tag{3.11}$$

$$\epsilon \frac{\partial \vec{E}}{\partial t} = \nabla \times \vec{H}. \tag{3.12}$$

From a numerical point of view, this is a set of coupled hyperbolic advection equations [84]. These are discretised by approximating the continuous differential operators by centered difference approximations in both space and time. For a full 3D field distribution on a rectangular Cartesian grid this can be achieved by using a spatial staggered grid for the electric and magnetic field as proposed by [85]. Figure 3.4, depicts an elementary "Yee cell". The main grid lines coincide with the position of the electric field variable and are tangential with them. The size of the cell is $\Delta x, \Delta y, \Delta z$, and the coordinates are indicated by indices i, j, k. The central difference for the time derivatives with time step Δt requires that $\vec{E}$ is computed at integer time steps n, while $\vec{H}$ is determined at half integer time points. This allows a "leap-frog" time

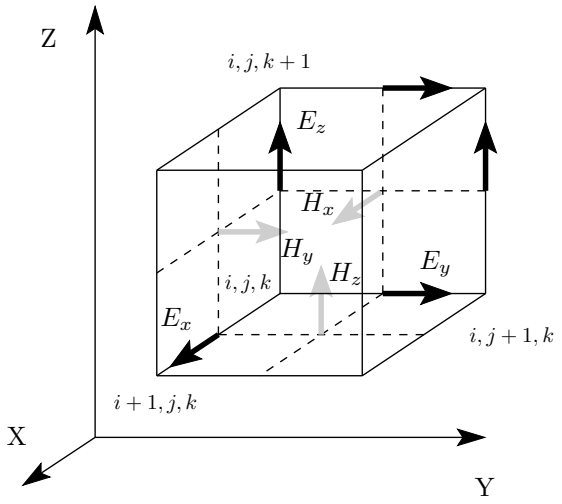

Figure 3.4: The elementary "Yee cell" with the spatial staggered arrangement of the electric and magnetic field components.

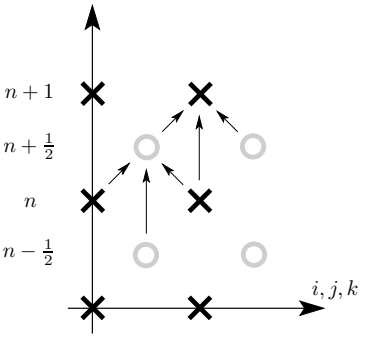

Figure 3.5: "Leap frog" time integration for advancing the fields in time.

integration [84] as depicted in Figure 3.5, where a field is advanced in time by using information of the complementary field type at an intermediate time point. Using the simplified notation

$$F(i\Delta x, j\Delta y, k\Delta z, n\Delta t) = F^n_{i,j,k} \tag{3.13}$$

the resulting finite-difference approximations for the X component of Maxwell's Equations (3.11) and (3.12) are

$$\begin{aligned} H^{n+\frac{1}{2}}_{x\ i,j+\frac{1}{2},k+\frac{1}{2}} &= H^{n-\frac{1}{2}}_{x\ i,j+\frac{1}{2},k+\frac{1}{2}} + \frac{\Delta t}{\mu\Delta z}\left(E^n_{y\ i,j+\frac{1}{2},k+1} - E^n_{y\ i,j+\frac{1}{2},k}\right) \\ &\quad - \frac{\Delta t}{\mu\Delta y}\left(E^n_{z\ i,j+1,k+\frac{1}{2}} - E^n_{z\ i,j,k+\frac{1}{2}}\right) \qquad (3.14) \\ E^{n+1}_{x\ i+\frac{1}{2},j,k} &= E^n_{x\ i+\frac{1}{2},j,k} + \frac{\Delta t}{\epsilon\Delta y}\left(H^{n+\frac{1}{2}}_{z\ i+\frac{1}{2},j+\frac{1}{2},k} - H^{n+\frac{1}{2}}_{z\ i+\frac{1}{2},j-\frac{1}{2},k}\right) \\ &\quad - \frac{\Delta t}{\epsilon\Delta z}\left(E^{n+\frac{1}{2}}_{y\ i+\frac{1}{2},j,k+\frac{1}{2}} - E^{n+\frac{1}{2}}_{y\ i+\frac{1}{2},j,k-\frac{1}{2}}\right). \qquad (3.15) \end{aligned}$$

Similar expressions for the Y and Z components can be derived by inspection from Figures 3.4 and 3.5.

Excitation and Perfect Conducting Surfaces

The excitation of the problem can be an internal source or an incident field. An internal current source can be incorporated by including the source term into the

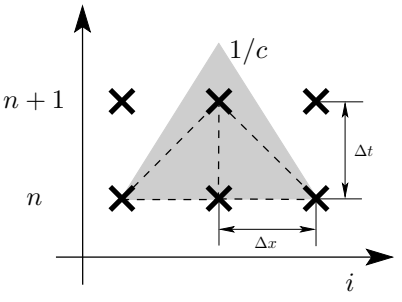

Figure 3.6: Explicit method with CFL stability condition.

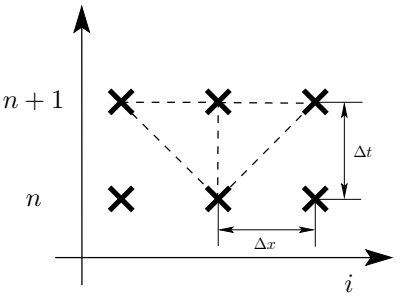

Figure 3.7: Unconditionally stable implicit method.

Maxwell Equation (3.12) also in discretised form and imposing its value [64]. In case of an incident field from a remote source, a plane wave field can be imposed at the boundaries of the computational domain [64]. Other excitation methods like imposing guided wave field patterns in a transmission line are also possible [86]. The excitation is usually a Gaussian pulse of which the pulse width is adjusted to cover the desired frequency spectrum.

Perfect conducting surfaces are fairly easily incorporated if the boundary coincides with the main grid lines of the Yee lattice. In this case the tangential electric field at the boundary is simply put to zero throughout the computation.

Stability, Explicit and Implicit Methods

A solution is called stable when it does not grow unbounded as time progresses. The "leap-frog" time integration of the basic algorithm is an explicit method : the field value at a certain moment only depend on results at earlier times. When using explicit methods, the size of the time step Δt is limited by the CFL (Courant, Friedrich, Lewy) stability condition [87], [88]

$$\Delta t \leq \frac{1}{c_{max}} \left(\frac{1}{\Delta x^2} + \frac{1}{\Delta y^2} + \frac{1}{\Delta z^2} \right)^{-1/2} \tag{3.16}$$

where c_{max} is the maximum velocity of light occurring in the computational domain. This is easily interpreted physically : the speed with which a certain field value is computed from the previous ones is limited by the physical speed of light as indicated in Figure 3.6 for a simple scalar problem without a spatial staggered grid. It is also possible to construct finite difference schemes that are not subject to this limitation and remain stable for any size of the time step. Such implicit methods [89] use finite differences for the time derivative similar as the one depicted in Figure 3.7. However, in such a case, field values depend on other field values at the same moment such that a matrix equation now has to be solved at each time step.

Numerical Accuracy and Dispersion

If the solution remains bounded, one still must consider the accuracy of the discrete approximation to the original continuous problem. Where FEM and BIE formulations are usually too involved to determine expressions for the discretisation error, this is more easily achieved for the simpler FDTD formulation. Due to the use of the centered differences, the discretisation error for the basic "Yee" algorithm is second order

$$\frac{\partial F}{\partial x} = \frac{F(x+\Delta x) - F(x)}{\Delta x} + O(\Delta x^2) \tag{3.17}$$

and similarly for $\Delta y, \Delta z, \Delta t$. Similarly to the FEM method, the finite difference approximations again result in numerical dispersion (see Chapter 5 in [90]). The different frequencies propagate at different speeds in the time domain, such that pulses will be distorted as they propagate through the FDTD mesh. The required accuracy may therefore require a lot finer mesh and smaller time step than calculated by the CFL condition to simply obtain a stable solution.

Radiation (RBC) and Absorbing (ABC) Boundary Conditions

As in the FEM, we need to constrain the size of the computational domain for open radiation problems. Again, radiation and absorbing boundary conditions have to be imposed on the boundaries of the domain.

Radiation Boundary Conditions (RBC's) are expressed globally and exactly with integral equations that relate the field values on the surface of the domain [91], [92]. They now have to formulated in the time domain and incorporated in the FDTD time stepping algorithm, which may reduce the efficiency of the computation.

Local approximations are again possible to simulate the outgoing wave nature at the boundary. Contrary to the FEM method were we seek vectorial expressions that can be used on an arbitrarily curved boundary surface, in FDTD we try to translate the radiation condition into finite difference expressions (usually on a straight boundary section) that can be used together with the basic finite difference Equations (3.14). As in FEM methods, the order of the derivative of the field at the boundary which is now expressed in discrete form determines the order of the RBC and its accuracy. The standard difference Equations (3.14) cannot be used at the boundary since field values from outside the boundary would be required. Therefore, new formulas are derived to find the boundary values that take into account the outgoing nature of the field as depicted in Figure 3.8. Waves propagating in the -Y direction satisfy a "one-way" wave equation (Sommerfeld radiation condition for $y \to -\infty$)

$$\left(\frac{\partial}{\partial y} - \frac{1}{c}\frac{\partial}{\partial t}\right) E = 0 \tag{3.18}$$

which can be discretised into Mur's first order RBC [93]

$$E_0^n = E_1^{n-1} + \frac{c\Delta t - \Delta y}{c\Delta t + \Delta y}\left(E_1^{n+1} - E_0^n\right). \tag{3.19}$$

The boundary still needs to be set sufficiently far from the structure under consideration, since the method only works for plane waves that are normally incident to

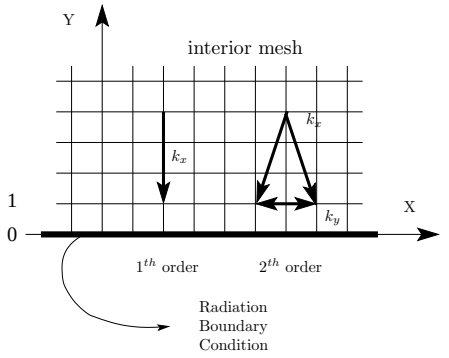

Figure 3.8: Approximate "local" radiation boundary conditions from "one-way" wave equations.

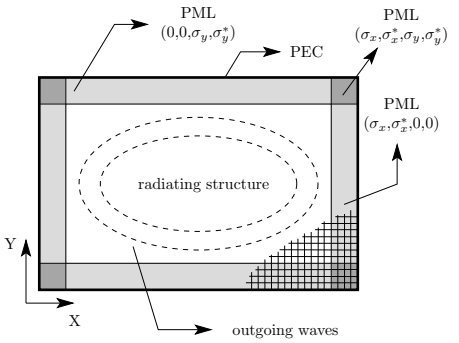

Figure 3.9: Truncation of the computational domain with a layer of absorbing material (PML).

the edge. The absorption of non normally incident waves can be improved by taking into account more derivatives of the field at the boundary into the "one-way" wave equation

$$\left(\frac{\partial}{\partial y} - \sqrt{\frac{1}{c^2}\frac{\partial^2}{\partial t^2} - \frac{\partial^2}{\partial x^2}}\right) E = 0 \tag{3.20}$$

such that slightly obliquely incident waves, for which we assume $\frac{\partial}{\partial y} \approx (1/c)\frac{\partial}{\partial t} \gg \frac{\partial}{\partial x}$ can also be absorbed. By expanded Equation (3.20) in a Taylor series, we get a second order derivative in the expression

$$\left(\frac{1}{c}\frac{\partial}{\partial t}\frac{\partial}{\partial y} - \frac{1}{c^2}\frac{\partial^2}{\partial t^2} + \frac{1}{2}\frac{\partial^2}{\partial x^2}\right) E = 0. \tag{3.21}$$

Subsequent discretisation gives the Engquist-Majda [94] and Mur's second order RBC [94], [95]. Again, the performance of absorbing boundary conditions improves as the grid resolution increases.

The energy of a field incident on the boundary can also be dissipated by wrapping the computational domain with a layer of lossy material, thus creating a numerical anechoic chamber as depicted in Figure 3.9. Important progress was achieved with the introduction of the "Perfectly Matched Layer" (PML) concept by Bérenger [78], which provides orders of magnitude improvement in performance over earlier techniques [64], [90], [96]. The progress was achieved by splitting each field component into two separate components and assigning separate electric $\sigma_x, \sigma_y, \sigma_z$ and magnetic conductivities $\sigma_x^*, \sigma_y^*, \sigma_z^*$ to each. In this way, a highly absorptive but non-physical medium is created, of which the reflection is theoretically null at any frequency and angle of incidence. The practical numerical implementation uses an absorbing layer of finite thickness backed by another simple (absorbing) boundary condition such that some energy is still reflected back. The remaining amount of reflection can be controlled by adjusting the thickness, number of cells and the conductivity profile of the

discrete PML layer [97]. Still, the behavior of a PML medium is not well understood [98] and research is still going on on how to include the PML in frequency domain problems [63].

Non Cartesian Grids

Another significant drawback of the FDTD method is the difficulty it has in modelling curved geometries and fine geometrical features.

A straightforward approach is to use a staircased approximation of the physical boundary. This can lead to formulations that cannot converge to the correct answer, no matter how fine the mesh is made to better resolve the boundary contour [99]. Without special measures, the fine mesh has to be extended over the whole computational domain, thus leading to an unneccesary increase of the computational effort and memory resources. A solution this problem consists of "subgridding" [100], [101] where a finer discretisation can be used in a specific region of space. Research in this area concentrates on maintaining overall second order accuracy, avoiding the use of the smallest time step to keep the solution stable and reducing numerical reflection at the transition between coarse and fine meshes [102].

Another approach is to reformulates the basic Yee-algorithm for grids that conform with the boundary. For simpler cases this can be done in curvilinear coordinates [103], [104]. For a general unstructured grid a generalised Yee-algorithm has been developed. This method is based on Maxwell's equations in integral form applied for an irregular finite volume of the mesh [105]. Several techniques are required to maintain the divergenceless nature of the field [106] and maintaining second order accuracy and stability [107].

3.5 Boundary Integral Equation Methods

Boundary Integral Equation (BIE) formulations are used both in the frequency domain (Section 3.5.1) and in the time domain (Section 3.5.2). The frequency domain discussion is somewhat more elaborate since much of its principles also apply to more complicated cases and can hence serve as the basis for the BIE formulation in a planar stratified medium which will be developed in the next few chapters.

In a differential equation approach, we attempt to solve a volumetric 3D problem using Maxwell equations or the vector Helmholtz wave equation directly under very complicated boundary conditions. The BIE formulation uses Green's theorem [33], [34] to reformulate the problem in terms of unknown surface functions. The main simplifications achieved are

- the reduction of the number of independent variables from 3 to 2,
- the automatic inclusion of the radiation condition,

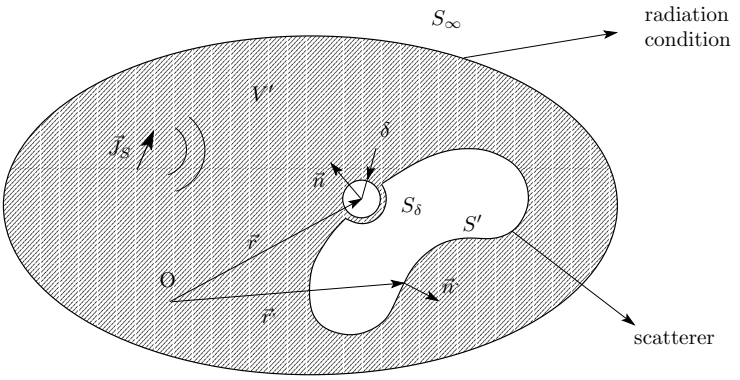

Figure 3.10: Generic volume V' and surface S' for the derivation of Boundary Integral Equations. On the outer limiting surface S_∞ receding to infinity the fields satisfy the radiation condition. The observation point approaches the scatterer surface S' with an appropriate limiting procedure.

- the imposition of the boundary conditions on the scatterer surface has become the formulation of the problem itself.

The main drawback is that the approach leads to integro-differential equations which are in principle more difficult to solve. The BIE solution is only practical when a Green's function for the specific problem is available in closed form (free space Green's function) or when it can be constructed efficiently numerically, as for a frequency domain integral equation in a planar stratified medium.

3.5.1 Boundary Integral Equations in Frequency Domain

Derivation of Boundary Integral Equations

In Section 2.5 of Chapter 2, we already used Green's theorem to obtain the field at a certain point in space as a function of source distributions in the volume of space V' and the tangential field values on the boundary surface S'. The observation point had to be excluded using a small sphere of vanishing radius δ to avoid $\vec{r} = \vec{r}'$. The factor 4π that this procedure produces is so common that it is usually incorporated in the Green's functions as

$$g(\vec{r},\vec{r}') = \frac{e^{-jkR}}{4\pi R}, \qquad \overline{G}(\vec{r},\vec{r}') = -j\omega\mu\left[\overline{I} + \frac{1}{k^2}\nabla\nabla\right]\frac{e^{-jkR}}{4\pi R} \tag{3.22}$$

which we will also assume in the remainder of this chapter. The field generated by the imposed current source $\vec{J}_S$ can then be written as the incident field $\vec{E}_{inc}$, $\vec{H}_{inc}$. To formulate the BIE, we now let the observation point approach the surface S' as

depicted in Figure 3.10 to express the boundary condition. The limiting procedure is now slightly altered. The contributions over half the surface S_δ are canceled by the contributions over the "indented" part of S'. As compared to Equations (2.22), (2.24), (2.23), (2.25) we now only obtain 2π times the field value at the observation point, which introduces an additional factor 2 in the equations below. Also, the surface integrals over S' now have to be evaluated in a principal value sense, excluding a small portion of the surface S' with radius δ. Using the dyadic and scalar Green's functions, the Electric Field Integral Equation (EFIE) is written as

$$\vec{n} \times \vec{E} = 2\vec{n} \times \left[\vec{E}_{inc} + \oint_{S'} \Big(\vec{n}' \times \vec{E} \; . \; \nabla' \times \overline{G} - j\omega\mu \; \vec{n}' \times \vec{H} \; . \; \overline{G} \Big) \, \mathrm{d}S' \right] \tag{3.23}$$

$$= 2\vec{n} \times \left[\vec{E}_{inc} + \oint_{S'} \Big(-j\omega\mu \; \vec{n}' \times \vec{H} \; g + \; \vec{n}' . \vec{E} \; \nabla' g + \vec{n}' \times \vec{E} \times \nabla' g \Big) \, \mathrm{d}S' \right] \tag{3.24}$$

and the Magnetic Field Integral Equation (MFIE) is

$$\vec{n} \times \vec{H} = 2\vec{n} \times \left[\vec{H}_{inc} + \oint_{S'} \Big(\vec{n}' \times \vec{H} \; . \; \nabla' \times \overline{G} + j\omega\epsilon \; \vec{n}' \times \vec{E} \; . \; \overline{G} \Big) \, \mathrm{d}S' \right] \tag{3.25}$$

$$= 2\vec{n} \times \left[\vec{H}_{inc} + \oint_{S'} \Big(j\omega\epsilon \; \vec{n}' \times \vec{E} \; g + \; \vec{n}' . \vec{H} \; \nabla' g - \vec{n}' \times \vec{H} \times \nabla' g \Big) \, \mathrm{d}S' \right] . \tag{3.26}$$

In these equations $\vec{E}$, $\vec{H}$ are the total fields, $\vec{E}^{inc}$, $\vec{H}^{inc}$ the incident fields imposed by the current source $\vec{J}_S$ in Figure 3.10, and the scattered field is generated by the equivalent induced electric and magnetic currents and charges $\vec{n}' \times \vec{H}$, $-\vec{n}' \times \vec{E}$, $\vec{n}' . \vec{E}$, $-\vec{n}' . \vec{H}$, on the surface S'. For a perfectly conducting surface, the main boundary conditions are

$$\vec{n} \times \vec{E} \;\; = \;\; 0 \tag{3.27}$$

$$\vec{n} \times \vec{H} \;\; = \;\; \vec{J} \tag{3.28}$$

and when Maxwell's equations are satisfied, these imply

$$\vec{n} . \vec{E} \;\; = \;\; -\nabla . \vec{J} / j\omega\epsilon \tag{3.29}$$

$$\vec{n} . \vec{H} \;\; = \;\; 0. \tag{3.30}$$

Using these boundary conditions the EFIE for a perfectly conducting surface becomes

$$-\vec{n} \times \vec{E}_{inc} \;\; = \;\; -\vec{n} \times j\omega\mu \oint_{S'} \vec{J} . \; \overline{G} \; \mathrm{d}S' \tag{3.31}$$

$$-\vec{n} \times \vec{E}_{inc} \;\; = \;\; \vec{n} \times \oint_{S'} \left(-j\omega\mu \vec{J} \; g + \left(\frac{\nabla' . \vec{J}}{-j\omega\epsilon} \right) \nabla' g \right) \; \mathrm{d}S' \tag{3.32}$$

while the MFIE is

$$\vec{J} = 2\vec{n} \times \left[\vec{H}_{inc} + \int\!\!\!\!\!\!\diagup_{S'} \vec{J} \,.\, \nabla' \times \overline{G} \; \mathrm{d}S' \right] \tag{3.33}$$

$$\vec{J} = 2\vec{n} \times \left[\vec{H}_{inc} - \int\!\!\!\!\!\!\diagup_{S'} \vec{J} \times \nabla' g \; \mathrm{d}S' \right]. \tag{3.34}$$

The first set of EFIE's are Fredholm integral equation of the first kind, where the current $\vec{J}$ only appears behind the integral sign, while the second set of MFIE's are of the second kind, because the unknown current $\vec{J}$ also appears outside of the integral operator.

Discretisation of the BIE

The use of the method of moments to solve integral equations has been described in [108], [56], [109], [110]. Formally, we have to solve an equation

$$\vec{L}\left[\vec{A}(\vec{r}')\right] = \vec{B}(\vec{r}) \tag{3.35}$$

where the unknown function $\vec{A}(\vec{r}')$ at the source point $\vec{r}'$ has to be determined, while the forcing function $\vec{B}(\vec{r})$ at the observation point $\vec{r}$ is assumed as excitation. The operator L is actually a vector integro-differential operator written symbolically as

$$\vec{L}\left[\vec{A}(\vec{r}')\right] = \int_{S'} \{1, \nabla, \nabla'\} \, K(\vec{r}, \vec{r}') \vec{A}(\vec{r}') \; \mathrm{d}S'. \tag{3.36}$$

The kernel $K(\vec{r}, \vec{r}')$ of the integro-differential equation is the Green's function relating the field at the observation point $\vec{r}$ to its source $\vec{A}$ at $\vec{r}'$. The unknown function $\vec{A}$ is represented with an expansion of vector basis functions

$$\vec{A} = \sum_{n=1}^{N} a_n \vec{A}_n \tag{3.37}$$

where the constants a_n now have to be determined. When inserting this into Equation (3.35) and using the linearity of the integro-differential operator, we get

$$\sum_{n=1}^{N} a_n \vec{L}\left[\vec{A}_n\right] = \vec{B}. \tag{3.38}$$

This equation can be enforced in an average sense by multiplying it with a weight function W_m and integrating it over an observation surface S

$$\int_S \vec{W}_m . \vec{L}\left[\vec{A}\right] \; \mathrm{d}S = \sum_{n=1}^{N} a_n \int_S \vec{W}_m . \vec{L}\left[\vec{A}_n\right] \; \mathrm{d}S = \int_S \vec{W}_m . \vec{B} \; \mathrm{d}S, \qquad m = 1, \ldots, M, \tag{3.39}$$

which can be written in matrix form as

$$[Z_{mn}]\,[A_n] = [B_m]\,. \tag{3.40}$$

The matrix elements Z_{mn} are more complicated than for the FEM case and involve a double surface integral of derivatives of two vector functions and the kernel function $K(\vec{r},\vec{r}')$,

$$Z_{mn} = \int_S \vec{W}_m(\vec{r}).\int_{S'} \{1,\nabla,\nabla'\}\,K(\vec{r},\vec{r}')\vec{A}_n(\vec{r}')\;\mathrm{d}S\;\mathrm{d}S' \tag{3.41}$$

which in general cannot be performed analytically. The evaluation of the matrix elements will be one of the time-consuming steps in the numerical solution of the BIE.

Choice of Basis and Test Functions

The basis or expansion functions should be able to accurately represent the unknown function [64], [111]. Mathematically speaking, they should be within the domain of the integro-differential operator [112]. On the other hand, they should minimize the computational effort to evaluate the matrix elements Z_{mn} of Equation (3.41). They should conform to the geometry of the problem and satisfy the boundary conditions on the edge of the domain [112]. Subdomain basis functions are defined over a small subsection of the domain. They are more flexible in modelling irregular shapes and appropriate for a broad class of solutions. Entire domain expansion functions are defined over the entire domain of the problem and are usually selected with a priori knowledge of the solution for a specific problem, such as the desired edge behaviour [113]. Their use gives a faster convergence as compared to subdomain expansion.

The weighting or test functions should be able to approximate the excitation or forcing function [111], [112]. Mathematically speaking, they should be in the range of the integro-differential operator [112]. It is also best that they stress the boundary conditions everywhere in the same measure [114].

The choice of expansion and weighting functions affects accuracy and rate of convergence of the numerical solution [115]. Generally speaking, both basis and test functions should be chosen with a particular integro-differential operator in mind. They have to satisfy certain minimum differentiability constraints [64], [111]. A discontinuous representation of the current gives rise to fictitious line charges at the discontinuous points. These produce singular potentials at the edges of the basis functions, and the situation is exacerbated if additional derivatives have to be computed to obtain the field. A crude numerical solution can obtained with a point matching procedure, since the field is finite at the sampling points in the middle of the subdomains. However, accuracy may actually decrease as the cell size is reduced [64], as the match points come closer to the singular field behaviour. Generally speaking, a smoother field is obtained by increasing the differentiability of the expansion and test functions and additional integrations to counterbalance the effect of the destabilizing differentiations.

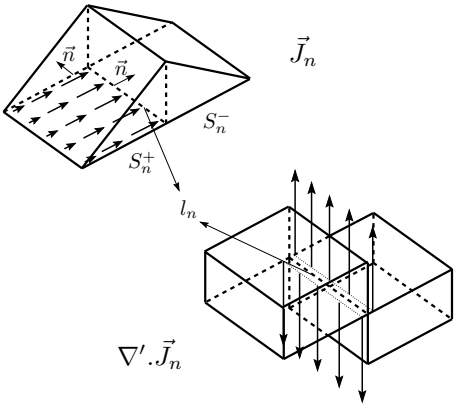

Figure 3.11: Rectangular rooftop function J_n and the charge pulse doublet $\nabla'.\vec{J}_n$.

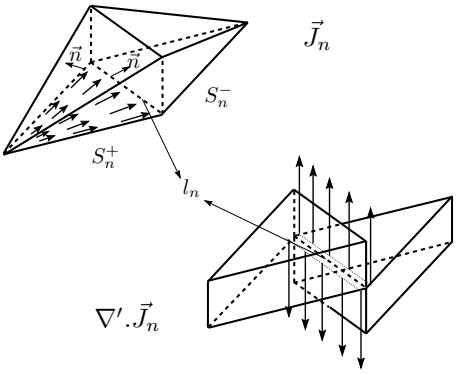

Figure 3.12: Triangular rooftop function J_n and the charge pulse doublet $\nabla'.\vec{J}_n$.

Rooftop Expansion Functions

The BIE equations are usually solved using the by now standard "rooftop" or RWG (Rao,Wilton,Glisson) basis functions introduced in [116], [117] for solving the EFIE, although they are now also used in MFIE formulations [118], [119]. These vector basis functions are depicted in Figure 3.11 and 3.12 for a rectangular and triangular support and are well suited for describing the surface current on an abritrary curved surface. The vector basis functions are associated with a common edge l_n of two segments and is directed from S_n^+ to S_n^-. The current varies linearly which will satisfy the differentiability requirements of the EFIE formulation. The current is tangential or zero on the outer edges of the segments, while the normal component across the common edge l_n is continuous. They can therefore also be considered as the lowest order members of a class of divergence conforming basisfunctions described by Nedelec [67]. The divergence within each segment is constant creating a charge pulse doublet as depicted in Figure 3.11 and 3.12 associated with each basis function. The line charges annihiliate each other if the Green's function is continuous across the common edge l_n. The continuous current expansion thus avoids non-physical charge accumulation. The current is written as

$$\vec{J} = \sum_{n=1}^{N} I_n \vec{J}_n \tag{3.42}$$

where I_n is the amplitude of the normal current component across edge l_n. These functions are now used to present a model evaluation of the matrix elements Z_{mn} of the EFIE.

Model Evaluation of Matrix Elements for the EFIE

The matrix elements Z_{mn} of Equation (3.41) are evaluated using the EFIE integro-differential operator working on rooftop basis functions. The approach shows that the

procedure mixes characteristics of point matching, pulse testing and Galerkin methods. The evaluation is given completely to be compared with the more complicated evaluation of the matrix elements for the 3D structures in a planar stratified medium given in Chapter 5. We start from the EFIE in dyadic form. As a first step, we evaluate the field $\vec{E}$ at an observation point $\vec{r}$ caused by the current $\vec{J}_n^{\pm}$ flowing on one of the segments $S_n^{\pm}$.

$$\vec{E}(\vec{J}_n^{\pm}) = -j\omega\mu \int\limits_{S_n^{\pm}} \left[\overline{I} + \frac{1}{k^2}\nabla\nabla\right] g(\vec{r},\vec{r}\,')\vec{J}_n^{\pm}\ \mathrm{d}S' \tag{3.43}$$

$$= -j\omega\mu \int\limits_{S_n^{\pm}} g\vec{J}_n^{\pm}\ \mathrm{d}S' + \frac{1}{j\omega\epsilon}\nabla \int\limits_{S_n^{\pm}} -\nabla' g\ .\ \vec{J}_n^{\pm}\ \mathrm{d}S' \tag{3.44}$$

where we used $\nabla g = -\nabla' g$. One derivative of the free space scalar Green's functions is now transferred to the source expansion function by using the vector relation

$$\nabla'(g\vec{J}) = \nabla' g\ .\ \vec{J} + g\nabla'.\vec{J} \tag{3.45}$$

of which the first term can be further evaluated using Gauss' theorem for surface integrals

$$\int\limits_{S'} \nabla'.\vec{J}\ \mathrm{d}S' = \int\limits_{l'} \vec{n}'.\vec{J}\ \mathrm{d}l' \tag{3.46}$$

where $\vec{n}'$ is the normal to the outer curve l' limiting the surface S'. This gives

$$\vec{E}(\vec{J}_n^{\pm}) = -j\omega\mu \int\limits_{S_n^{\pm}} g\vec{J}_n^{\pm}\ \mathrm{d}S' - \nabla \int\limits_{S_n^{\pm}} \frac{g}{\epsilon}\left(\frac{\nabla'.\vec{J}_n^{\pm}}{-j\omega}\right)\ \mathrm{d}S' - \nabla \int\limits_{l_n} \frac{g}{\epsilon}\left(\frac{-\vec{n}'.\vec{J}_n^{\pm}}{-j\omega}\right)\ \mathrm{d}l'. \tag{3.47}$$

The last term is the field of the line charge on the edge l_n, which is the only edge where the current has a non-zero normal component. A similar approach is used when the field is integrated with the weighting function $\vec{J}_m^{\pm}$ in a Galerkin approach to obtain the part $Z_{m^{\pm}n^{\pm}}$ of the total matrix element Z_{mn}

$$Z_{m^{\pm}n^{\pm}} = \int\limits_{S_m^{\pm}} \vec{J}_m^{\pm}\ .\ \vec{E}(\vec{J}_n^{\pm})\ \mathrm{d}S \tag{3.48}$$

$$= -j\omega\mu \int\limits_{S_m^{\pm}} \vec{J}_m^{\pm}\ .\ \int\limits_{S_n^{\pm}} g\vec{J}_n^{\pm}\ \mathrm{d}S'\mathrm{d}S - j\omega \int\limits_{S_m^{\pm}} \left(\frac{\nabla'.\vec{J}_m^{\pm}}{-j\omega}\right) \int\limits_{S_n^{\pm}} \frac{g}{\epsilon}\left(\frac{\nabla'.\vec{J}_m^{\pm}}{-j\omega}\right)\ \mathrm{d}S'\mathrm{d}S$$

$$- j\omega \int\limits_{l_m} \left(\frac{-\vec{n}.\vec{J}_m^{\pm}}{-j\omega}\right) \int\limits_{S_n^{\pm}} \frac{g}{\epsilon}\left(\frac{\nabla'.\vec{J}_n^{\pm}}{-j\omega}\right)\ \mathrm{d}S'\mathrm{d}l$$

$$- j\omega \int\limits_{l_m} \left(\frac{-\vec{n}.\vec{J}_m^{\pm}}{-j\omega}\right) \int\limits_{l_n} \frac{g}{\epsilon}\left(\frac{-\vec{n}'.\vec{J}_n^{\pm}}{-j\omega}\right)\ \mathrm{d}l'\mathrm{d}l$$

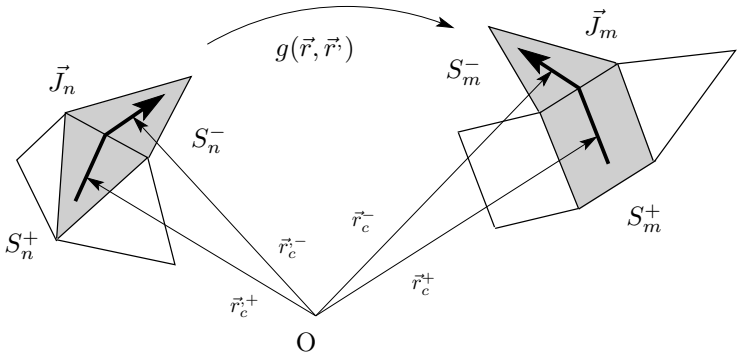

Figure 3.13: Computation of a matrix element Z_{mn}. The vector functions $\vec{J}_n$ and $\vec{J}_m$ are coupled through a Green's function $g(\vec{r},\vec{r}')$.

$$- j\omega \int\limits_{S_m^\pm} \left(\frac{\nabla . \vec{J}_m^\pm}{-j\omega} \right) \int\limits_{l_n} \frac{g}{\epsilon} \left(\frac{-\vec{n}' . \vec{J}_n^\pm}{-j\omega} \right) \, \mathrm{d}l' \mathrm{d}S \quad (3.49)$$

where the first term represents current to current coupling and the second charge to charge coupling. The last tree terms are contributions caused by the line charges accumulating on the edges l_m, l_n of the observation and source segments $S_m^\pm$, $S_n^\pm$ as depicted in Figure 3.11 and 3.12. The total matrix element Z_{mn} is obtained by adding the contributions of all combinations of segments $\pm$ together as

$$\begin{aligned} Z_{mn} &= Z_{m^+n^+} + Z_{m^-n^+} + Z_{m^+n^-} + Z_{m^-n^-} \\ &= -j\omega\mu \int\limits_{S_m} \vec{J}_m . \int\limits_{S_n} g(\vec{r},\vec{r}') \; \vec{J}_n \; \mathrm{d}S' - j\omega\epsilon \int\limits_{S_m} Q_m \int\limits_{S_n} g(\vec{r},\vec{r}') \; Q_n \; \mathrm{d}S' \mathrm{d}S \\ &\quad -j\omega \int\limits_{l_m} \lambda_m \int\limits_{S_n} \frac{1}{\epsilon} \left(g(l_m^+,\vec{r}') - g(l_m^-,\vec{r}') \right) Q_n \; \mathrm{d}S' \mathrm{d}l \\ &\quad -j\omega \int\limits_{l_m} \lambda_m \int\limits_{l_n} \frac{1}{\epsilon} \left(g(l_m^+,l_n^+) - g(l_m^-,l_n^+) - g(l_m^+,l_n^-) + g(l_m^-,l_n^-) \right) \lambda_n \; \mathrm{d}l \mathrm{d}l' \\ &\quad -j\omega \int\limits_{S_m} Q_m \int\limits_{l_n} \frac{1}{\epsilon} \left(g(\vec{r},l_n^+) - g(\vec{r},l_n^-) \right) \lambda_n \; \mathrm{d}l' \mathrm{d}S \end{aligned} \quad (3.50)$$

where Q_m, Q_n are the surface charges over S_m, S_n and λ_m, λ_n the line charges over the common edges l_m, l_n. In the above Equation (3.50), the third and fourth term contain line integrals which vanish if the Green's function is continuous over the observation edge l_m. Similarly, the fourth and fifth term vanish if the Green's

function is continuous over the common source edge l_n. We will only concentrate on the evaluation of the regular surface integral contributions. Like in the FEM case, the separate computation of the contribution of different segments of the basisfunctions is useful since a lot of the double surface integrals can be reused for the basisfunctions associated with the other edges of the segments as depicted in Figure 3.13. Also notice that, contrary to the FEM case, all matrix element are non-vanishing even if they do not overlap spatially, thanks to the presence of the Green's function. The regular surface integrals of $Z_{m^{\pm}n^{\pm}}$ can be evaluated as

$$\int_{S_m^{\pm}} \vec{J}_m^{\pm}. \int_{S_n^{\pm}} g(\vec{r},\vec{r}')\vec{J}_n^{\pm}\ \mathrm{d}S'\mathrm{d}S \quad \approx \quad S_m^{\pm}\vec{J}_m^{\pm}(\vec{r}_c^{\pm}). \int_{S_n^{\pm}} g(\vec{r}_c^{\pm},\vec{r}')\vec{J}_n^{\pm}(\vec{r}')\ \mathrm{d}S' \tag{3.51}$$

$$\int_{S_m^{\pm}} Q_m^{\pm} \int_{S_n^{\pm}} g(\vec{r},\vec{r}')Q_n^{\pm}\ \mathrm{d}S'\mathrm{d}S \quad \approx \quad S_m^{\pm}Q_m^{\pm} \int_{S_n^{\pm}} g(\vec{r}_c^{\pm},\vec{r}')Q_n^{\pm}\ \mathrm{d}S' \tag{3.52}$$

were the value at the observation point is taken at the center $\vec{r}_c^{\pm}$ of the segment $S_m^{\pm}$. The last evaluation of Equation (3.52) can also be interpreted as the use of a pulse testing function (razor blade testing), having unit value along the line connecting the centers of the segments over the middle of the common edge l_n since

$$\int_{\vec{r}_c^{+}}^{\vec{r}_c^{-}} \nabla\phi.\ \mathrm{d}\vec{l} = \phi(\vec{r}_c^{-}) - \phi(\vec{r}_c^{+}). \tag{3.53}$$

Extraction of the Green's Function Singular Behaviour

The numerical evaluation of integrals of the type

$$\int_{S'} \vec{r}' \frac{e^{-jkR}}{R}\ \mathrm{d}S' \tag{3.54}$$

with $R = |\vec{r} - \vec{r}'|$ can be done numerically, except when observation and source coordinates coincide [120], [121]. In this case, the singular behaviour for $\vec{r} = \vec{r}'$ corresponds to the near field or static field behaviour for $\omega = k = 0$ which can be extracted

$$\int_{S'} \vec{r}' \left(\frac{e^{-jkR}}{R} - \frac{1}{R}\right)\ \mathrm{d}S' + \int_{S'} \vec{r}' \left(\frac{1}{R}\right)\ \mathrm{d}S' \tag{3.55}$$

such that the first part remains finite and smooth for numerical evaluation, while the second part can be readded after analytical evaluation [122]. This procedure formally corresponds to the evaluation of the surface integrals in a principal value sense.

Deficiencies of BIE Formulations

Integral equations have theoretical problems for a number of practical situations. Since the matrix description is but a discrete approximation of the IE, these problems carry over and produce inaccurate solutions or even singular matrices.

Internal Resonances

The EFIE and MFIE fail to give a unique solution whenever the surface on which they are applied forms a conducting closed cavity capable of sustaining a resonating field distribution [123], [124]. The problem can be alleviated with a Combined Field Integral Equation (CFIE) [125] or a combined source formulation [126].

The EFIE was derived for the"outside" scattering problem by letting the observation point approach the surface from outside (superscript +). Applying the same procedure for the inside of the surface S' (superscript -), where there is no source $\vec{J}_S$ generating an incident field, but retaining the original direction of the normal vector $\vec{n}$ we obtain the "outside" and "inside" EFIE formulations

$$-\vec{n} \times j\omega\mu \oint_{S'} \vec{J}^{+}.\overline{G}\ \mathrm{d}S' \quad = \quad -\vec{n} \times \vec{E}^{+}_{inc} \tag{3.56}$$

$$-\vec{n} \times j\omega\mu \oint_{S'} \vec{J}^{-}.\overline{G}\ \mathrm{d}S' \quad = \quad \vec{0} \tag{3.57}$$

where $\vec{J}^{+} = \vec{n} \times \vec{H}^{+}$ and $\vec{J}^{-} = -\vec{n} \times \vec{H}^{-}$. The left half of these equations has the same form. We know that a closed electric conducting cavity can sustain a resonating field distribution with $-\vec{n} \times \vec{E} = \vec{0}$ on the inner surface. It is therefore possible that there exist non trivial solutions to the homogeneous second problem (3.57) for certain values of the frequency called resonant frequencies. The matrix representation of this problem thus has zero determinant at a resonant frequency. At such frequencies the solution of the outside problem (3.56) thus also becomes problematic with the same singular matrix.

The "outside" and "inside" MFIE equations are

$$\vec{J}^{+} - 2\vec{n} \times \left[\oint_{S'} \vec{J}^{+}.\nabla \times \overline{G}\ \mathrm{d}S' \right] \quad = \quad 2\vec{n} \times \vec{H}^{+}_{inc} \tag{3.58}$$

$$\vec{J}^{-} + 2\vec{n} \times \left[\oint_{S'} \vec{J}^{-}.\nabla \times \overline{G}\ \mathrm{d}S' \right] \quad = \quad \vec{0}. \tag{3.59}$$

The second "inside" MFIE (3.59) becomes unsolvable at the resonance frequency of the electric conducting cavity. The left hand side of the "outside" MFIE (3.58) is not exactly the same as the "inside" MFIE, but using reciprocity, one can show that both matrix descriptions have the same determinant [34]. This is true because it can be shown that the homogeneous form of the "outside" MFIE corresponds to the "inside" formulation for a perfect magnetic conducting cavity for which $\vec{n} \times \vec{H} = \vec{0}$ at the boundary [125]. Since this is the dual of the electric cavity problem, they have the same resonant frequencies. It is thus demonstrated that the "outside" MFIE has the same problematic behaviour as the "outside' 'EFIE.

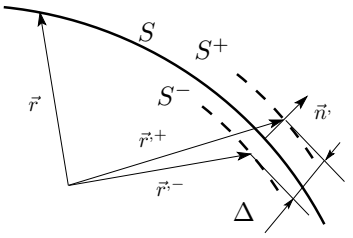

Figure 3.14: Geometry of surfaces for the derivation of the Boundary Integral Equations for infinitely thin surfaces.

Geometry of Scattering Problem

The EFIE can be used without modification for infinitely thin scatterers, while the MFIE formulation is fraught with numerical instabilities in the zero-thickness limit [127]. This behaviour can be inferred by letting the two sides of the surface S^+ and S^- approach each other as depicted in Figure 3.14. Using the same approach as before, the EFIE's become

$$-\vec{n} \times \vec{E}^+_{inc} = -j\omega\mu\vec{n} \times \oint_{S^+} \vec{J}^+ . \overline{G}^+ \, \mathrm{d}S' \tag{3.60}$$

$$-\vec{n} \times \vec{E}^-_{inc} = -j\omega\mu\vec{n} \times \oint_{S^-} \vec{J}^- . \overline{G}^- \, \mathrm{d}S' \tag{3.61}$$

while the MFIE's (now expressed with the scalar Green's function) become

$$\vec{J^+} = +2\vec{n} \times [\, \vec{H}^+_{inc} - \oint_{S^+} \vec{J}^+ \times \nabla' g \, \mathrm{d}S' \,] \tag{3.62}$$

$$\vec{J^-} = -2\vec{n} \times [\, \vec{H}^-_{inc} - \oint_{S^-} \vec{J}^- \times \nabla' g \, \mathrm{d}S' \,]. \tag{3.63}$$

Adding each set together for a vanishing thickness $\Delta \to 0$ gives the integral equations for the surface current $\vec{J}^+ + \vec{J}^-$ as

$$-\vec{n} \times \left(\vec{E}^+_{inc} + \vec{E}^-_{inc} \right) = -j\omega\mu \oint_S \left(\vec{J}^+ + \vec{J}^- \right) . \overline{G}^+ \, \mathrm{d}S' \tag{3.64}$$

$$\vec{J}^+ + \vec{J}^- = 2\vec{n} \times \left[(\vec{H}^+_{inc} - \vec{H}^-_{inc}) - \lim_{\Delta \to 0} \left(\oint_{S^+} \vec{J}^+ \times \nabla' g \, \mathrm{d}S' - \oint_{S^-} \vec{J}^- \times \nabla' g \, \mathrm{d}S' \right) \right]. \tag{3.65}$$

The EFIE presents no further problems since $\overline{G}^+ = \overline{G}^-$. For the second MFIE we appear to obtain $\vec{J}^+ - \vec{J}^-$ behind the integral sign, but we also have $\nabla' g^- = -\nabla' g^+$,

such that after a series expansion of $\nabla' g$ in the direction along the normal $\vec{n}'$, we obtain

$$\vec{J}^{+} + \vec{J}^{-} = 2\vec{n} \times (\vec{H}^{+}_{inc} - \vec{H}^{-}_{inc}) - \vec{n} \times \lim_{\Delta \to 0} \Delta \oint_{S^{+}} (\vec{J}^{+} + \vec{J}^{-})(\vec{n}'.\nabla')\nabla' g^{+} \, \mathrm{d}S' \tag{3.66}$$

The excitation $\vec{H}^{+}_{inc} - \vec{H}^{-}_{inc}$ disappears for very thin plates. The remaining integral gives a finite value expressing the identity with the left side, but is very unstable to evaluate. It thus becomes impossible to solve the unknown surface current from the incident field. As a consequence, thin wire problems can only be solved with an EFIE, while the MFIE is better suited for closed surfaces [38]. The Numerical Electromagnetics Code (NEC) [128] uses the EFIE for wires and thin surfaces and the MFIE for closed surfaces.

Low Frequency Ill Conditioning of the EFIE

The numerical solution of the EFIE becomes problematic at low frequencies. This is a problem when the size of the whole object becomes small in terms of the wavelength [129], but also for a resonant structure for which very fine geometrical details have to be modeled [130]. The basic problem is the decoupling of the electromagnetic field at low frequencies into separate magnetostatic and electrostatic fields. This decoupling manifests itself in the current which undergoes a natural Helmholtz decomposition

$$\vec{J} = \vec{J}^{sol} + \vec{J}^{irr} \tag{3.67}$$

into a solenoidal current $\vec{J}^{sol}$ which tends to flow in closed loops and produces only a magnetostatic field

$$\nabla'.\vec{J}^{sol} = 0 \tag{3.68}$$

and an irrotational current $\vec{J}^{irr}$ of which the divergence is proportional to frequency and thus transforms itself into the electrostatic charge producing only an electrostatic field

$$\lim_{\omega \to 0} \frac{\nabla'.\vec{J^{irr}}}{-j\omega} = Q. \tag{3.69}$$

The standard EFIE formulation using

$$\vec{E} = -j\omega\mu \int_{S'} g\vec{J} \, \mathrm{d}S' - \nabla \int_{S'} \frac{g}{\epsilon} \left(\frac{\nabla'.\vec{J}}{-j\omega} \right) \, \mathrm{d}S' \tag{3.70}$$

does not automatically take this decomposition into account. At low frequencies the contribution from the vector potential vanishes while inserting Equation (3.67) into the scalar potential and taking into account the properties (3.68),(3.69) shows that it produces an electrostatic field in which the solenoidal current has no part. The EFIE matrix description now becomes singular. First, the integration of an electrostatic field along any closed loop is zero, which means that the rows of the matrix, of

which the testing paths constitute a closed loop, become linearly dependent. Second, the solenoidal current is a nontrivial solution of the homogeneous form of the EFIE, making the matrix singular. If the Helmholtz decomposition of the current is taken explicitly into account with the proper frequency dependence of its components, the EFIE naturally separates into separate integral equations for the electrostatic and magnetostatic problems [131], which were already solved separately in [132]. Such a decomposition is achieved by using "loop" and "star" basis functions introduced in [133]. The new basis functions can be derived from the standard rooftop expansion functions by a number of matrix operations on the original EFIE matrix description [134].

3.5.2 Boundary Integral Equations in Time Domain

The time domain counterparts of the electric and magnetic field integral equations for perfectly conducting surfaces (3.32), (3.34) are usually solved starting from

$$-\vec{n} \times \frac{\partial \vec{E}_{inc}(\vec{r},t)}{\partial t} = \vec{n} \times \left[\frac{\partial^2}{\partial t^2} \frac{\mu}{4\pi} \oint\limits_{S'} \frac{\vec{J}(\vec{r}',\tau)}{R} \, \mathrm{d}S' - \nabla \frac{1}{4\pi\epsilon} \oint\limits_{S'} \frac{\nabla'.\vec{J}(\vec{r}',\tau)}{R} \, \mathrm{d}S' \right] \tag{3.71}$$

$$\vec{J}(\vec{r},t) = 2\vec{n} \times \left[\vec{H}_{inc}(\vec{r},t) + \frac{1}{4\pi} \oint\limits_{S'} \left(\frac{1}{R^2} + \frac{1}{cR} \frac{\partial}{\partial \tau} \right) \vec{J}(\vec{r}',\tau) \times \frac{\vec{r}-\vec{r}'}{R} \, \mathrm{d}S' \right] \tag{3.72}$$

where the retarded time τ is given by

$$\tau = t - |\vec{r} - \vec{r}'|/c. \tag{3.73}$$

The fact that the field at an observation point $\vec{r}$ at time t is determined by the incident field at that point and time and the current at the other positions $\vec{r}'$ at earlier times τ (which has already been calculated) allows a solution of the integral equation by a Marching on in Time (MoT) algorithm. Expanding both the spatial and temporal variation of the current

$$\vec{J}(\vec{r},t) \quad = \quad \sum_{n=1}^{N_s} \sum_{j=0}^{N_t} I_{nj} \vec{J}_n(\vec{r}) T_j(t) \tag{3.74}$$

and testing the integral equation in both space and time coordinates generally gives a matrix equation of the form

$$[Z_{mn}]_0 [I_n]_j \quad = \quad [F_{inc,m}]_j + \sum_{k=0}^{j-1} [Z_{mn}]_{j-k} [I_n]_k. \tag{3.75}$$

where the matrix elements $Z_{mn,j-k}$ depend on the geometrical position of the spatial expansion functions $\vec{J}_m$, $\vec{J}_n$ and a time shift $j-k$ because of the retarded time τ. The

matrix Z_0 has to be inverted only once, at the start of the MoT algorithm. When the temporal testing functions are delta functions (point matching), the method becomes explicit with a diagonal matrix Z_0 [135], but other types of time testing functions give implicit algorithms with a very sparse Z_0 [136]. Two principle obstacles have impeded the widespread use of time domain integral equations. The first is the computational cost which scales unfavorably with problem size. This can be partially remedied with a time domain version of the Fast Multipole Method (FMM) also called a Plane Wave Time Domain (PWTD) algorithm [137], [138]. The second is that the solution often exhibits late-time spurious fluctuations of growing amplitude that eventually diverge. These late-time instabilities seem to be caused by the approximations made in the space-time discretisation [139], [140] and occur even when the CFL stability condition is satisfied [141]. Instabilities in explicit schemes can be postponed by more accurate approximations, but for very demanding geometries with sharp corners, only implicit schemes seem to provide stability [136], [142]. Nevertheless, even accurate implicit algorithms are still capable of developing instabilities when the spectrum of the excitation contains the resonant frequencies of the closed surface, a problem similar to the frequency domain EFIE's and MFIE's. In this case the problem occurs at the formulation stage such that only very accurate implicit algorithms based on a Combined Field Integral Equation (CFIE) formulation are unconditionally stable [143]. Unfortunately, time domain integral equations are not suited to analyse scattering problems in stratified media because the Green's function is not available in closed form in the space-time domain.

3.6 Commercially Available Full Wave Software

This section gives a list of some commercially available software packages for the analysis of high frequency electromagnetic problems with complicated three dimensional geometries.

Finite Element Method

- **HFSS**, High Frequency Structure Simulator, Ansoft Corporation, http://www.ansoft.com
- **AI*EMAX**, Ansys Inc., http://www.ansys.com

Finite Difference Time Domain

- **Microwave Studio**, Finite Volume Time Domain, CST Computer Simulation Technology, http://www.cst.de
- **Micro-stripes**, TLM (Transmission Line Matrix) method, which is strongly related to the FDTD method, Flomerics Ltd., hhtp://www.micro-stripes.com

- **Fidelity**, Zeland Software Inc., http://www.zeland.com
- **XFDTD**, Remcom Inc., http://www.remcom.com
- **SEMCAD**, Schmid & Partner Engineering AG, http://www.semcad.com
- **Concerto**, Vector Fields Ltd., http://www.vectorfields.com

Frequency Domain Integral Equation

Integral Equations in free space, capable of dealing with metallic surfaces and attached wires by combining EFIE and MFIE formulations

- **SuperNEC2.0**, Numerical Electromagnetics Code, Poynting Antennas and Electromagnetics, http://www.poynting.co.za
- **EMC2000**, Aerospatiale Matra, http://www.emc2000.org

Integral Equation for planar stratified media, using an EFIE formulation, capable of analysing planar thin metallic surfaces, and short small vertical currents. These are the so-called 2.5D or 3D planar simulators.

- **Sonnet *em***, Sonnet Software Inc., http://www.sonnetusa.com
- **EMSight**, AWR Applied Wave Research Inc., http://www.mwoffice.com
- **Momentum**, Agilent Technologies, EEsof EDA, http://www.agilent.com/eesof-eda
- **Ensemble**, Ansoft Corporation, http://www.ansoft.com
- **MAGMAS**, ESAT-TELEMIC, Katholieke Universiteit Leuven

Integral Equation for planar stratified media, using an EFIE formulation and capable of dealing with arbitrary 3D metallic surfaces.

- **IE3D** Integral Equation 3 Dimensional, Zeland Software Inc., http://www.zeland.com
- **FEKO** FEldberechnung bei Körpern mit beliebiger Oberfläche, EMSS Electro-Magnetic Software and Systems, http://www.feko.co.za

3.7 Conclusions

This chapter has reviewed some of the most successful numerical techniques used in practice for electromagnetic field analysis. The techniques can be classified as differential or integral equation based and whether they are formulated in the time or frequency domain. The theoretical approach, the basic algorithm and main limitations of the Finite Element Method (FEM), the Finite Difference Time Domain (FDTD) algorithm, and frequency and time domain Boundary Integral Equations (BIE's) have been discussed. A basic overview and understanding of these methods is deemed necessary for a sound judgement of the more specific theoretical and numerical methods presented in this work. The more elaborate discussion on frequency domain BIE's has also provided the setting for the formulation and application of this technique to the analysis of 3D structures in planar stratified media, which will be developed in full detail in the next two chapters.

Chapter 4

The Spectral Electromagnetic Field of a 3D Current Source in a Planar Stratified Medium

4.1 Introduction

A lot of real-life problems in ElectroMagnetic radiation, coupling, Interference (EMI) and Compatibility (EMC) involve metallic structures which are located in a medium consisting of a number of planar stacked layers with different electromagnetic properties : planar and 3D antennas [144], Microwave and Millimeterwave Integrated Circuits (MMIC's) [3], Micro-Electromechanical Systems (MEMS) [145], [146], traditional and Radio Frequency (RF) Printed Circuit Boards (PCB's) [147], [148], high speed digital circuits [149], [150], traditional interconnects [151], [152], and electronics packaging [153], [154], [155], [156], and state of the art Multi-Chip Modules (MCM's) and Ball Grid Array (BGA) interconnection and packaging technology [150], [157]. Such devices can only be modeled accurately by taking into account the influence of the surrounding medium. In differential equation based methods like the FEM of Section 3.4.1, and the FDTD technique of Section 3.4.2, any material composition can be incorporated by changing the properties ϵ, μ of the medium locally, such that the basic algorithms presented in Section 3.4 can be implemented almost without change. With such an approach however, one has to rely purely on computational power to resolve the relevant physical phenomena in a numerical manner. The integral equation methods of Section 3.5 hinge upon Green's theorem [33], which can only be applied if an appropriate Green's function is available. For the homogeneous surround assumed in Sections 3.5.1 and 3.5.2, the dyadic and scalar Green's functions are available in closed form. If the integral equation approach is to be applied efficiently for a planar

layered surround, the presence of this medium has to be incorporated into the Green's function(s) itself. However, the determination of these functions is considerably more involved than for a homogeneous medium. First, instead of a single Green's function, several distinct functions arise. Secondly, the Green's functions are not completely available in closed form in the spatial domain, but have to be constructed partially numerically. Nevertheless, their determination still incorporates a lot of analytical processing, which makes the integral equation approach more robust and efficient than the differential equation formulations.

This chapter concentrates on the determination of the electric and magnetic dyadic Green's functions that express the total electric and magnetic field in the spectral domain generated by a 3D electric current source embedded within an arbitrary stratified medium.

The determination of the field in a stratified medium was originally pioneered by Sommerfeld himself, as early as 1909 [158]. He studied the generation of radio waves by horizontal and vertical dipole antennas and their resulting propagation above a lossy half space [36]. Subsequent interest continued to be within the domain of radiowave propagation and geophysical probing [159], [160], [161], extending the analysis from a halfspace to stratified media with multiple layers. Kong [162] avoided the Hertz potential approach and solved for the electric and magnetic fields directly, using a TM/TE decomposition of the field to obtain the spectral Green's dyad. The formal equivalence of these two approaches has been shown [163]. Interest in the problem was revived when the quasi-static analyses of microwave transmission media [164], [165] was found insatisfactory. The frequency dependent propagation characteristics could be determined accurately numerically by formulating the problem as an integral equation in which the dyadic Green's function appeared as the kernel [166], [167], [168], [169]. The important transmission line analog of Section 4.8 was established within this context [170]. The method acquired the name Spectral Domain Approach (SDA) [171]. The planar nature of these transmission media made that only the transverse part of the dyadic spectral Green's function was needed and that the location of the currents was restricted to the interfaces of the layers [170], [172], [173], [11], [14]. Complete spectral dyadic Green's functions for 3D source currents with arbitrary position within the layer structure were re-established in [174], [163], [175], [176], [177], [178], [179], [180], [181], [182]. However, the derivations often continued to use Hertz and vector potential approaches [173], [177], [179], or still used a formulation separating direct and scattered Green's functions instead of using the advantageous transmission line analogy [175], [177], [179], [180]. The resulting expressions are often given for a limited number of layers only [177], [178], [179] and no general notation was established.

Our derivation is based on earlier work by Vandenbosch [11] and Demuynck [14], who already established the field of transverse electric current sources located at the interfaces of the layers of an arbitrarily layered medium. This work has not found full recognition due to a somewhat unconventional notation. We expand the derivation to a full 3D electric current source located at any arbitrary position. We follow

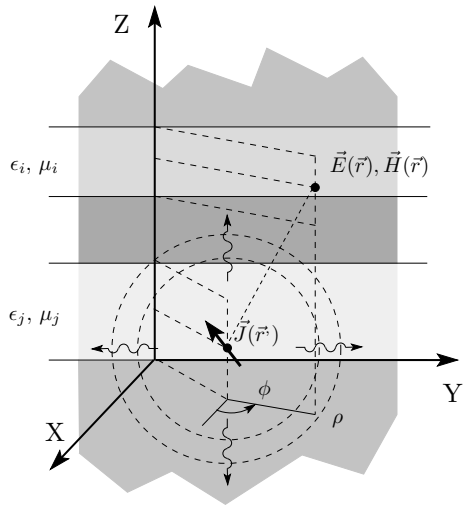

Figure 4.1: a 3D current source embedded within a planar multilayered medium.

the TM/TE decomposition of the field and use the transmission line formalism in its most general form as in [173], [182]. We introduce an improved notation similar to the ones which has appeared recently in [182], [183], [184]. We present a completely new factorisation for an arbitrary Green's function in Section 4.9 which explicitly separates the z and z' dependence in simple and symmetric form. The factorised form leads to a number of important derivative relations (Section 4.11). The factorisation and derivative relations together allow easier analytical manipulations. This facilitates the physical interpretation in Chapter 5 and allows to evaluate part of the reaction integrals analytically in Chapter 6.

4.2 The Problem Statement

Figure 4.1 shows a generic planar stratified medium consisting of an arbitrary number of flat stacked layers. We take the X, Y plane to be parallel to the stratification of the medium, while the Z axis is normal to the layers. Each layer extends infinitely far in the transverse X, Y direction, is assumed to be homogeneous and characterised by a dielectric permittivity ϵ_k, a magnetic permeability μ_k and thickness d_k. The outermost top and bottom layers also extend to infinity in the normal Z direction and can be used to model either open half spaces or electrically conducting limiting planes. A current source $\vec{J}$ with X, Y and Z components is located at any arbitrary source position x', y', z'

$$\vec{J}(x', y', z') = \vec{J}\delta(x - x')\delta(y - y')\delta(z - z'). \tag{4.1}$$

Our task consists of determining the electromagnetic field at any other arbitrary observation position x, y, z.

4.3 The Spectral Domain Approach

The field in this complicated environment can be determined by an approach originally pioneered by Sommerfeld himself [36], and recently called the Spectral Domain Approach (SDA) when applied for the analysis of microwave problems in layered media [171].

4.3.1 Definition of the Fourier Transform

A Fourier transform of the spatial transverse x, y coordinates maps any quantity $F(x, y, z)$ onto its spectral counterpart $\widetilde{F}(k_x, k_y, z)$ defined in the corresponding transverse wavenumber k_x, k_y domain. The Fourier transform and its inverse transformation used in this work are defined as

$$\mathfrak{F}\{F(x,y,z)\} = \widetilde{F}(k_x,k_y,z) = \iint_{-\infty}^{+\infty} F(x,y,z)e^{+jk_x x}e^{+jk_y y}\,\mathrm{d}x\mathrm{d}y \tag{4.2}$$

$$\mathfrak{F}^{-1}\{\widetilde{F}(k_x,k_y,z)\} = F(x,y,z) = \frac{1}{(2\pi)^2}\iint_{-\infty}^{+\infty} \widetilde{F}(k_x,k_y,z)e^{-jk_x x}e^{-jk_y y}\,\mathrm{d}k_x\mathrm{d}k_y. \tag{4.3}$$

Notice that the z coordinate along the stratification of the medium remains unaffected.

4.3.2 Problem Statement in the Spectral Domain

Applying the Fourier transform for the excitation in the layer structure of Figure 4.1 transforms the point source into a planar sheet of dipoles,

$$\mathfrak{F}\{\vec{J}\delta(x-x')\delta(y-y')\delta(z-z')\} = \vec{J}e^{+jk_x x'}e^{+jk_y y'}\delta(z-z') \tag{4.4}$$

parallel to stratification of the medium. It will be most helpful to interpret this mathematical operation as a reduction of the three dimensional geometry of Figure 4.1 to the one-dimensional problem pictured in Figure 4.2. The planar current sheet will cause plane waves to travel back and forth along the Z direction within each layer. It is only this variation that we need to concentrate on at this point. Any spatial variation of the field as a function of ρ, ϕ in Figure 4.1 will be contained in the amplitude of the plane waves which will depend on the spectral wavenumbers k_x, k_y. Figure 4.2 also introduces conventions for numbering the layers and the interfaces in

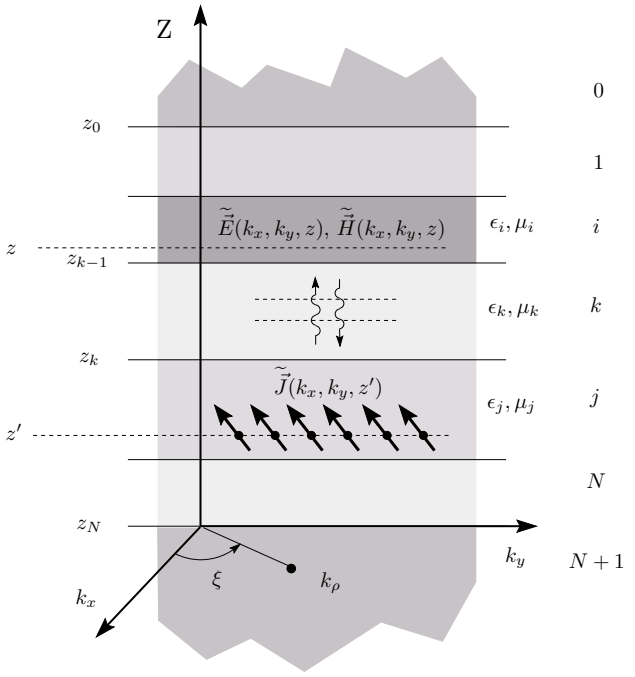

Figure 4.2: The layer structure in the spectral domain contains a uniform sheet of dipole currents as an excitation.

between. The first top layer gets the number 0, the last bottom layer is the $(N+1)^{th}$ layer. An arbitrary layer k is delimited above by the interface $k-1$ at z_{k-1} and stops on the bottom side at interface k with coordinate z_k. It has a thickness $d_k = z_{k-1} - z_k$. The source is located at z' in layer j, and the observation point is located at z in layer i.

4.4 Maxwell's Equations and Boundary Conditions

The set of independent Maxwell equations (4.5), (4.6), together with the excitation and boundary conditions depicted in Figure 4.1 (boundary conditions on the interfaces between dielectric layers and radiation conditions at infinity) constitute a well-posed boundary value problem with a unique solution. However, since the SDA approach has transformed the excitation into a current sheet parallel to the interfaces between the layers, we know that the solution consists of plane waves traveling along z. These are best described by the homogeneous set of Maxwell equations

$$\nabla \times \vec{E} \quad = \quad -j\omega\mu_k \vec{H} \tag{4.5}$$

$$\nabla \times \vec{H} \quad = \quad +j\omega\epsilon_k \vec{E}. \tag{4.6}$$

The excitation of the problem is treated on an equal footing with the other boundary conditions by incorporating the excitation into them,

$$\vec{i}_z \times (\vec{E}^{>} - \vec{E}^{<}) \quad = \quad \frac{1}{j\omega\epsilon_k} \nabla \times (\vec{J}.\vec{i}_z)\vec{i}_z \tag{4.7}$$

$$\vec{i}_z \times (\vec{H}^{>} - \vec{H}^{<}) \quad = \quad \vec{J} - (\vec{J}.\vec{i}_z)\vec{i}_z \tag{4.8}$$

which are the generalised boundary conditions [185] at a planar interface with an arbitrary oriented but uniform current sheet. The superscripts $>$ and $<$ indicate the field values just above and below the plane where the boundary conditions are applied. These boundary conditions express continuity of the tangential fields at the material interfaces when no current is present, in which case the right hand side members vanish. They give the step change in tangential field values for transverse currents that are located at the interface of two layers (in which case the right hand side of Equation (4.5) disappears) and for 3D current distributions located completely within a certain layer (this gives the ϵ_k for the Z component of the current in Equation (4.7)). We now need to transpose the spatial derivative operations of the above equations into the spectral domain. Using

$$\mathfrak{F}\left\{\frac{\partial}{\partial x}F(x,y,z)\right\} = -jk_x\ \widetilde{F}(k_x,k_y,z) \tag{4.9}$$

$$\mathfrak{F}\left\{\frac{\partial}{\partial y}F(x,y,z)\right\} = -jk_y\ \widetilde{F}(k_x,k_y,z) \tag{4.10}$$

$$\mathfrak{F}\left\{\frac{\partial}{\partial z}F(x,y,z)\right\} = +\frac{\partial}{\partial z}\ \widetilde{F}(k_x,k_y,z) \tag{4.11}$$

we obtain the spectral form of the homogeneous Maxwell equations in any layer k

$$-jk_y\widetilde{E}_z - \frac{\partial}{\partial z}\widetilde{E}_y \quad = \quad -j\omega\mu_k\widetilde{H}_x \tag{4.12}$$

$$+\frac{\partial}{\partial z}\widetilde{E}_x - j_x\widetilde{E}_z \quad = \quad -j\omega\mu_k\widetilde{H}_y \tag{4.13}$$

$$-jk_x\widetilde{E}_y + jk_y\widetilde{E}_x \quad = \quad -j\omega\mu_k\widetilde{H}_z \tag{4.14}$$

$$-jk_y\widetilde{H}_z - \frac{\partial}{\partial z}\widetilde{H}_y \quad = \quad j\omega\epsilon_k\widetilde{E}_x \tag{4.15}$$

$$+\frac{\partial}{\partial z}\widetilde{H}_x - j_x\widetilde{H}_z \quad = \quad j\omega\epsilon_k\widetilde{E}_y \tag{4.16}$$

$$-jk_x\widetilde{H}_y + jk_y\widetilde{H}_x \quad = \quad j\omega\epsilon_k\widetilde{E}_z \tag{4.17}$$

and the spectral generalised boundary conditions as

$$-\widetilde{E}_y^{>} + \widetilde{E}_y^{<} \quad = \quad \frac{-jk_y}{j\omega\epsilon_k}\widetilde{J}_z \tag{4.18}$$

$$+\widetilde{E}_x^{>} - \widetilde{E}_x^{<} \quad = \quad \frac{+jk_x}{j\omega\epsilon_k}\widetilde{J}_z \tag{4.19}$$

$$-\widetilde{H}_y^{>} + \widetilde{H}_y^{<} \quad = \quad \widetilde{J}_x \tag{4.20}$$

$$+\widetilde{H}_x^{>} - \widetilde{H}_x^{<} \quad = \quad \widetilde{J}_y. \tag{4.21}$$

4.5 TM/TE Decomposition of the Field

The field described by the set of Equations (4.12), (4.13), (4.14), (4.15), (4.16), (4.17), can be rearranged to express the transverse field components as a function of only $\widetilde{E}_z$ and $\widetilde{H}_z$ which can thus be selected as the primary unknowns. With $k_\rho^2 = k_x^2 + k_y^2$ we obtain

$$\widetilde{E}_x = -\frac{jk_x}{k_\rho^2}\frac{\partial \widetilde{E}_z}{\partial z} - \frac{\omega\mu_k k_y}{k_\rho^2}\widetilde{H}_z \quad (4.22) \qquad \widetilde{H}_x = +\frac{\omega\epsilon_k k_y}{k_\rho^2}\widetilde{E}_z - \frac{jk_x}{k_\rho^2}\frac{\partial \widetilde{H}_z}{\partial z} \quad (4.24)$$

$$\widetilde{E}_y = -\frac{jk_y}{k_\rho^2}\frac{\partial \widetilde{E}_z}{\partial z} + \frac{\omega\mu_k k_x}{k_\rho^2}\widetilde{H}_z \quad (4.23) \qquad \widetilde{H}_y = -\frac{\omega\epsilon_k k_x}{k_\rho^2}\widetilde{E}_z - \frac{jk_y}{k_\rho^2}\frac{\partial \widetilde{H}_z}{\partial z}. \quad (4.25)$$

The TM part of the field is obtained from the above set by putting $\widetilde{H}_z = 0$ and retaining $\widetilde{E}_z$ as independent variable. The TE part requires $\widetilde{E}_z = 0$ and retains $\widetilde{H}_z$.

$$\widetilde{E}_x^{TM} = -\frac{jk_x}{k_\rho^2}\frac{\partial \widetilde{E}_z}{\partial z} \quad (4.26) \qquad \widetilde{E}_x^{TE} = -\frac{\omega\mu_k k_y}{k_\rho^2}\widetilde{H}_z \quad (4.30)$$

$$\widetilde{E}_y^{TM} = -\frac{jk_y}{k_\rho^2}\frac{\partial \widetilde{E}_z}{\partial z} \quad (4.27) \qquad \widetilde{E}_y^{TE} = +\frac{\omega\mu_k k_x}{k_\rho^2}\widetilde{H}_z \quad (4.31)$$

$$\widetilde{H}_x^{TM} = +\frac{\omega\epsilon_k k_y}{k_\rho^2}\widetilde{E}_z \quad (4.28) \qquad \widetilde{H}_x^{TE} = -\frac{jk_x}{k_\rho^2}\frac{\partial \widetilde{H}_z}{\partial z} \quad (4.32)$$

$$\widetilde{H}_y^{TM} = -\frac{\omega\epsilon_k k_x}{k_\rho^2}\widetilde{E}_z \quad (4.29) \qquad \widetilde{H}_y^{TE} = -\frac{jk_y}{k_\rho^2}\frac{\partial \widetilde{H}_z}{\partial z} \quad (4.33)$$

The wave equations in the spectral domain for the chosen independent field components $\widetilde{E}_z$, $\widetilde{H}_z$ can be obtained by inserting Equations (4.23), (4.24) into (4.12) and (4.22), (4.25) into (4.15)

$$\frac{\partial^2 \widetilde{E}_z}{\partial z^2} - \gamma_k^2 \widetilde{E}_z = 0 \quad (4.34)$$

$$\frac{\partial^2 \widetilde{H}_z}{\partial z^2} - \gamma_k^2 \widetilde{H}_z = 0. \quad (4.35)$$

These equations demonstrate that each field component within a certain layer k indeed consists of upward and downward traveling waves as depicted in Figure 4.2, with a propagation constant γ_k defined as

$$\gamma_k^2 = k_\rho^2 - \omega^2\mu_k\epsilon_k. \quad (4.36)$$

4.6 TM/TE Decomposition of the Current

The TM/TE decomposition of the field enforces a similar separation on the current

$$\widetilde{J}_x = \widetilde{J}_x^{TM} + \widetilde{J}_x^{TE} \tag{4.37}$$
$$\widetilde{J}_y = \widetilde{J}_y^{TM} + \widetilde{J}_y^{TE} \tag{4.38}$$
$$\widetilde{J}_z = \widetilde{J}_z^{TM} + \widetilde{J}_z^{TE}. \tag{4.39}$$

The TM components of the currents are determined by expressing the boundary conditions (4.18), (4.19), (4.20), (4.21) as a function of the independent variable $\widetilde{E}_z$, giving a set of 4 equations which can only be satisfied simultaneously if

$$\widetilde{J}_z^{TM} = \widetilde{J}_z \tag{4.40}$$
$$k_y \widetilde{J}_x^{TM} = k_x \widetilde{J}_y^{TE}. \tag{4.41}$$

The remaining 2 independent boundary conditions that couple the TM part of the field to the TM part of the current are

$$j\left(\frac{\partial \widetilde{E}_z^{>}}{\partial z} - \frac{\partial \widetilde{E}_z^{<}}{\partial z}\right) = -\frac{k_\rho^2}{j\omega\epsilon_j}\widetilde{J}_z \tag{4.42}$$
$$\omega\left(\epsilon^{>}\widetilde{E}_z^{>} - \epsilon^{<}\widetilde{E}_z^{<}\right) = \frac{k_\rho^2}{k_x}\widetilde{J}_x^{TM}. \tag{4.43}$$

Similarly, when inserting the transverse TE field expressions as a function of $\widetilde{H}_z$, we can only satisfy the 4 boundary conditions simultaneously when

$$\widetilde{J}_z^{TE} = 0 \tag{4.44}$$
$$k_x \widetilde{J}_x^{TE} = -k_y \widetilde{J}_y^{TE}. \tag{4.45}$$

The remaining 2 independent boundary conditions that relate the TE part of the current to the TE field are

$$\omega\left(\mu^{>}\widetilde{H}_z^{>} - \mu^{<}\widetilde{H}_z^{<}\right) = 0 \tag{4.46}$$
$$j\left(\frac{\partial \widetilde{H}_z^{>}}{\partial z} - \frac{\partial \widetilde{H}_z^{<}}{\partial z}\right) = \frac{k_\rho^2}{k_y}\widetilde{J}_x^{TE}. \tag{4.47}$$

By inserting Equations (4.40), (4.41), and (4.44), (4.45) into the decomposition (4.37), (4.38), (4.39), we can solve for the currents that excite the TM and TE parts of the field independently,

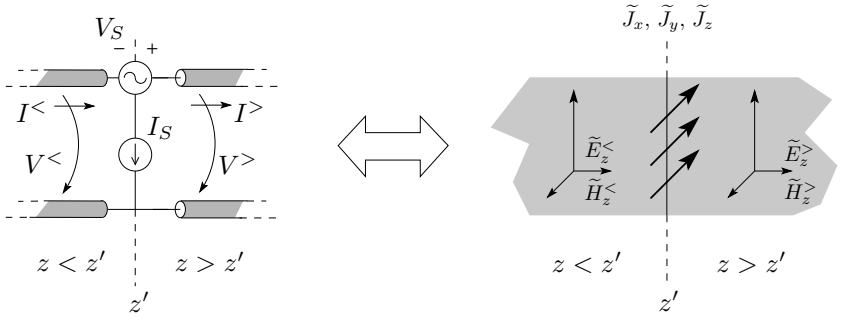

Figure 4.3: Equivalence between the voltages and currents on a transmission line with the electric and magnetic fields in a planar stratified medium.

$$\widetilde{J}_x^{TM} = k_x \frac{k_x \widetilde{J}_x + k_y \widetilde{J}_y}{k_\rho^2} \quad (4.48) \qquad \widetilde{J}_x^{TE} = k_y \frac{k_y \widetilde{J}_x - k_x \widetilde{J}_y}{k_\rho^2} \quad (4.51)$$

$$\widetilde{J}_y^{TM} = k_y \frac{k_x \widetilde{J}_x + k_y \widetilde{J}_y}{k_\rho^2} \quad (4.49) \qquad \widetilde{J}_y^{TE} = -k_x \frac{k_y \widetilde{J}_x - k_x \widetilde{J}_y}{k_\rho^2} \quad (4.52)$$

$$\widetilde{J}_z^{TM} = \widetilde{J}_z \quad (4.50) \qquad \widetilde{J}_z^{TE} = 0 \quad (4.53)$$

and this has been interpreted before as a simple rotation of the transverse k_x, k_y wavenumber coordinate system [170], [181].

4.7 Identification with a Transmission Line

The above boundary conditions for the fields and currents at the point of excitation can be identified with the excitation of a transmission line with a series voltage V_S and a shunt current source I_S as depicted in Figure 4.3. At the excitation point, we have for the chosen reference directions of voltage and current

$$V^> - V^< = +V_S \quad (4.54)$$

$$I^> - I^< = -I_S. \quad (4.55)$$

The voltages and currents on the left and right sides satisfy the transmission line equations

$$\frac{\partial V(z)}{\partial z} = -\frac{\gamma}{Y} I(z) \quad (4.56) \qquad \frac{\partial I(z)}{\partial z} = -\gamma Y V(z) \quad (4.57)$$

where γ is the propagation constant and Y the characteristic admittance of the transmission line.

We thus see the defining equations for the TM part of field and current Equations (4.42), (4.43) can be mapped onto Equations (4.54), (4.55) by choosing

$$j\frac{\partial \widetilde{E}_z}{\partial z} = V \quad (4.58) \qquad V_S = -\frac{k_\rho^2}{j\omega\epsilon_j}\widetilde{J}_z \quad (4.60)$$

$$\omega\epsilon\widetilde{E}_z = I \quad (4.59) \qquad I_S = -\frac{k_\rho^2}{k_x}\widetilde{J}_x^{TM}. \quad (4.61)$$

The TE part of field and current described by Equations (4.46), (4.47) are similarly mapped onto (4.54), (4.55) by now choosing

$$\omega\mu\widetilde{H}_z = V \quad (4.62) \qquad V_S = 0 \quad (4.64)$$

$$j\frac{\partial \widetilde{H}_z}{\partial z} = I \quad (4.63) \qquad I_S = -\frac{k_\rho^2}{k_y}\widetilde{J}_x^{TE}. \quad (4.65)$$

We see that the TM and TE systems each give rise to an equivalent transmission line problem with characteristic admittances

$$Y_k^{TM} = \frac{j\omega\epsilon_k}{\gamma_k} \quad (4.66) \qquad Y_k^{TE} = \frac{\gamma_k}{j\omega\mu_k}. \quad (4.67)$$

The determination of the electromagnetic field of a 3D current source is thus reduced to solving two equivalent transmission line problems [170]. The following section therefore concentrates on the general solution for the excitation of a cascaded transmission line problem. These expressions are then simply transposed to the field problem to obtain the Green's functions for the electromagnetic field in Section 4.12.

4.8 The Transmission Line Formalism

Although "basic" transmission line theory is well established, we repeat the basic definitions to establish the notation for the following sections, and to acquire the basic tools to derive the factorised form of the Green's functions.

Figure 4.4 depicts a cascade connection of transmission line sections k located between z_k and z_{k-1}, each defined by a propagation constant γ_k and a characteristic admittance Y_k. The first and last sections are numbered 0 and $N+1$ respectively.

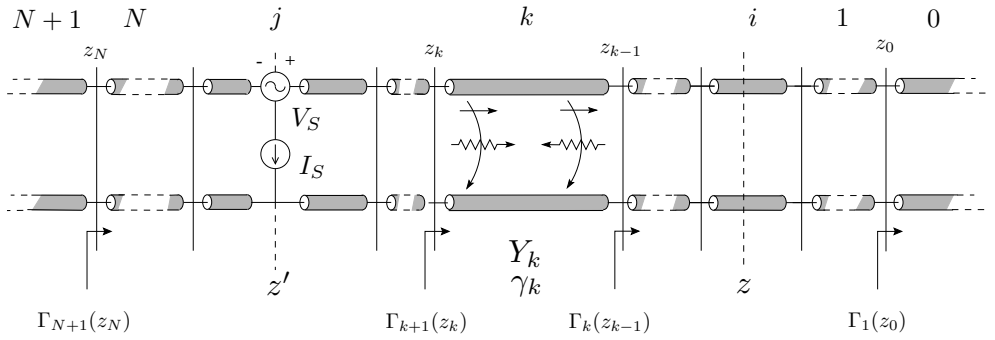

Figure 4.4: Transmission line network analog for the field problem in the spectral domain in a plane stratified medium.

The excitation of the problem is assumed to consist of a series voltage source V_S and shunt current source I_S (superscript $S = I, V$) located at z' in the source section j (denoted in subscript). The problem is to obtain the voltages and currents ($F = I, V$) at the observation coordinate z in a certain observation section i (also in subscript). The notation for these quantities is decided upon as

$$F_{ij}^{S,\lessgtr}(z, z') \tag{4.68}$$

where the slight differences for $z > z'$ or $z < z'$ necessitate the additional superscript. The complete expressions are constructed in this section and subsequently simplified in Section 4.9.

4.8.1 "Basic" Transmission Line Theory

Within a certain section k, the voltage and current consists of a superposition of left and right traveling waves with a fixed complex amplitude. We choose the reference position for these amplitudes at the left most position z_k

$$V_k(z) = V_k^+(z_k)e^{-\gamma_k(z-z_k)} + V_k^-(z_k)e^{+\gamma_k(z-z_k)} \tag{4.69}$$

$$I_k(z) = Y_k\left[V_k^+(z_k)e^{-\gamma_k(z-z_k)} - V_k^-(z_k)e^{+\gamma_k(z-z_k)}\right]. \tag{4.70}$$

The reflection coefficient $\Gamma(z)$ at any position z is the ratio of forward and backward traveling waves at that position

$$\Gamma_k(z) = \frac{V_k^-(z_k)e^{+\gamma_k(z-z_k)}}{V_k^+(z_k)e^{-\gamma_k(z-z_k)}} = \Gamma_k(z_k)e^{+2\gamma_k(z-z_k)} = \frac{Y_k - Y_k(z)}{Y_k + Y_k(z)}. \tag{4.71}$$

In the last expression, $Y_k(z)$ is the admittance at any position z, defined as the ratio of the total current to voltage at that position

$$Y_k(z) = \frac{I_k(z)}{V_k(z)} = Y_k\frac{1 - \Gamma_k(z)}{1 + \Gamma_k(z)}. \tag{4.72}$$

The total voltage, total current and thus the admittance are continuous upon crossing to another section, but the reflection coefficient is not. The above notions are in principle sufficient to solve the cascaded transmission line problem of Figure 4.4.

4.8.2 Standard Solution for the Cascaded Transmission Line Problem for Arbitrary z, z' Positions

The material presented below is similar to the description in [173], [11], [14]. We first need to determine the equivalent input admittance at the immediate left and right side of the source position z'. These are determined by a set of two inward recurrence computations. Two sets of reflection coefficients and admittances denoted as $\Gamma_k^>(z)$, $Y_k^>(z)$ and $\Gamma_k^<(z)$, $Y_k^<(z)$ are thus determined. Since their values at the outermost left side z_k of section k will occur frequently, and to avoid the formulas from becoming petrifying, we introduce a simplified notation

$$\Gamma_k^> \equiv \Gamma_k^>(z_k) \quad (4.73) \qquad \Gamma_k^< \equiv \Gamma_k^>(z_k) \quad (4.75)$$

$$Y_k^> \equiv Y_k^>(z_k) \quad (4.74) \qquad Y_k^< \equiv Y_k^<(z_k) \quad (4.76)$$

while their values at other z-positions will be explicitly indicated. Note that Y_k (without the superscripts $\lessgtr$) just remains the characteristic impedance of section k.

The Inward Recurrence Procedures

The first recurrence procedure determines the set $\Gamma_k^>(z)$, $Y_k^>(z)$ which will be valid in any computation for which $z > z'$. The computation starts at the outermost right side and proceeds inwards in a recursive manner. The value of $\Gamma_1(z_0)$, $Y_1(z_0)$ are known because of the unbounded medium or metallic ground plane. In the top right side of Figure 4.5, assuming the value of $Y_k^>$ to be known, we can then determine the next $Y_{k+1}^>$ with

$$\Gamma_{k+1}^> = e^{-2\gamma_k(z_k - z_{k+1})} \frac{Y_{k+1} - Y_k^>}{Y_{k+1} + Y_k^>} \quad (4.77)$$

$$Y_{k+1}^> = Y_{k+1} \frac{1 - \Gamma_{k+1}^>}{1 + \Gamma_{k+1}^>}. \quad (4.78)$$

The last step to obtain $Y_j^>(z')$ depends on the exact source position z' and is obtained from

$$\Gamma_j^>(z') = e^{-2\gamma_j(z_{j-1} - z')} \frac{Y_j - Y_{j-1}^>}{Y_j + Y_{j-1}^>} \quad (4.79)$$

$$Y_j^>(z') = Y_j \frac{1 - \Gamma_j^>(z')}{1 + \Gamma_j^>(z')}. \quad (4.80)$$

The second recurrence procedure determines the set $\Gamma_k^<(z)$, $Y_k^<(z)$ which will be valid in any computation for which $z < z'$. The computation starts at the outermost left side. The value of $\Gamma_{N+1}(z_N)$, $Y_{N+1}(z_N)$ are known because of the unbounded medium or metallic ground plane. In the top left side of Figure 4.5, assuming the value of $Y_k^<$ to be known, we can then determine the next values $Y_{k-1}^<$ with

$$\Gamma_k^< = \frac{Y_k - Y_k^<}{Y_k + Y_k^<} \tag{4.81}$$

$$Y_{k-1}^< = Y_k \frac{1 - \Gamma_k^< e^{+2\gamma_k(z_{k-1}-z_k)}}{1 + \Gamma_k^< e^{-2\gamma_k(z_{k-1}-z_k)}}. \tag{4.82}$$

The last step to obtain $Y_j^<(z')$ depends on the exact source position z' and is obtained from

$$\Gamma_j^<(z') = e^{+2\gamma_j(z'-z_j)} \frac{Y_j - Y_j^<(z_j)}{Y_j + Y_j^<(z_j)} \tag{4.83}$$

$$Y_j^<(z') = Y_j \frac{1 - \Gamma_j^<(z')}{1 + \Gamma_j^<(z')}. \tag{4.84}$$

The Excitation at the Source Position

With the equivalent admittances $Y_j^<(z')$, $Y_j^>(z')$ available, all voltages and currents excited by V_S, I_S can now be determined at the immediate left and right side of the source position z' as

$$V_{jj}^{V,\lessgtr}(z', z') = \frac{Y_j^{\gtrless}(z')}{Y_j^<(z') - Y_j^>(z')} V_S \tag{4.85}$$

$$I_{jj}^{V,\lessgtr}(z', z') = \frac{Y_j^<(z') Y_j^>(z')}{Y_j^<(z') - Y_j^>(z')} V_S \tag{4.86}$$

$$V_{jj}^{I,\lessgtr}(z', z') = \frac{1}{Y_j^<(z') - Y_j^>(z')} I_S \tag{4.87}$$

$$I_{jj}^{I,\lessgtr}(z', z') = \frac{Y_j^{\lessgtr}(z')}{Y_j^<(z') - Y_j^>(z')} I_S. \tag{4.88}$$

In the above is it assumed that we everywhere select either the upper or either the lower symbols throughout an expression. In the remaining, we shall assume the excitation to consist of unit voltage $V_S = 1V$ and current $I_S = 1A$ sources.

The Outward Recurrence Procedures

Now that the the voltages and currents at z' have been determined, they can easily be constructed for an arbitrary observation position z. This is done with a set of

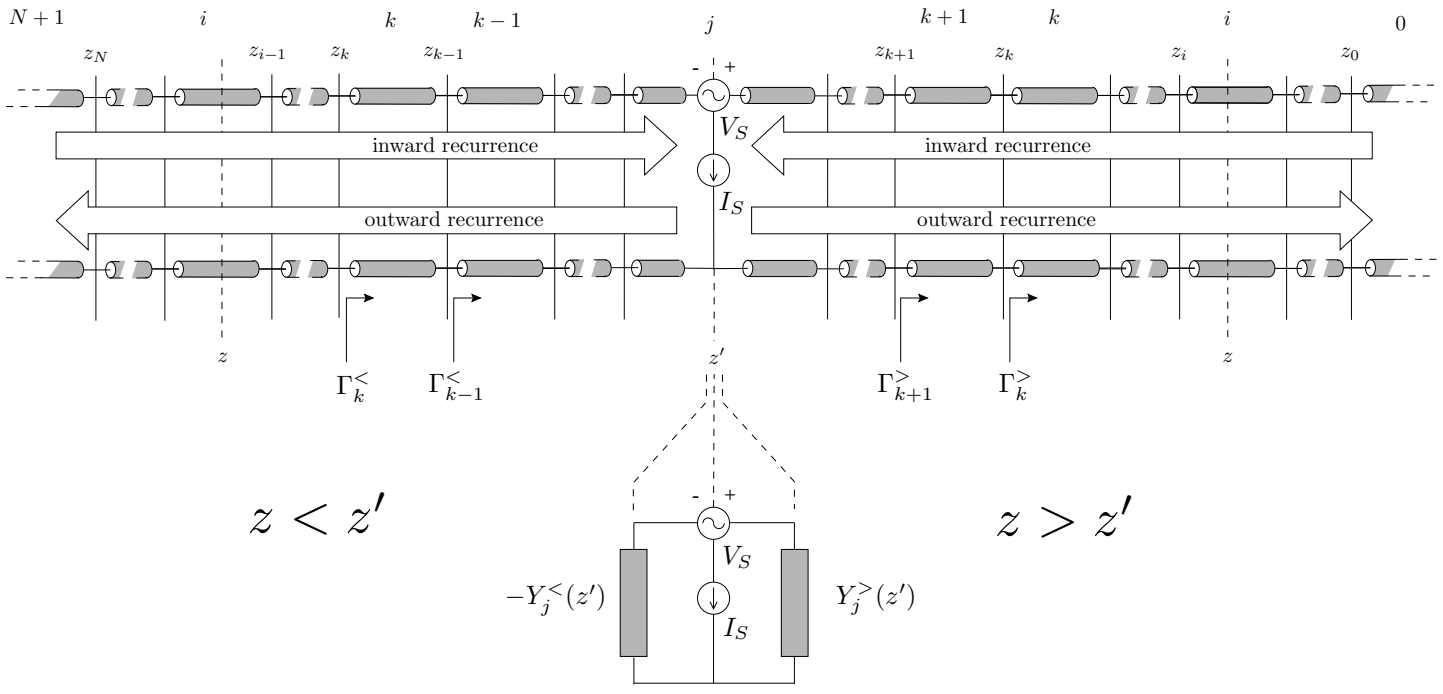

Figure 4.5: The recurrence procedures on the equivalent transmission line network analog for determining the spectral electromagnetic field in a planar multilayered medium. The inward recurrence procedure determine the admittances $Y_j^<(z')$, $Y_j^>(z')$ at the source position. The outward procedures then compute the voltages and currents for $z < z'$ and $z > z'$.

two outward recurrence procedures. Two sets of voltages and currents denoted as $V_k^>(z)$, $I_k^>(z)$ and $V_k^<(z)$, $I_k^<(z)$ are thus determined. Again, their values at z_k are abbreviated to

$$V_k^> \equiv V_k^>(z_k) \quad (4.89) \qquad V_k^< \equiv V_k^<(z_k) \quad (4.91)$$
$$I_k^> \equiv I_k^>(z_k) \quad (4.90) \qquad I_k^< \equiv I_k^<(z_k) \quad (4.92)$$

while their values at other z-positions will be explicitly indicated.

The first outward procedure computes the voltages and currents for $z > z'$. Looking at the bottom right side of Figure 4.5, and assuming $V_{k+1}^>$, $I_{k+1}^>$ to be known, the next $V_k^>$, $I_k^>$ are obtained from

$$V_k^> = V_{k+1}^> \frac{e^{-\gamma_{k+1}(z_k - z_{k+1})} + \Gamma_{k+1}^> e^{+\gamma_{k+1}(z_k - z_{k+1})}}{1 + \Gamma_{k+1}^>} \quad (4.93)$$

$$I_k^> = I_{k+1}^> \frac{e^{-\gamma_{k+1}(z_k - z_{k+1})} 1 - \Gamma_{k+1}^> e^{+\gamma_{k+1}(z_k - z_{k+1})}}{1 - \Gamma_{k+1}^>}. \quad (4.94)$$

The first step in this procedure depends on the source position z'

$$V_{j-1}^> = V_j^>(z') \frac{e^{-\gamma_j(z_{j-1} - z')} + \Gamma_j^>(z') e^{+\gamma_j(z_{j-1} - z')}}{1 + \Gamma_j^>(z')} \quad (4.95)$$

and the last step on the observation coordinate z

$$V_i^>(z) = V_i^> \frac{e^{-\gamma_i(z - z_i)} + \Gamma_i^> e^{+\gamma_i(z - z_i)}}{1 + \Gamma_i^>}. \quad (4.96)$$

The second outward procedure computes the voltages and currents for $z < z'$. Looking at the bottom left side of Figure 4.5, and assuming $V_{k-1}^<$, $I_{k-1}^<$ to be known, the next $V_k^<$, $I_k^<$ are obtained from

$$V_k^< = V_{k-1}^< \frac{1 + \Gamma_k^<}{e^{-\gamma_k(z_{k-1} - z_k)} + \Gamma_k^< e^{+\gamma_k(z_{k-1} - z_k)}} \quad (4.97)$$

$$I_k^< = I_{k-1}^< \frac{1 - \Gamma_k^<}{e^{-\gamma_k(z_{k-1} - z_k)} - \Gamma_k^< e^{+\gamma_k(z_{k-1} - z_k)}}. \quad (4.98)$$

The first step in this procedure depends on the source position z'

$$V_j^< = V_j^<(z') \frac{1 + \Gamma_j^<(z')}{e^{-\gamma_j(z' - z_j)} + \Gamma_j^<(z') e^{+\gamma_j(z' - z_j)}} \quad (4.99)$$

and the last step on the observation coordinate z

$$V_i^<(z) = V_i^<(z_{i-1}) \frac{e^{-\gamma_i(z_{i-1} - z)} + \Gamma_i^< e^{+\gamma_i(z_{i-1} - z)}}{1 + \Gamma_i^<}. \quad (4.100)$$

4.8.3 An Example Expression

The complete expression for a quantity like $V_{ij}^{I,>}(z,z')$ obtained with the standard solution method using Equations (4.87), (4.93), (4.95), (4.96) is

$$\begin{aligned} V_{ij}^{I,>}(z,z') &= \frac{e^{-\gamma_i(z-z_i)}+\Gamma_i^{>}e^{+\gamma_i(z-z_i)}}{1+\Gamma_i^{>}} \\ &\quad \prod_{k=j-1}^{i+1} \frac{e^{-\gamma_k(z_{k-1}-z_k)}+\Gamma_k^{>}e^{+\gamma_k(z_{k-1}-z_k)}}{1+\Gamma_k^{>}} \\ &\quad \frac{e^{-\gamma_j(z_{j-1}-z')}+\Gamma_j^{>}(z')e^{-\gamma_j(z_{j-1}-z')}}{1+\Gamma_j^{>}(z')} \\ &\quad \frac{1}{Y_j^{<}(z')-Y_j^{>}(z')}. \end{aligned} \tag{4.101}$$

An arbitrary Green's function such as the one above thus depends on the spectral wavenumber k_ρ and the source and observation z, z' coordinates. A major problem with this standard approach is the rather complicated dependence on the source z' coordinate through $Y_j^{>}(z')$, $Y_j^{<}(z')$, $\Gamma_j^{>}(z')$ and $\Gamma_j^{<}(z')$ which has to be traced even further with Equations (4.79), (4.80), (4.83), (4.84). This standard approach thus impedes easy analytical manipulation and an efficient computation of the Green's functions. However, this problem was solved by using a specially developed factorised form for an arbitrary Green's function valid for an arbitrary number of layers.

4.9 Factorised Form for Arbitrary Green's Function

In this section, the standard expressions for the Green's functions are rewritten in a form which explicitly separates the observation z and source z' coordinate dependence in simple and symmetrical form.

This factorisation has in itself two major consequences :

- it greatly facilitates the analytical manipulation of the resulting expressions. The factorisation allows to write down compact, powerful and easy to use expressions for derivatives with respect to z and z'. These allow to derive the mixed potential field expressions of the next Chapter 5 from the full spectral electric Green's dyad derived in this chapter. The factorisation with the derivative relations allows to obtain relatively simple closed form expressions for the z, z' dependent part of the reaction integrals as demonstrated in Chapter 6.
- the factorisation is the cornerstone for the efficient numerical computation of Green's functions which have to be constructed in far larger numbers for 3D structures than for simple planar or 2D structures.

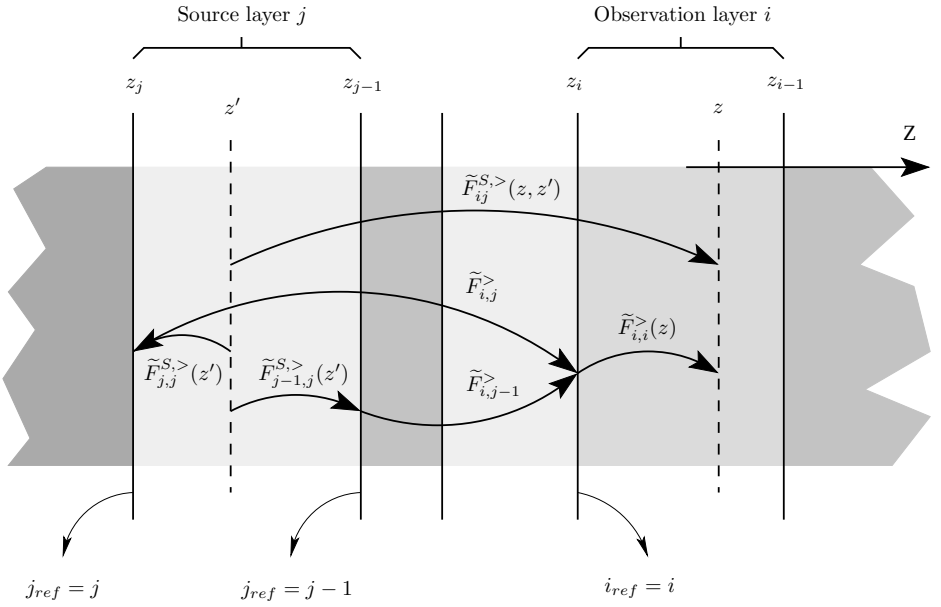

Figure 4.6: Two example factorisations of a Green's function $F^{S,>}_{ij}(z,z')$ into a transfer function $F^{>}_{i_{ref},j_{ref}}$, an observation shift function $F^{>}_{i,i_{ref}}(z)$ and source shift functions $F^{S,>}_{j_{ref},j}(z')$ by choosing "reference planes" $i_{ref}=i$ and $j_{ref}=j,j-1$.

To achieve such a factorisation, we use the concept of "reference planes".

4.9.1 General Approach : Choice of "Reference Planes"

The general idea is given in Figure 4.6, which depicts a situation in which $z > z'$. Instead of computing a Green's function $F^{S,\lessgtr}_{ij}(z,z')$ in the old-fashioned manner, we introduce "reference planes" i_{ref}, j_{ref} for the observation and source sections of the transmission line. These reference planes are positioned at the outermost left $j_{ref}=j$ or right side $j_{ref}=j-1$ of the section at z_j or z_{j-1} as depicted in Figure 4.6 for the source section. The Green's function can now always be factorised as

$$F^{S,\lessgtr}_{ij}(z,z') \quad = \quad F^{\lessgtr}_{i,i_{ref}}(z) \;\; F^{\lessgtr}_{i_{ref},j_{ref}} \;\; F^{S,\lessgtr}_{j_{ref},j}(z') \tag{4.102}$$

into

- a source shift function $F^{S,\lessgtr}_{j_{ref},j}(z')$ to obtain the value at the reference interface j_{ref}, starting from the correct source position z' in section j,
- a transfer function $F^{\lessgtr}_{i_{ref},j_{ref}}$ from the source reference plane j_{ref} to the observation reference plane i_{ref},

- and an observation shift function $F^{\lessgtr}_{i,i_{ref}}(z)$ to obtain the correct observation position in section i starting from the reference interface i_{ref}.

All possible formulas are given for completeness in Appendix A. It may seem superfluous to be able to choose two reference interfaces, but it may occur that some of the quantities are 0 at a reference interface, (for example the voltage is zero if the reference interface coincides with a perfectly conducting ground plane.) while they are not in the other reference plane. If both reference planes in a certain layer are perfectly conducting, the medium in between is necessarily a homogeneous one and all expression become self evident. We now indicate the main steps of the derivation to arrive at these expressions for the particular case $V^{I,>}_{ij}(z,z')$ with reference planes $i_{ref}=i$, $j_{ref}=j$.

4.9.2 The Transfer Functions

By the choice of the reference planes $i_{ref}=i, j_{ref}=j$ the transfer function only transmits the voltage or current from z_j to z_i and does not depend on z or z', but only on the thicknesses d_k of the intervening sections. For the case $z>z'$, the voltage transfer function is given simply by

$$V^{>}_{i,j}=\prod_{k=j}^{i+1}\frac{e^{-\gamma_k d_k}+\Gamma^{>}_k e^{+\gamma_k d_k}}{1+\Gamma^{>}_k}. \tag{4.103}$$

An overview of the other possible transfer functions is given in Appendix A.1.

4.9.3 The Observation Shift Functions

In principle, the dependence on the observation position z is already present in factorised form. For $i_{ref}=i$, we merely rewrite the expression

$$V^{>}_{i,i}(z)=\frac{e^{-\gamma_i(z-z_i)}+\Gamma^{>}_i e^{+\gamma_i(z-z_i)}}{1+\Gamma^{>}_i} \tag{4.104}$$

by inserting the explicit expression for the reflection coefficient

$$\Gamma^{>}_i=\frac{Y_i-Y^{>}_i}{Y_i+Y^{>}_i} \tag{4.105}$$

to obtain an expression

$$V^{>}_{i,i}(z)=\frac{1}{2Y_i}\left((Y_i+Y^{>}_i)e^{-\gamma_i(z-z_i)}+(Y_i-Y^{>}_i)e^{+\gamma_i(z-z_i)}\right) \tag{4.106}$$

which will be symmetrical with the expressions for the source shift functions. An overview of the other required observation shift functions is given in Appendix A.2.

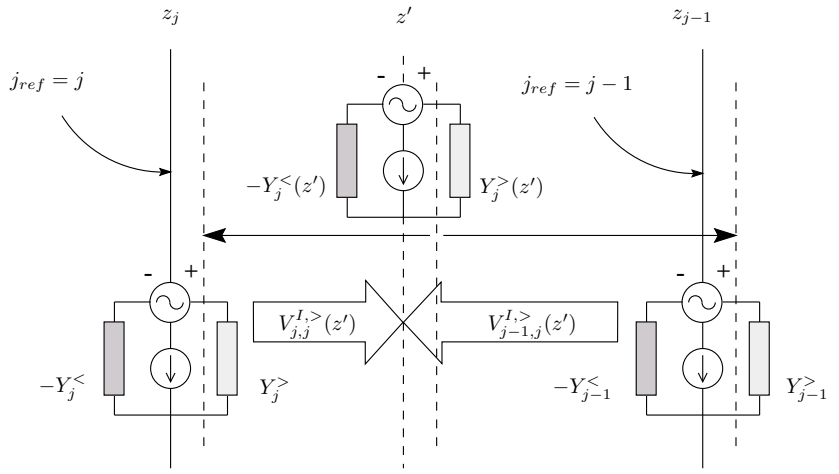

Figure 4.7: The voltage at the reference interface $j_{ref} = j, j-1$ generated by a source at the position z' in layer j can also be obtained by positioning the source at that reference interface and multiplying the generated voltage with the source shift functions $V_{j,j}^{I,>}(z')$ or $V_{j-1,j}^{I,>}(z')$.

4.9.4 The Source Shift Functions

The derivation of the source shift functions is more involved, although the final result will be surprisingly simple and recognizable. The line of reasoning is supported visually by Figure 4.7. We compute the voltage generated by the current source located at z' at its immediate right side as given by Equation (4.87). Since the reference plane was chosen at z_j, we now need to transfer this voltage to z_j. Although the voltage that we computed is only physically useful for $z > z'$, we can still shift it to the left side of the source provided we use the reflection coefficient $\Gamma_j^>$ such that we start from

$$V_{j,j}^{I,>}(z') = \frac{1+\Gamma_j^>}{e^{-\gamma_j(z'-z_j)} + \Gamma_j^> e^{+\gamma_j(z'-z_j)}} \frac{1}{Y_j^<(z') - Y_j^>(z')}. \tag{4.107}$$

Our goal is to extract the apparently extremely complicated z'- dependence of this formula in closed form. To achieve this, we insert the expressions Equations (4.80) and (4.83) for $Y_j^>(z')$ and $Y_j^<(z')$ with the help of Equation (4.71) as a function of quantities defined at z_j

$$Y_j^<(z') = Y_j \frac{1-\Gamma_j^< e^{+2\gamma_j(z'-z_j)}}{1+\Gamma_j^< e^{+2\gamma_j(z'-z_j)}} \tag{4.108}$$

$$Y_j^>(z') = Y_j \frac{1-\Gamma_j^> e^{+2\gamma_j(z'-z_j)}}{1+\Gamma_j^> e^{+2\gamma_j(z'-z_j)}} \tag{4.109}$$

such that the second part of Equation (4.107) can be simplified as

$$\frac{\left(e^{-\gamma_j(z'-z_j)}+\Gamma_j^{<}e^{+\gamma_j(z'-z_j)}\right)\left(e^{-\gamma_j(z'-z_j)}+\Gamma_j^{>}e^{+\gamma_j(z'-z_j)}\right)}{2Y_j\left(\Gamma_j^{>}-\Gamma_j^{<}\right)}. \tag{4.110}$$

By working out the denominator further as a function of the admittances using

$$\Gamma_j^{\lessgtr}=\frac{Y_j-Y_j^{\lessgtr}}{Y_j+Y_j^{\lessgtr}} \tag{4.111}$$

we obtain

$$\frac{1}{\Gamma_j^{>}-\Gamma_j^{<}}=\frac{\left(Y_j+Y_j^{>}\right)\left(Y_j+Y_j^{<}\right)}{2Y_j}\frac{1}{Y_j^{<}-Y_j^{>}} \tag{4.112}$$

of which the second factor is the same as the second factor of our starting point Equation (4.107), and is now the voltage generated by the same source as before, but now located at z_j instead of z'. Inserting Equations (4.110), (4.112) into Equation (4.107), and replacing the remaining reflection coefficients by their definitions Equation (4.111), one finally succeeds by further analytical manipulation at reducing our point of departure Equation (4.107) to simply

$$V_{j,j}^{I,>}(z')=\frac{1}{2Y_j}\Big((Y_j+Y_j^{<})e^{-\gamma_j(z'-z_j)}+(Y_j-Y_j^{<})e^{+\gamma_j(z'-z_j)}\Big)\frac{1}{Y_j^{<}-Y_j^{>}}. \tag{4.113}$$

This formula needs to be interpreted as depicted in the lower part of Figure 4.7. The second part of this expression is indeed the voltage generated by the same source at its immediate right side, but when it is located at z_j. Multiplication with a function that depends on z' gives the voltage at the same position z_j if the source would be located at z'. The first part of the expression thus effectively shifts the source into the source section to the position z'. A similar derivation can be made when the reference interface is located z_{j-1}, a case which is also depicted in Figure 4.7. Notice that the first part is completely symmetrical with the observation shift function of Equation (4.106). The formula thus basically expresses reciprocity and could have been derived as such, provided that our intuitive capacities are sufficient for correctly distinguishing the use of $\Gamma_j^{<}$ and $\Gamma_j^{>}$, as can be seen from the collected formulas of Appendix A.3, which gives an overview of all possible expressions for the source shift functions. The above derivation on the other hand provides an adequate mathematical compass for the correct derivation of these formulas.

4.9.5 The Example Revisited

The apparently complicated example expression of Equation (4.101) can thus be written much simpler with Equations (4.103), (4.106) and (4.113) as

$$V_{ij}^{I,>}(z,z') \quad = \quad \frac{1}{2Y_i}\Big((Y_i+Y_i^{>})e^{-\gamma_i(z-z_i)}+(Y_i-Y_i^{>})e^{+\gamma_i(z-z_i)}\Big)$$

$$\prod_{k=j}^{i+1} \frac{e^{-\gamma_k d_k} + \Gamma_k^{>} e^{+\gamma_k d_k}}{1 + \Gamma_k^{>}}$$
$$\frac{1}{2Y_j} \left((Y_j + Y_j^{<}) e^{-\gamma_j (z' - z_j)} + (Y_j - Y_j^{<}) e^{+\gamma_j (z' - z_j)} \right)$$
$$\frac{1}{Y_j^{<} - Y_j^{>}} \tag{4.114}$$

in which the z and z' dependence are explicitly separated in a simple and symmetrical form. No further z, z' dependence than the one already explicitly indicated above needs to be traced any further.

4.10 Reciprocity Relations

Apart from the factorisation, reciprocity relations can also be used to limit the number of functions that has to be computed. Starting from the general electromagnetic reciprocity theorems, we can easily derive [182], [186], [183]

$$\widetilde{I}^{V}_{i,j}(z, z') = \widetilde{I}^{V}_{j,i}(z', z) \tag{4.115}$$
$$\widetilde{V}^{I}_{i,j}(z, z') = \widetilde{V}^{I}_{j,i}(z', z) \tag{4.116}$$
$$\widetilde{I}^{I}_{i,j}(z, z') = \widetilde{V}^{V}_{j,i}(z', z). \tag{4.117}$$

These relations are also required to verify reciprocity in the analytical formulas of Chapter 6.

4.11 The Missing Derivative Relations

In Chapters 2 and 3, we often used the property of the free space Green's function

$$\nabla = -\nabla'. \tag{4.118}$$

This relation is valid because of the total translational invariance in a homogeneous medium. However, in a multilayered medium there is only translational invariance in the transverse x, y coordinates, so we can only use

$$\nabla_t = -\nabla'_t \tag{4.119}$$

while for the z, z' variables, this operation cannot be performed since the layers of the medium are "in the way". More general formulas for this case can be determined by inspection from the expressions for the factorised form of the Green's functions in

Appendix A. For derivatives involving the observation z coordinate, we see from the equations of Appendix A.2 that

$$\frac{\partial}{\partial z}\ \widetilde{I}^{T,\lessgtr}_{i,i_{ref}}(z) = -\gamma_i Y_i^T\ \widetilde{V}^{T,\lessgtr}_{i,i_{ref}}(z) \tag{4.120}$$

$$\frac{\partial}{\partial z}\ \widetilde{V}^{T,\lessgtr}_{i,i_{ref}}(z) = -\frac{\gamma_i}{Y_i^T}\ \widetilde{I}^{T,\lessgtr}_{i,i_{ref}}(z) \tag{4.121}$$

which are actually the well known transmission line relations. Note that the propagation constant and characteristic admittance of the observation layer i appear by taking derivatives with respect to z. For derivatives with respect to the source z' coordinate, we see from the explicit expression of Appendix A.3 that

$$\frac{\partial}{\partial z'}\widetilde{F}^{V^T,\lessgtr}_{j_{ref},j}(z') = -\gamma_j Y_j^T\ \widetilde{F}^{I^T,\lessgtr}_{j_{ref},j}(z') \tag{4.122}$$

$$\frac{\partial}{\partial z'}\widetilde{F}^{I^T,\lessgtr}_{j_{ref},j}(z') = -\frac{\gamma_j}{Y_j^T}\ \widetilde{F}^{V^T,\lessgtr}_{j_{ref},j}(z') \tag{4.123}$$

where instead of the voltage or current itself, the source type now changes. Also, the propagation constant and characteristic admittance of the source section j are involved. Similar relations were apparently established in [182], [186] using reciprocity, but no special significance or application as we will give in Chapters 5 and 6 was given there.

4.12 The Electromagnetic Field in Dyadic Form

All components of the electric and magnetic field can now be determined as a function of the components of the electric current source. These relations constitute the electric $\widetilde{\overline{G^e}}$ and magnetic $\widetilde{\overline{G^h}}$ dyadic Green's functions in the spectral domain

$$\begin{bmatrix}\widetilde{E}_x\\ \widetilde{E}_y\\ \widetilde{E}_z\end{bmatrix}=\begin{bmatrix}\widetilde{G}^e_{xx} & \widetilde{G}^e_{xy} & \widetilde{G}^e_{xz}\\ \widetilde{G}^e_{yx} & \widetilde{G}^e_{yy} & \widetilde{G}^e_{yz}\\ \widetilde{G}^e_{zx} & \widetilde{G}^e_{zy} & \widetilde{G}^e_{zz}\end{bmatrix}\begin{bmatrix}\widetilde{J}_x\\ \widetilde{J}_y\\ \widetilde{J}_z\end{bmatrix} \tag{4.124}$$

$$\begin{bmatrix}\widetilde{H}_x\\ \widetilde{H}_y\\ \widetilde{H}_z\end{bmatrix}=\begin{bmatrix}\widetilde{G}^h_{xx} & \widetilde{G}^h_{xy} & \widetilde{G}^h_{xz}\\ \widetilde{G}^h_{yx} & \widetilde{G}^h_{yy} & \widetilde{G}^h_{yz}\\ \widetilde{G}^h_{zx} & \widetilde{G}^h_{zy} & \widetilde{G}^h_{zz}\end{bmatrix}\begin{bmatrix}\widetilde{J}_x\\ \widetilde{J}_y\\ \widetilde{J}_z\end{bmatrix}. \tag{4.125}$$

These relations are unique. The components of $\widetilde{\overline{G^e}}$ and $\widetilde{\overline{G^h}}$ always have the same (numerical) value, although the symbols in which they are written can differ considerably. We now derive these expressions and immediately arrange them in a form which links them with the form they take in a homogeneous medium. At this point, we neglect delta-function contributions (see [182], [187], [186]) which arise when the source and observation points coincide. They will be taken up again when we deal with the evaluation of the reaction integrals in Chapter 6.

From the mapping of the TM and TE parts of the field with an equivalent transmission line of Section 4.7, we can now express the independent $\widetilde{E}_z$ and $\widetilde{H}_z$ field components in a layer i as a function of the current and voltage sources in layer j with the Green's function notation of Section 4.9.1 as

$$\widetilde{E}_{iz} = \frac{1}{\omega\epsilon_i}\left[-\frac{k_\rho^2}{k_x}\,\widetilde{I}_{ij}^{I^{TM}}\,\widetilde{J}_{jx}^{TM} - k_\rho^2\,\frac{\widetilde{I}_{ij}^{V^{TM}}}{j\omega\epsilon_j}\,\widetilde{J}_{jz}^{TM}\right] \tag{4.126}$$

$$\widetilde{H}_{iz} = \frac{1}{\omega\mu_i}\left[-\frac{k_\rho^2}{k_y}\,\widetilde{V}_{ij}^{I^{TE}}\,\widetilde{J}_{jx}^{TE}\right] \tag{4.127}$$

All other field components can be derived from $\widetilde{E}_{iz}$ and $\widetilde{H}_{iz}$ using Equations (4.22), (4.23), (4.24), (4.25).

4.12.1 The Electric Field

Introducing the independent field components (4.126), (4.127) into the equations for the transverse electric field (4.22), (4.23), we collect together

$$\widetilde{E}_{ix} = + \widetilde{V}_{ij}^{I^{TM}}\widetilde{J}_{jx}^{TM} + \widetilde{V}_{ij}^{I^{TE}}\widetilde{J}_{jx}^{TE} - jk_x\frac{\partial}{\partial z}\left(\frac{I_{ij}^{V^{TM}}}{j\omega\epsilon_i j\omega\epsilon_j}\right)\widetilde{J}_{jz}^{TM} \tag{4.130}$$

$$\widetilde{E}_{iy} = + \frac{k_x}{k_y}\widetilde{V}_{ij}^{I^{TM}}\widetilde{J}_{jx}^{TM} - \frac{k_x}{k_y}\widetilde{V}_{ij}^{I^{TE}}\widetilde{J}_{jx}^{TE} - jk_y\frac{\partial}{\partial z}\left(\frac{I_{ij}^{V^{TM}}}{j\omega\epsilon_i j\omega\epsilon_j}\right)\widetilde{J}_{jz}^{TM} \tag{4.131}$$

$$\widetilde{E}_{iz} = -\frac{jk_\rho^2}{k_x}\frac{\partial}{\partial z}\left(\frac{\widetilde{V}_{ij}^{I^{TM}}}{-\gamma_i^2}\right)\widetilde{J}_{jx}^{TM} + \left(\frac{\partial^2}{\partial z^2}+k_i^2\right)\left(\frac{I_{ij}^{V^{TM}}}{j\omega\epsilon_i j\omega\epsilon_j}\right)\widetilde{J}_{jz}^{TM} \tag{4.132}$$

where the first terms in Equations (4.130), (4.131), (4.132) were obtained using the TM transmission line relations (4.120), (4.121) and in the last term of Equation (4.132), we realize that k_ρ^2 operates on the Green's function and could thus be replaced using

$$k_\rho^2 = \frac{\partial^2}{\partial z^2} + k_i^2. \tag{4.133}$$

Finally, introducing the expression (4.48), (4.51), (4.50) for $\widetilde{J}_x^{TM}$, $\widetilde{J}_x^{TE}$, $\widetilde{J}_z^{TM}$, and rearranging some terms, we obtain the full spectral electric dyadic Green's function valid in an arbitrary plane-stratified environment and given in Equation (4.128).

$$\begin{bmatrix} \widetilde{E}_{ix} \\ \widetilde{E}_{iy} \\ \widetilde{E}_{iz} \end{bmatrix} = \begin{bmatrix} \widetilde{V}_{ij}^{I^{TE}} + jk_x jk_x \left(\dfrac{\widetilde{V}_{ij}^{I^{TE}} - \widetilde{V}_{ij}^{I^{TM}}}{k_\rho^2} \right) & + jk_x jk_y \left(\dfrac{\widetilde{V}_{ij}^{I^{TE}} - \widetilde{V}_{ij}^{I^{TM}}}{k_\rho^2} \right) & - jk_x \dfrac{\partial}{\partial z} \left(\dfrac{\widetilde{I}_{ij}^{V^{TM}}}{j\omega\epsilon_i j\omega\epsilon_j} \right) \\ + jk_y jk_x \left(\dfrac{\widetilde{V}_{ij}^{I^{TE}} - \widetilde{V}_{ij}^{I^{TM}}}{k_\rho^2} \right) & \widetilde{V}_{ij}^{I^{TE}} + jk_y jk_y \left(\dfrac{\widetilde{V}_{ij}^{I^{TE}} - \widetilde{V}_{ij}^{I^{TM}}}{k_\rho^2} \right) & - jk_y \dfrac{\partial}{\partial z} \left(\dfrac{\widetilde{I}_{ij}^{V^{TM}}}{j\omega\epsilon_i j\omega\epsilon_j} \right) \\ -\dfrac{\partial}{\partial z} jk_x \left(\dfrac{\widetilde{V}_{ij}^{I^{TM}}}{-\gamma_i^2} \right) & -\dfrac{\partial}{\partial z} jk_y \left(\dfrac{\widetilde{V}_{ij}^{I^{TM}}}{-\gamma_i^2} \right) & -\dfrac{\mu_i}{\epsilon_j} \widetilde{I}_{ij}^{V^{TM}} + \dfrac{\partial}{\partial z} \dfrac{\partial}{\partial z} \left(\dfrac{\widetilde{I}_{ij}^{V^{TM}}}{j\omega\epsilon_i j\omega\epsilon_j} \right) \end{bmatrix} \begin{bmatrix} \widetilde{J}_{jx} \\ \widetilde{J}_{jy} \\ \widetilde{J}_{jz} \end{bmatrix}$$

The full spectral electric dyadic Green's function $\overline{\widetilde{G}}^e$ for an arbitrary plane-stratified medium. (4.128)

$$\begin{bmatrix} \widetilde{H}_{ix} \\ \widetilde{H}_{iy} \\ \widetilde{H}_{iz} \end{bmatrix} = \begin{bmatrix} + jk_x jk_y \left(\dfrac{\widetilde{I}_{ij}^{I^{TM}} - \widetilde{I}_{ij}^{I^{TE}}}{k_\rho^2} \right) & -\widetilde{I}_{ij}^{I^{TM}} - jk_x jk_x \left(\dfrac{\widetilde{I}_{ij}^{I^{TM}} - \widetilde{I}_{ij}^{I^{TE}}}{k_\rho^2} \right) & -jk_y \left(\dfrac{\widetilde{I}_{ij}^{V^{TM}}}{j\omega\epsilon_j} \right) \\ +\widetilde{I}_{ij}^{I^{TM}} + jk_y jk_y \left(\dfrac{\widetilde{I}_{ij}^{I^{TM}} - \widetilde{I}_{ij}^{I^{TE}}}{k_\rho^2} \right) & - jk_x jk_y \left(\dfrac{\widetilde{I}_{ij}^{I^{TM}} - \widetilde{I}_{ij}^{I^{TE}}}{k_\rho^2} \right) & +jk_x \left(\dfrac{\widetilde{I}_{ij}^{V^{TM}}}{j\omega\epsilon_j} \right) \\ +jk_y \left(-\dfrac{\widetilde{V}_{ij}^{I^{TE}}}{j\omega\mu_i} \right) & -jk_x \left(-\dfrac{\widetilde{V}_{ij}^{I^{TE}}}{j\omega\mu_i} \right) & 0 \end{bmatrix} \begin{bmatrix} \widetilde{J}_{jx} \\ \widetilde{J}_{jy} \\ \widetilde{J}_{jz} \end{bmatrix}$$

The full spectral magnetic dyadic Green's function $\overline{\widetilde{G}}^h$ for an arbitrary plane-stratified medium. (4.129)

4.12.2 The Magnetic Field

Introducing the independent field components (4.126), (4.127) into the equations for the transverse magnetic field (4.24), (4.25), we obtain similarly

$$\widetilde{H}_{ix} = - \quad \frac{k_y}{k_x}\widetilde{I}_{ij}^{I^{TM}}\widetilde{J}_{jx}^{TM} + \frac{k_x}{k_y}\widetilde{I}_{ij}^{I^{TE}}\widetilde{J}_{jx}^{TE} - jk_y\frac{\partial}{\partial z}\left(\frac{\widetilde{I}^{V^{TM}}}{j\omega\epsilon_j}\right)\widetilde{J}_{jz}^{TM} \quad (4.134)$$

$$\widetilde{H}_{iy} = + \quad \widetilde{I}_{ij}^{I^{TM}}\widetilde{J}_{jx}^{TM} + \quad \widetilde{I}_{ij}^{I^{TE}}\widetilde{J}_{jx}^{TE} + jk_x\frac{\partial}{\partial z}\left(\frac{\widetilde{I}^{V^{TM}}}{j\omega\epsilon_j}\right)\widetilde{J}_{jz}^{TM} \quad (4.135)$$

$$\widetilde{H}_{iz} = \quad -\frac{1}{\omega\mu_i}\frac{k_\rho^2}{k_y}\widetilde{V}_{ij}^{I^{TE}}\widetilde{J}_{ix}^{TE} \quad (4.136)$$

where the second term in Equations (4.134), (4.135) were obtained with the transmission line Equations (4.120), (4.121) for the TE system. Finally, we replace $\widetilde{J}_x^{TM}$, $\widetilde{J}_x^{TE}$, $\widetilde{J}_z^{TM}$ with (4.48), (4.51), (4.50) and rearrange terms to obtain the full spectral magnetic dyadic Green's function, given in Equation (4.129).

4.12.3 The Homogeneous Medium

The explicit expressions for the full spectral electric and magnetic dyadic Green's functions for a planar multilayered surround given in Equations (4.128) and (4.129) seem fairly complicated. We therefore take a look at how these expressions reduce to the corresponding free space formulations when the medium is a homogeneous one. This will establish the necessary intuitive physical link with the widely used free space electric and magnetic field formulations. It will also indicate how to expand any theoretical development or numerical method originally developed for the homogeneous case to the more complicated stratified medium. Finally, the static near field of a current source in a certain layer j is the same as the field in a homogeneous medium with parameters ϵ_j, μ_j.

For a homogeneous medium characterised by ϵ, μ, the admittances $Y^>(z')$ and $Y^<(z')$ at the source position z' reduce to simply the free space wave impedance of the medium

$$Y^>(z') = +Y \quad (4.137)$$

$$Y^<(z') = -Y \quad (4.138)$$

which can be used Equations (4.85), (4.86), (4.87), (4.88) for the currents and voltages generated at the source position. The waves traveling outward from the source are then simply propagated by $e^{-\gamma|z-z'|}$.

For the spectral electric Green's dyad in Equation (4.128), we see that in $\widetilde{G}_{xx}^e$, $\widetilde{G}_{yy}^e$,

$\widetilde{G}^e_{zx}$, $\widetilde{G}^e_{zy}$ and $\widetilde{G}^e_{xz}$, $\widetilde{G}^e_{yz}$, $\widetilde{G}^e_{zz}$ we can immediately simplify

$$\widetilde{V}^{I^{TE}} = -\frac{1}{2Y^{TE}}\, e^{-\gamma|z-z'|} = -\frac{1}{2}\,\frac{j\omega\mu}{\gamma}\, e^{-\gamma|z-z'|} \tag{4.139}$$

$$\widetilde{V}^{I^{TM}} = -\frac{1}{2Y^{TM}}\, e^{-\gamma|z-z'|} = -\frac{1}{2}\,\frac{\gamma}{j\omega\epsilon}\, e^{-\gamma|z-z'|} \tag{4.140}$$

$$\widetilde{I}^{V^{TM}} = +\frac{Y^{TM}}{2}\, e^{-\gamma|z-z'|} = +\frac{1}{2}\,\frac{j\omega\epsilon}{\gamma}\, e^{-\gamma|z-z'|} \tag{4.141}$$

and this allows to work out the remaining expressions in $\widetilde{G}^e_{xx}$, $\widetilde{G}^e_{xy}$, $\widetilde{G}^e_{yx}$, $\widetilde{G}^e_{yy}$ as

$$\frac{\widetilde{V}^{I^{TE}} - \widetilde{V}^{I^{TM}}}{k_\rho^2} = +\frac{1}{2}\left(\frac{\gamma}{j\omega\epsilon} - \frac{j\omega\mu}{\gamma}\right)\frac{e^{-\gamma|z-z'|}}{k_\rho^2} = +\frac{1}{2}\frac{1}{j\omega\epsilon}\frac{e^{-\gamma|z-z'|}}{\gamma} \tag{4.142}$$

where we made use of $\gamma^2 + k^2 = k_\rho^2$. All expressions in the spectral electric dyadic Green's function now have a common factor $e^{-\gamma|z-z'|}/\gamma$.

For the magnetic field, we already determined $\widetilde{V}^{I^{TE}}$ for use in $\widetilde{G}^h_{zx}$, $\widetilde{G}^h_{zy}$ and $\widetilde{I}^{V^{TM}}$ that appears in $\widetilde{G}^e_{xz}$, $\widetilde{G}^e_{xz}$. The remaining expressions need slightly more interpretation. First, we verify that

$$\widetilde{I}^{I^{TM}} = \pm\frac{1}{2}e^{\gamma|z-z'|} \tag{4.143}$$

$$\widetilde{I}^{I^{TE}} = \pm\frac{1}{2}e^{\gamma|z-z'|} \tag{4.144}$$

such that the expression

$$\frac{\widetilde{I}^{I^{TM}} - \widetilde{I}^{I^{TE}}}{k_\rho^2} = 0 \tag{4.145}$$

vanishes completely from $\widetilde{G}^h_{xx}$, $\widetilde{G}^h_{xy}$, $\widetilde{G}^h_{yx}$, $\widetilde{G}^h_{yy}$. The remaining term in $\widetilde{G}^h_{xy}$, $\widetilde{G}^h_{yx}$, is best rewritten using Equation 4.120 as

$$\widetilde{I}^{I^{TM}} = j\omega\epsilon\frac{\partial}{\partial z}\left(-\frac{\widetilde{V}^{I^{TM}}}{\gamma^2}\right) \tag{4.146}$$

such that the common factor $e^{-\gamma|z-z'|}/\gamma$ of the electric field expression also appears in the magnetic field formulation.

In a homogeneous medium, the full spectral electric and magnetic dyadic Green's functions from Equation (4.128) and (4.129) can thus be written with a single free

space scalar Green's function as

$$\begin{bmatrix} \widetilde{E}_x \\ \widetilde{E}_y \\ \widetilde{E}_z \end{bmatrix} = -j\omega\mu \begin{bmatrix} 1+\frac{1}{k^2}jk_xjk_x & +\frac{1}{k^2}jk_xjk_y & -\frac{1}{k^2}jk_x\frac{\partial}{\partial z} \\ +\frac{1}{k^2}jk_yjk_x & 1+\frac{1}{k^2}jk_yjk_y & -\frac{1}{k^2}jk_y\frac{\partial}{\partial z} \\ -\frac{1}{k^2}\frac{\partial}{\partial z}jk_x & -\frac{1}{k^2}\frac{\partial}{\partial z}jk_y & 1+\frac{1}{k^2}\frac{\partial}{\partial z}\frac{\partial}{\partial z} \end{bmatrix} \frac{e^{-\gamma|z-z'|}}{2\gamma} \begin{bmatrix} \widetilde{J}_x \\ \widetilde{J}_y \\ \widetilde{J}_z \end{bmatrix} \quad (4.147)$$

$$\begin{bmatrix} \widetilde{H}_x \\ \widetilde{H}_y \\ \widetilde{H}_z \end{bmatrix} = \begin{bmatrix} 0 & \frac{\partial}{\partial z} & -jk_y \\ -\frac{\partial}{\partial z} & 0 & +jk_x \\ +jk_y & -jk_x & 0 \end{bmatrix} \frac{e^{-\gamma|z-z'|}}{2\gamma} \begin{bmatrix} \widetilde{J}_x \\ \widetilde{J}_y \\ \widetilde{J}_z \end{bmatrix}. \quad (4.148)$$

These expressions become even more familiar when we perform the inverse Fourier transform back to the spatial domain. In case of a homogeneous medium, the inverse Fourier transform Equation (4.3) of the free space scalar Green's function can by way of exception be performed in closed form by the Sommerfeld identity Equation (B.1) of Appendix B.1

$$\mathfrak{F}^{-1}\left\{\frac{e^{-\gamma|z-z'|}}{2\gamma}\right\} = \mathfrak{F}^{-1}\left\{\frac{e^{-\sqrt{k_\rho^2-k^2}|z-z'|}}{2\sqrt{k_\rho^2-k^2}}\right\} = \frac{e^{-jkR}}{4\pi R} \quad (4.149)$$

where $R = \sqrt{(x-x')^2+(y-y')^2+(z-z')^2}$ is the distance between source and observation point in the spatial domain. Taking into account the Fourier transform relations (4.9), (4.10), (4.11) the electric and magnetic dyadic Green's function in the spatial domain are written as

$$\vec{E} = -j\omega\mu\left[\,\overline{I}+\frac{1}{k^2}\nabla\nabla\,\right]\,\frac{e^{-jkR}}{4\pi R}\,.\,\vec{J} \quad (4.150)$$

$$\vec{H} = \left[\,\nabla\times\overline{I}\,\right]\,\frac{e^{-jkR}}{4\pi R}\,.\,\vec{J} = \nabla\times\,\frac{e^{-jkR}}{4\pi R}\,\vec{J}. \quad (4.151)$$

These results thus testify as to the validity of the spectral domain approach, since the same expressions for the electric and magnetic field were previously derived by application of Green's theorem in Chapter 2.

4.13 Conclusions

In this chapter, we have determined the expressions for the electric and magnetic fields in the spectral domain, generated by a three dimensional point-like current source

embedded within a general stratified medium. These expressions constitute the full spectral electric and magnetic dyadic Green's functions. To achieve this, we solved Maxwell's equations under the appropriate boundary conditions by a Spectral Domain Approach. The set of vector equations can be simplified into two scalar transmission line problems, which can be identified with the TM and TE decomposition of fields and currents. The further solution was initially treated with basic transmission line theory to solve the cascaded transmission line network analog of the stratified medium. However, the standard expressions obtained in this way were felt to be too complicated to manipulate in a straightforward manner and they impede an efficient numerical analysis of three dimensional structures. A new and simple factorised form for an arbitrary Green's function explicitly separating the z and z' coordinate dependence in simple and symmetric form was thus developed. This factorisation facilitates the analytical manipulation of all Green's function expressions in the remainder of the text and is the cornerstone of the computation of the Green's functions to analyse three dimensional structures in planar stratified media.

Chapter 5

The Electric Field in Dyadic, Mixed Potential and Hybrid Form.

5.1 Introduction

In the previous chapter, we obtained the full spectral electric dyadic Green's function for a 3D point-like current source in an arbitrary plane stratified medium. This Green's function appears as the kernel of the BIE that we will solve. However, instead of using these expressions directly with a brute-force purely numerical approach, the expressions can be re-arranged into other forms which allow better to keep in touch with the physical reality of the problem.

Historically, full wave electromagnetic BIE formulations have been applied first to analyse thin wire antennas [188], [189] which can only be handled with the EFIE. Later on, the main application was in the prediction of the Radar Cross Section (RCS) of aerospace vehicles. For these larger closed smooth surfaces the MFIE was found to be better suited [38]. Initial solution of the EFIE thus took place in free space and in the spatial domain. It was found that instead of using the dyadic field formulation directly, rearranging the expression to a so called Mixed Potential Integral Equation (MPIE) offers considerable advantages for the numerical solution as well as for preserving physical insight. The analysis of planar antennas and circuits in stratified media mostly involves thin open structures, thus using the EFIE. Initial simple geometries like planar transmission line cross sections were analysed using the dyadic Green's function in the spectral domain [166]. The advantages of the more physical MPIE approach in the space domain resurfaced when more complicated

arbitrarily shaped planar antennas and circuits had to be analysed [190]. These space domain MPIE approaches were gradually extended to deal with fully 3D structures in layered media [191].

We introduce the dyadic and mixed potential electric field formulations for a homogeneous medium in Section 5.2. We derive the mixed potential form from the dyadic expression in the space domain in Section 5.2.1 with a derivation which focuses on the physical meaning of the frequency dependence and the presence of spatial derivatives in the components of the dyad. The same operations for a homogeneous medium are then transposed to the spectral domain in Section 5.2.2. We then apply the same physics based derivation to the full spectral Green's dyad for a stratified medium in Section 5.3. We obtain the "basic" mixed potential form of Section 5.3.1 which has a simple vector potential but multiple scalar potential kernels. From the "basic" form, we derive the more familiar single scalar potential kernel formulations in Section 5.3.2, but these exhibit a dyadic vector potential. It is thus demonstrated that MPIE representations can be obtained without an a priori choice of scalar potential kernel, suitable components of the dyadic vector potential kernel, or any gauge condition. It is believed that in this way the problems of the non-uniqueness of the scalar potential kernel and/or the dyadic nature of the vector potential kernel surface more clearly. The return to more familiar space domain via the inverse Fourier transform (Section 5.4) leads to the Sommerfeld integral representation. The physical interpretation takes place in the space domain and is given in Section 5.5. In Section 5.6, we relate the mixed potential formulations with the Sommerfeld problem and demonstrate for the first time that the transition between them strictly satisfies the mathematical gauge transformation formalism, applied for the case of a planar stratified medium. Finally, after studying the relation of the field formulation with the geometry of the problem in Section 5.7, we formulate a new hybrid dyadic mixed potential formulation for the electric field in Section 5.8.

This new hybrid field formulation is matched to "quasi 3D" structures, which are not fully three dimensional in a strict sense, but still allows to analyse most problems in planar stratified media that one first thinks of as fully three dimensional. By focusing on this specific geometry, the typical theoretical and numerical problems of standard total dyadic or total mixed potential formulations are avoided and all analytical possibilities can be exploited to the utmost, as demonstrated further in the evaluation of the reaction integrals in Chapter 6.

5.2 Dyadic and Mixed Potential Form in Free Space

We first introduce the dyadic and mixed potential forms for the case of a homogeneous medium in the spatial domain in Section 5.2.1, where the essential features are clearly displayed. Preparing the derivation of the field formulations in a general stratified medium we take a look at the form they take in the spectral domain in Section 5.2.2.

5.2.1 The Spatial Domain

In a homogeneous medium characterised by μ, ϵ, a surface current $\vec{J}(\vec{r}')$ located at $\vec{r}'$ on a perfectly conducting surface S' generates an electric field $\vec{E}(\vec{r})$ at $\vec{r}$ given in dyadic form as

$$\vec{E}(\vec{r}) \quad = \quad -j\omega\mu \int\limits_{S'} \left[\overline{I} + \frac{1}{k^2} \nabla\nabla \right] G.\ \vec{J}(\vec{r}')\ \mathrm{d}S' \tag{5.1}$$

where $\overline{I}$ is the unit dyadic, $k = \omega\sqrt{\mu\epsilon}$ and $G = e^{-jkR}/4\pi R$ the free space Green's function. In the above equation, the operators between brackets are assumed to operate on G to obtain the components of the dyadic Green's function. Due to the double spatial derivative, these components have a hypersingular $1/R^3$ behaviour, which is undesirable from a numerical point of view. No special attention is given to the frequency dependence of the expressions, which makes physical interpretation difficult.

Equation (5.1) can be transformed into a mixed potential form by performing the following transformations on the part containing the double derivatives. In the first step, the outer derivatives are brought out of the surface integral

$$\int\limits_{S'} [\ \nabla\nabla\ ]\, G.\vec{J}\ \mathrm{d}S' = \nabla \int\limits_{S'} \nabla G.\vec{J}\ \mathrm{d}S' \tag{5.2}$$

were we neglect for the moment the additional contributions that occur for the singular case $\vec{r} = \vec{r}'$ [192], [193], [194]. In the second and third step, we transfer the inner derivatives from the Green's function to the current. The second step uses the property

$$\nabla G(\vec{r}, \vec{r}\,') = -\nabla' G(\vec{r}, \vec{r}\,') \tag{5.3}$$

which is only valid for a homogeneous medium. In the third step these derivatives are then transferred to the current with a partial integration

$$\int\limits_{S'} -\nabla G'.\vec{J}\ \mathrm{d}S' = \int\limits_{S'} \left\{ G\ \nabla'.\vec{J} - \nabla'.(\ G\vec{J}\ ) \right\}\ \mathrm{d}S' \tag{5.4}$$

where the second term on the right hand side can give an additional line integral contributions to the field if the current crosses an interface between different layers of the medium and the function G is discontinuous [191]. For the moment, we will neglect the special contributions from the first and third step, but we will generalise the second step as this will be sufficient to derive the main expressions. We thus obtain

$$\vec{E}(\vec{r}) \quad = \quad -j\omega \int\limits_{S'} \frac{\mu e^{-jkR}}{4\pi R}\ \vec{J}(\vec{r}')\ \mathrm{d}S' - \nabla \int\limits_{S'} \frac{e^{-jkR}}{4\pi\epsilon R} \left(\frac{\nabla'.\vec{J}(\vec{r}')}{-j\omega} \right)\ \mathrm{d}S'. \tag{5.5}$$

The first part of this expression is the vector potential contribution generated by the current. In the quasi-static limit, this contribution is proportional to frequency and then describes magnetostatic and low frequency electric induction phenomena. The second part is the scalar potential generated by the charge. It is inversely proportional to frequency, such that in the static limit, this describes all familiar electrostatic phenomena. This way of writing thus conveys a lot of physical information. Also, only a basic $1/R$ spatial singular behaviour is present in both the scalar and vector potential kernels, which is numerically convenient.

5.2.2 The Spectral Domain

In the spectral domain, we shall omit the integration over the surface S' not to overburden the matrix notation. The spectral domain counterpart of the dyadic expression Equation (5.1) was already determined in Section 4.12.3 of Chapter 4, and is written as

$$\begin{bmatrix} \widetilde{E}_x \\ \widetilde{E}_y \\ \widetilde{E}_z \end{bmatrix} = -j\omega\mu \begin{bmatrix} 1+\frac{1}{k^2}jk_xjk_x & +\frac{1}{k^2}jk_xjk_y & -\frac{1}{k^2}jk_x\frac{\partial}{\partial z} \\ +\frac{1}{k^2}jk_yjk_x & 1+\frac{1}{k^2}jk_yjk_y & -\frac{1}{k^2}jk_y\frac{\partial}{\partial z} \\ -\frac{1}{k^2}\frac{\partial}{\partial z}jk_x & -\frac{1}{k^2}\frac{\partial}{\partial z}jk_y & 1+\frac{1}{k^2}\frac{\partial}{\partial z}\frac{\partial}{\partial z} \end{bmatrix} \widetilde{G} \begin{bmatrix} \widetilde{J}_x \\ \widetilde{J}_y \\ \widetilde{J}_z \end{bmatrix} \tag{5.6}$$

where $\widetilde{G} = e^{-\gamma|z-z'|}/2\gamma$ is the free space Green's function in the spectral domain. The first step of Equation (5.2) translates into the spectral domain as

$$\begin{bmatrix} +jk_xjk_x & +jk_xjk_y & -jk_x\frac{\partial}{\partial z} \\ +jk_yjk_x & +jk_yjk_y & -jk_y\frac{\partial}{\partial z} \\ -\frac{\partial}{\partial z}jk_x & -\frac{\partial}{\partial z}jk_x & +\frac{\partial}{\partial z}\frac{\partial}{\partial z} \end{bmatrix} \widetilde{G} \begin{bmatrix} \widetilde{J}_x \\ \widetilde{J}_y \\ \widetilde{J}_z \end{bmatrix} = \begin{bmatrix} -jk_x \\ -jk_y \\ \frac{\partial}{\partial z} \end{bmatrix} \begin{bmatrix} -jk_x & -jk_y & -\frac{\partial}{\partial z'} \end{bmatrix} \widetilde{G} \begin{bmatrix} \widetilde{J}_x \\ \widetilde{J}_y \\ \widetilde{J}_z \end{bmatrix} \tag{5.7}$$

while the equivalent of the second step of Equation (5.3) becomes

$$\begin{bmatrix} -jk_x \\ -jk_y \\ +\frac{\partial}{\partial z} \end{bmatrix} \widetilde{G}(k_\rho, z, z') = - \begin{bmatrix} +jk_x \\ +jk_y \\ +\frac{\partial}{\partial z'} \end{bmatrix} \widetilde{G}(k_\rho, z, z'). \tag{5.8}$$

In the third step, the inner derivatives are transferred to the current with a sign change in a partial integration process as in Equation (5.4), but as we suppress the

surface integrals, we abbreviate this transition in the spectral domain as

$$\left[-jk_x \; -jk_y \; -\frac{\partial}{\partial z'}\right]\widetilde{G}\begin{bmatrix}\widetilde{J}_x\\ \widetilde{J}_x\\ \widetilde{J}_z\end{bmatrix} \rightarrow \widetilde{G}\left(+jk_x\widetilde{J}_x + jk_y\widetilde{J}_y + \frac{\partial \widetilde{J}_z}{\partial z'}\right). \tag{5.9}$$

The mixed potential form of Equation (5.5) thus transforms into the spectral domain as

$$\begin{bmatrix}\widetilde{E}_x\\ \widetilde{E}_y\\ \widetilde{E}_z\end{bmatrix} = -j\omega\mu\widetilde{G}\begin{bmatrix}\widetilde{J}_x\\ \widetilde{J}_y\\ \widetilde{J}_z\end{bmatrix} - \begin{bmatrix}-jk_x\\ -jk_y\\ +\dfrac{\partial}{\partial z}\end{bmatrix}\frac{\widetilde{G}}{\epsilon}\left(\frac{+jk_xJ_x + jk_yJ_y + \dfrac{\partial J_z}{\partial z'}}{-j\omega}\right). \tag{5.10}$$

5.3 Dyadic and Mixed Potential Form in a Stratified Medium

In determining electric field formulations for a general multilayered medium, several complications arise. First, the expressions are only available in closed form in the spectral domain, while the expressions in the spatial domain have to be determined (partially) in a numerical manner via an inverse Fourier transform. Analytical manipulation is thus generally easier in the spectral domain. Second, instead of a single scalar Green's function, the field is determined by several different Green's functions. Although a dyadic formulation is unique, mixed potential forms are not. In the following section, we will derive mixed potential forms from the unique dyadic representation in the spectral domain.

5.3.1 The "Basic" Mixed Potential Form

The derivation starts from the unique full spectral electric Green's dyad of Equation (4.128) of Chapter 4. This expression is similar to the free space electric Green's dyad of Equation (5.6), except that instead of a single scalar Green's function, 5 different functions appear. We abbreviate it symbolically as

$$\overline{\overline{\widetilde{G}}}^e = -j\omega\begin{bmatrix}\widetilde{G}_{xx} & 0 & 0\\ 0 & \widetilde{G}_{xx} & 0\\ 0 & 0 & \widetilde{G}_{zz}\end{bmatrix} + \frac{1}{j\omega}\begin{bmatrix}\begin{bmatrix}+jk_xjk_x & +jk_xjk_y\\ +jk_yjk_x & +jk_yjk_y\end{bmatrix}\widetilde{\phi}_t & \begin{bmatrix}-jk_x\\ -jk_y\end{bmatrix}\dfrac{\partial}{\partial z}\;\widetilde{\phi}_z'\\ +\dfrac{\partial}{\partial z}\begin{bmatrix}-jk_x & -jk_y\end{bmatrix}\widetilde{\phi}_{zt} & +\dfrac{\partial}{\partial z}\dfrac{\partial}{\partial z}\;\widetilde{\phi}_z'\end{bmatrix}.$$

(5.11)

which foreshadows the meaning of the components as scalar and vector potential components. Identification with Equation (4.128) reveals

$$\widetilde{G}_{xx} = \frac{\widetilde{V}_{ij}^{I^{TE}}}{-j\omega} \quad (5.12) \qquad \widetilde{G}_{zz} = \frac{\mu_i}{\epsilon_j}\frac{\widetilde{I}_{ij}^{V^{TM}}}{j\omega} \quad (5.13)$$

$$\widetilde{\phi}_t = j\omega\frac{\widetilde{V}_{ij}^{I^{TE}} - \widetilde{V}_{ij}^{I^{TM}}}{k_\rho^2} \quad (5.14) \qquad \widetilde{\phi}_z{}' = \frac{\widetilde{I}_{ij}^{V^{TM}}}{j\omega\epsilon_i\epsilon_j} \quad (5.15) \quad \widetilde{\phi}_{zt} = -j\omega\frac{\widetilde{V}_{ij}^{I^{TM}}}{\gamma_i^2} \quad (5.16)$$

To derive mixed potential forms, we need to transfer the inner derivatives in Equation (5.11) to the current in a partial integration process. The Green's functions $\widetilde{G}_{ij}^{S^T}$ show translational invariance only in the transverse x, y coordinates, such that we can continue using

$$\begin{bmatrix} -jk_x \\ -jk_y \end{bmatrix} \widetilde{G}_{ij}^{S^T}(k_\rho, z, z') = -\begin{bmatrix} +jk_x \\ +jk_y \end{bmatrix} \widetilde{G}_{ij}^{S^T}(k_\rho, z, z') \quad (5.17)$$

in the same manner as in Equation (5.8). However, for the z, z' derivatives, we have to rely on the generalisations established in Equations (4.120), (4.121), (4.122) and (4.123). We can neglect the factorisation and the distinction between $z > z'$ and $z < z'$ at this points and use

$$\frac{\partial}{\partial z}\ \widetilde{I}_{ij}^{S^T} = -\gamma_i Y_i^T\ \ \widetilde{V}_{ij}^{S^T} \quad (5.18) \qquad \frac{\partial}{\partial z'}\ \widetilde{F}_{ij}^{V^T} = -\gamma_j Y_j^T\ \ \widetilde{F}_{ij}^{I^T} \quad (5.20)$$

$$\frac{\partial}{\partial z}\ \widetilde{V}_{ij}^{S^T} = -\frac{\gamma_i}{Y_i^T}\ \ \widetilde{I}_{i,j}^{S^T} \quad (5.19) \qquad \frac{\partial}{\partial z'}\ \widetilde{F}_{ij}^{I^T} = -\frac{\gamma_j}{Y_j^T}\ \ \widetilde{F}_{ij}^{V^T}. \quad (5.21)$$

We now attempt to perform the three step process on the part of Equation (5.11) containing the double derivatives. In the first step, the outer derivatives are again separated as in Equation (5.7), but taking into account the multiple scalar potential functions as

$$\begin{bmatrix} \begin{bmatrix} +jk_xjk_x & +jk_xjk_y \\ +jk_yjk_x & +jk_yjk_y \end{bmatrix} \widetilde{\phi}_t & \begin{bmatrix} -jk_x \\ -jk_y \end{bmatrix}\frac{\partial}{\partial z}\ \widetilde{\phi}_z{}' \\ +\frac{\partial}{\partial z}\begin{bmatrix} -jk_x & -jk_y \end{bmatrix} \widetilde{\phi}_{zt} & +\frac{\partial}{\partial z}\frac{\partial}{\partial z}\ \widetilde{\phi}_z{}' \end{bmatrix} \begin{bmatrix} \begin{bmatrix} \widetilde{J}_{xj} \\ \widetilde{J}_{yj} \end{bmatrix} \\ \widetilde{J}_{zj} \end{bmatrix} =$$

$$\begin{bmatrix} \widetilde{E}_{ix} \\ \widetilde{E}_{iy} \\ \widetilde{E}_{iz} \end{bmatrix} = -j\omega \begin{bmatrix} \dfrac{\widetilde{V}_{ij}^{I^{TE}}}{-j\omega} & 0 & 0 \\ 0 & \dfrac{\widetilde{V}_{ij}^{I^{TE}}}{-j\omega} & 0 \\ 0 & 0 & \dfrac{\mu_i}{\epsilon_j}\dfrac{\widetilde{I}_{ij}^{V^{TM}}}{j\omega} \end{bmatrix} \begin{bmatrix} \widetilde{J}_{xj} \\ \widetilde{J}_{yj} \\ \widetilde{J}_{zj} \end{bmatrix} - \begin{bmatrix} \begin{bmatrix} -jk_x \\ -jk_y \end{bmatrix} \begin{bmatrix} j\omega\dfrac{\widetilde{V}_{ij}^{I^{TE}} - \widetilde{V}_{ij}^{I^{TM}}}{k_\rho^2} & -j\omega\dfrac{\widetilde{V}_{ij}^{I^{TM}}}{\gamma_j^2} \end{bmatrix} \\ +\dfrac{\partial}{\partial z} \begin{bmatrix} -j\omega\dfrac{\widetilde{V}_{ij}^{I^{TM}}}{\gamma_i^2} & -j\omega\dfrac{\widetilde{V}_{ij}^{I^{TM}}}{\gamma_j^2} \end{bmatrix} \end{bmatrix} \begin{bmatrix} \dfrac{+jk_x\widetilde{J}_{xj} + jk_y\widetilde{J}_{yj}}{-j\omega} \\ \dfrac{\partial\widetilde{J}_{zj}}{\partial z'} \\ \dfrac{}{-j\omega} \end{bmatrix}$$

The "basic" mixed potential form for the electric field in an arbitrary plane-stratified medium with multiple scalar potential kernels but a simple vector potential kernel. (5.22)

$$\begin{bmatrix} \begin{bmatrix} -jk_x \\ -jk_y \end{bmatrix} \begin{bmatrix} [-jk_x \ -jk_y] & \widetilde{\phi}_t & \dfrac{\partial}{\partial z}\,\widetilde{\phi}_z{}' \end{bmatrix} \\ +\dfrac{\partial}{\partial z} \begin{bmatrix} [-jk_x \ -jk_y]\,\widetilde{\phi}_{zt} & \dfrac{\partial}{\partial z}\,\widetilde{\phi}_z{}' \end{bmatrix} \end{bmatrix} \begin{bmatrix} \begin{bmatrix} \widetilde{J}_{xj} \\ \widetilde{J}_{yj} \end{bmatrix} \\ \widetilde{J}_{zj} \end{bmatrix} \tag{5.23}$$

which is interpreted according to the rules of block matrix multiplication. To apply the second and third step, we have to distinguish between transverse and z derivatives. For the inner transverse derivatives in Equation (5.23), we use Equation (5.17) such that their transfer to the current in the second and third step can again be abbreviated as

$$[-jk_x \ -jk_y]\widetilde{\phi} \begin{bmatrix} \widetilde{J}_{xj} \\ \widetilde{J}_{yj} \end{bmatrix} \rightarrow \widetilde{\phi}\left(+jk_x\widetilde{J}_{xj} + jk_y\widetilde{J}_{yj}\right) \tag{5.24}$$

valid for $\widetilde{\phi} = \widetilde{\phi}_t, \widetilde{\phi_{zt}}$. We now perform the second and third step for transferring the z derivatives to the current. The inner z derivatives of $\widetilde{\phi}_z{}'$ of Equation (5.11) are converted into a z' derivative in the second step using Equations (4.66), (5.18), (5.21)

$$\begin{aligned} \frac{\partial}{\partial z}\left(-\frac{\widetilde{I}^{V^{TM}}}{j\omega\epsilon_i\epsilon_j}\right)\ \widetilde{J}_{jz} &= -\frac{1}{j\omega\epsilon_i\epsilon_j}\left(-\gamma_i Y_i^{TM}\widetilde{V}_{ij}^{V^{TM}}\right)\ \widetilde{J}_{jz} \\ &= -\frac{1}{j\omega\epsilon_i\epsilon_j}\left(-\gamma_i\frac{j\omega\epsilon_i}{\gamma_i}\widetilde{V}_{ij}^{V^{TM}}\right)\ \widetilde{J}_{jz} \\ &= +\frac{1}{\epsilon_j}\left(-\frac{Y_j^{TM}}{\gamma_j}\frac{\partial}{\partial z'}\widetilde{V}_{ij}^{I^{TM}}\right)\ \widetilde{J}_{jz} \\ &= +\frac{1}{\epsilon_j}\left(-\frac{j\omega\epsilon_j}{\gamma_j^2}\frac{\partial}{\partial z'}\widetilde{V}_{ij}^{I^{TM}}\right)\ \widetilde{J}_{jz} \end{aligned} \tag{5.25}$$

and we then transfer the z' derivative to the current in the third step with a partial integration to obtain

$$-\frac{1}{j\omega}\frac{\partial}{\partial z}\int\limits_{z'}\frac{\partial}{\partial z'}\left(-\frac{\widetilde{I}^{V^{TM}}}{j\omega\epsilon_i\epsilon_j}\right)\ \widetilde{J}_{jz}\ \mathrm{d}z' = -\frac{\partial}{\partial z}\int\limits_{z'}\left(\frac{-j\omega\widetilde{V}_{ij}^{I^{TM}}}{\gamma_j^2}\right)\frac{\partial\widetilde{J}_{jz}}{\partial z'}\ \mathrm{d}z' \tag{5.26}$$

were we see that the transfer of derivatives also involves a change of the Green's function $\widetilde{\phi}_z{}'$ to a function $\widetilde{\phi}_z$ which is thus the scalar potential of charges associated with vertical current components

$$\widetilde{\phi}_z = -j\omega\frac{\widetilde{V}_{ij}^{I^{TM}}}{\gamma_j^2}. \tag{5.27}$$

If we neglect the special contributions that can arise in the first and third step, we obtain the "basic" mixed potential form given fully in Equation (5.22). This can be written symbolically as

$$\begin{bmatrix} \widetilde{E}_{ix} \\ \widetilde{E}_{iy} \\ \widetilde{E}_{iz} \end{bmatrix} = -j\omega \begin{bmatrix} \widetilde{G}_{xx} & 0 & 0 \\ 0 & \widetilde{G}_{xx} & 0 \\ 0 & 0 & \widetilde{G}_{zz} \end{bmatrix} \begin{bmatrix} \widetilde{J}_{jx} \\ \widetilde{J}_{jy} \\ \widetilde{J}_{jz} \end{bmatrix} - \begin{bmatrix} \begin{bmatrix} -jk_x \\ -jk_y \end{bmatrix} \begin{bmatrix} \widetilde{\phi}_t & \widetilde{\phi}_z \end{bmatrix} \\ +\dfrac{\partial}{\partial z} \begin{bmatrix} \widetilde{\phi}_{zt} & \widetilde{\phi}_z \end{bmatrix} \end{bmatrix} \begin{bmatrix} \widetilde{Q}_{jt} \\ \widetilde{Q}_{jz} \end{bmatrix} \tag{5.28}$$

where $\widetilde{Q}_{jz}$ and $\widetilde{Q}_{jt}$ are the charges associated with the vertical and horizontal components of the current

$$\widetilde{Q}_{jz} = \frac{\partial \widetilde{J}_{jz}}{\partial z'} / (-j\omega) \tag{5.29}$$

$$\widetilde{Q}_{jt} = \frac{+jk_x \widetilde{J}_{jx} + jk_y \widetilde{J}_{jy}}{-j\omega}. \tag{5.30}$$

The field remains determined by 5 different functions, 2 vector potential components $\widetilde{G}_{xx}$, $\widetilde{G}_{zz}$ and 3 scalar potential functions $\widetilde{\phi}_t$, $\widetilde{\phi}_z$ and $\widetilde{\phi}_{zt}$. The occurrence of several distinct scalar potential functions is not a problem if currents are horizontal or vertical and even for an inclined current it can in principle be used as such [13], [195], [196] although the physical interpretation is problematic. However, one may prefer to work with a single scalar potential if one estimates that this compensates the other complications that such a formulation inevitably entrains. We will now derive such single scalar potential formulations below.

5.3.2 Classical Mixed Potential Formulations

Single scalar potential formulations can be derived from the "basic" mixed potential form by assuming that one of the 3 scalar potential functions is valid for the total charge and absorbing the correction terms into the vector potential. We follow the same classification as in [191].

Formulation A

A possible choice for the single scalar potential is $\widetilde{\phi}_{zt}$. we replace $\widetilde{\phi}_z$ in Equation (5.28) with $\widetilde{\phi}_{zt}$ and absorb the correction terms into the vector potential kernel. The extra vector potential components can thus be computed from

$$-j\omega \begin{bmatrix} \widetilde{G}^A_{xz} \\ \widetilde{G}^A_{yz} \\ \widetilde{G}^A_{zz} \end{bmatrix} \widetilde{J}_{jz} = - \begin{bmatrix} -jk_x \\ -jk_y \\ \dfrac{\partial}{\partial z} \end{bmatrix} \left(\widetilde{\phi}_z - \widetilde{\phi}_{zt} \right) \begin{pmatrix} \dfrac{\partial \widetilde{J}_{jz}}{\partial z'} \\ \dfrac{}{-j\omega} \end{pmatrix}. \tag{5.31}$$

Similarly, we replace $\widetilde{\phi}_t$ in Equation (5.28) with $\widetilde{\phi}_{zt}$ and compute the other modifications of the vector potential kernel from

$$-j\omega \begin{bmatrix} \widetilde{G}^A_{xx} & \widetilde{G}^A_{xy} \\ \widetilde{G}^A_{yx} & \widetilde{G}^A_{yy} \end{bmatrix} \begin{bmatrix} \widetilde{J}_{jx} \\ \widetilde{J}_{jy} \end{bmatrix} = - \begin{bmatrix} -jk_x \\ -jk_y \\ \dfrac{\partial}{\partial z} \end{bmatrix} \left(\widetilde{\phi}_t - \widetilde{\phi}_{zt} \right) \left(\frac{+jk_x \widetilde{J}_{jx} + jk_y \widetilde{J}_{jy}}{-j\omega} \right). \quad (5.32)$$

In the above expressions, the partial derivatives of the current in the right hand sides have to be transferred back to the Green's functions in order to obtain the vector potential components. An example of such a computation will be given for Formulation C below. This gives the single scalar potential formulation written fully in Equation (5.34), and symbolically as

$$\begin{bmatrix} \widetilde{E}_{ix} \\ \widetilde{E}_{iy} \\ \widetilde{E}_{iz} \end{bmatrix} = -j\omega \begin{bmatrix} \widetilde{G}_{xx} + \widetilde{G}^A_{xx} & \widetilde{G}^A_{xy} & \widetilde{G}^A_{xz} \\ \widetilde{G}^A_{yx} & \widetilde{G}_{xx} + \widetilde{G}^A_{yy} & \widetilde{G}^A_{yz} \\ 0 & 0 & \widetilde{G}^A_{zz} \end{bmatrix} \begin{bmatrix} \widetilde{J}_{jx} \\ \widetilde{J}_{jy} \\ \widetilde{J}_{jz} \end{bmatrix} - \begin{bmatrix} -jk_x \\ -jk_y \\ \dfrac{\partial}{\partial z} \end{bmatrix} \widetilde{\phi}_{zt} \widetilde{Q}_j \quad (5.33)$$

where the total charge $\widetilde{Q}_j = \widetilde{Q}_{jz} + \widetilde{Q}_{jt}$ now appears. The field remains determined by 5 functions, namely $\widetilde{\phi}_{zt}$, $\widetilde{G}_{xx}$, $\widetilde{G}_{zz}$, $\widetilde{G}^A_{xx}$ and $\widetilde{G}^A_{xy}$ while $\widetilde{G}^A_{yy}$, $\widetilde{G}^A_{yx}$ are easily determined from the previous two (see Section 5.4). This mixed potential form has been used for example in [197], [198].

Formulation B

Another choice for the single scalar potential is $\widetilde{\phi}_z$. In Equation (5.11), we replace $\widetilde{\phi}_{zt}$ with $\widetilde{\phi}_z$ and absorb the correction terms into the vector potential kernel

$$-j\omega \begin{bmatrix} \widetilde{G}^B_{zx} & \widetilde{G}^B_{zy} \end{bmatrix} \begin{bmatrix} \widetilde{J}_{jx} \\ \widetilde{J}_{jy} \end{bmatrix} = -\frac{\partial}{\partial z} \left(\widetilde{\phi}_{zt} - \widetilde{\phi}_z \right) \left(\frac{+jk_x \widetilde{J}_{jx} + jk_y \widetilde{J}_{jy}}{-j\omega} \right). \quad (5.36)$$

Similarly, we replace $\widetilde{\phi}_t$ in Equation (5.28) with $\widetilde{\phi}_z$ and absorb these corrections in the vector potential kernel

$$-j\omega \begin{bmatrix} \widetilde{G}^B_{xx} & \widetilde{G}^B_{xy} \\ \widetilde{G}^B_{yx} & \widetilde{G}^B_{yy} \end{bmatrix} \begin{bmatrix} \widetilde{J}_{jx} \\ \widetilde{J}_{jy} \end{bmatrix} = - \begin{bmatrix} -jk_x \\ -jk_y \end{bmatrix} \left(\widetilde{\phi}_t - \widetilde{\phi}_z \right) \left(\frac{+jk_x \widetilde{J}_{jx} + jk_y \widetilde{J}_{jy}}{-j\omega} \right). \quad (5.37)$$

The result is the single scalar potential formulation written fully in Equation (5.35),

$$\begin{bmatrix} \widetilde{E}_{ix} \\ \widetilde{E}_{iy} \\ \widetilde{E}_{iz} \end{bmatrix} = -j\omega \begin{bmatrix} \frac{\widetilde{V}_{ij}^{I^{TE}}}{-j\omega} - \frac{jk_x jk_x}{j\omega k_\rho^2}\left(\widetilde{V}_{ij}^{I^{TE}} + \frac{k_i^2}{\gamma_i^2}\widetilde{V}_{ij}^{I^{TM}}\right) & -\frac{jk_x jk_y}{j\omega k_\rho^2}\left(\widetilde{V}_{ij}^{I^{TE}} + \frac{k_i^2}{\gamma_i^2}\widetilde{V}_{ij}^{I^{TM}}\right) & -jk_x\frac{\mu_i\epsilon_i - \mu_j\epsilon_j}{\epsilon_j\gamma_i^2}\widetilde{V}_{ij}^{V^{TM}} \\ -\frac{jk_y jk_x}{j\omega k_\rho^2}\left(\widetilde{V}_{ij}^{I^{TE}} + \frac{k_i^2}{\gamma_i^2}\widetilde{V}_{ij}^{I^{TM}}\right) & \frac{\widetilde{V}_{ij}^{I^{TE}}}{-j\omega} - \frac{jk_y jk_y}{j\omega k_\rho^2}\left(\widetilde{V}_{ij}^{I^{TE}} + \frac{k_i^2}{\gamma_i^2}\widetilde{V}_{ij}^{I^{TM}}\right) & -jk_y\frac{\mu_i\epsilon_i - \mu_j\epsilon_j}{\epsilon_j\gamma_i^2}\widetilde{V}_{ij}^{V^{TM}} \\ 0 & 0 & \frac{\mu_i}{\epsilon_j}\frac{\widetilde{I}_{ij}^{V^{TM}}}{j\omega} + \frac{\partial}{\partial z}\frac{\mu_i\epsilon_i - \mu_j\epsilon_j}{\epsilon_j\gamma_i^2}\widetilde{V}_{ij}^{V^{TM}} \end{bmatrix} \begin{bmatrix} \widetilde{J}_{jx} \\ \widetilde{J}_{jy} \\ \widetilde{J}_{jz} \end{bmatrix}$$

$$- \begin{bmatrix} -jk_x \\ -jk_y \\ +\frac{\partial}{\partial z} \end{bmatrix} \left(-j\omega\frac{\widetilde{V}_{ij}^{I^{TM}}}{\gamma_i^2}\right) \left(\frac{+jk_x\widetilde{J}_{jx} + jk_y\widetilde{J}_{jy} + \frac{\partial\widetilde{J}_{jz}}{\partial z}}{-j\omega}\right)$$

Formulation A for the mixed potential form of the electric field in the spectral domain for an arbitrary plane-stratified medium with a single scalar potential kernel $\widetilde{\phi}_{zt}$ and a dyadic vector potential kernel. (5.34)

$$\begin{bmatrix} \widetilde{E}_{ix} \\ \widetilde{E}_{iy} \\ \widetilde{E}_{iz} \end{bmatrix} = -j\omega \begin{bmatrix} \dfrac{\widetilde{V}_{ij}^{I^{TE}}}{-j\omega} - \dfrac{jk_x jk_x}{j\omega k_\rho^2}\left(\widetilde{V}_{ij}^{I^{TE}} + \dfrac{k_j^2}{\gamma_j^2}\widetilde{V}_{ij}^{I^{TM}}\right) & -\dfrac{jk_x jk_y}{j\omega k_\rho^2}\left(\widetilde{V}_{ij}^{I^{TE}} + \dfrac{k_j^2}{\gamma_j^2}\widetilde{V}_{ij}^{I^{TM}}\right) & 0 \\ -\dfrac{jk_y jk_x}{j\omega k_\rho^2}\left(\widetilde{V}_{ij}^{I^{TE}} + \dfrac{k_j^2}{\gamma_j^2}\widetilde{V}_{ij}^{I^{TM}}\right) & \dfrac{\widetilde{V}_{ij}^{I^{TE}}}{-j\omega} - \dfrac{jk_y jk_y}{j\omega k_\rho^2}\left(\widetilde{V}_{ij}^{I^{TE}} + \dfrac{k_j^2}{\gamma_j^2}\widetilde{V}_{ij}^{I^{TM}}\right) & 0 \\ -jk_x\dfrac{\mu_i\epsilon_i - \mu_j\epsilon_j}{\epsilon_i\gamma_j^2}\widetilde{I}_{ij}^{I^{TM}} & -jk_y\dfrac{\mu_i\epsilon_i - \mu_j\epsilon_j}{\epsilon_i\gamma_j^2}\widetilde{I}_{ij}^{I^{TM}} & \dfrac{\mu_i}{\epsilon_j}\dfrac{\widetilde{I}_{ij}^{V^{TM}}}{j\omega} \end{bmatrix} \begin{bmatrix} \widetilde{J}_{jx} \\ \widetilde{J}_{jy} \\ \widetilde{J}_{jz} \end{bmatrix}$$

$$- \begin{bmatrix} -jk_x \\ -jk_y \\ +\dfrac{\partial}{\partial z} \end{bmatrix} \left(-j\omega\frac{\widetilde{V}_{ij}^{I^{TM}}}{\gamma_j^2}\right) \left(\frac{+jk_x\widetilde{J}_{jx} + jk_y\widetilde{J}_{jy} + \dfrac{\partial\widetilde{J}_{jz}}{\partial z}}{-j\omega}\right)$$

Formulation B for the mixed potential form of the electric field in the spectral domain for an arbitrary plane-stratified medium with a single scalar potential kernel $\widetilde{\phi}_z$ and a dyadic vector potential kernel. (5.35)

and written symbolically as

$$\begin{bmatrix} \widetilde{E}_{ix} \\ \widetilde{E}_{iy} \\ \widetilde{E}_{iz} \end{bmatrix} = -j\omega \begin{bmatrix} \widetilde{G}_{xx} + \widetilde{G}^B_{xx} & \widetilde{G}^B_{yz} & 0 \\ \widetilde{G}^B_{yx} & \widetilde{G}_{xx} + \widetilde{G}^B_{yy} & 0 \\ \widetilde{G}^B_{zx} & \widetilde{G}^B_{zy} & \widetilde{G}^B_{zz} \end{bmatrix} \begin{bmatrix} \widetilde{J}_{jx} \\ \widetilde{J}_{jy} \\ \widetilde{J}_{jz} \end{bmatrix} - \begin{bmatrix} -jk_x \\ -jk_y \\ \dfrac{\partial}{\partial z} \end{bmatrix} \widetilde{\phi}_z \widetilde{Q}_j. \quad (5.38)$$

For his case, the 5 functions determining the electric field are $\widetilde{\phi}_z$, $\widetilde{G}_{xx}$, $\widetilde{G}_{zz}$, $\widetilde{G}^B_{xx}$, $\widetilde{G}^B_{zx}$ while the other components $\widetilde{G}^B_{yy}$, $\widetilde{G}^B_{zy}$ can be easily determined from the previous two with the relations of Section 5.4. This formulations has been used in [199].

Formulation C

If we choose the scalar potential $\widetilde{\phi}_t$ to be valid for the total charge, we obtain a formulation which has certain advantages over the other choices [191]. We replace $\widetilde{\phi}_z$ in Equation (5.28) with $\widetilde{\phi}_t$ and compute the modification of the vector potential kernel from

$$-j\omega \begin{bmatrix} \widetilde{G}^C_{xz} \\ \widetilde{G}^C_{yz} \\ \widetilde{G}^C_{zz} \end{bmatrix} \widetilde{J}_{jz} = - \begin{bmatrix} -jk_x \\ -jk_y \\ \dfrac{\partial}{\partial z} \end{bmatrix} \left(\widetilde{\phi}_z - \widetilde{\phi}_t \right) \begin{pmatrix} \dfrac{\partial \widetilde{J}_{jz}}{\partial z'} \\ -j\omega \end{pmatrix}. \quad (5.40)$$

The explicit expressions for $\widetilde{G}^C_{zx}$, $\widetilde{G}_{zy}$, $\widetilde{G}^C_{zz}$ are obtained by transferring the derivatives from the current back to the Green's functions as demonstrated below. The inverse operation of the third step again involves the partial integration

$$\int_{z'} \left(-\frac{\widetilde{V}^{I^{TM}}_{ij}}{\gamma_j^2} - \frac{\widetilde{V}^{I^{TE}}_{ij} - \widetilde{V}^{I^{TM}}_{ij}}{k_\rho^2} \right) \frac{\partial \widetilde{J}_{jz}}{\partial z'} \, \mathrm{d}z' = \int_{z'} \frac{\partial}{\partial z'} \left(\frac{\widetilde{V}^{I^{TM}}_{ij}}{\gamma_j^2} + \frac{\widetilde{V}^{I^{TE}} - \widetilde{V}^{I^{TM}}}{k_\rho^2} \right) \widetilde{J}_{jz} \quad (5.41)$$

and we then use Equations (4.66), (5.21) to simplify the factor appearing in front of the current as

$$\begin{aligned} \left(-\frac{\widetilde{V}^{V^{TM}}_{ij}}{j\omega\epsilon_j} - \frac{j\omega\mu_j}{k_\rho^2} \widetilde{V}^{V^{TE}}_{ij} + \frac{\gamma_j^2}{k_\rho^2 j\omega\epsilon_j} \widetilde{V}^{V^{TM}}_{ij} \right) \widetilde{J}_{jz} = \\ \left(-\frac{j\omega\mu_j}{k_\rho^2} \widetilde{V}^{V^{TE}}_{ij} + \frac{1}{j\omega\epsilon_j} \left(\frac{\gamma_j^2 - k_\rho^2}{k_\rho^2} \right) \widetilde{V}^{V^{TM}}_{ij} \right) \widetilde{J}_{jz} = \\ -j\omega\mu_j \frac{\widetilde{V}^{V^{TE}}_{ij} - \widetilde{V}^{V^{TM}}_{ij}}{k_\rho^2} \widetilde{J}_{jz} \end{aligned} \quad (5.42)$$

$$\begin{bmatrix} \widetilde{E}_{ix} \\ \widetilde{E}_{iy} \\ \widetilde{E}_{iz} \end{bmatrix} = -j\omega \begin{bmatrix} \dfrac{\widetilde{V}_{ij}^{I^{TE}}}{-j\omega} & 0 & -jk_x\mu_j \dfrac{\widetilde{V}_{ij}^{V^{TE}} - \widetilde{V}_{ij}^{V^{TM}}}{k_\rho^2} \\ 0 & \dfrac{\widetilde{V}_{ij}^{I^{TE}}}{-j\omega} & -jk_y\mu_j \dfrac{\widetilde{V}_{ij}^{V^{TE}} - \widetilde{V}_{ij}^{V^{TM}}}{k_\rho^2} \\ -jk_y\mu_i \dfrac{\widetilde{I}_{ij}^{I^{TM}} - \widetilde{I}_{ij}^{I^{TE}}}{k_\rho^2} & -jk_y\mu_i \dfrac{\widetilde{I}_{ij}^{I^{TM}} - \widetilde{I}_{ij}^{I^{TE}}}{k_\rho^2} & \dfrac{\mu_i}{\epsilon_j}\dfrac{\widetilde{I}_{ij}^{V^{TM}}}{j\omega} + \dfrac{\partial}{\partial z}\mu_j \dfrac{\widetilde{V}_{ij}^{V^{TE}} - \widetilde{V}_{ij}^{V^{TM}}}{k_\rho^2} \end{bmatrix} \begin{bmatrix} \widetilde{J}_{jx} \\ \widetilde{J}_{jy} \\ \widetilde{J}_{jz} \end{bmatrix}$$

$$- \begin{bmatrix} -jk_x \\ -jk_y \\ +\dfrac{\partial}{\partial z} \end{bmatrix} \left(j\omega \frac{\widetilde{V}_{ij}^{I^{TE}} - \widetilde{V}_{ij}^{I^{TM}}}{k_\rho^2} \right) \left(\frac{+jk_x\widetilde{J}_{jx} + jk_y\widetilde{J}_{jy} + \dfrac{\partial \widetilde{J}_{jz}}{\partial z}}{-j\omega} \right)$$

Formulation C for the mixed potential form of the electric field in the spectral domain for an arbitrary plane-stratified medium with a single scalar potential kernel $\widetilde{\phi}_t$ and a dyadic vector potential kernel. (5.39)

where we used $k_j^2 = \gamma_j^2 - k_\rho^2$ in the last step. From Equation (5.40) we obtain the last column in the vector potential kernel of Equation (5.39). Similarly, we replace $\widetilde{\phi}_{zt}$ in Equation (5.28) with $\widetilde{\phi}_t$ and compute the remaining vector potential components from

$$-j\omega \left[\widetilde{G}_{zx}^C \quad \widetilde{G}_{zy}^C \right] \begin{bmatrix} \widetilde{J}_{jx} \\ \widetilde{J}_{jy} \end{bmatrix} = -\frac{\partial}{\partial z} \left(\widetilde{\phi}_{zt} - \widetilde{\phi}_t \right) \left(\frac{+jk_x \widetilde{J}_{jx} + jk_y \widetilde{J}_{jy}}{-j\omega} \right) \tag{5.43}$$

where the transverse derivatives operating on the current are transferred back to the Green's function using the shorthand Equation (5.24) and the z derivatives worked out with Equations (4.66) and (5.19). We obtain the single scalar potential formulation written fully in Equation (5.39), and symbolically as

$$\begin{bmatrix} \widetilde{E}_{ix} \\ \widetilde{E}_{iy} \\ \widetilde{E}_{iz} \end{bmatrix} = -j\omega \begin{bmatrix} \widetilde{G}_{xx} & 0 & \widetilde{G}_{xz}^C \\ 0 & \widetilde{G}_{xx} & \widetilde{G}_{yz}^C \\ \widetilde{G}_{zx}^C & \widetilde{G}_{zy}^C & \widetilde{G}_{zz} + \widetilde{G}_{zz}^C \end{bmatrix} \begin{bmatrix} \widetilde{J}_{jx} \\ \widetilde{J}_{jy} \\ \widetilde{J}_{jz} \end{bmatrix} - \begin{bmatrix} -jk_x \\ -jk_y \\ \dfrac{\partial}{\partial z} \end{bmatrix} \widetilde{\phi}_t \widetilde{Q}_j. \tag{5.44}$$

The field remains determined by 5 functions, namely $\widetilde{\phi}_t$, $\widetilde{G}_{xx}$, $\widetilde{G}_{zz} + \widetilde{G}_{zz}^C$, $\widetilde{G}_{xz}^C$, $\widetilde{G}_{zx}^C$ while $\widetilde{G}_{yz}^C$, $\widetilde{G}_{zy}^C$ are easily determined from the previous two as discussed in Section 5.4. This formulation has found extensive use as in [200], [201], [202] and is implemented in the commercial software Package EMSS FEKO.

5.4 The Inverse Fourier Transform

The above field formulations now have to be transformed back to the spatial domain, where their physical significance can be better examined. From the definition of the inverse Fourier transform and the current in the spectral domain Equations (4.3) and (4.4) of Chapter 4, we see that the spatial domain quantities typically require evaluation of expressions of the form

$$\frac{1}{(2\pi)^2} \iint_{-\infty}^{+\infty} \widetilde{F}(k_x, k_y, z, z') e^{-jk_x(x-x')} e^{-jk_y(y-y')} \, \mathrm{d}k_x \mathrm{d}k_y. \tag{5.45}$$

The resulting space domain quantity $F(x - x', y - y', z, z')$ shows translational invariance in the transverse coordinates which is a consequence of the assumption of a stratified and transversely unbounded medium. The z, z' dependence can be disregarded at this point since it is not affected by the Fourier transform. By inspecting the dyadic expression of Equation (4.128) of Chapter 4 and the MPIE formulations Equations (5.22), (5.34), (5.35), (5.39) we see that the function $\widetilde{F}(k_x, k_y)$ typically is composed of transmission line quantities $\widetilde{F}_{ij}^{S^T}(k_\rho, z, z')$ which are even functions of k_ρ,

possibly divided by k_ρ^2, γ_k^2 and in some cases multiplied with the spectral wavenumbers jk_x, jk_y. To obtain the spatial domain equivalents of such expressions, we must avail ourselves of the labours of professed mathematicians.

Sommerfeld Integral Representation

If $\widetilde{F}(k_x, k_y)$ does not depend on k_x, k_y separately, but is an even function of only k_ρ, then the corresponding spatial domain expression depends on the radial distance ρ only. This can be seen by introducing polar coordinates in the spatial and spectral domain as

$$x - x' = \rho\cos\phi \tag{5.46}$$
$$y - y' = \rho\sin\phi \tag{5.47}$$
$$\rho = \sqrt{(x-x')^2 + (y-y')^2} \tag{5.48}$$
$$\phi = \arctan\left(\frac{y-y'}{x-x'}\right) \tag{5.49}$$
$$k_x = k_\rho\cos\xi \tag{5.50}$$
$$k_y = k_\rho\sin\xi \tag{5.51}$$
$$k_\rho = \sqrt{k_x^2 + k_y^2} \tag{5.52}$$
$$\xi = \arctan\left(\frac{k_y}{k_x}\right) \tag{5.53}$$

such that Equation (5.45) reduces to

$$F(\rho,\phi) \;=\; \frac{1}{2\pi}\int_0^{+\infty}\widetilde{F}(k_\rho)\;\;\frac{1}{2\pi}\int_0^{2\pi} e^{-j\rho k_\rho\cos(\phi-\xi)}\;\mathrm{d}\xi\;\;k_\rho\mathrm{d}k_\rho. \tag{5.54}$$

With the help of ([203], p.902, formula 8.511.4)

$$e^{-jz\cos\theta} = \sum_{n=-\infty}^{+\infty}(-j)^n J_n(z)e^{-jn\theta} \tag{5.55}$$

we obtain the integral representation of the Bessel functions of the 1^{th} kind and integer order n as

$$J_n(z) = \frac{(-j)^n}{2\pi}\int_0^{2\pi}\cos n\theta\; e^{-jz\cos\theta}\;\mathrm{d}\theta \tag{5.56}$$

such that the angular dependence disappears from Equation (5.54) to give the one-dimensional Fourier-Bessel integral

$$F(\rho) = \frac{1}{2\pi}\int_0^{+\infty}\widetilde{F}(k_\rho)J_0(\rho k_\rho)\;k_\rho\mathrm{d}k_\rho = S_0\left\{\widetilde{F}(k_\rho)\right\}. \tag{5.57}$$

where S_0 is the lowest order representative of a more general class of Sommerfeld

integrals [36] defined as

$$S_n\left\{\widetilde{F}(k_\rho)\right\} = \frac{1}{2\pi}\int_0^{2\pi} \widetilde{F}(k_\rho) J_n(\rho k_\rho) k_\rho^n \; k_\rho \mathrm{d}k_\rho \tag{5.58}$$

These resulting one-dimensional integrals are the only ones that have to be evaluated numerically as discussed in Chapter 7, instead of the double numerical integrals originally present in Equation (5.45).

If the wavenumbers k_x, k_y appear as separate factors $\widetilde{F}(k_x,k_y) = jk_x\widetilde{F}(k_\rho)$, $jk_y\widetilde{F}(k_\rho)$, $jk_xjk_x\widetilde{F}(k_\rho)$, $jk_yjk_y\widetilde{F}(k_\rho)$, $jk_xjk_y\widetilde{F}(k_\rho)$, the dependence on the azimuth angle ϕ can be separated analytically from the dependence on ρ, and the inverse Fourier transform can still be computed with the one-dimensional Sommerfeld integrals S_n defined above. From Equation (4.9), we obtain

$$\mathfrak{F}^{-1}\left\{ \quad jk_x\widetilde{F}(k_\rho)\right\} = \frac{\partial}{\partial x}\mathfrak{F}^{-1}\left\{\widetilde{F}(k_\rho)\right\} \tag{5.59}$$

$$= \left[\qquad\qquad -\cos\phi\frac{\partial}{\partial\rho}\right] \; \frac{1}{2\pi}\int_0^{+\infty} \widetilde{F}(k_\rho) J_0(\rho k_\rho) \; k_\rho \mathrm{d}k_\rho \tag{5.60}$$

$$\mathfrak{F}^{-1}\left\{jk_xjk_x\widetilde{F}(k_\rho)\right\} = \frac{\partial}{\partial x}\frac{\partial}{\partial x}\mathfrak{F}^{-1}\left\{\widetilde{F}(k_\rho)\right\} \tag{5.61}$$

$$= \left[\frac{\sin^2\phi}{\rho}\frac{\partial}{\partial\rho} + \cos^2\phi\frac{\partial^2}{\partial\rho^2}\right] \; \frac{1}{2\pi}\int_0^{+\infty} \widetilde{F}(k_\rho) J_0(\rho k_\rho) \; k_\rho \mathrm{d}k_\rho \tag{5.62}$$

where the expressions for the spatial derivatives in cylindrical coordinates are valid if they operate on a function $F(\rho)$. These first and second order spatial derivatives of the Bessel functions can be computed from ([203], p. 916, formula 8.473.4, 8.472.2, 8.473.1)

$$\frac{\partial J_0(\rho k_\rho)}{\partial\rho} = -k_\rho J_1(\rho k_\rho) \tag{5.63}$$

$$\frac{\partial J_1(\rho k_\rho)}{\partial\rho} = -k_\rho J_2(\rho k_\rho) + \frac{1}{\rho}J_1(\rho k_\rho) \tag{5.64}$$

$$J_2(\rho k_\rho) = \frac{2}{\rho k_\rho}J_1(\rho k_\rho) - J_0(\rho k_\rho) \tag{5.65}$$

such that higher order Sommerfeld integrals make their appearance. Using standard trigonometric identities, all expressions can be simplified to obtain the results summarized below

$$\mathfrak{F}^{-1}\{\widetilde{F}(k_\rho)\} = S_o\{\widetilde{F}(k_\rho)\} \tag{5.66}$$

$$\mathfrak{F}^{-1}\{-jk_x\widetilde{F}(k_\rho)\} = -\cos\phi \; S_1\{\widetilde{F}(k_\rho)\} \tag{5.67}$$

$$\mathfrak{F}^{-1}\{-jk_y\widetilde{F}(k_\rho)\} = -\sin\phi\ S_1\{\widetilde{F}(k_\rho)\} \tag{5.68}$$

$$\mathfrak{F}^{-1}\{jk_xjk_x\widetilde{F}(k_\rho)\} = +\frac{1}{2}[\cos 2\phi\ S_2\{\widetilde{F}(k_\rho)\} - S_o\{k_\rho^2\widetilde{F}(k_\rho)\}] \tag{5.69}$$

$$\mathfrak{F}^{-1}\{jk_yjk_y\widetilde{F}(k_\rho)\} = -\frac{1}{2}[\cos 2\phi\ S_2\{\widetilde{F}(k_\rho)\} + S_o\{k_\rho^2\widetilde{F}(k_\rho)\}] \tag{5.70}$$

$$\mathfrak{F}^{-1}\{jk_xjk_y\widetilde{F}(k_\rho)\} = +\frac{1}{2}\sin 2\phi\ S_2\{\widetilde{F}(k_\rho)\} \tag{5.71}$$

In principle, we are now in a position to write down the dyadic and mixed potential field formulations in the spatial domain.

The Expressions in the Spatial Domain

By straightforward application of the above formulas we obtain the full electric dyadic Green's function in the space domain as given in Equation (5.72). The dyadic can be used as such in the space domain as was done in [204], [205], [206], [207] and this is also done in the commercial software package Zeland Software IE3D. The spectral domain dyadic Green's function was rearranged into the spectral domain mixed potential formulations A,B,C of Equations (5.34), (5.35), (5.39). The space domain equivalent of the popular formulation C which is used in the commercial software package EMSS FEKO is given fully in Equation (5.73), while the space domain equivalents of formulations A,B can be found easily.

5.5 Physical Interpretation

We investigate the physical significance of the above expressions by comparison with the simpler expressions for a homogeneous medium in the spatial domain. However, for a stratified medium, the field cannot be written in closed form in the spatial domain and the space domain behaviour has to be deferred from the spectral domain closed form expressions. From the spectral asymptotic behaviour, we extract the corresponding spatial singular and low frequency quasi-static behaviour. This will be shown to correspond also to the assumption of a homogeneous medium in Section 5.5.2. We first trace the appearance of the azimuth angle ϕ in Section 5.5.1.

5.5.1 The ϕ Azimuth Angular Dependence

The azimuth angle ϕ as it appears in Equations (5.72), (5.73) makes the expressions depend on the relative position of source and observation point $x-x', y-y'$ and not only on the lateral distance ρ. It appears by application of the Sommerfeld integral relations Equations (5.67), (5.68), (5.69), (5.70), (5.71). From the derivation of these expressions in Section 5.4, it is clear that this angle is actually the result of a spatial derivative in the transverse X, Y plane performed in cylindrical coordinates. The

$$\begin{bmatrix} S_0\left\{\frac{\widetilde{V}_{ij}^{I^{TE}}+\widetilde{V}_{ij}^{I^{TM}}}{2}\right\}+\cos 2\phi\ S_2\left\{\frac{\widetilde{V}_{ij}^{I^{TE}}-\widetilde{V}_{ij}^{I^{TM}}}{2k_\rho^2}\right\} & +\sin 2\phi\ S_2\left\{\frac{\widetilde{V}_{ij}^{I^{TE}}-\widetilde{V}_{ij}^{I^{TM}}}{2k_\rho^2}\right\} & +\cos\phi\ S_1\left\{\frac{\widetilde{V}_{ij}^{V^{TM}}}{j\omega\epsilon_j}\right\} \\ +\sin 2\phi\ S_2\left\{\frac{\widetilde{V}_{ij}^{I^{TE}}-\widetilde{V}_{ij}^{I^{TM}}}{2k_\rho^2}\right\} & S_0\left\{\frac{\widetilde{V}_{ij}^{I^{TE}}+\widetilde{V}_{ij}^{I^{TM}}}{2}\right\}+\cos 2\phi\ S_2\left\{\frac{\widetilde{V}_{ij}^{I^{TE}}-\widetilde{V}_{ij}^{I^{TM}}}{2k_\rho^2}\right\} & +\sin\phi\ S_1\left\{\frac{\widetilde{V}_{ij}^{V^{TM}}}{j\omega\epsilon_j}\right\} \\ -\cos\phi\ S_1\left\{\frac{\widetilde{I}_{ij}^{I^{TM}}}{j\omega\epsilon_i}\right\} & -\sin\phi\ S_1\left\{\frac{\widetilde{I}_{ij}^{I^{TM}}}{j\omega\epsilon_i}\right\} & S_0\left\{k_\rho^2\frac{\widetilde{I}_{ij}^{V^{TM}}}{j\omega\epsilon_i j\omega\epsilon_j}\right\} \end{bmatrix}$$

The spatial domain full electric dyadic Green's functions $\overline{G}^e$ in an arbitrary plane-stratified medium. (5.72)

$$\vec{E}_i = -j\omega \begin{bmatrix} S_0\left\{\frac{\widetilde{V}_{ij}^{I^{TE}}}{-j\omega}\right\} & 0 & -\cos\phi\ S_1\left\{\mu_j \frac{\widetilde{V}_{ij}^{V^{TE}} - \widetilde{V}_{ij}^{V^{TM}}}{k_\rho^2}\right\} \\ 0 & S_0\left\{\frac{\widetilde{V}_{ij}^{I^{TE}}}{-j\omega}\right\} & -\sin\phi\ S_1\left\{\mu_j \frac{\widetilde{V}_{ij}^{V^{TE}} - \widetilde{V}_{ij}^{V^{TM}}}{k_\rho^2}\right\} \\ -\cos\phi\ S_1\left\{\frac{\widetilde{I}_{ij}^{I^{TM}} - \widetilde{I}_{ij}^{I^{TE}}}{k_\rho^2}\right\} & -\sin\phi\ S_1\left\{\frac{\widetilde{I}_{ij}^{I^{TM}} - \widetilde{I}_{ij}^{I^{TE}}}{k_\rho^2}\right\} & \frac{\mu_i}{j\omega\epsilon_j} S_0\left\{\widetilde{I}_{ij}^{V^{TM}} + \frac{k_j^2}{k_\rho^2}\left(\widetilde{I}_{ij}^{V^{TE}} + \frac{\gamma_i^2}{k_i^2}\widetilde{I}_{ij}^{V^{TM}}\right)\right\} \end{bmatrix} .\vec{J}_j$$

$$-\nabla\ S_0\left\{j\omega \frac{\widetilde{V}_{ij}^{I^{TE}} - \widetilde{V}_{ij}^{I^{TM}}}{k_\rho^2}\right\}\left(\frac{\nabla'.\vec{J}_j}{-j\omega}\right)$$

Formulation C for the mixed potential form of the electric field in the spatial domain for an arbitrary plane-stratified medium with a single scalar potential kernel $\widetilde{\phi}_t$ and a dyadic vector potential kernel. (5.73)

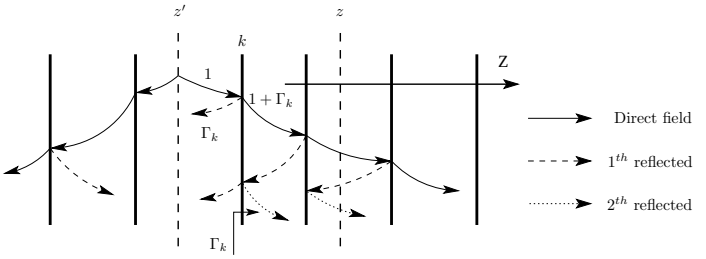

Figure 5.1: The value of the spectral Green's function for large spectral wavenumbers k_ρ is most easily obtained via the multiple reflection interpretation.

ϕ dependence is in this way extracted in closed form from the numerical ρ dependence. Nevertheless, the evaluation of reaction integrals now has to be done in two ρ, ϕ variables, which requires extra computation time for numerical evaluation and more complicated formulas if closed form evaluation is possible [207]. The space domain mixed potential formalism avoids such complications by exploiting the physical significance of the spatial derivatives, such that only the distance between source and observation point appears in the Green's functions.

5.5.2 Spatial Singular Behaviour and Frequency Dependence

This section discusses the spectral asymptotic, the spatial singular, the low frequency or (quasi)-static of the Green's functions, and this is also equivalent with assuming a homogeneous medium.

The spectral domain transmission line expressions for the Green's of Section 4.8 of Chapter (4) can also be obtained by making a multiple reflection construction as depicted in Figure 5.1. At the source position z', waves are generated as if the source layer was a homogeneous medium, and then travel through the layer structure undergoing multiple reflections and transmissions at the layer interfaces, using the reflection and transmission coefficient as if there was a single interface, to arrive at the observation position z in layer i. Working out the summation of all these contributions would reproduce the exact expressions of Section 4.8.

The value of the spectral Green's function $\widetilde{F}(k_\rho)$ for $k_\rho \to \infty$ is called the asymptotic spectral behaviour. It determines the value of the spatial Green's function $F(\rho)$ for $\rho \to 0$, the spatial singular behaviour at the origin of the spatial domain. This can be seen from the definition Equation (5.58), where the period of the Bessel function in the spectral domain becomes infinitely large, such that the dominant contribution in the integral comes from the slowly decaying value of $\widetilde{F}(k_\rho)$ at infinity. The asymptotic spectral behaviour of $\widetilde{F}(k_\rho)$ can be obtained from the transmission line expressions of Section 4.8 of Chapter (4) by expanding all expressions in series for large k_ρ. If only

the dominant terms are required, the central simplification consists of

$$\lim_{k_\rho\to\infty}\gamma_k=\lim_{k_\rho\to\infty}\sqrt{k_\rho^2-\omega^2\mu_k\epsilon_k}\approx k_\rho. \tag{5.74}$$

This assumption is equivalent to assuming $\omega\to 0$, which is the static case. The waves on the equivalent transmission line now decay very fast, such that the field at a certain point is determined by the direct field only. The field components that undergo a reflection somewhere have to travel a larger distance and are damped more severely as depicted in Figure 5.1. If the observation point is in the same layer as the source point, neglecting the reflected waves amounts to the assumption of a homogeneous medium.

The dominant frequency dependence and asymptotic spectral behaviour for the TM Green's functions is given by

$$\lim_{k_\rho,1/\omega\to\infty}\widetilde{V}_{ij}^{V^{TM,\lessgtr}} \approx \mp\frac{\epsilon^{\gtrless}}{\epsilon^{<}+\epsilon^{>}}\prod_k(1+\Gamma_k^{TM})^{\mp 1}\quad e^{-k_\rho|z-z'|} \tag{5.75}$$

$$\lim_{k_\rho,1/\omega\to\infty}\widetilde{I}_{ij}^{V^{TM,\lessgtr}} \approx +\frac{\epsilon^{<}\epsilon^{>}}{\epsilon^{<}+\epsilon^{>}}\prod_k(1-\Gamma_k^{TM})^{\mp 1}\frac{j\omega}{k_\rho}e^{-k_\rho|z-z'|} \tag{5.76}$$

$$\lim_{k_\rho,1/\omega\to\infty}\widetilde{V}_{ij}^{I^{TM,\lessgtr}} \approx -\frac{1}{\epsilon^{<}+\epsilon^{>}}\prod_k(1+\Gamma_k^{TM})^{\mp 1}\frac{k_\rho}{j\omega}e^{-k_\rho|z-z'|} \tag{5.77}$$

$$\lim_{k_\rho,1/\omega\to\infty}\widetilde{I}_{ij}^{I^{TM,\lessgtr}} \approx \pm\frac{\epsilon^{\lessgtr}}{\epsilon^{<}+\epsilon^{>}}\prod_k(1-\Gamma_k^{TM})^{\mp 1}\quad e^{-k_\rho|z-z'|} \tag{5.78}$$

while for the TE set we obtain

$$\lim_{k_\rho,1/\omega\to\infty}\widetilde{V}_{ij}^{V^{TE,\lessgtr}} \approx \mp\frac{\mu^{\lessgtr}}{\mu^{<}+\mu^{>}}\prod_k(1+\Gamma_k^{TE})^{\mp 1}\quad e^{-k_\rho|z-z'|} \tag{5.79}$$

$$\lim_{k_\rho,1/\omega\to\infty}\widetilde{I}_{ij}^{V^{TE,\lessgtr}} \approx +\frac{1}{\mu^{<}+\mu^{>}}\prod_k(1-\Gamma_k^{TE})^{\mp 1}\frac{k_\rho}{j\omega}e^{-k_\rho|z-z'|} \tag{5.80}$$

$$\lim_{k_\rho,1/\omega\to\infty}\widetilde{V}_{ij}^{I^{TE,\lessgtr}} \approx -\frac{\mu^{<}\mu^{>}}{\mu^{<}+\mu^{>}}\prod_k(1+\Gamma_k^{TE})^{\mp 1}\frac{j\omega}{k_\rho}e^{-k_\rho|z-z'|} \tag{5.81}$$

$$\lim_{k_\rho,1/\omega\to\infty}\widetilde{I}_{ij}^{I^{TE,\lessgtr}} \approx \pm\frac{\mu^{\gtrless}}{\mu^{<}+\mu^{>}}\prod_k(1-\Gamma_k^{TE})^{\mp 1}\quad e^{-k_\rho|z-z'|} \tag{5.82}$$

where $\epsilon^{\lessgtr}$, $\mu_{\lessgtr}$ are the properties of the medium at the immediate left and right of the excitation point z'. The products just represent the transmission across the intervening interfaces k between z' and z as a function of the local asymptotic reflection coefficients

$$\Gamma_k^{TM} = \frac{\epsilon_k-\epsilon_{k-1}}{\epsilon_k+\epsilon_{k-1}} \tag{5.83}$$

$$\Gamma_k^{TE} = \frac{\mu_{k-1}-\mu_k}{\mu_{k-1}+\mu_k}. \tag{5.84}$$

Spectral Asymptotic behaviour	Singular Spatial Behaviour
$e^{-k_\rho \Delta}/k_\rho^3$	$R \ln R - R$
$e^{-k_\rho \Delta}/k_\rho^2$	$\ln R$
$e^{-k_\rho \Delta}/k_\rho$	$1/R$
$e^{-k_\rho \Delta}$	$1/R^2$
$k_\rho e^{-k_\rho \Delta}$	$1/R^3$

Table 5.1: Summary of the correspondence between spectral asymptotic and spatial singular behaviour.

These expressions can be used to extract the asymptotic behaviour as described in Section 7.2 of Chapter (7).

To obtain the corresponding spatial singular behaviour, we insert these asymptotic expressions into the spectral domain formulations, and perform the inverse Fourier transform using the Sommerfeld integral relations (5.66), (5.67), (5.68), (5.69), (5.70), (5.71) which now be evaluated analytically using the relations of Appendix B.4. As a useful mnemonic device, the relations given in Tables B.1 and B.2 are simplified as in Table 5.1. Notice that performing a spatial derivative aggravates the spatial singular behaviour as we move down in the above table.

5.5.3 Discussion of the Field Formulations

The Full Spectral Electric Dyadic Green's Function

For the full spectral electric dyadic Green's function of Equation (4.128), the dominant low frequency and spectral asymptotic behaviour separates the components into a first group which is proportional with frequency

$$\lim_{k_\rho, 1/\omega \to \infty} \widetilde{V}_{ij}^{I^{TE}}, \frac{\mu_i}{\epsilon_j} \widetilde{I}_{ij}^{V^{TM}} \sim j\omega \frac{e^{-k_\rho |z-z'|}}{k_\rho} \tag{5.85}$$

and which will give a basic $1/R$ spatial singular behaviour. The second group is inversely proportional with frequency

$$\lim_{k_\rho, 1/\omega \to \infty} \frac{\widetilde{V}_{ij}^{I^{TM}}}{-\gamma_i^2}, \frac{\widetilde{I}_{ij}^{V^{TM}}}{j\omega\epsilon_i j\omega\epsilon_j}, \frac{\widetilde{V}_{ij}^{I^{TE}} - \widetilde{V}_{ij}^{I^{TM}}}{k_\rho^2} \sim \frac{1}{j\omega} \frac{e^{-k_\rho |z-z'|}}{k_\rho} \tag{5.86}$$

and are accompanied by double spatial derivatives. In the corresponding space domain expressions of Equation (5.72), the frequency dependence is neglected while the spatial derivatives give rise to a dependence on the azimuth angle ϕ and a hypersingular $1/R^3$ behaviour.

The "Basic" Mixed Potential Form

The observations made above provide a guideline to obtain the "basic" mixed potential form of Equation (5.35). The vector potential components are obtained by extracting the frequency dependence $j\omega$ from the first group

$$\lim_{k_\rho,1/\omega\to\infty} \frac{\widetilde{V}^{I^{TE}}}{-j\omega}, \frac{\mu_i}{\epsilon_j}\frac{\widetilde{I}^{V^{TM}}_{ij}}{j\omega} \sim \frac{e^{-k_\rho|z-z'|}}{k_\rho} \tag{5.87}$$

and isolating the $1/j\omega$ dependence from the second group of scalar potential candidates

$$\lim_{k_\rho,1/\omega\to\infty} -j\omega\frac{\widetilde{V}^{I^{TM}}_{ij}}{\gamma_i^2}, +j\omega\frac{\widetilde{V}^{I^{TE}}_{ij} - \widetilde{V}^{I^{TM}}_{ij}}{k_\rho^2}, -j\omega\frac{\widetilde{V}^{I^{TM}}_{ij}}{\gamma_j^2} \sim \frac{e^{-k_\rho|z-z'|}}{k_\rho}. \tag{5.88}$$

These functions asymptotic equivalent functions are independent of frequency and all show the basic $1/R$ spatial singular behaviour. Since all spatial derivatives have been given a physical interpretation, the azimuth angle ϕ does not appear. However, the multiple scalar potentials make the formulation distinct from the familiar single scalar potential free space case, such that the evaluation of reaction integrals has to be reformulated. Another possible disadvantage of this formulation is the discontinuous behaviour of $\widetilde{G}^A_{zz}$, $\widetilde{\phi}_{zt}$ and $\widetilde{\phi}_z$ as we move from one layer to another. This is easily investigated as all voltages and currents are continuous across the interfaces, and the discontinuous behaviour is caused by the presence of $\epsilon_k, \mu_k, \gamma_k$ in the expressions.

Formulations A,B

In formulations A,B of Equations (5.34), (5.35), we choose ϕ_{zt} and ϕ_z as single scalar potential kernels. Apart from being discontinuous themselves, they also introduce modifications into the vector potential kernels which are also discontinuous and have a dominant behaviour

$$\lim_{k_\rho,1/\omega\to\infty} \frac{1}{j\omega k_\rho^2}\left(\widetilde{V}^{I^{TE}}_{ij} + \frac{k_i^2}{\gamma_i^2}\widetilde{V}^{I^{TM}}_{ij}\right) \sim \frac{e^{-k_\rho|z-z'|}}{k_\rho^3} \tag{5.89}$$

$$\lim_{k_\rho,1/\omega\to\infty} \frac{\mu_i\epsilon_i - \mu_j\epsilon_j}{\epsilon_i\gamma_j^2}\widetilde{V}^{V^{TM}}_{ij} \sim \frac{e^{-k_\rho|z-z'|}}{k_\rho^2} \tag{5.90}$$

with similar expressions for formulation B. From the corresponding spatial domain singular behaviour and taking into account the double and single spatial derivatives that have to be performed (because of the $-jk_x$, $-jk_y$), we see that they have a basic $1/R$ spatial singular behaviour and are independent of frequency. On the other hand, they still show a dependence on the azimuth angle ϕ. It is thus seen that

the enforcement of a single scalar potential introduces contributions into the vector potential kernel containing unexpected derivatives, which are difficult to interpret physically. The numerical evaluation of the single scalar potential contribution can be done easily but the vector potential contribution now becomes more complicated.

Formulation C

With the choice of the continuous scalar potential kernel $\widetilde{\phi}_t$, we obtain modifications of the vector potential kernel that behave as

$$\lim_{k_\rho, 1/\omega \to \infty} \frac{\widetilde{V}_{ij}^{V^{TE}} - \widetilde{V}_{ij}^{V^{TM}}}{k_\rho^2} \sim \frac{e^{-k_\rho}}{k_\rho^2}. \tag{5.91}$$

They are again valid vector potential contributions in the sense that the are independent of frequency and have a basic $1/R$ spatial singular behaviour, but the ϕ dependence on the azimuth angle is a valid counterargument. The advantage of this formulation is that in most practical cases all layers have $\mu_k = \mu_o$ such that all contributions become continuous.

5.5.4 The Multiple Scalar Potential Problem

From the physical point of view, the fact that the scalar potential in a multilayered medium is not unique [13], [201], [195], [196], [208], [209], [210] has astonished many a reader, impregnated as we are with the mental picture of a dimensionless and directionless point charge. However, strictly speaking, a single scalar potential V that gives the electric field from $\vec{E} = -\nabla V$ is only defined at zero frequency.

A related physical question concerns the interpretation of the charges Q_{jt} and Q_{jz} defined in Equations (5.29) and (5.30) as true charges. In the case of a single scalar potential, the electrostatic charge follows from the total charge by expanding the current in series as a function of frequency

$$Q_{electrostatic} = \lim_{\omega \to 0} \frac{\nabla' . \left(\vec{J}^0 + j\omega \vec{J}^1 + (j\omega)^2 \vec{J}^2 + (j\omega)^3 \vec{J}^3 + \ldots \right)}{-j\omega} = \nabla' . \vec{J}^1 \tag{5.92}$$

where the magnetostatic current is electrically neutral since it always flows in closed loops such that $\nabla' . \vec{J}^0 = 0$. This line of reasoning fails however for a 3D current distribution if the scalar potentials are different since $\nabla' . \vec{J}^0 = 0$ does not automatically imply that $\nabla'_t . \vec{J}^0_t = 0$ and $\partial J^0_z / \partial z' = 0$ separately.

We can somewhat ease our psychological discomfort about the multiple scalar potential problem and solve the above apparent problems by examining more closely the low frequency and static limit behaviour of the mixed potential formulations. In the static limit we have $\nabla \times \vec{E} = \vec{0}$, so there must exist a single scalar potential such that $\vec{E} = -\nabla V$. This remains valid of course for a layered medium. The different scalar

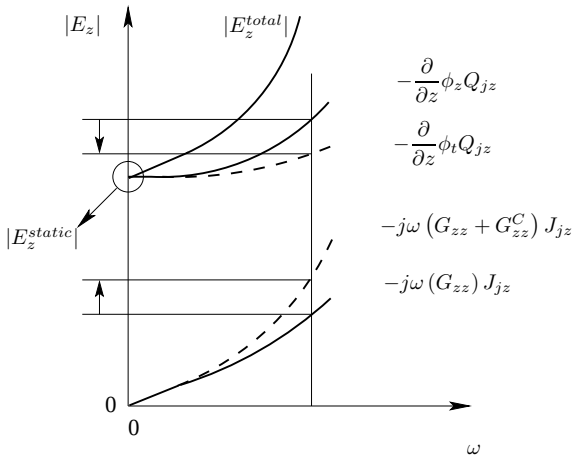

Figure 5.2: The contributions of different scalar potentials to the unique electric field are compensated by the vector potential contributions. The scalar potentials converge to the unique static scalar potential when the frequency tends to zero. The vector potentials remain different but vanish with zero frequency.

potentials $\widetilde{\phi}_z$, $\widetilde{\phi}_{zt}$, $\widetilde{\phi}_t$ of Equations (5.22), (5.34) , (5.35) and (5.39) converge to "the" single static scalar potential when the frequency tends to zero

$$\left.\begin{array}{l} \lim\limits_{\omega\to 0}\left(-j\omega\dfrac{\widetilde{V}_{ij}^{I^{TM}}}{\gamma_i^2}\right) \\ \lim\limits_{\omega\to 0}\left(-j\omega\dfrac{\widetilde{V}_{ij}^{I^{TM}}}{\gamma_j^2}\right) \\ \lim\limits_{\omega\to 0}\left(+j\omega\dfrac{\widetilde{V}_{ij}^{I^{TE}}-\widetilde{V}_{ij}^{I^{TM}}}{k_\rho^2}\right) \end{array}\right\} \sim -j\omega\frac{\widetilde{V}_{ij}^{I^{TM}}}{k_\rho^2}. \tag{5.93}$$

Since the total electric field is unique, the different behaviour of the scalar potential contributions as a function of frequency is compensated by the different vector potential contributions. The vector potentials remain different, but their contributions to the electric field vanishes with frequency. This is illustrated in Figure 5.2, where we sketch a possible behaviour of the contributions to the Z component of the electric field by the scalar and vector potential contributions of the mixed potential formulation B with that of formulation C. In the following Section 5.6 we will prove mathematically that the different scalar and vector potentials always give identical electric and magnetic fields at all frequencies.

5.6 The Mathematical Interpretation

In this section, we will link our results with a number of well established facts in electromagnetic theory. In Section 5.6.2, we will identify the mixed potential formulations with the original solutions derived by Sommerfeld himself. To avoid the somewhat outdated Hertz potential approach, we first discuss the more modern scalar and vector potential approach in Section 5.6.1. Although we have not followed this approach in this work, it does allow to place the different Sommerfeld solutions and the multiple possible MPIE formulations in a broader perspective. In Section 5.6.3, we prove that these phenomena can be classified as gauge transformations, applied to the case of a planar multilayered medium.

5.6.1 Vector and Scalar Potential, Gauge Condition

From the form of Maxwell's field equations it follows [42] that it is always possible to write the fields as a function of a scalar potential V and a vector potential $\vec{A}$ as

$$\vec{E} = -j\omega\vec{A} - \nabla V \tag{5.94}$$

$$\vec{H} = \nabla \times \vec{A}. \tag{5.95}$$

The solution of the boundary value problem is in many, but not all cases simplified by introduction of the new independent variables A_x, A_y, A_z and V. A gauge condition linking $\vec{A}$ with V has to be chosen to completely determine $\vec{A}$. These conditions take the form

$$\nabla.\vec{A} = 0 \tag{5.96}$$

$$\nabla.\vec{A} = -j\omega\mu\epsilon V \tag{5.97}$$

where the Coulomb gauge (5.96) is suited to deal with static problems, and the Lorentz gauge (5.97) is better suited to analyse electrodynamic phenomena. The solution of the boundary value problem for the vector and scalar potentials $\vec{A}$, V can be obtained as a function of the current

$$\vec{A} = \int_{S'} \overline{G}^A.\vec{J}\,\mathrm{d}S' \tag{5.98}$$

$$V = \int_{S'} \phi\left(\frac{\nabla'.\vec{J}}{-j\omega}\right) \tag{5.99}$$

where ϕ is the scalar potential kernel, and $\overline{G}^A$ the vector potential kernel, which for complicated boundary value problems, such as the 3D current source in a multilayered medium, has to be allowed a dyadic nature. Following this approach as in [191], [210], [195], [196], [208], [209], [201] one is thus confronted with the choice of the gauge condition, and with an often suspicious a priori choice of the in principle 9 components of $\overline{G}^A$. These problems were avoided in our more physical derivation starting from the dyadic Green's function.

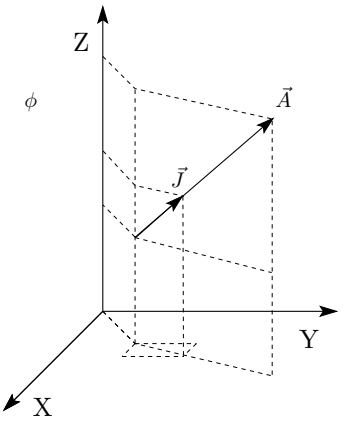

Figure 5.3: The scalar and vector potential for a homogeneous medium. The vector potential is everywhere parallel to the generating current element.

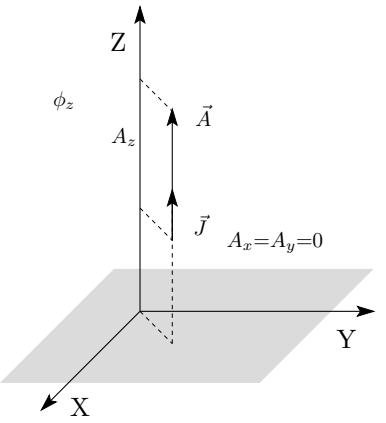

Figure 5.4: The field of a vertical current element in a layered medium can be described with a single vector potential component A_z, and a scalar potential ϕ_z.

5.6.2 The Sommerfeld Problem

The dyadic nature of the vector potential kernel with the higher order Sommerfeld integrals was already established by Sommerfeld [36] in studying wave generation and propagation by dipole antennas above a lossy half space. Using a Hertz vector potential approach [211], he noticed that this vectorial potential acquired components which were not parallel to the generating current element [36].

In a homogeneous medium, we have Equation (5.10)

$$\vec{E} = -j\omega\mu \int_{S'} \begin{bmatrix} G & 0 & 0 \\ 0 & G & 0 \\ 0 & 0 & G \end{bmatrix} .\vec{J}\, \mathrm{d}S' - \nabla \int_{S'} G \left(\frac{\nabla' .\vec{J}}{-j\omega\epsilon} \right) \mathrm{d}S' \qquad (5.100)$$

such that the vector potential is everywhere parallel to the current source. This is depicted in Figure 5.3.

From the "basic" mixed potential form and formulation B, we derive that for a Z oriented current element in a layered medium

$$\vec{E} = -j\omega \int_{S'} \begin{bmatrix} 0 \\ 0 \\ G_{zz} \end{bmatrix} J_z \, \mathrm{d}S' - \nabla \int_{S'} \phi_z \left(\frac{\frac{\partial J_z}{\partial z'}}{-j\omega} \right) \mathrm{d}S' \qquad (5.101)$$

the field can be described with one vector potential component A_z ([36], Section 32, The vertical antenna over an arbitrary earth), such that the vector potential remains parallel to the current. It's evaluation involves only the lowest order Sommerfeld

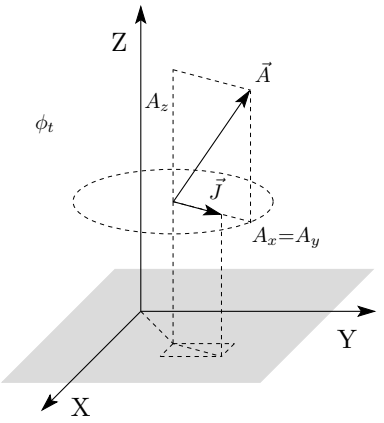

Figure 5.5: The "traditional" Sommerfeld choice $A_x = A_y$, A_z to describe the field of a horizontal current element. The vector potential is no longer parallel to the current. A different scalar potential ϕ_t now occurs.

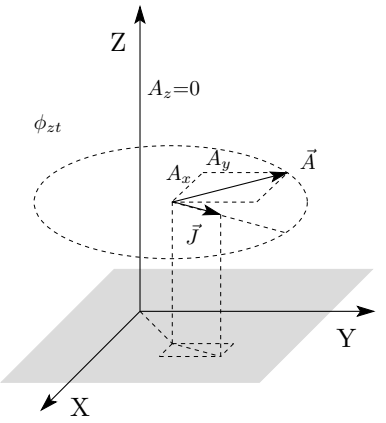

Figure 5.6: The alternative choice A_x, A_y to describe the field of a horizontal current element. The vector potential is not parallel to the generating current element either and yet another scalar potential ϕ_{zt} appears.

integral and no angular dependence in the azimuth plane, which is natural because of the cylindrical symmetry of the field. This situation is depicted in Figure 5.4.

From formulation C, we derive the "traditional" Sommerfeld choice for the components of the vector potential $A_x = A_y$, and A_z to obtain the field of a horizontal current element ([36], Section 33, The horizontal antenna over an arbitrary earth), [212],

$$\vec{E} = -j\omega \int_{S'} \begin{bmatrix} G_{xx} & 0 \\ 0 & G_{xx} \\ G^C_{zx} & G^C_{zy} \end{bmatrix} . \vec{J}_t \, \mathrm{d}S' - \nabla \int_{S'} \phi_t \left(\frac{\nabla'_t . \vec{J}_t}{-j\omega} \right) \mathrm{d}S'. \qquad (5.102)$$

Higher order Sommerfeld integrals and an azimuth angular dependence are now incorporated to describe the azimuth variation of the field. Notice that the vector potential is no longer parallel to the generating current element as depicted in Figure 5.5. The scalar potential is now different from the one in the previous case [209].

Although widely used, the above choice is not the only one possible to obtain the field for a horizontal current element. From Formulation A we obtain

$$\vec{E} = -j\omega \int_{S'} \begin{bmatrix} G_{xx} & G^A_{xy} \\ G^A_{yx} & G_{xx} \\ 0 & 0 \end{bmatrix} . \vec{J}_t \, \mathrm{d}S' - \nabla \int_{S'} \phi_{zt} \left(\frac{\nabla' . \vec{J}_t}{-j\omega} \right) \mathrm{d}S' \qquad (5.103)$$

that the components A_x, A_y can also be used [208]. The third scalar potential ϕ_{zt} is now required. This situation is depicted in Figure 5.6.

5.6.3 The Gauge Transformation

The fields expressed as a function of the vector and scalar potential remain unaltered under a so called gauge transformation with a function ψ (a particularly clear exposition can be found in [42])

$$\vec{A}' = \vec{A} + \nabla\psi \tag{5.104}$$
$$V' = V - j\omega\psi \tag{5.105}$$

This can be seen easily by deriving the field from these new potentials

$$\vec{E} = -j\omega \quad \vec{A}' \qquad -\nabla \quad V' \tag{5.106}$$
$$= -j\omega \ (\ \vec{A} + \nabla\psi \ ) \ - \nabla \ (\ V - j\omega\psi \ ) \tag{5.107}$$
$$= -j\omega \quad \vec{A} \qquad -\nabla \quad V \tag{5.108}$$
$$\vec{H} = \nabla \times \quad \vec{A}' \tag{5.109}$$
$$= \nabla \times (\ \vec{A} + \nabla\psi \ ) \tag{5.110}$$
$$= \nabla \times \quad \vec{A} \tag{5.111}$$

For the electric field, this has to be interpreted physically by saying that if we change the contribution to the field by the charge, this has to be compensated by a corresponding change in the vector potential field contribution. For the magnetic field, this change has no effect since the change in vector potential can always be written as $\nabla\psi$, for which $\nabla \times \nabla\psi = \vec{0}$.

The Gauge Transformation in the Multilayered Medium

We now prove that the transition between the proposed mixed potential forms A, B, C are gauge transformations. For the electric field we transform the operations on the scalar and vector potentials

$$\vec{E} = -j\omega \quad \vec{A}^B \qquad -\nabla \quad V^B \tag{5.112}$$
$$= -j\omega \ (\ \vec{A}^B + \nabla\psi^{CB} \ ) - \nabla \ (\ V^B - j\omega\psi^{CB} \ ) \tag{5.113}$$
$$= -j\omega \quad \vec{A}^C \qquad -\nabla \quad V^C \tag{5.114}$$

into the operations on the scalar and dyadic vector potential kernels themselves

$$\vec{E} = -j\omega \int_{S'} \ \overline{G}^B . \vec{J} \, \mathrm{d}S' \qquad -\nabla \int_{S'} \ \phi^B \, \frac{\nabla' . \vec{J}}{-j\omega} \, \mathrm{d}S' \tag{5.115}$$
$$= -j\omega \int_{S'} \left[\overline{G}^B + (\overline{G}^C - \overline{G}^B) \right] . \vec{J} \, \mathrm{d}S' - \nabla \int_{S'} \left[\phi^B + (\phi^C - \phi^B) \right] \frac{\nabla' . \vec{J}}{-j\omega} \, \mathrm{d}S' \tag{5.116}$$
$$= -j\omega \int_{S'} \ \overline{G}^C . \vec{J} \, \mathrm{d}S' \qquad -\nabla \int_{S'} \ \phi^C \, \frac{\nabla' . \vec{J}}{-j\omega} \, \mathrm{d}S' . \tag{5.117}$$

The gauge function to transform mixed potential form B into formulation C is thus obtained from

$$\psi^{CB} = -\frac{1}{j\omega}\int\limits_{S'} \left(\phi^C - \phi^B\right) \frac{\nabla'.\vec{J}}{-j\omega}\,\mathrm{d}S' \tag{5.118}$$

and the change in the dyadic vector potential kernel is obtained from

$$\int\limits_{S'} \left[\overline{G}^C - \overline{G}^B\right].\vec{J}\,\mathrm{d}S' = -\frac{1}{j\omega}\nabla\int\limits_{S'} \left(\phi^C - \phi^B\right) \frac{\nabla'.\vec{J}}{-j\omega}\,\mathrm{d}S' \tag{5.119}$$

To obtain the explicit expressions for the change of the dyadic vector potential kernel, we need to transfer the derivatives from the current to the Green's functions. This is done in a partial integration process, which behaves differently for the transverse and z derivatives. We thus write

$$\int\limits_{S'} \left[\overline{G}^C - \overline{G}^B\right].\vec{J}\,\mathrm{d}S' =$$

$$-\frac{1}{j\omega}\begin{bmatrix} \nabla_t\int\limits_{S'}(\phi_t-\phi_z)\frac{\nabla'.\vec{J}_t}{-j\omega}\,\mathrm{d}S' & + \nabla_t\int\limits_{S'}(\phi_t-\phi_z)\frac{\frac{\partial J_z}{\partial z'}}{-j\omega}\,\mathrm{d}S' \\ +\frac{\partial}{\partial z}\int\limits_{S'}(\phi_t-\phi_{zt}+\phi_{zt}-\phi_z)\frac{\nabla'.\vec{J}_t}{-j\omega}\,\mathrm{d}S' + \frac{\partial}{\partial z}\int\limits_{S'}(\phi_t-\phi_z)\frac{\frac{\partial J_z}{\partial z'}}{-j\omega}\,\mathrm{d}S' & \end{bmatrix} \tag{5.120}$$

were we replaced ϕ^C, ϕ^B by ϕ_t, ϕ_{zt}. The transfer of derivatives to the Green's functions was already done in Section 5.3.2, and we need not even work this out completely again. Using immediately Equations (5.36), (5.37), (5.40), (5.43) and dropping the now superfluous integral over the current we obtain the corresponding change of the dyadic vector potential kernel as

$$\left[\overline{G}^C - \overline{G}^B\right] = \begin{bmatrix} -G^B_{xx} & -G^B_{xy} & +G^C_{xz} \\ -G^B_{yx} & -G^B_{yy} & +G^C_{yz} \\ -G^B_{zx}+G^C_{zx} & -G^B_{zy}+G^C_{zy} & +G^C_{zz} \end{bmatrix} \tag{5.121}$$

which are indeed the modifications required to transform the dyadic vector potential kernel of formulation B (5.35) into the one of formulation C (5.39). The same line of reasoning allows to transform formulation C to A and back to B by gauge functions ψ^{AC} and ψ^{BA}.

The magnetic field remains unaltered and can be obtained from all vector potentials $\vec{A}^A$, $\vec{A}^B$, $\vec{A}^C$. This is true because the transitions between them have the form of

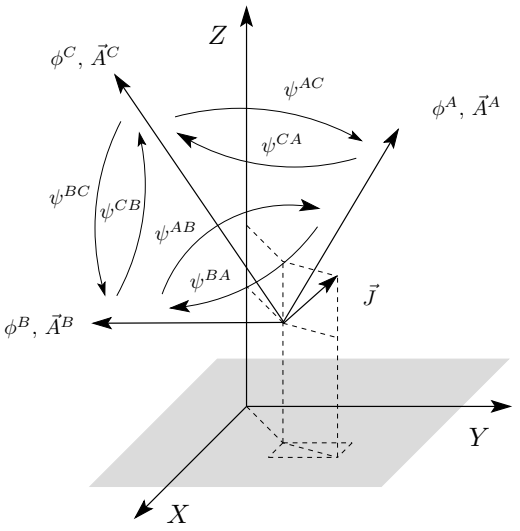

Figure 5.7: The gauge transformation in the multilayered medium. The electric and magnetic fields are unique while the scalar and vector potentials are not. The potentials can be transformed into one another by gauge transformations with gauge functions ψ.

a gradient of a scalar gauge function as in Equation (5.119). By Equation (4.5), the magnetic dyadic Green's function of Equation (4.129) is related to the dyadic electric Green's function of Equation (4.128) and the dyadic vector potential kernels of Equations (5.34), (5.35) and (5.39) as

$$\overline{G}^h = -\frac{1}{j\omega\mu_i}\nabla\times G^e = \frac{1}{\mu_i}\nabla\times\overline{G}^A \tag{5.122}$$

$$= \frac{1}{\mu_i}\nabla\times\overline{G}^B \tag{5.123}$$

$$= \frac{1}{\mu_i}\nabla\times\overline{G}^C. \tag{5.124}$$

The general situation is depicted in Figure 5.7. The electric field and magnetic fields are unique. The scalar and dyadic vector potential kernels are not. They are related by gauge transformations. In the static limit, the electric field is determined by the scalar potential which becomes unique, while the vector potential contributions to the electric field, which remain essentially different, vanish with frequency. The magnetic field can always be derived from the different dyadic vector potential kernels at all frequencies.

We have thus demonstrated that the Sommerfeld problem and the multiple possible MPIE formulations are phenomena to be classified under the more general theory of gauge transformations in electromagnetic theory, applied to the multilayered medium.

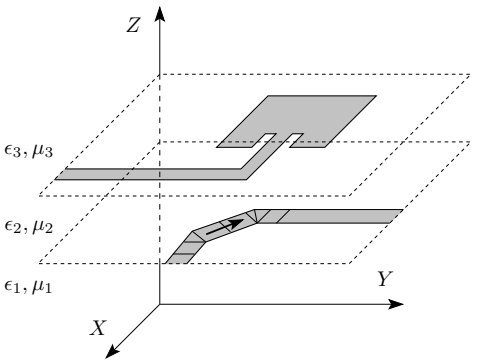

Figure 5.8: The familiar planar or 2D structure in a multilayered medium.

Although this interpretation must have lingered in the back of the mind of many a mathematical electrician in the field of integral equations and wave propagation in multilayered media, we have now confirmed this suspicion for the first time.

5.7 Field Formulations for 2D to 3D Geometries

Now that we have acquired a basic knowledge of several possible formulations for the electric field, we can investigate how they can be used for the integral equation analysis of geometrically complex structures located in a multilayered medium.

The Planar or 2D Structure

Figure 5.8 shows the well known planar structure. The metal surfaces of the passive microwave circuit or antenna can be assumed to have zero thickness and are usually deposited at the interface of two dielectric media. The conductors are planar which means that they are parallel to the layers constituting the background medium. The surrounding medium is embedded within the Green's function operators and for a single conducting surface or several conducting surfaces at the same interface such as the simplest single layer microstrip circuits and antennas [164], [213], [190] the remaining problem is essentially reduced to a 2D problem involving only the transverse x, y coordinates. When the conductors are located at different interfaces, such as in multiconductor transmission lines [169], [170], [214], [215] and stacked patch antennas [216], the problem actually becomes 3D, but when the surfaces remain planar, their z-separation is just a parameter in the construction of the Green's functions, and the analysis remains essentially 2D.

Initially, the dispersion characteristics of microstrip transmission lines were determined with an integral equation analysis of the cross section only. Although reduced

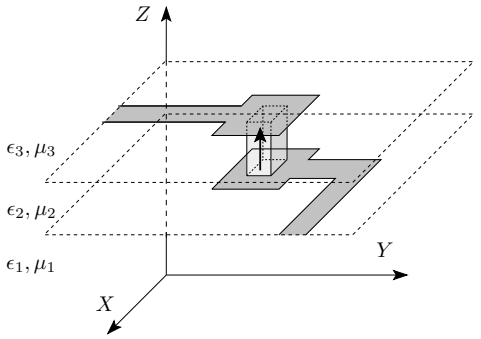

Figure 5.9: A "3D planar" or 2.5D structure. Vertical currents are confined to a single "thin" dielectric layer. They can be assumed constant and the horizontal current components can be neglected.

to a 1D problem, all transverse field and current components need to be modeled. These simple problems often used an EFIE formulation [164], [167], [169], [170], [166] were only the transverse part of the dyadic Green's function of Equation (4.128) is required. The analysis of planar problems such as microstrip discontinuities initially continued to use an EFIE formulation [213], [217], [204], [205], [206], [207], [218] but when more complicated and arbitrarily shaped configurations had to be analysed the advantages of the more physical MPIE formulation appeared again [200], [219] [220], [221], [216], [222], [190], [223], [224], [225], [214], [215]. Theoretically, when only the transverse or horizontal fields and currents are involved the field can be cast into MPIE form using only the transverse parts of the formulations (5.34), (5.35), (5.39).

The "3D Planar" or 2.5D Structures

The analysis of real life problems such as probe feeds for patch antennas [226], [227], [228], [229], [230], [210], [231], [232], [13] via's and through holes, [233], [234], [235], [236] bond-wires, air-bridges [235], [236], [237], [238], [239], [240], [241] and interconnections [151], [152] in planar circuits and printed circuit boards all require a limited capability to model strictly vertical currents. Because of the small dimensions, transverse current components on the vertical conductors can be neglected. When the substrate is thin, the Z component can be assumed constant as in [235], [237], [240], [241]. This is however no longer valid for thicker substrates where the variation of the current in the Z direction has to be taken into account [228], [229], [230], [210], [232], [13], [240] Usually, the current cannot cross the interface between adjacent dielectric layers. Such a situation is depicted in Figure 5.9.

Such problems were analysed with EFIE formulations in [226], [227], [237], [235], [241] and with MPIE formulations in [239], [240], [13]. Since the currents flow either horizontal or either vertical, no problems are experienced with the different scalar potential kernels, and [210] even switches between the mixed potential formulations B

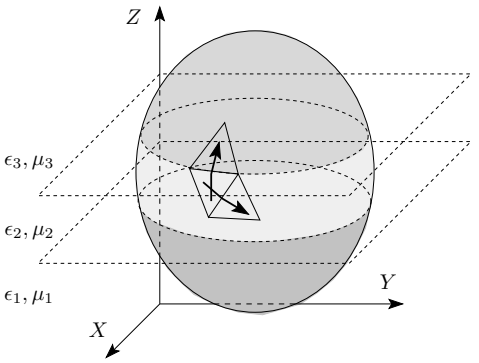

Figure 5.10: A full 3D structure. An arbitrary curved surface is modeled using currents with arbitrary orientation.

and C depending on the orientation of source and observation currents. A combination of EFIE and MPIE was used in [235], where the MPIE was used to model mutual coupling between planar currents and the EFIE for vertical fields and currents, but this hybrid formulation was only implemented for a single layer medium.

Several commercial software packages that use the BIE can analyse 2.5D geometries such as Sonnet *em*, AWR EMSight, Agilent Momentum and Ansoft Ensemble.

The Full 3D Structure

Figure 5.10 depicts a full 3D problem [183], [191], [242], [243]. The defining characteristic of a really 3D problem is that the current can have arbitrary orientation at all positions in the layer structure. This is usually combined with large vertical dimensions and the current can cross the interfaces between adjacent layers. Such problems can in principle still be analysed with an EFIE formulation [244]. When using an MPIE formulation, we cannot avoid the multiple scalar potential problem [208], [209]. On at least one occasion, an inclined plane was analysed with the "basic" mixed potential form [196], using the distinct scalar potential kernels, but mostly the single scalar potential formulation C of [191] is used, for inclined wire antennas [199], [201] and inclined planes [245] crossing the interface between two unbounded media, which is a very simple stratified medium (no surface waves can occur). For these formulations, the problems are shifted to the dyadic vector potential kernel.

Some commercial software packages that offer full 3D capability for arbitrarily shaped surfaces in arbitrarily multilayered environments are EMSS FEKO and Zeland Software IE3D.

The "Quasi 3D" Structure

Figure 5.11 depicts the "quasi 3D" geometry we will concentrate on. Vertical surfaces

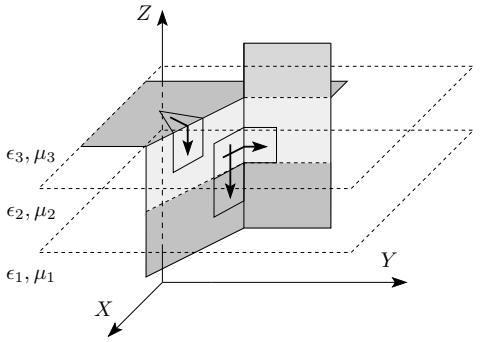

Figure 5.11: A "quasi 3D" structure composed of horizontal and strictly vertical surfaces. These can cross interfaces between dielectric layers and all current components are modeled.

can be arbitrarily large and can cross dielectric interfaces. The current flowing on the surface is decomposed into vertical and horizontal components. These will be expanded with rectangular rooftop functions, while triangular functions can only be used on the horizontal conductors. In this way, the theoretical problems of a fully 3D formulation, the multiple scalar potentials or the appearance of a dyadic vector potential kernel, are altogether avoided. The field formulation can be specifically adapted to the geometry as a hybridisation of dyadic and mixed potential formulations, derived in the following section.

This geometry was already treated in [246], [247], [248] [249], [184], [250] but using a the total MPIE formulation, and the implementations were limited to single and double layered structures.

The formulation is not fully 3D in the sense that at the basic level, the expansion functions for the current cannot have arbitrary orientation, although it is possible to treat fully 3D structures by making a staircase approximation for an arbitrarily shaped surface.

5.8 The Hybrid Dyadic-Mixed Potential Form

In this section we establish a hybrid formulation for the electric field. The formulation is derived keeping in mind the geometry it is intended to be used for. We can thus match the theoretical formulation to the structure under consideration.

5.8.1 The Spectral Domain

The Transverse Field-Current Relations

We will continue to express the horizontal components of the electric field as a function of the transverse current components with a mixed potential formulation. Since the reaction integrals involving the horizontal components will have to be done in a numerical fashion anyhow the space domain MPIE formalism remains the mechanism to deal with the Green's function singularity for this part of the formulation. From Equation (5.39), we thus retain the transverse part

$$\begin{bmatrix} \widetilde{E}_{ix} \\ \widetilde{E}_{iy} \end{bmatrix} = -j\omega \begin{bmatrix} \dfrac{\widetilde{V}^{I^{TE}}}{-j\omega} & 0 \\ 0 & \dfrac{\widetilde{V}^{I^{TE}}}{-j\omega} \end{bmatrix} \begin{bmatrix} \widetilde{J}_{jx} \\ \widetilde{J}_{jy} \end{bmatrix} - \begin{bmatrix} -jk_x \\ -jk_y \end{bmatrix} \left(j\omega \frac{\widetilde{V}_{ij}^{I^{TE}} - \widetilde{V}_{ij}^{I^{TM}}}{k_\rho^2} \right) \left(\frac{+jk_x\widetilde{J}_{jx} + jk_y\widetilde{J}_{jy}}{-j\omega} \right). \quad (5.125)$$

From Section 5.5, we recall that both the scalar and vector potential Green's function exhibit a spectral asymptotic $e^{-k_\rho \Delta}/k_\rho$ and a spatial $1/R$ singular behaviour.

The Vertical Field Generated by the Vertical Current

The Z components of field and current were expressed in dyadic form in Equation (4.128) as

$$\widetilde{E}_{iz} = -j\omega\mu_i \left[1 + \frac{1}{k_i^2}\frac{\partial^2}{\partial z^2} \right] \left(\frac{\widetilde{I}_{ij}^{V^{TM}}}{j\omega\epsilon_j} \right) \widetilde{J}_{jz}. \quad (5.126)$$

A mixed potential form can in principle be established by using the derivative relations of Section 4.11 of Chapter 4 to obtain

$$\widetilde{E}_{iz} = -j\omega \left(\frac{\mu_i}{\epsilon_j} \frac{\widetilde{I}_{ij}^{V^{TM}}}{j\omega} \right) \widetilde{J}_{jz} - \frac{\partial}{\partial z} \left(-j\omega \frac{\widetilde{V}_{ij}^{I^{TM}}}{\gamma_j^2} \right) \left(\frac{\dfrac{\partial \widetilde{J}_{jz}}{\partial z'}}{-j\omega} \right) \quad (5.127)$$

as in the "basic" mixed potential form of Equation (5.22). However, using the same derivative relations, it becomes possible to integrate arbitrary Green's functions with the current expansion functions for the z, z' coordinates, and there is no further need to use an MPIE formulation. It is then more economical to integrate the dyadic expression immediately with the expansion currents for the current. We simplify Equation (5.126) with the help of $\gamma_i^2 = k_\rho^2 - k_i^2$ as

$$\left[1 + \frac{1}{k_i^2}\frac{\partial^2}{\partial z^2} \right] \widetilde{I}_{ij}^{V^{TM}} = \left[1 + \frac{\gamma_i^2}{k_i^2} \right] \widetilde{I}_{ij}^{V^{TM}} = \frac{k_\rho^2}{k_i^2} \widetilde{I}_{ij}^{V^{TM}} \quad (5.128)$$

such that we finally obtain

$$\widetilde{E}_{iz} = k_\rho^2 \frac{\widetilde{I}_{ij}^{V^{TM}}}{j\omega\epsilon_i j\omega\epsilon_j} \widetilde{J}_{jz}. \quad (5.129)$$

The well known problems with this dyadic Green's functions is that it shows a $k_\rho e^{-k_\rho \Delta}$ spectral asymptotic and a $1/R^3$ spatial singular behaviour. The analytical integration of the z, z' dependence will be done with rooftop functions. This will lead to a $R \ln R - R$ spatial singular behaviour, as demonstrated in Chapter 7.

The Transverse Field of a Vertical Current Element

For the horizontal field of a Z oriented current, we select from the full spectral electric Green's dyad Equation (4.128) the subset

$$\begin{bmatrix} \widetilde{E}_{ix} \\ \widetilde{E}_{iy} \end{bmatrix} = \begin{bmatrix} -jk_x \\ -jk_y \end{bmatrix} \frac{\partial}{\partial z} \left(\frac{\widetilde{I}_{ij}^{V^{TM}}}{j\omega\epsilon_i j\omega\epsilon_j} \right) \widetilde{J}_{jz} \tag{5.130}$$

for which we will combine the above two techniques. The horizontal derivatives are retained as in an MPIE formulation, but the z derivatives are absorbed in the Green's function to give

$$\begin{bmatrix} \widetilde{E}_{ix} \\ \widetilde{E}_{iy} \end{bmatrix} = -\frac{1}{j\omega} \begin{bmatrix} -jk_x \\ -jk_y \end{bmatrix} \left(\frac{\widetilde{V}_{ij}^{V^{TM}}}{\epsilon_j} \right) \widetilde{J}_{jz}. \tag{5.131}$$

The spectral asymptotic behaviour is

$$\lim_{k_\rho, 1/\omega \to \infty} \widetilde{V}_{ij}^{V^{TM}} = e^{-k_\rho \Delta} \tag{5.132}$$

giving a corresponding $1/R^2$ spatial singular behaviour. This singularity is transformed by integrating the Green's function with the z' dependent part of the J_{jz} rooftop function. The result will be a $\ln R$ singularity only.

The Vertical Electric Field of a Transverse Current

Similarly, the vertical field generated by a transverse current is selected from Equation (4.128) as

$$\widetilde{E}_{iz} = \frac{\partial}{\partial z} \left(-jk_x - jk_y \right) \left(\frac{\widetilde{V}_{ij}^{I^{TM}}}{-\gamma_i^2} \right) \begin{bmatrix} \widetilde{J}_{jx} \\ \widetilde{J}_{jy} \end{bmatrix}. \tag{5.135}$$

By transferring the inner derivatives to the current in a partial integration and absorbing the z-derivative in the Green's function this is transformed into

$$\widetilde{E}_{iz} = \left(\frac{\widetilde{I}_{ij}^{I^{TM}}}{\epsilon_i} \right) \left(\frac{+jk_x \widetilde{J}_{jx} + jk_y \widetilde{J}_{jy}}{-j\omega} \right). \tag{5.136}$$

The spectral asymptotic behaviour of the occurring Green's function

$$\lim_{k_\rho, 1/\omega \to \infty} \widetilde{I}_{ij}^{I^{TM}} = e^{-k_\rho \Delta} \tag{5.137}$$

$$\begin{bmatrix} \widetilde{E}_{ix} \\ \widetilde{E}_{iy} \end{bmatrix} = -j\omega \begin{bmatrix} \dfrac{\widetilde{V}^{I^{TE}}}{-j\omega} & 0 \\ 0 & \dfrac{\widetilde{V}^{I^{TE}}}{-j\omega} \end{bmatrix} \begin{bmatrix} \widetilde{J}_{jx} \\ \widetilde{J}_{jy} \end{bmatrix} - \begin{bmatrix} -jk_x \\ -jk_y \end{bmatrix} \left(j\omega \frac{\widetilde{V}_{ij}^{I^{TE}} - \widetilde{V}_{ij}^{I^{TM}}}{k_\rho^2} \right) \left(\frac{+jk_x\widetilde{J}_{jx} + jk_y\widetilde{J}_{jy}}{-j\omega} \right)$$

$$\widetilde{E}_{iz} = k_\rho^2 \frac{\widetilde{I}_{ij}^{V^{TM}}}{j\omega\epsilon_i j\omega\epsilon_j} \widetilde{J}_{jz}$$

$$\begin{bmatrix} \widetilde{E}_{ix} \\ \widetilde{E}_{iy} \end{bmatrix} = -\frac{1}{j\omega} \begin{bmatrix} -jk_x \\ -jk_y \end{bmatrix} \left(\frac{\widetilde{V}_{ij}^{V^{TM}}}{\epsilon_j} \right) \widetilde{J}_{jz}$$

$$\widetilde{E}_{iz} = \left(\frac{\widetilde{I}_{ij}^{I^{TM}}}{\epsilon_i} \right) \left(\frac{+jk_x\widetilde{J}_{jx} + jk_y\widetilde{J}_{jy}}{-j\omega} \right)$$

The spectral domain hybrid dyad - mixed potential form for the electric field in an arbitrary plane-stratified medium. The transverse field current relations use an MPIE formalism, while the vertical relations are written in dyadic form. (5.133)

$$\vec{E}_{it} = -j\omega S_0 \left\{ \frac{\widetilde{V}^{I^{TE}}}{-j\omega} \right\} \vec{J}_{jt} - \nabla_t S_0 \left\{ j\omega \frac{\widetilde{V}_{ij}^{I^{TE}} - \widetilde{V}_{ij}^{I^{TM}}}{k_\rho^2} \right\} \left(\frac{\nabla_t' . \vec{J}_{jt}}{-j\omega} \right)$$

$$\widetilde{E}_{iz} = S_0 \left\{ k_\rho^2 \frac{\widetilde{I}_{ij}^{V^{TM}}}{j\omega\epsilon_i j\omega\epsilon_j} \right\} \widetilde{J}_{jz}$$

$$\vec{E}_{it} = -\frac{1}{j\omega} \nabla_t S_0 \left\{ \frac{\widetilde{V}_{ij}^{V^{TM}}}{\epsilon_j} \right\} \widetilde{J}_{jz}$$

$$\widetilde{E}_{iz} = S_0 \left\{ \frac{\widetilde{I}_{ij}^{I^{TM}}}{\epsilon_i} \right\} \left(\frac{\nabla_t' . \vec{J}_{jt}}{-j\omega} \right)$$

The spatial domain hybrid dyad - mixed potential form for the electric field in an arbitrary plane-stratified medium. The transverse field current relations use an MPIE formalism, while the vertical relations are written in dyadic form. (5.134)

again gives a $1/R^2$ spatial singularity. By integrating this with the rooftop expansion function of the observation current J_{iz}, this is abated to a $\ln R$ behaviour.

The results for the spectral domain expressions are collected in Equation (5.133).

5.8.2 The Spatial Domain

The remaining derivatives in the transverse coordinates are all retained in the space domain. The hybrid field formulation in the spatial domain is given in Equation (5.134). Notice the simplicity of this expression as compared to the total MPIE formulation of Equation (5.73). No azimuth angular dependence and no higher order Sommerfeld integrals are present.

5.9 Conclusions

In this chapter, a physics based derivation of several mixed potential formulations for the electric field in a planar stratified medium was given, starting from the unique full spectral electric dyadic Green's function established in the previous chapter. The Sommerfeld integral representation was introduced to obtain the corresponding expressions in the space domain. Considerable attention was spent on the physical interpretation and meaning. On the mathematical side, we have proven that the single scalar potential kernel mixed potential formulations are related by the gauge transformation formalism, applied for the case of a multilayered medium. We classified practical occurring problems in planar stratified media according to their geometry as 2D, 2.5D, fully 3D and "quasi 3D" and examined the field formulations that can be applied for their BIE analysis. The "quasi 3D" geometry is not fully 3D since we assume that the current always flows on horizontal or strictly vertical surfaces, but most practical problems are seen to fall within this assumption. Furthermore, for this particular geometry, one can exploit the analytical possibilities of the SDA approach to the utmost. The field formulation was adapted to this geometry as a hybrid dyadic - mixed potential formulation, that avoids typical theoretical and numerical problems of standard available "total" mixed potential formulations. The geometry also allows to perform all z, z' dependent parts of the reaction integrals in closed form as worked out in Chapter 6.

Chapter 6

Combined Spectral-Space Domain Solution of the Integral Equation

6.1 Introduction

The solution of the Boundary Integral Equation for realistic engineering problems has to be done numerically. Discretising the current with appropriate expansion functions and applying the method of moments as described in Section 3.5.1 of Chapter 3 discretises the whole integral equation into a matrix equation which can be solved using standard linear algebra technology. Apart from the time spent in solving this system of equations, a considerable amount of "matrix fill" time is required to compute the matrix elements. They are obtained by evaluating "reaction integrals". In the first Section 6.2, we discuss how the evaluation of these integrals is determined by the nature of the field in the planar stratified medium and the geometry of the metallic structure to be analysed. Building on this experience, and using the new hybrid field formulation developed in the previous chapter 5, we also propose a new combined spectral-space domain approach in Section 6.3. In this approach, all integrations in the transverse x, y coordinates are done numerically with the space domain mixed potential formalism, while all z integrations involve the dyadic part of the formulation and are done completely in closed form in the spectral domain. This newly developed analytical part of the evaluation is worked out completely in Section 6.4. Further details on how the inverse Fourier transform and any remaining space domain integrals are actually performed are postponed to the next Chapter 7.

6.2 Evaluation of Reaction Integrals

Application of the method of moments as described in Section 3.5.1 of Chapter 3 transforms the integral equation into a matrix equation of which the matrix elements are "reaction integrals" as in Section 2.9.1 of the type

$$Z_{mn} = -\frac{\int\limits_{S_m} \vec{J}_m.\vec{E}_m(\vec{J}_n)\ \mathrm{d}S}{I_m I_n} \tag{6.1}$$

which is the mathematical description of the electromagnetic coupling from a source current $\vec{J}_n$ to an observation current $\vec{J}_m$. The efficiency and accuracy of this computation is roughly determined by three factors

- The field formulation,
- Spectral or space domain evaluation of the integrals,
- The geometry of the problem.

The Field Formulation. The expressions for the field $\vec{E}_m(\vec{J}_n)$ for a planar stratified medium were discussed in Chapter 5, and can be written in a dyadic form as in Equation 5.72, in mixed potential form as in Equation (5.73), or in the hybrid form of Equation (5.134). For an extended "source" current distribution $\vec{J}_n$, all formulations lead to integrals of the type

$$\int\limits_{S_m} \vec{J}_m(\vec{r}).\int\limits_{S_n} \overline{G}(\vec{r},\vec{r}').\vec{J}_n(\vec{r}')\ \mathrm{d}S'\ \mathrm{d}S \tag{6.2}$$

such that the double surface integration over S_m and S_n requires to evaluate a four-fold integral.

Spectral and Space Domain Evaluation. In the layered medium, the components of the Green's functions are obtained via the Spectral Domain Approach (SDA). The scalar expressions that have to be evaluated in the above Equation (6.2) are integrals of the type

$$\int\limits_{S_m} f_m(x,y,z) \int\limits_{S_n} \iint\limits_{-\infty}^{+\infty} \widetilde{G}(k_x,k_y,z,z') e^{-jk_x(x-x')} e^{-jk_y(y-y')}\ \mathrm{d}k_x \mathrm{d}k_y\ \ f_n(x',y',z')\ \mathrm{d}S' \mathrm{d}S. \tag{6.3}$$

The double spectral integration over k_x, k_y makes the total integral a six-fold one. The sequence of evaluation as given in Equation (6.3) is called a space domain evaluation

of the reaction integral. If the coordinate dependence of the test and basis functions is separable as

$$f(x,y,z) = h(x,y)\ v(z) \tag{6.4}$$

the integrations in the transverse x, y plane can brought inside of the spectral integral to obtain

$$\int_z v_m(z) \int_{z'} \iint_{-\infty}^{+\infty} \widetilde{h}_m(k_x,k_y)\widetilde{G}(k_x,k_y,z,z')\widetilde{h}_n^*(k_x,k_y)\ \mathrm{d}k_x\mathrm{d}k_y\ \ v_n(z')\ \mathrm{d}z'\mathrm{d}z \tag{6.5}$$

where $\widetilde{h}_m(k_x,k_y)$ and $\widetilde{h}_n(k_x,k_y)$ are the Fourier transforms of the transverse parts of the test and expansion functions. This part of the reaction integral is now evaluated in the spectral domain.

The Geometry is perhaps the strongest factor influencing the method of evaluation for Z_{mn}.

For the simple 2D or planar geometry of Figure 5.8, the coordinate dependence of the test and expansion functions is separable because they are located at fixed z_m, z_n positions such that $v_m(z) = \delta(z - z_m)$, $v_n(z') = \delta(z' - z_n)$. In this case, the remaining spatial integrations have to be performed only for a limited number of combinations z_m, z_n which are treated as parameters in the computations, and the remaining surface integrations are essentially two-dimensional in x, y or ρ, ϕ. In a spectral domain EFIE approach, the integrals reduce to

$$\iint_{-\infty}^{+\infty} \widetilde{h}_m(k_x,k_y)\widetilde{G}(k_x,k_y,z_m,z_n)\widetilde{h}_n^*(k_x,k_y)\ \mathrm{d}k_x\mathrm{d}k_y. \tag{6.6}$$

This approach has been applied to analyse simple essentially 1D problems like transmission line cross sections [166], [164], [167], [168], [165], [169], [170], [218] and linear printed dipole antennas [251]. Extension to 2D structures was carried out to analyse microstrip antennas [252] and printed circuits [213], [253]. The Fourier transforms of simple linear basis functions on rectangular or triangular domains can be done in closed form [254], [255]. The integrals are evaluated by a double numerical procedure in the k_x, k_y domain [256] or can be transformed into a k_ρ, ϕ coordinate system [257], [258]. The $1/R^3$ hypersingularity problem translates into a slow decay of the spectral dyadic Green's function as a function of k_x, k_y or k_ρ. In the spectral domain approach, this slow decay is accelerated by multiplication with the Fourier transforms of the basis functions [259]. The convergence can be accelerated further by a special analytical treatment of the spectral asymptotes [258], [238], [260], [261]. In a space domain EFIE approach, the integrals typically reduce to

$$\int_{S_m} h_m(x,y) \int_{S_n} \left\{ \begin{array}{c} 1 \\ \cos\phi \\ \sin\phi \end{array} \right\} \int_0^{+\infty} \widetilde{G}(k_\rho,z_m,z_n) \left\{ \begin{array}{c} J_0(\rho k_\rho) \\ J_1(\rho k_\rho) \\ J_2(\rho k_\rho) \end{array} \right\}\ k_\rho \mathrm{d}k_\rho\ \ h_n(x',y')\ \mathrm{d}S'\mathrm{d}S. \tag{6.7}$$

as it has been used for 1D problems in [262], [263], [217],[204] and more complicated 2D problems in [205], [206], [207]. The angular ϕ dependence is separated analytically by Equations (5.66), (5.67), (5.68), (5.69) and (5.70) of Chapter 5, while the remaining one-dimensional higher order Sommerfeld integrals have to be done numerically. Care has to be exercised with the correct treatment of the $1/R^3$ singularity in the integrations for which the necessary more complicated formulas have to be developed [207], [264]. In a space domain MPIE approach, the angular ϕ dependence and the hypersingular behaviour can be avoided by a physical interpretation of spatial derivatives. In this case, the integrals simplify to

$$\int\limits_{S_m} h_m(x,y) \int\limits_{S_n} \int\limits_{0}^{+\infty} \widetilde{G}(k_\rho, z_m, z_n) J_0(\rho k_\rho)\ k_\rho \mathrm{d}k_\rho\ \ h_n(x',y')\ \mathrm{d}S' \mathrm{d}S \tag{6.8}$$

were only lowest order Sommerfeld integrals are required. This approach has found widespread use especially to model arbitrarily shaped printed 2D planar microstrip structures [190], [225], [214], [215] for which it is superior to the Spectral Domain Approach [265]. The remaining basic $1/R$ singularity is still treated with asymptotic analytical techniques. In all of these cases, the slow asymptotic spectral decay or the corresponding spatial singular behaviour is extracted in closed form and treated further analytically, such that the distinction between a spectral or a space domain approach is primarily situated in the remaining numerical evaluation of the reaction integrals [259], [257].

For a general 3D structure as the one of Figure 5.10, where the current test and expansion functions can have arbitrary orientation, the z coordinate dependence is in general not separable, and a spectral domain approach is then not possible. A space domain evaluation of the form (6.3) has to be performed. The complete 3D dyadic formulation has been used in [244], [266], and implemented in Zeland Sofware IE3D, while the MPIE formulation C is very popular [267], [268], and used in EMSS FEKO. However, from the explicit expressions Equations (5.72) and (5.73) of Chapter 5, we see that for a completely 3D case, both formulations contain an angular ϕ dependence and higher order Sommerfeld integrals. Apart from this, the currents are now also distributed in a continuous manner over all z, z' positions. In this case, the spatial domain expressions for all Green's function components have to be tabulated not only as a function of ρ, but also as a function of z and z', The surface integrations are performed completely numerically by interpolation from this precalculated data base. Special care has to be exercised in the numerical integration, as some Green's function components can be discontinuous across the interface between different dielectric layers [191], [249]. This approach is computationally very expensive.

For the 2.5D and "quasi 3D" structures of Figures 5.9 and 5.11 of Chapter 5, the z coordinate is separable from the transverse x, y dependence provided that the current on the vertical surfaces is decomposed into horizontal and vertical components and expanded with only rectangular rooftop functions. In many cases, the separability is not really used and the z, z' integrals continue to be evaluated in a purely numerical

manner combined with a spectral domain approach as in Equation (6.5) for the transverse integrations as in [236], [237], [269], or with a space domain approach as in [239], [247], [248], [249], [246] which is thus actually the same method as for a completely 3D structure as given in Equation (6.3). However, it becomes possible to perform the z, z' integrations analytically by moving them also inside of the integration in the spectral domain, which can be an inverse Fourier transform in case of a horizontal space domain approach as in Equation (6.3)

$$\int_{S_m} h_m(x,y) \int_{S_n} \mathfrak{F}^{-1} \left\{ \int_z v_m(z) \int_{z'} \widetilde{G}(k_\rho, z, z') \; v_n(z') \; \mathrm{d}z' \mathrm{d}z \right\} h_n(x',y') \; \mathrm{d}S' \; \mathrm{d}S \qquad (6.9)$$

as in [240], [250], [184], or a spectral domain evaluation of the transverse integrals as in Equation (6.5)

$$\iint_{-\infty}^{+\infty} \widetilde{h}_m(k_x,k_y) \int_z v_m(z) \int_{z'} \widetilde{G}(k_x,k_y,z,z') v_n(z') \; \mathrm{d}z' \mathrm{d}z \;\; \widetilde{h}_n^*(k_x,k_y) \; \mathrm{d}k_x \mathrm{d}k_y \qquad (6.10)$$

as in [235], [241]. These approaches are however limited to only a constant vertical current in a single layered medium as in [235], [241], [240] or both current components but only in a two layered medium [250], [184], where the expressions for the Green's functions are still relatively simple.

6.3 Combined Spectral-Space Domain Approach

In this work, we perform all z, z' dependent integrals in closed form in the spectral domain, while all transverse integrations use the space domain formalism. The approach is combined with newly developed hybrid dyadic-mixed potential field formulation of Chapter 5. The analytical integrations are based on the derivative relations (Section 4.11) and factorisation (Section 4.9) of the Green's functions, valid for an arbitrary number of layers in the medium. The analytical integrations will reduce the spectral asymptotic and spatial singular behaviour of the dyadic part of the formulation, while in the space domain part of the solution, the transfer of derivatives to the test and expansion functions reduces the spatial singularity to be integrated. In this newly developed combined spectral-space domain, the spectral domain closed form evaluation of the dyadic parts, numerical inverse Fourier transform and space domain mixed potential evaluation are interleaved depending on the type of electromagnetic coupling, determined by the direction of fields and currents as worked out completely below. In this way, not only the field formulation, but also the evaluation of the reaction integrals is matched to the "quasi 3D" geometry in a planar stratified medium.

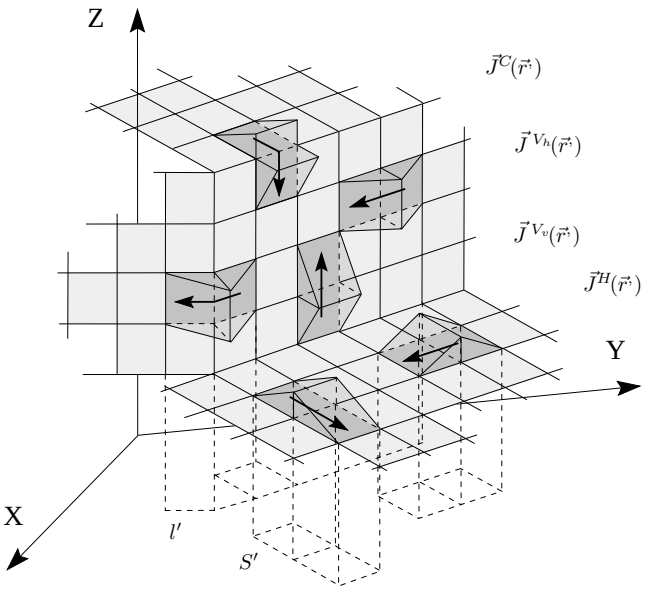

Figure 6.1: Expansion of the surface current on a "quasi 3D" structure with rooftop expansion functions. The current on a vertical surface is decomposed into its horizontal and vertical components.

6.3.1 Discretisation of the Current

The different types of expansion functions that can occur in a "quasi 3D" structure are depicted in Figure 6.1. The electric current on a horizontal conductor $\vec{J}^H(\vec{r})$ is expanded using standard rooftop or RWG basis functions defined over a rectangular or triangular support as defined already in Chapter 3 and denoted as

$$\vec{J}^H(\vec{r}) = \vec{\Delta}(x', y')\delta(z' - z_n) \tag{6.11}$$

$$\nabla'.\ \vec{J}^H(\vec{r}) = \Pi(x', y')\delta(z' - z_n) \tag{6.12}$$

where in our mind's eye, the notation Δ recalls the linear behaviour, and Π the constant behaviour of these functions as a function of the transverse coordinates x', y' over the supporting domain S', while the z_n coordinate remains fixed. The line charge at the edge where the rooftop function reaches unity will be taken up further in the process of evaluating the reaction integrals. The current distribution on a vertical conductor $\vec{J}^V(\vec{r})$ is decomposed into its horizontal and vertical components

$$\vec{J}^V(\vec{r}) = \vec{J}^{V_v}(\vec{r}) + \vec{J}^{V_h}(\vec{r}) \tag{6.13}$$

which will both be expanded using only rectangular rooftop functions, such that the x', y' and z' coordinate dependence become separable

$$\vec{J}^{V_v}(\vec{r}) = \Pi(x', y')\vec{\Delta}(z') \tag{6.14}$$

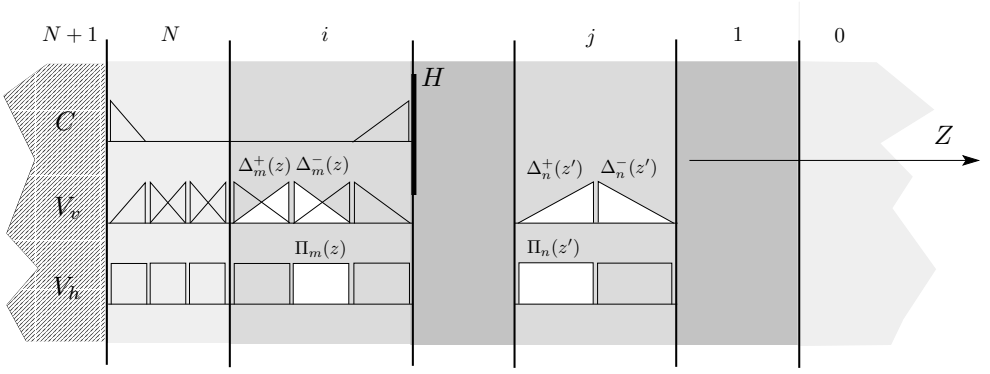

Figure 6.2: Discretisation of the current along the Z axis for analytical evaluation of the z, z' dependent part of the reaction integrals.

$$\vec{J}^{V_h}(\vec{r}) \quad = \quad \vec{\Delta}(x', y')\Pi(z') \tag{6.15}$$

where x', y' now runs over the line segment l' as depicted in Figure 6.1. To let horizontal and vertical surfaces connect or intersect each other, we also introduce "connections" $\vec{J}^C(\vec{r})$ which are rooftops functions defined partly over a horizontal and partly over a vertical segment. These connecting currents need not be considered separately, since the formulas can be obtained by combining those of the horizontal and vertical currents in the appropriate manner.

The subdomains S', l' in the X, Y plane can in principle have arbitrary location. The analytical and numerical techniques to evaluate the transverse x, y parts of the reaction integrals as will be given in Chapter 7 can handle such a configuration. However, the discretisation along the Z axis is more restricted, because the z, z' dependent part of the reaction integrals will be done completely analytically. Figure 6.2 shows the conventions. The interfaces between the different layers of the medium automatically create borders for the segmentation along the Z axis. Each layer has an integer number of segments. In this way it is ensured that the test and basis functions either overlap perfectly along the Z axis or do not overlap at all, which facilitates the analytical evaluation. In this way also, contributions to the field when a basisfunction crosses an interface are also incorporated automatically when the $Z_{m^{\pm}n^{\pm}}$ are added together.

6.3.2 Overview of Types of Reaction Integrals

The resulting Method of Moments (MoM) "impedance" or "coupling" matrix Z can now be partitioned into several blocks as depicted in Figure 6.3, according to whether the test and expansion functions are located on a horizontal conductor (indicated with H symbol), on a vertical surface (V), or partly on both for the "cornered"

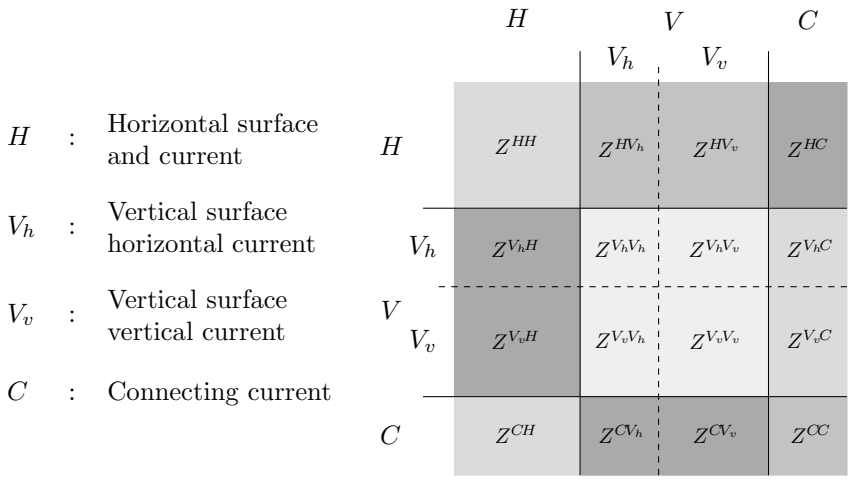

Figure 6.3: Partitioning of the Method of Moments (MoM) "impedance" or "coupling" matrix according to location on the surface and orientation of test or "observation" functions and expansion or "source" functions.

(C) expansion functions. The currents on the vertical surface are further cataloged depending on their orientation which can still be horizontal (V_h) or vertical (V_v). The test or "observation" functions are traced through the rows of Z, and the expansion or "source" functions can be found in the columns of Z. All elements of a particular block are evaluated using the same fixed formula. All possible formulas to fill the blocks Z^{HH}, Z^{VV}, Z^{HV} and Z^{VH} are now discussed in full detail. The formulas to evaluate the elements of the block matrices involving "cornered" expansion functions Z^{CC}, Z^{HC}, Z^{VC} and their reciprocal counterparts Z^{CH}, Z^{CV} are obtained by combinations of the formulas presented below.

Each matrix elements Z_{mn} is composed of four contributions $Z_{m^{\pm}n^{\pm}}$ as already defined in Chapter 3. Each contribution refers to the coupling between the half rooftop functions $\vec{J}_m^{\pm}$, $\vec{J}_n^{\pm}$ flowing on the parts $S_m^{\pm}$, $S_n^{\pm}$ of the total surfaces S_m, S_n as defined in Figures (3.11), (3.12) and (3.13) of Chapter 3. For a horizontal rooftop on a horizontal surface $\vec{J}_n^H$, l_n is the common edge of S_n^+ and S_n^- as depicted in Figure 6.4. For a horizontal rooftop on a vertical surface $\vec{J}_n^{V_h}$, the projections of $S_n^{\pm}$ in the X, Y plane are denoted as $l_n^{\pm}$ as depicted in Figure 6.6. For a vertical oriented current on a vertical surface $\vec{J}_n^{V_v}$, these projections coincide and the edge is again referenced as l_n and depicted in Figure 6.5.

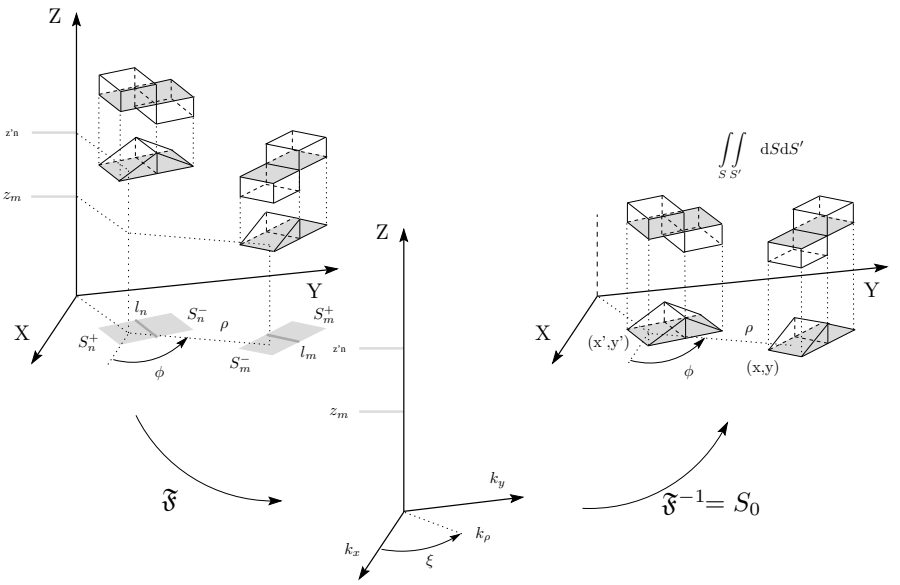

Figure 6.4: Space domain evaluation of Z_{mn}^{HH} for two horizontal currents on a horizontal surface. The Green's functions are constructed via the spectral domain, where the z-separation enters as a parameter.

6.3.3 Space Domain Evaluation of Z_{mn}^{HH}

The space domain MPIE formulation that relates the transverse field $\vec{E}_{it}$ in a layer i to the transverse current $\vec{J}_n^{\pm}$ located in layer j was already obtained in Equation (5.134) of Chapter 5, but here we also need to take into account the field generated by the line charges at the the edge l_n of the surface $S_n^{\pm}$

$$\vec{E}_{it} = -j\omega \int\limits_{S_n^{\pm}} S_0 \left\{ \frac{\widetilde{V}_{ij}^{I^{TE}}}{-j\omega} \right\} \vec{\Delta}_n^{\pm} \, \mathrm{d}S' - \nabla_t \int\limits_{S_n^{\pm}} S_0 \left\{ j\omega \frac{\widetilde{V}_{ij}^{I^{TE}} - \widetilde{V}_{ij}^{I^{TM}}}{k_\rho^2} \right\} \left(\frac{\pm \Pi_n}{-j\omega} \right) \, \mathrm{d}S'$$
$$- \nabla_t \int\limits_{l_n} S_0 \left\{ j\omega \frac{\widetilde{V}_{ij}^{I^{TE}} - \widetilde{V}_{ij}^{I^{TM}}}{k_\rho^2} \right\} \left(\frac{-\vec{n}'.\vec{\Delta}_n^{\pm}}{-j\omega} \right) \, \mathrm{d}l' \qquad (6.16)$$

as in Equation (3.47). Upon inserting this into Equation (6.1), we obtain

$$Z_{m^{\pm}n^{\pm}}^{HH} = -j\omega \int\limits_{S_m^{\pm}} \vec{\Delta}_m^{\pm}(x,y). \int\limits_{S_n^{\pm}} S_0 \left\{ \frac{\widetilde{V}_{ij}^{I^{TE}}}{-j\omega} \right\} \vec{\Delta}_n^{\pm}(x',y') \, \mathrm{d}S' \mathrm{d}S$$
$$-j\omega \int\limits_{S_m^{\pm}} \left(\frac{\pm \Pi_m(x,y)}{-j\omega} \right) \int\limits_{S_n^{\pm}} S_0 \left\{ j\omega \frac{\widetilde{V}_{ij}^{I^{TE}} - \widetilde{V}_{ij}^{I^{TM}}}{k_\rho^2} \right\} \left(\frac{\pm \Pi_n(x',y')}{-j\omega} \right) \, \mathrm{d}S' \mathrm{d}S$$

$$-j\omega\int\limits_{l_m}\left(\frac{-\vec{n}.\vec{\Delta}_m^{\pm}(x,y)}{-j\omega}\right)\int\limits_{S_n^{\pm}}S_0\left\{j\omega\frac{\widetilde{V}_{ij}^{I^{TE}}-\widetilde{V}_{ij}^{I^{TM}}}{k_\rho^2}\right\}\left(\frac{\pm\Pi_n(x',y')}{-j\omega}\right)\,\mathrm{d}S'\mathrm{d}l$$

$$-j\omega\int\limits_{l_m}\left(\frac{-\vec{n}.\vec{\Delta}_m^{\pm}(x,y)}{-j\omega}\right)\int\limits_{l_n}S_0\left\{j\omega\frac{\widetilde{V}_{ij}^{I^{TE}}-\widetilde{V}_{ij}^{I^{TM}}}{k_\rho^2}\right\}\left(\frac{-\vec{n}'.\vec{\Delta}_n^{\pm}(x',y')}{-j\omega}\right)\,\mathrm{d}l'\mathrm{d}l$$

$$-j\omega\int\limits_{S_m^{\pm}}\left(\frac{\pm\Pi_m(x,y)}{-j\omega}\right)\int\limits_{l_n}S_0\left\{j\omega\frac{\widetilde{V}_{ij}^{I^{TE}}-\widetilde{V}_{ij}^{I^{TM}}}{k_\rho^2}\right\}\left(\frac{-\vec{n}'.\vec{\Delta}_n^{\pm}(x',y')}{-j\omega}\right)\,\mathrm{d}l'\mathrm{d}S \quad (6.17)$$

similar to Equation (3.48) of Chapter 3. The first term is electromagnetic coupling between the currents. The second term couples the electric charges. The third and fourth term normally vanish when two observation horizontal half rooftops are combined together, while the the last two terms vanish when two source horizontal half rooftops are combined together. However, when the half rooftop functions are part of "cornered" connection rooftop functions as depicted in Figure 6.8 of Section 6.3.6, the contribution of the line charges has to be taken into account. It will be explained there how because of the nature of the arising integrals, the third term is then evaluated together with Equation (6.24) for $Z_{mn}^{V_vH}$ of Section 6.3.5, the fourth term is brought over to Equation (6.19) for $Z_{mn}^{V_vV_v}$ of Section 6.3.4, while the last term is transferred to Equation (6.22) for $Z_{mn}^{HV_v}$ of Section 6.3.5. The space domain approach is evident from the sequence of operations in Equation (6.17). The Green's functions are first computed in the spectral domain in which the z,z'-separation $\Delta = |z-z'|$ enters the computation as a parameter. After the inverse Fourier transform to the space domain, the evaluation of the surface integrals is essentially two-dimensional in the transverse x,y coordinates and takes place as described in Section 7.3 of the next Chapter. Using the results of Section 5.8.1 of Chapter 5, we see that a worst case $e^{-k_\rho\Delta}/k_\rho$ spectral asymptotic and a basic $1/R$ spatial singular behaviour has to be integrated. The block matrix Z^{HH} of the total MoM Z matrix of Figure 6.3 can now be filled.

6.3.4 Combined Spectral-Space Domain Evaluation of $Z_{mn}^{V_vV_v}$, $Z_{mn}^{V_hV_h}$

The evaluation of Equation (6.1) for two vertical currents $\vec{J}_m$, $\vec{J}_n$ could be done with a space domain approach as

$$Z_{m^{\pm}n^{\pm}}^{V_vV_v} = \int\limits_{S_m^{\pm}}\Pi_m(x,y)\vec{\Delta}_m^{\pm}(z).\int\limits_{S_n^{\pm}}S_0\left\{k_\rho^2\frac{\widetilde{V}_{ij}^{I^{TM}}}{j\omega\epsilon_i j\omega\epsilon_j}\right\}\Pi_n(x',y')\vec{\Delta}_n^{\pm}(z')\,\mathrm{d}S'\mathrm{d}S \quad (6.18)$$

but the numerical inverse Fourier transform would be difficult, since we know from Section 5.8.1 of Chapter 5 that a $k_\rho e^{-k_\rho\Delta}$ spectral asymptotic behaviour has to be

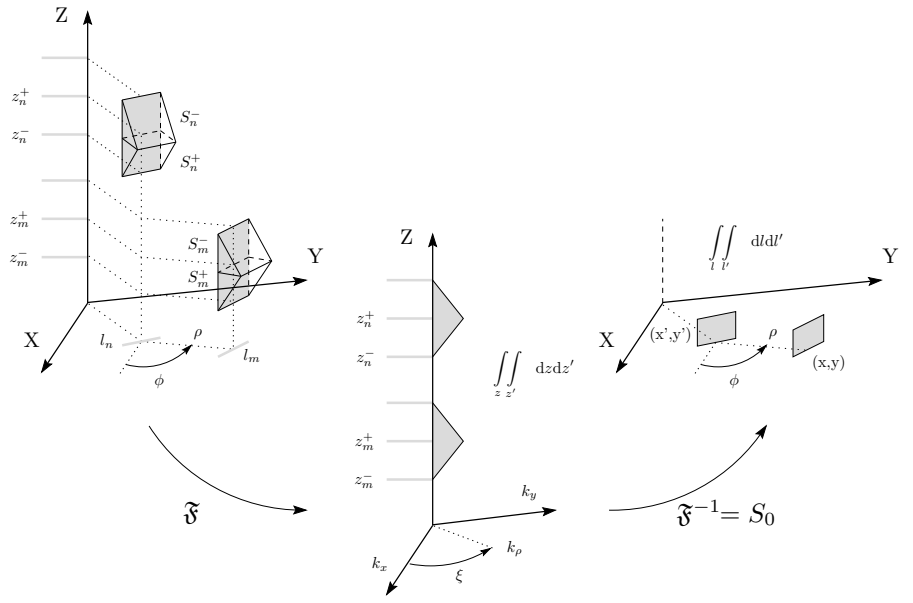

Figure 6.5: Combined spectral-space domain evaluation of $Z_{mn}^{V_vV_v}$ for two vertical currents flowing on a vertical surface. The z, z' dependent parts of the reaction integrals are evaluated in closed form in the spectral domain, and the remaining ρ integration is performed in the space domain after the inverse Fourier transform.

extracted, and a $1/R^3$ spatial singularity has to be integrated. We therefore bring the z, z' dependent part of the surface integrals "inside" of the inverse Fourier transform

$$Z_{m^\pm n^\pm}^{V_vV_v} = \int_{l_m} \Pi_m(x,y) \int_{l_n} S_0 \left\{ \int_{z_m^-}^{z_m^+} \Delta_m^\pm(z) \int_{z_n^-}^{z_n^+} k_\rho^2 \frac{\widetilde{V}_{ij}^{I^{TE}}}{j\omega\epsilon_i j\omega\epsilon_j} \Delta_n^\pm(z')\ \mathrm{d}z'\mathrm{d}z \right\} \Pi_n(x',y')\ \mathrm{d}l'\mathrm{d}l \tag{6.19}$$

where l_m, l_n are the projections of the surfaces $S_m^\pm$, $S_n^\pm$ on the X, Y plane. The z, z' integration of the Green's function with the linear functions $\Delta_m^\pm(z)$, $\Delta_n^\pm(z')$ can be done analytically as worked out in Section 6.4.7. By evaluating these formulas in the spectral domain, the spectral asymptotic behaviour is abated to a worst case e^{-k_ρ}/k_ρ^2, such that only a remaining $\ln R$ has to dealt with when evaluating the line integrals in the space domain. The sequence of operations is depicted in Figure 6.5. The approach is called a combined spectral-space domain approach, since the reaction integrals are evaluated partly in the spectral domain, and partly in the space domain.

The previous technique is applied for all z, z' dependent integrals. When two horizontal currents flow on a vertical surface as depicted in Figure 6.6, the z, z' integrations

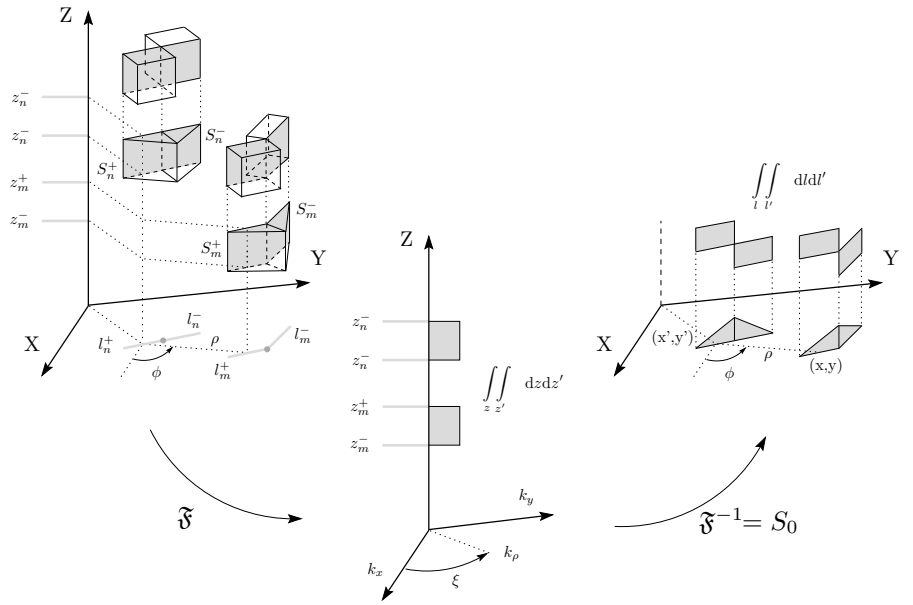

Figure 6.6: The combined spectral-space domain approach is applied for all z, z' dependent parts, as for the matrix elements $Z_{mn}^{V_hV_h}$ describing coupling between two horizontal currents flowing on a vertical surface.

of Equation (6.17) can again be shifted "inside" of the inverse Fourier transform as

$$Z_{m^\pm n^\pm}^{V_hV_h} = -j\omega \int_{l_m^\pm} \vec{\Delta}_m^\pm . \int_{l_n^\pm} S_0 \left\{ \int_{z_m^-}^{z_m^+} \Pi_m \int_{z_n^-}^{z_n^+} \frac{\widetilde{V}_{ij}^{I^{TE}}}{-j\omega} \Pi_n \, \mathrm{d}z'\mathrm{d}z \right\} \vec{\Delta}_n^\pm \, \mathrm{d}l'\mathrm{d}l$$
$$-j\omega \int_{l_m^\pm} \left(\frac{\pm\Pi_m}{-j\omega} \right) \int_{l_n^\pm} S_0 \left\{ \int_{z_m^-}^{z_m^+} \Pi_m \int_{z_n^-}^{z_n^+} \frac{\widetilde{V}_{ij}^{I^{TE}} - \widetilde{V}_{ij}^{I^{TM}}}{k_\rho^2} \Pi_n \, \mathrm{d}z'\mathrm{d}z \right\} \left(\frac{\pm\Pi_n}{-j\omega} \right) \, \mathrm{d}l'\mathrm{d}l. \quad (6.20)$$

The line charges now never give a contribution, since no half rooftops are ever associated with a horizontal current on a vertical surface. The analytical integrations can be done with the formulas of Section 6.4.5.

6.3.5 The Cross-Coupling Terms $Z_{mn}^{HV_v}$, $Z_{mn}^{V_vH}$

When Equation (6.1) has to be evaluated for the case of a horizontal observation current $\vec{J}_m$ and a vertical source current $\vec{J}_n$ as depicted in Figure 6.7, we insert

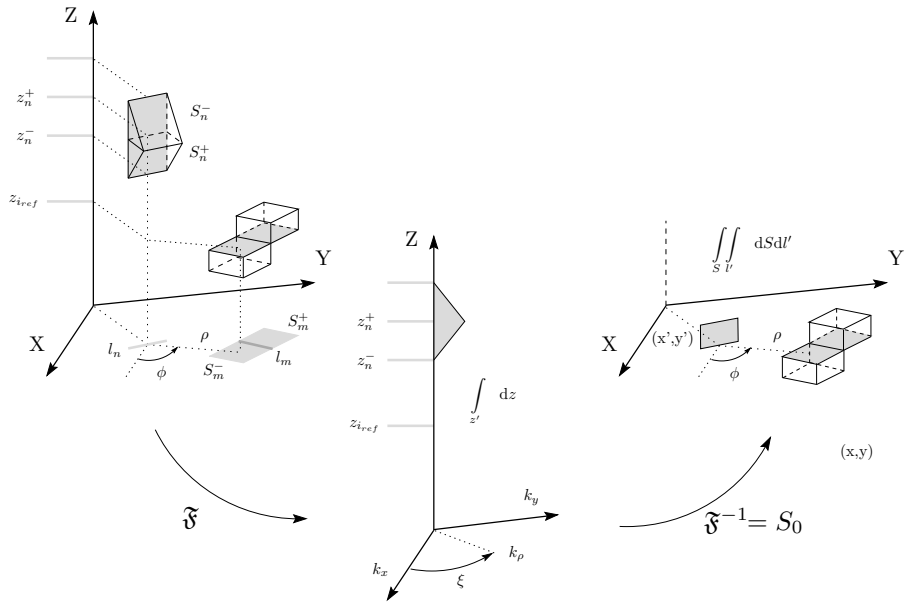

Figure 6.7: Combined spectral-space domain evaluation of the cross-coupling term $Z_{mn}^{HV_v}$ from a vertical current on a vertical surface to a horizontal current on a horizontal surface.

Equation (5.134) of Chapter 5 into Equation (6.1)

$$Z_{m^{\pm}n^{\pm}}^{HV_v} = \int\limits_{S_m^{\pm}} \vec{\Delta}_m^{\pm}(x,y).\nabla_t \int\limits_{S_n^{\pm}} S_0 \left\{ \frac{\widetilde{V}_{ij}^{V^{TM}}}{\epsilon_j} \right\} \Pi_n(x',y') \Delta_n^{\pm}(z')\ \mathrm{d}S'\mathrm{d}S \quad (6.21)$$

and combine the techniques from the previous cases. The singular behaviour of the Green's function is circumvented by transferring the transverse derivative ∇_t to the observation current $\Delta_m^{\pm}$ in a partial integration, and an additional closed form integration in the spectral domain to obtain

$$\begin{aligned} Z_{m^{\pm}n^{\pm}}^{HV_v} = &- \int\limits_{S_m^{\pm}} \left(\frac{\pm\Pi_m(x,y)}{-j\omega} \right) \int\limits_{l_n} S_0 \left\{ \int\limits_{z_n^-}^{z_n^+} \frac{\widetilde{V}_{ij}^{V^{TM}}}{\epsilon_j} \Delta_n^{\pm}(z')\ \mathrm{d}z' \right\} \Pi_n(x',y')\ \mathrm{d}l'\mathrm{d}S \\ &- \int\limits_{l_m} \left(\frac{-\vec{n}.\vec{\Delta}_m^{\pm}(x,y)}{-j\omega} \right) \int\limits_{l_n} S_0 \left\{ \int\limits_{z_n^-}^{z_n^+} \frac{\widetilde{V}_{ij}^{V^{TM}}}{\epsilon_j} \Delta_n^{\pm}(z')\ \mathrm{d}z' \right\} \Pi_n(x',y')\ \mathrm{d}l'\mathrm{d}l. \quad (6.22) \end{aligned}$$

The second term normally vanishes when two horizontal observation half rooftop functions are combined, but it does have to be taken into account in case the half rooftop functions is part of a "cornered" connection rooftop which serves as testing

function. For such a case, the second term is added to Equation (6.19) for $Z_{mn}^{V_vV_v}$ of Section 6.3.4, since there, we already evaluate a double line integral in the space domain.

For the reciprocal coupling from a horizontal source current $\vec{J}_n$ to a vertical observation current $\vec{J}_n$, we start from Equation (5.134) of Chapter 5

$$E_{iz} = \int\limits_{S_m^{\pm}} S_0\left\{\frac{\widetilde{I}_{ij}^{I^{TM}}}{\epsilon_i}\right\}\left(\frac{\pm\Pi_m(x',y')}{-j\omega}\right)\,\mathrm{d}S' + \int\limits_{l_m} S_0\left\{\frac{\widetilde{I}_{ij}^{I^{TM}}}{\epsilon_i}\right\}\left(\frac{-\vec{n}.\vec{\Delta}_n^{\pm}(x',y')}{-j\omega}\right)\,\mathrm{d}l' \quad (6.23)$$

where we now have to take into account the field from the line charge at the edge l_m of $S_m^{\pm}$ which occurs because of the partial integration in the x', y' source coordinates. Inserting this into Equation (6.1) and performing all possible z, z'-integrations analytically as before, we obtain

$$\begin{aligned} Z_{m^{\pm}n^{\pm}}^{V_vH} = &+ \int\limits_{l_m}\Pi_m(x,y)\int\limits_{S_n^{\pm}} S_0\left\{\int\limits_{z_m^-}^{z_m^+}\Delta_m^{\pm}(z)\frac{\widetilde{I}_{ij}^{I^{TM}}}{\epsilon_i}\,\mathrm{d}z\right\}\left(\frac{\pm\Pi_n(x',y')}{-j\omega}\right)\,\mathrm{d}S'\mathrm{d}l \\ &+ \int\limits_{l_m}\Pi_m(x,y)\int\limits_{l_n} S_0\left\{\int\limits_{z_m^-}^{z_m^+}\Delta_m^{\pm}(z)\frac{\widetilde{I}_{ij}^{I^{TM}}}{\epsilon_i}\,\mathrm{d}z\right\}\left(\frac{-\vec{n}.\vec{\Delta}_n^{\pm}(x',y')}{-j\omega}\right)\,\mathrm{d}l'\mathrm{d}l. \quad (6.24) \end{aligned}$$

As before, the second term vanishes when two horizontal source half rooftop functions are combined, but it gives a contribution when the half rooftop is part of a "cornered" connection rooftop function which serves as the source function. In that case, the second term is also added to Equation (6.19) for $Z_{mn}^{V_vV_v}$ of Section 6.3.4, where the same type of double line integral is already evaluated.

The z and z' integrals in Equations (6.22), (6.24) are performed analytically in Section 6.4.3.

6.3.6 Treatment of the Line Charge Contributions

Now that the necessary formulas are available, we focus on the treatment of the field contributions from the line charges as they first appeared in Section 6.3.3. We will give a detailed explanation of the treatment only for the line charge terms of Equation (6.17), as the essential features can be most easily derived from this case. A similar line of reasoning can be applied for all other cases.

In Equation (6.17) we had to consider the case that half a rooftop function is not always combined with its companion to constitute a "complete" expansion function for a horizontal current as in Figure 6.4, but can also appear by itself when it is a part of a "cornered" connection rooftop which describes the flow of current from the

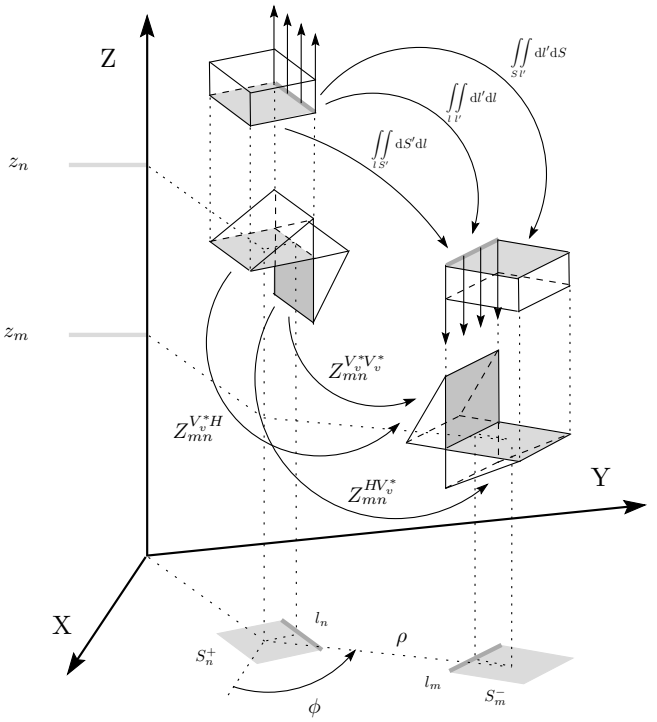

Figure 6.8: The field contributions due to line charges occurring by considering only "half" rooftop functions can be taken into account by absorbing their contribution in the "regular" formulas to obtain $Z_{mn}^{V_v^* H}$, $Z_{mn}^{V_v^* V_v^*}$ and $Z_{mn}^{H V_v^*}$.

horizontal surface over the connecting edge to a vertical surface as depicted in Figure 6.8. The third term of Equation (6.17) for $Z_{m^{\pm}n^{\pm}}^{HH}$ is the field of the source surface charge $\Pi_n/(-j\omega)$ which couples with the observation line charge $-\vec{n}.\vec{\Delta}_m^{\pm}/(-j\omega)$ and has to be taken into account. This observation line charge only occurs when the horizontal observation half rooftop is "connected" with half a vertical rooftop function, and it is in the evaluation of the first term of Equation (6.24) for $Z_{m^{\pm}n^{\pm}}^{V_v H}$ from the source charge to this vertical half rooftop that the same type of integral is already evaluated. We therefore don't evaluate the third term of Equation (6.17) for $Z_{m^{\mp}n^{\pm}}^{HH}$ separately there, but include it in Equation (6.24) for $Z_{m^{\pm}n^{\pm}}^{V_v H}$ to give

$$Z_{m^{\pm}n^{\pm}}^{V_v^* H} = + \int_{l_m} \Pi_m(x,y) \int_{S_n^{\pm}} S_0 \left\{ \int_{z_m^-}^{z_m^+} \Delta_m^{\pm}(z) \frac{\widetilde{I}_{ij}^{I^{TM}}(z,z_n)}{\epsilon_i} \,\mathrm{d}z \right.$$
$$\left. + (\mp 1_m) j\omega \frac{\widetilde{V}_{ij}^{I^{TE}}(z_m^{\pm},z_n) - \widetilde{V}_{ij}^{I^{TM}}(z_m^{\pm},z_n)}{k_\rho^2} \right\} \left(\frac{\pm \Pi_n(x',y')}{-j\omega} \right) \,\mathrm{d}S'\mathrm{d}l \quad (6.25)$$

where $\mp 1_m$ is just the sign of the line charge $-\vec{n}.\vec{\Delta}_m^{\pm}$. The addition in the spectral domain is not just a useful shift, but is strictly required. The closed form formulas of Section 6.4.2 for the integral in the spectral domain, will give a non integrable singularity for the line integral over l_m in the space domain. In Section 6.4.8, it will be shown that this field contribution from the line charge of half the vertical rooftop will be compensated by the line charge of half the horizontal rooftop. A similar line of reasoning leads to the inclusion of the line-line charge interaction fourth term of Equation (6.17) for $Z_{m^{\mp}n^{\mp}}^{HH}$ into Equation (6.19) for $Z_{m^{\pm}n^{\pm}}^{V_vV_v}$

$$Z_{m^{\pm}n^{\pm}}^{V_v^*V_v^*} = \int_{l_m} \Pi_m(x,y) \int_{l_n} S_0 \left\{ \int_{z_m^-}^{z_m^+} \Delta_m^{\pm}(z) \int_{z_n^-}^{z_n^+} k_\rho^2 \frac{\widetilde{V}_{ij}^{I^{TM}}(z,z')}{j\omega\epsilon_i j\omega\epsilon_j} \Delta_n^{\pm}(z') \, \mathrm{d}z'\mathrm{d}z \right.$$
$$\left. + (\mp 1_m)(\mp 1_n) \frac{\widetilde{V}_{ij}^{I^{TE}}(z_m,z_n) - \widetilde{V}_{ij}^{I^{TM}}(z_m,z_n)}{k_\rho^2} \right\} \Pi_n(x',y') \, \mathrm{d}l'\mathrm{d}l \quad (6.26)$$

where $\mp 1_m$, $\mp 1_n$ are the signs of the line charges $-\vec{n}.\vec{\Delta}_m^{\pm}$ and $-\vec{n}'.\vec{\Delta}_n^{\pm}$. Finally, incorporating the line charge to surface charge last term of Equation (6.17) for $Z_{m^{\pm}n^{\mp}}^{HH}$ into Equation (6.22) for $Z_{m^{\pm}n^{\pm}}^{HV_v}$ gives

$$Z_{m^{\pm}n^{\pm}}^{HV_v^*} = -\int_{S_m^{\pm}} \left(\frac{\pm\Pi_m(x,y)}{-j\omega} \right) \int_{l_n} S_0 \left\{ \int_{z_n^-}^{z_n^+} \frac{\widetilde{V}_{ij}^{V^{TM}}(z_m,z')}{\epsilon_j} \Delta_n^{\pm}(z') \, \mathrm{d}z' \right.$$
$$\left. + (\mp 1_n) j\omega \frac{\widetilde{V}_{ij}^{I^{TE}}(z_m,z_n^{\pm}) - \widetilde{V}_{ij}^{I^{TM}}(z_m,z_n^{\pm})}{k_\rho^2} \right\} \Pi_n(x',y') \, \mathrm{d}l'\mathrm{d}S \quad (6.27)$$

with $\mp 1_n$ the sign of the line charge $-\vec{n}'.\vec{\Delta}_n^{\pm}$. The systematic and consistent shifting of line charge contributions to the appropriate formula results in overall symmetrical formulas and therefore the resulting "impedance" Z-matrix will remain totally symmetric.

6.3.7 Remaining Terms for the Vertical Surface $Z_{mn}^{V_hV_v}$, $Z_{mn}^{V_vV_h}$

From Equations (6.22), (6.24) for $Z_{m^{\pm}n^{\pm}}^{HV_v}$, $Z_{m^{\pm}n^{\pm}}^{V_vH}$ which are valid for horizontal currents on horizontal surfaces, we immediately obtain the further refinements in case the horizontal currents flow on a vertical surface. For the case depicted in Figure 6.9, we can start from Equation (6.22). The second line charge contribution now never gives a contribution since a horizontal current on a vertical surface will always be part of a "complete" rooftop expansion function. Exploiting the opportunity to perform

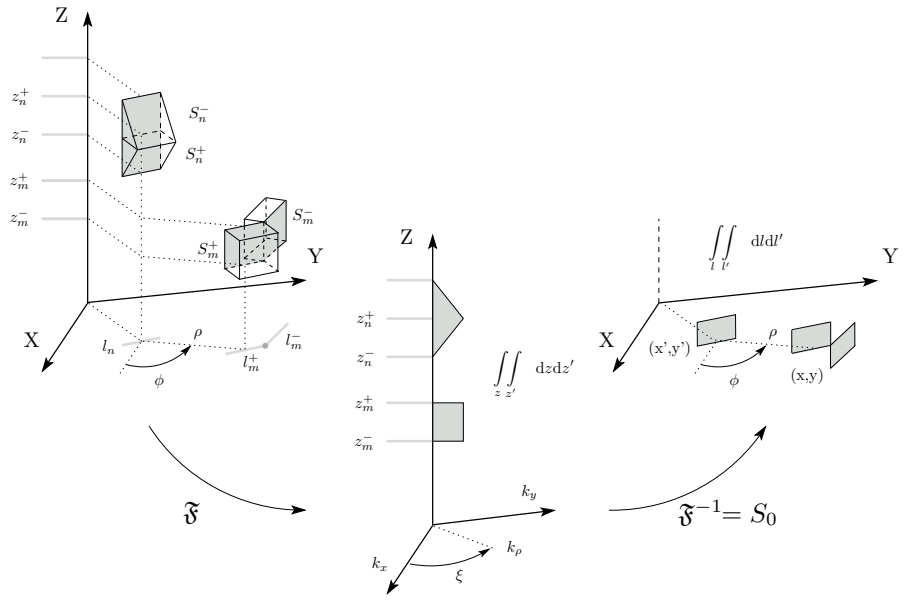

Figure 6.9: Combined spectral-space domain evaluation of the cross-coupling term $Z_{mn}^{V_hV_v}$ from a vertical current to a horizontal current both flowing on a vertical surface.

additional z, z' integrations analytically in the first term gives

$$Z_{m^\pm n^\pm}^{V_hV_v} = \int_{l_m^\pm} \left(\frac{\pm \Pi_m(x,y)}{-j\omega} \right) \int_{l_n} S_0 \left\{ \int_{z_m^-}^{z_m^+} \Pi_m(z) \int_{z_n^-}^{z_n^+} \frac{\widetilde{V}_{ij}^{V^{TM}}}{\epsilon_j} \Delta_n^\pm(z')\ \mathrm{d}z'\mathrm{d}z \right\} \Pi_n(x',y')\ \mathrm{d}l'\mathrm{d}l. \tag{6.28}$$

The reciprocal coupling is derived in a similar manner from Equation (6.24) as

$$Z_{m^\pm n^\pm}^{V_vV_h} = \int_{l_m} \Pi_m(x,y) \int_{l_n^\pm} S_0 \left\{ \int_{z_m^-}^{z_m^+} \Delta_m^\pm(z) \int_{z_n^-}^{z_n^+} \frac{\widetilde{I}_{ij}^{I^{TM}}}{\epsilon_i} \Pi_n(z')\ \mathrm{d}z'\mathrm{d}z \right\} \left(\frac{\pm \Pi_n(x',y')}{-j\omega} \right)\ \mathrm{d}l'\mathrm{d}l. \tag{6.29}$$

The analytical formulas for the z, z' integrals in Equations (6.28), (6.29) are derived in Section 6.4.6. We now have all the tools to fill the block matrix Z^{VV} of the total MoM matrix Z of Figure 6.3.

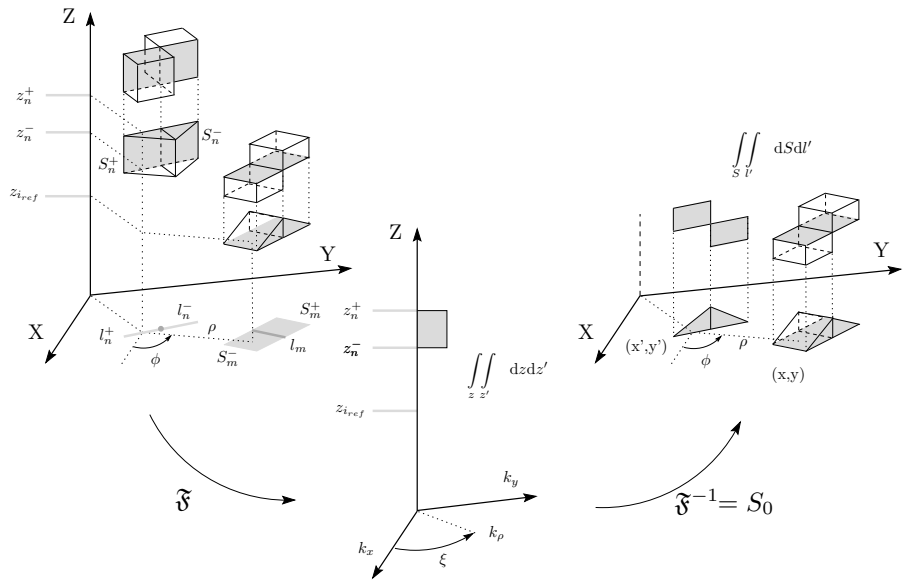

Figure 6.10: Combined spectral-space domain approach for the cross-coupling term $Z_{mn}^{HV_h}$ between two horizontal currents, one of which flows on a vertical and the other on a horizontal surface.

6.3.8 The Remaining Cross-Coupling Formulas for Z^{HV_h}, Z^{V_hH}

The first remaining case is depicted in Figure 6.10, where we consider two horizontal currents, of which the observation current flows on a horizontal surface and can be part of a "cornered" connecting rooftop while the source current flows on a vertical surface and thus always consists of two half rooftops. This means that the the last two terms of Equation (6.17) for $Z_{m^\pm n^\pm}^{HH}$ do not appear, while in the remaining terms, we shift the z, z' integrations "inside" of the inverse Fourier transform as

$$Z_{m^\pm n^\pm}^{HV_h} = -j\omega \int\limits_{S_m^\pm} \vec{\Delta}_m^\pm(x,y). \int\limits_{l_n^\pm} S_0 \left\{ \int\limits_{z_n^-}^{z_n^+} \frac{\widetilde{V}_{ij}^{I^{TE}}}{-j\omega} \Pi_n(z')\ \mathrm{d}z' \right\} \vec{\Delta}_n^\pm(x',y')\ \mathrm{d}l'\mathrm{d}S$$

$$-j\omega \int\limits_{S_m^\pm} \left(\frac{\pm\Pi_m(x,y)}{-j\omega} \right) \int\limits_{l_n^\pm} S_0 \left\{ \int\limits_{z_n^-}^{z_n^+} j\omega \frac{\widetilde{V}_{ij}^{I^{TE}} - \widetilde{V}_{ij}^{I^{TM}}}{k_\rho^2} \Pi_n(z')\ \mathrm{d}z' \right\} \left(\frac{\pm\Pi_n(x',y')}{-j\omega} \right)\ \mathrm{d}l'\mathrm{d}S$$

$$-j\omega \int\limits_{l_m^\pm} \left(\frac{-\vec{n}.\vec{\Delta}_m^\pm}{-j\omega} \right) \int\limits_{l_n^\pm} S_0 \left\{ \int\limits_{z_n^-}^{z_n^+} j\omega \frac{\widetilde{V}_{ij}^{I^{TE}} - \widetilde{V}_{ij}^{I^{TM}}}{k_\rho^2} \Pi_n(z')\ \mathrm{d}z' \right\} \left(\frac{\pm\Pi_n(x',y')}{-j\omega} \right) \mathrm{d}l'\mathrm{d}l. \quad (6.30)$$

The third term of the above equation involves a double line integral in the spatial domain which is already performed to evaluate $Z_{mn}^{V_vV_h}$ Equation (6.29) of Section 6.3.7 and is thus incorporated there.

For the reciprocal coupling depicted from a horizontal current on a horizontal surface or as part of a "cornered" connection to a complete horizontal current on a vertical surface one derives in a similar manner from Equation (6.17) for $Z_{m^{\pm}n^{\pm}}^{HH}$ the specialisation

$$
\begin{aligned}
Z_{m^{\pm}n^{\pm}}^{V_hH} &= -j\omega \int\limits_{l_m^{\pm}} \vec{\Delta}_m^{\pm}(x,y). \int\limits_{S_n^{\pm}} S_0 \left\{ \int\limits_{z_m^-}^{z_m^+} \Pi_m(z) \frac{\widetilde{V}_{ij}^{I^{TE}}}{-j\omega} \, \mathrm{d}z \right\} \vec{\Delta}_n^{\pm}(x',y') \, \mathrm{d}S' \mathrm{d}l \\
&-j\omega \int\limits_{l_m^{\pm}} \left(\frac{\pm \Pi_m(x,y)}{-j\omega} \right) \int\limits_{S_n^{\pm}} S_0 \left\{ \int\limits_{z_m^-}^{z_m^+} \Pi_m(z) j\omega \frac{\widetilde{V}_{ij}^{I^{TE}} - \widetilde{V}_{ij}^{I^{TM}}}{k_\rho^2} \, \mathrm{d}z \right\} \left(\frac{\pm \Pi_n(x',y')}{-j\omega} \right) \, \mathrm{d}S' \mathrm{d}l \\
&-j\omega \int\limits_{l_m^{\pm}} \left(\frac{\pm \Pi_m(x,y)}{-j\omega} \right) \int\limits_{l_n^{\pm}} S_0 \left\{ \int\limits_{z_m^-}^{z_m^+} \Pi_m(z) j\omega \frac{\widetilde{V}_{ij}^{I^{TE}} - \widetilde{V}_{ij}^{I^{TM}}}{k_\rho^2} \, \mathrm{d}z \right\} \left(\frac{-\vec{n}'.\vec{\Delta}_n^{\pm}}{-j\omega} \right) \mathrm{d}l' \mathrm{d}l \qquad (6.31)
\end{aligned}
$$

The third line charge term of the above equations is transferred to $Z_{ij}^{V_hV_v}$ Equation (6.28) of Section 6.3.7. The analytical formulas required to evaluate Equations (6.30), (6.31) are given in Section 6.4.2. All formulas to fill the remaining blocks Z^{HV} and Z^{VH} of the total MoM Z matrix are now available.

6.4 Spectral Domain Analytical Evaluation

In this section, after stating the notation to be used (Section 6.4.1), all z, z' integrations are performed in closed form. We don't give the formulas in the same sequence as they appeared in the previous section, but slowly build up the formulas from the simplest to the most complicated ones. In each case we verify that closed form spectral integration results in an improvement of the spectral asymptotic and corresponding spatial singular behaviour such that only convergent integrals can arise in the evaluation of the reaction integrals in the space domain as worked out in Section 7.3 of Chapter 7. Special sections are devoted to the correct treatment of the singularity occurring for $z = z'$ (Section 6.4.4), and the canceling of singular line charge contributions in the spectral domain (Section 6.4.8).

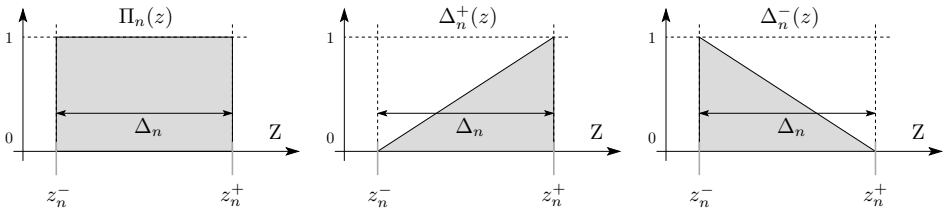

(a) The pulse function $\Pi_n(z)$.

(b) The linear function $\Delta_n^+(z)$.

(c) The linear function $\Delta_n^-(z)$.

Figure 6.11: Pulse function and linear functions $\Pi_n(z)$, $\Delta_n^+(z)$, $\Delta_n^-(z)$ as test and expansion functions for charge and current.

6.4.1 Definitions

The functions used as test and expansion functions for the z, z' dependent behaviour are depicted in Figure 6.11. The pulse function $\Pi_n(z)$ of Figure 6.11(a) is defined as

$$\begin{aligned} \Pi_n(z) &= 1 && , z_n^- < z < z_n^+ \\ &= 0 && , z < z_n^-, z > z_n^+ \end{aligned} \tag{6.32}$$

and can be used for the constant charge pulses as well as the constant part of horizontal currents on a vertical surface. The functions $\Pi_n^+(z)$, $\Pi_n^-(z)$ depicted in Figures 6.11(b), 6.11(c) are linear functions with a positive or negative slope indicated in superscript and defined as

$$\begin{aligned} \Delta_n^+(z) &= \frac{z - z_n^-}{\Delta_n} && , z_n^- < z < z_n^+ \\ &= 0 && , z < z_n^-, z > z_n^+ \end{aligned} \tag{6.33}$$

$$\begin{aligned} \Delta_n^-(z) &= \frac{z_n^+ - z}{\Delta_n} && , z_n^- < z < z_n^+ \\ &= 0 && , z < z_n^-, z > z_n^+ \end{aligned} \tag{6.34}$$

varying between 0 and 1 on the domain z_n^-, z_n^+ of length $\Delta_n = z_n^+ - z_n^-$.

6.4.2 Analytical Integration of $\Pi(z)$

The simplest analytical integrations are those that only use a single pulse test or expansion function $\Pi(z)$. With the help of the derivative relations for Green's functions of Section 4.11 of Chapter 4, the integrals can be worked out by simple partial integration. We also use the factorisation of Section 4.9 of Chapter 4, since the integrals

only involve the z or z' dependent parts of the Green's function. In Equation (6.30) for $Z^{HV_h}_{m^{\pm}n^{\pm}}$ a pulse expansion or "source" function $\Pi_n(z')$ has to be integrated for both the charge and current expansion

$$\int_{z_n^-}^{z_n^+} \widetilde{V}_{ij}^{I^{TE}}(z_m, z')\Pi_n(z')\,\mathrm{d}z' = \frac{j\omega\mu_j}{\gamma_j^2}\widetilde{V}^{TE}_{i,i_{ref}}(z_m)\widetilde{V}^{TE}_{i_{ref},j_{ref}}\left[\widetilde{V}^{V^{TE}}_{j_{ref},j}(z_n^-) - \widetilde{V}^{V^{TE}}_{j_{ref},j}(z_n^+)\right] \quad (6.35)$$

$$\int_{z_n^-}^{z_n^+} \widetilde{V}_{ij}^{I^{TM}}(z_m, z')\Pi_n(z')\,\mathrm{d}z' = \frac{1}{j\omega\epsilon_j}\widetilde{V}^{TM}_{i,i_{ref}}(z_m)\widetilde{V}^{TM}_{i_{ref},j_{ref}}\left[\widetilde{V}^{V^{TM}}_{j_{ref},j}(z_n^-) - \widetilde{V}^{V^{TM}}_{j_{ref},j}(z_n^+)\right] \quad (6.36)$$

while for the reciprocal formula Equation (6.31) for $Z^{V_hH}_{m^{\pm}n^{\pm}}$,

$$\int_{z_m^-}^{z_m^+} \Pi_m(z)\widetilde{V}_{ij}^{I^{TE}}(z, z_n)\,\mathrm{d}z = \frac{j\omega\mu_i}{\gamma_i^2}\left[\widetilde{I}^{TE}_{i,i_{ref}}(z_m^-) - \widetilde{I}^{TE}_{i,i_{ref}}(z_m^+)\right]\widetilde{I}^{TE}_{i_{ref},j_{ref}}\widetilde{I}^{TE}_{j_{ref},j}(z_n) \quad (6.37)$$

$$\int_{z_m^-}^{z_m^+} \Pi_m(z)\widetilde{V}_{ij}^{I^{TM}}(z, z_n)\,\mathrm{d}z' = \frac{1}{j\omega\epsilon_i}\left[\widetilde{I}^{TM}_{i,i_{ref}}(z_m^-) - \widetilde{I}^{TM}_{i,i_{ref}}(z_m^+)\right]\widetilde{I}^{TM}_{i_{ref},j_{ref}}\widetilde{I}^{TM}_{j_{ref},j}(z_n) \quad (6.38)$$

the pulse function $\Pi_m(z)$ is used as test or "observation" function. Notice that by the choice of the discretisation along the Z axis as discussed in Section 6.3.1, the observation point never falls within the integration interval. These formulas are evaluated in the spectral domain. We verify with the asymptotic expansions of Section 5.5.2 of Chapter 5 that in the above formulas, all expressions have a $e^{-k_\rho\Delta}/k_\rho^2$ spectral asymptotic and a corresponding $\ln(\sqrt{\rho^2+\Delta^2}+\Delta)$ spatial singular behaviour. The analytical line integration of this function can always be done, since it converges even for $\Delta = 0$.

6.4.3 Analytical Integration of $\Delta^{\pm}(z)$

When linear expansion or testing functions occur, the integrations are only slightly more complicated. Inserting $\Delta_n^{\pm}(z')$, $\Delta_m^{\pm}(z)$ for the vertical currents in $Z^{HV_v}_{m^{\pm}n^{\pm}}$, $Z^{V_vH}_{m^{\pm}n^{\pm}}$ of Equations (6.22), (6.24) gives

$$\begin{aligned}\int_{z_n^-}^{z_n^+} \frac{\widetilde{V}_{ij}^{V^{TM}}(z_m, z')}{j\omega\epsilon_j}\Delta_n^{\pm}(z')\,\mathrm{d}z' &= \mp 1_n \widetilde{V}^{TM}_{i,i_{ref}}(z_m)\widetilde{V}^{TM}_{i_{ref},j_{ref}}\frac{\widetilde{V}_{j_{ref},j}^{I^{TM}}(z_n^{\pm})}{\gamma_j^2} \\ &\quad + \widetilde{V}^{TM}_{i_{ref},i}(z_m)\widetilde{V}^{TM}_{i_{ref},j_{ref}}\left[\frac{\widetilde{V}^{V^{TM}}_{j_{ref},j}(z_n^-) - \widetilde{V}^{V^{TM}}_{j_{ref},j}(z_n^+)}{j\omega\epsilon_j\gamma_j^2\Delta_n}\right] \quad (6.39)\end{aligned}$$

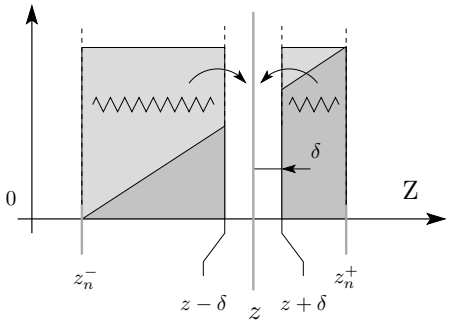

Figure 6.12: Evaluation of the z, z' integrations in a principal value sense when the observation point falls within the source distribution.

$$\int_{z_m^-}^{z_m^+} \Delta_m^{\pm}(z) \frac{\widetilde{I}_{ij}^{TM}(z, z_n)}{j\omega\epsilon_i} \, \mathrm{d}z = \mp 1_m \frac{\widetilde{V}_{i,i_{ref}}^{TM}(z_m^{\pm})}{\gamma_i^2} \widetilde{V}_{i_{ref},j_{ref}}^{TM} \widetilde{V}_{j_{ref},j}^{I^T M}(z_n) + \left[\frac{\widetilde{I}_{i,i_{ref}}^{TM}(z_m^-) - \widetilde{I}_{i,i_{ref}}^{TM}(z_m^+)}{j\omega\epsilon_i\gamma_i^2\Delta_m} \right] \widetilde{I}_{i_{ref},j_{ref}}^{TM} \widetilde{I}_{j_{ref},j}^{I^{TM}}(z_n). \quad (6.40)$$

We here recall the convention that for all double signed quantities $\Delta_n^{\pm}$, $z_n^{\pm}$, $\pm 1_n$ with subscript n we choose everywhere either the upper or either the lower sign, corresponding with the choice of the function $\Delta_n^{\pm}$ with positive or negative slope, and independently for all double signed quantities $\Delta_m^{\pm}$, $z_m^{\pm}$, $\pm 1_m$, with subscript m, we take everywhere the upper or lower sign now corresponding with the function $\Delta_m^{\pm}$ with positive or negative slope. In the above formulas, the first terms on the right sides have a $e^{-k_\rho \Delta}/k_\rho$ and the remaining terms at most a $e^{-k_\rho \Delta}/k_\rho^2$ spectral asymptotic behaviour. In the spatial domain, the line integrals of $1/\sqrt{\rho^2 + \Delta^2}$ diverge for $\Delta = 0$. This non-integrable singular field behaviour is caused by the accumulated line charge at the edge of the half rooftop function $\Delta^{\pm}(z)$ at the position $z^{\pm}$. This contribution for $\Delta = 0$ is however always canceled by the line charge at the edge of another vertical or horizontal half rooftop. These last line charge contributions can be seen in the modified Equations (6.25), (6.27).

6.4.4 Evaluation in Principal Value Sense

Until now, the observation point z has always been located outside of the source distribution at z'. Special care has to be exercised when the observation point is moved inside of the source distribution as depicted in Figure 6.12. In this case, the z, z' integrals have to be evaluated in a principal value sense [192], [193], [194] as already indicated in Chapter 2. The observation point is excluded from the integration domain with a principal "volume" $]z-\delta, z+\delta[$ with "radius" δ. Upon taking the limit

$\delta \to 0$, the values of the Green's function expressions at the edges are obtained from the voltages and currents at the immediate left and right sides of the source as given in Equations (4.85), (4.86), (4.87) and (4.88) of Chapter 4. Together with the extraction of the asymptotes in the spectral domain (see Section 7.2 of Chapter 7) and the analytical integration of their spatial domain singular counterparts as a function of x, y or ρ, ϕ (see Section 7.3.4 of Chapter 7), all total x, y, z integrals are evaluated in a principal value sense.

6.4.5 Analytical Integration of Combinations $\Pi(z)$

For the formulas in Equation (6.20) for $Z_{m^{\pm}n^{\pm}}^{V_hV_h}$, the pulse functions appear together as expansion and test function and have to be integrated over z as well as over z'. A complication now arises since the observation point can now coincide with the source point $z = z'$. In this case, the integral has to be evaluated in a principal sense as explained above. The results are

$$\int_{z_m^-}^{z_m^+} \Pi_m(z) \int_{z_n^-}^{z_n^+} \widetilde{V}_{ij}^{I^{TE}}(z,z')\Pi_n(z')\,\mathrm{d}z'\mathrm{d}z = -\frac{j\omega\mu_j}{\gamma_j^2}\Delta_n\delta_{mn} + \frac{j\omega\mu_i}{\gamma_i^2}\left[\widetilde{I}_{i,i_{ref}}^{TE}(z_m^-) - \widetilde{I}_{i,i_{ref}}^{TE}(z_m^+)\right]\widetilde{I}_{i_{ref},j_{ref}}^{TE}\frac{j\omega\mu_j}{\gamma_j^2}\left[\widetilde{I}_{j_{ref},j}^{V^{TE}}(z_n^-) - \widetilde{I}_{j_{ref},j}^{V^{TE}}(z_n^+)\right] \quad (6.41)$$

$$\int_{z_m^-}^{z_m^+} \Pi_m(z) \int_{z_n^-}^{z_n^+} \widetilde{V}_{ij}^{I^{TM}}(z,z')\Pi_n(z')\,\mathrm{d}z'\mathrm{d}z = -\frac{1}{j\omega\epsilon_j}\Delta_n\delta_{mn} + \frac{1}{j\omega\epsilon_i}\left[\widetilde{I}_{i,i_{ref}}^{TM}(z_m^-) - \widetilde{I}_{i,i_{ref}}^{TM}(z_m^+)\right]\widetilde{I}_{i_{ref},j_{ref}}^{TM}\frac{1}{j\omega\epsilon_j}\left[\widetilde{I}_{j_{ref},j}^{V^{TM}}(z_n^-) - \widetilde{I}_{j_{ref},j}^{V^{TM}}(z_n^+)\right] \quad (6.42)$$

where the first terms on the right hand sides appear as a result from the principal value procedure and only occur when the "source" and "observation" function overlap (case $\delta_{mn} = 1$). Inserting these formulas into Equation (6.20) for the current and charge expansions, these give a worst case $e^{-k_\rho\Delta}/k_\rho^2$ spectral and $\ln(\sqrt{\rho^2+\Delta^2}+\Delta)$ behaviour, which can be safely integrated. The remaining expressions give even less spatial singular contributions with worst case $e^{-k_\rho\Delta}/k_\rho^3$ spectral asymptotes.

6.4.6 Analytical Integration of Combinations $\Pi(z)$, $\Delta^{\pm}(z)$

Formulas become more complicated as we need to combine pulse and linear functions in Equations (6.28), (6.29) for $Z_{m^{\pm}n^{\pm}}^{V_hV_v}$, $Z_{m^{\pm}n^{\pm}}^{V_vV_h}$. Evaluating the integrals with sufficient

care for the case $z = z'$ gives

$$\int_{z_m^-}^{z_m^+} \Pi_m(z) \int_{z_n^-}^{z_n^+} \frac{\widetilde{V}_{ij}^{V^{TM}}(z,z')}{j\omega\epsilon_j} \Delta_n^{\pm}(z')\, \mathrm{d}z'\mathrm{d}z = \frac{\mp 1_n}{j\omega\epsilon_j\gamma_j^2}\delta_{mn}$$
$$+\frac{\widetilde{I}_{i,i_{ref}}^{TM}(z_m^-) - \widetilde{I}_{i,i_{ref}}^{TM}(z_m^+)}{j\omega\epsilon_i} \widetilde{I}_{i_{ref},j_{ref}}^{TM} \left[\mp 1_n \frac{\widetilde{I}_{j_{ref},j}^{I^{TM}}(z_n^{\pm})}{\gamma_j^2} + \frac{\widetilde{I}_{j_{ref},j}^{I^{TM}}(z_n^-) - \widetilde{I}_{j_{ref},j}^{I^{TM}}(z_n^+)}{j\omega\epsilon_j\gamma_j^2\Delta_n} \right] \quad (6.43)$$

$$\int_{z_m^-}^{z_m^+} \Delta_m^{\pm}(z) \int_{z_n^-}^{z_n^+} \frac{\widetilde{I}_{ij}^{I^{TM}}(z,z')}{j\omega\epsilon_i} \Pi_n(z')\, \mathrm{d}z'\mathrm{d}z = \frac{\pm 1_m}{j\omega\epsilon_i\gamma_i^2}\delta_{mn}$$
$$\mp 1_m \frac{\widetilde{V}_{i,i_{ref}}^{TM}(z_m^{\pm})}{\gamma_i^2} \widetilde{V}_{i_{ref},j_{ref}}^{TM} \left[\frac{\widetilde{V}_{j_{ref},j}^{V^{TM}}(z_n^-) - \widetilde{V}_{j_{ref},j}^{V^{TM}}(z_n^+)}{j\omega\epsilon_j} \right]$$
$$+\frac{\widetilde{I}_{i,i_{ref}}^{TM}(z_m^-) - \widetilde{I}_{i,i_{ref}}^{TM}(z_m^+)}{j\omega\epsilon_i\gamma_i^2\Delta_m} \widetilde{I}_{i_{ref},j_{ref}}^{TM} \left[\frac{\widetilde{I}_{j_{ref},j}^{V^{TM}}(z_n^-) - \widetilde{I}_{j_{ref},j}^{V^{TM}}(z_n^+)}{j\omega\epsilon_j} \right] \quad (6.44)$$

with the same convention for the double signed quantities as before. The terms that occur for the case of overlapping test and expansion functions ($\delta_{mn} = 1$) give the most singular $\ln\rho$ contributions with $\Delta = 0$. The first terms between brackets give $\ln(\sqrt{\rho^2+\Delta^2}+\Delta)$ quasi-singularities in the space domain, since the contributions for $\Delta = 0$ are canceled as they are again line-charge contributions that will be canceled by other line-charge terms. The remaining terms give even less singular contributions.

6.4.7 Analytical Integration of Combinations $\Delta^{\pm}(z)$

The most complicated formulas result when linear test and expansion functions have to be integrated together as in in the central part of Equation (6.19) for $Z_{m^{\pm}n^{\pm}}^{V_vV_v}$. Being especially careful with the principal value evaluation of the integral as discussed in Section 6.4.4, the result is

$$\int_{z_m^-}^{z_m^+} \Delta_m^{\pm}(z) \int_{z_n^-}^{z_n^+} k_\rho^2 \frac{\widetilde{V}_{ij}^{I^{TM}}(z,z')}{j\omega\epsilon_i j\omega\epsilon_j} \Delta_n^{\pm}(z')\, \mathrm{d}z'\mathrm{d}z = + \left[\frac{1}{j\omega\epsilon_i}\frac{k_\rho^2}{\gamma_j^2}\frac{\Delta_n}{6} - \frac{1}{j\omega\epsilon_j}\frac{\Delta_n}{6} \right] 2^{\delta^{\pm}}\delta_{mn}$$
$$\mp 1_m k_\rho^2 \frac{\widetilde{V}_{i,i_{ref}}^{TM}(z_m^{\pm})}{\gamma_i^2} \widetilde{V}_{i_{ref},j_{ref}}^{TM} \left[\mp 1_n \frac{\widetilde{V}_{j_{ref},j}^{I^{TM}}(z_n^{\pm})}{\gamma_j^2} + \frac{\widetilde{V}_{j_{ref},j}^{V^{TM}}(z_n^-) - \widetilde{V}_{j_{ref},j}^{V^{TM}}(z_n^+)}{j\omega\epsilon_j\gamma_j^2\Delta_n} \right]$$
$$+k_\rho^2 \frac{\widetilde{I}_{i,i_{ref}}^{TM}(z_m^-) - \widetilde{I}_{i,i_{ref}}^{TM}(z_m^+)}{j\omega\epsilon_i\gamma_i^2\Delta_m} \widetilde{I}_{i_{ref},j_{ref}}^{TM} \left[\mp 1_n \frac{\widetilde{I}_{j_{ref},j}^{I^{TM}}(z_n^{\pm})}{\gamma_j^2} + \frac{\widetilde{I}_{j_{ref},j}^{I^{TM}}(z_n^-) - \widetilde{I}_{j_{ref},j}^{I^{TM}}(z_n^+)}{j\omega\epsilon_j\gamma_j^2\Delta_n} \right] \quad (6.45)$$

where the first term between brackets is only present when the "source" function n and "observation" function m overlap (case $\delta_{mn} = 1$). The factor 2 has to be included

when the functions have the same slope (case $\delta^{\pm} = 1$).

The slowest decay in the spectral domain again comes from the first two "self-coupling" terms between brackets for overlapping test and expansion functions (and thus located within the same layer $\epsilon_i = \epsilon_j$), since

$$\lim_{k_\rho \to \infty} \left[\frac{1}{j\omega\epsilon_i} \frac{k_\rho^2}{\gamma_j^2} \frac{\Delta_n}{6} - \frac{1}{j\omega\epsilon_j} \frac{\Delta_n}{6} \right] \delta_{mn} \sim \frac{1}{j\omega\epsilon_j} \frac{\Delta_n}{6} \left[\frac{k_\rho^2}{k_\rho^2} \left(1 + \frac{k_j^2}{k_\rho^2} \right) - 1 \right] \sim \frac{1}{k_\rho^2} \quad (6.46)$$

such that the worst case spatial singularity is again $\ln \rho$, which can be integrated without diverging. The next problematic behaviour comes from the third term

$$\lim_{k_\rho \to \infty} k_\rho^2 \frac{\widetilde{V}_{ij}^{I^{TM}}(z_m^{\pm}, z_n^{\pm})}{\gamma_i^2 \gamma_j^2} \sim \frac{1}{k_\rho} \quad (6.47)$$

that gives non-integrable $1/\sqrt{\rho^2 + \Delta^2}$ singularities in the space domain when $\Delta = 0$. In the next section, it will be demonstrated that these problematic terms always disappear when the above formula is combined for two vertical half rooftop functions, or when the appropriate line charge contributions of half a horizontal rooftop are added. The remaining terms all give $\ln(\sqrt{\rho^2 + \Delta^2} + \Delta)$ or less singular contributions.

6.4.8 Canceling of Singular Line Charge Fields

In this section, we verify explicitly that singular contributions arising from line charges cancel when all contributions to obtain the total matrix element Z_{mn} are added together. This is verified for two cases : the coupling between two vertical rooftops as depicted in Figure 6.13, and for the coupling between two "cornered" rooftop functions as depicted in Figure 6.14. Similar verifications can be made for all other cases.

In Figure 6.13 we consider the coupling between two complete vertical rooftop functions. The four terms in $Z_{mn}^{V_v V_v} = Z_{m^+n^+}^{V_v V_v} + Z_{m^-n^+}^{V_v V_v} + Z_{m^+n^-}^{V_v V_v} + Z_{m^-n^-}^{V_v V_v}$ are all evaluated using Equation (6.45). The singular field contributions in the spatial domain due to the line charges will cancel eachother since we find for the corresponding spectral asymptotic behaviour

$$\lim_{k_\rho \to \infty} \left[+ \frac{\widetilde{V}_{lk}^{I^{TM}}(z_m^+, z_n^+)}{\gamma_l^2 \gamma_k^2} - \frac{\widetilde{V}_{ik}^{I^{TM}}(z_m^-, z_n^+)}{\gamma_i^2 \gamma_k^2} - \frac{\widetilde{V}_{lj}^{I^{TM}}(z_m^+, z_n^-)}{\gamma_l^2 \gamma_j^2} + \frac{\widetilde{V}_{ij}^{I^{TM}}(z_m^-, z_n^-)}{\gamma_i^2 \gamma_j^2} \right] = 0 \quad (6.48)$$

even when the source current and/or observation currents cross the interface between different layers, in which case $k = j+1$ and/or $l = i+1$. Notice that there are no special contributions from the line charge in case the rooftop is located completely within a single layer, similar to the canceling when the rooftop is located in a homogeneous medium, since then $k = j$ and/or $l = i$, such that Equation (6.48) holds for all k_ρ.

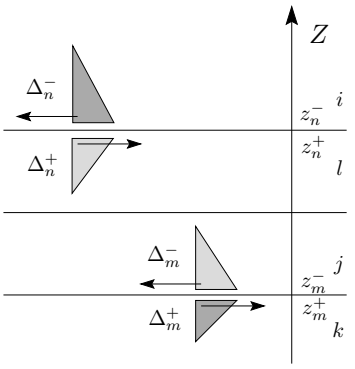

Figure 6.13: Line charges associated with the rooftop expansion functions of two vertical currents in different layers.

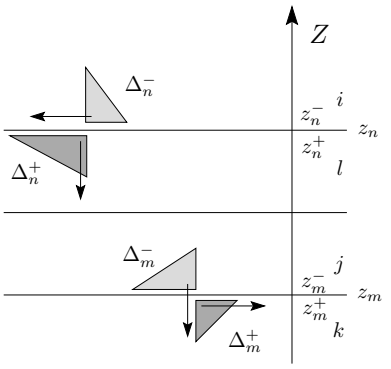

Figure 6.14: Line charges associated with "cornered" rooftop expansion functions in different layers.

For two "cornered" rooftop functions as depicted in Figure 6.14, the total matrix element consists of $Z_{mn}^{CC} = Z_{m^{\mp}n^{\mp}}^{HH} + Z_{m^{\pm}n^{\pm}}^{V_v^*V_v^*} + Z_{m^{\pm}n^{\mp}}^{V_v^*H} + Z_{m^{\mp}n^{\pm}}^{HV_v^*}$. The second term $Z_{m^{\pm}n^{\pm}}^{V_v^*V_v^*}$ Equation (6.26) is evaluated by inserting Equation (6.45) such that the singular contribution resulting from the line charge line charge interaction from the vertical rooftop is compensated by the line charge line charge interaction from the horizontal rooftop of $Z_{m^{\mp}n^{\mp}}^{HH}$ Equation (6.17) which was added in Equation (6.26)

$$\lim_{k_\rho\to\infty}\left[(\mp 1_m)(\mp 1_n)k_\rho^2\frac{\widetilde{V}_{lk}^{I^{TM}}(z_m^+,z_n^+)}{\gamma_l^2\gamma_k^2} - (\mp 1_m)(\mp 1_n)\frac{\widetilde{V}_{ij}^{I^{TM}}(z_m,z_n)}{k_\rho^2}\right] = 0. \tag{6.49}$$

The third term $Z_{m^{\pm}n^{\mp}}^{V_v^*H}$ Equation (6.25) is evaluated by inserting Equation (6.40) such that the singular contribution resulting from the interaction of the surface charge of the horizontal rooftop to the line charge of the vertical rooftop is compensated by the surface charge to line charge interaction charge interaction from $Z_{m^{\mp}n^{\pm}}^{HH}$ Equation (6.17) which was added in Equation (6.25)

$$\lim_{k_\rho\to\infty}\left[\mp 1_m\frac{\widetilde{V}_{lk}^{I^{TM}}(z_m^{\pm},z_n)}{\gamma_l^2} - (\mp 1_m)\frac{\widetilde{V}_{lk}^{I^{TM}}(z_m^{\pm},z_n)}{k_\rho^2}\right] = 0. \tag{6.50}$$

Finally, the fourth term $Z_{m^{\mp}n^{\pm}}^{HV_v^*}$ Equation (6.27) is evaluated by inserting Equation (6.39) such that the singular contribution resulting from the interaction of the line charge of the vertical rooftop to the surface charge of the horizontal rooftop is compensated by the line charge to surface charge interaction charge interaction from $Z_{m^{\pm}n^{\mp}}^{HH}$ Equation (6.17) which was added in Equation (6.27)

$$\lim_{k_\rho\to\infty}\left[\mp 1_n\frac{\widetilde{V}_{lk}^{I^{TM}}(z_m,z_n^{\pm})}{\gamma_k^2} - (\mp 1_n)\frac{\widetilde{V}_{lk}^{I^{TM}}(z_m,z_n^{\pm})}{k_\rho^2}\right] = 0. \tag{6.51}$$

6.5 Conclusions

This chapter has reviewed the evaluation of the reaction integrals to obtain the elements of the discrete matrix version of the BIE. In this work, the evaluation has been completely reformulated to take into account the planar nature of the stratified surround and the geometry of the structures to be analysed. Traditional space and spectral domain techniques are blended in a new combined spectral space domain evaluation. All transverse x, y and x', y' integrations use the space domain mixed potential formalism, while all z, z' integrations involve the dyadic parts of the formulation and are done completely analytically in the spectral domain . The transition from spectral to space domain with the inverse Fourier transform is done at an optimal intermediate stage of the evaluation, depending on the type of electromagnetic coupling considered. The closed form formulas for the Galerkin evaluation of all possible combinations of pulse and rooftop expansion functions were given in a compact form, and valid for an arbitrarily stratified medium. These results could only be obtained thanks to the derivative relations and factorised form of the Green's functions also developed earlier in this work.

Chapter 7

Numerical and Analytical Techniques

7.1 Introduction

Although the Boundary Integral Equation for the electric field in a general planar stratified medium needs to be solved numerically, the transformation of the theoretical formulation to a numerical result for a practical problem involves many analytical steps, producing an overall hybrid analytical-numerical technique. In this chapter, we shall therefore not fully descend into the rubble strewn territory of the purely numerical details, but concentrate on the analytical aspects of the numerical treatment. Section 7.2 describes how the physically important behaviour of the electromagnetic field in the spatial domain can be extracted analytically from the numerical inverse Fourier transform. With the electric field available partially in numerical form and partially analytically, one can then complete the remaining evaluation of the reaction integrals in the spatial domain also in a numerico- analytical manner as described in Section 7.3. We have now reached the point were the only remaining task is to solve the linear systems of equations to obtain the main result of the BIE, the (approximate) vector current distribution over the entire metallic "scatterer". Additional postprocessing transforms this underlying fundamental solution of the problem to directly observable and measurable quantities more of interest to the practical engineer like impedance matrix, scattering matrix description, examples of which will be given in the next Chapter 8.

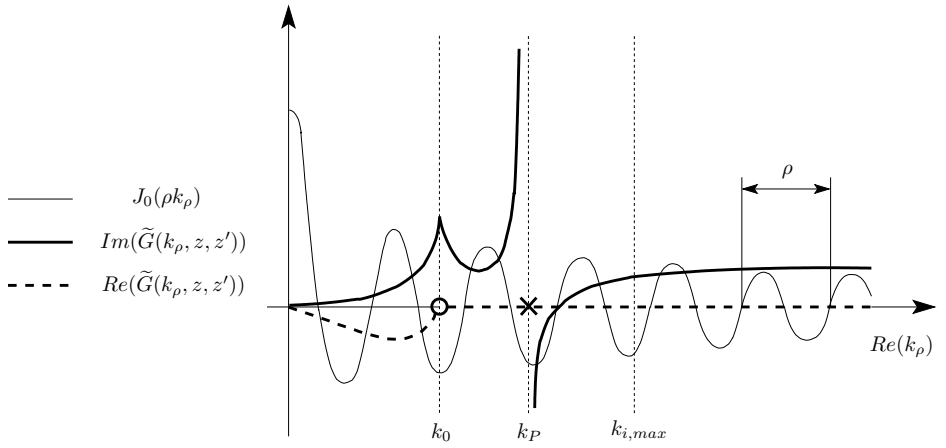

Figure 7.1: Typical behaviour of the factors in the integrand of the Fourier-Bessel Integral of Equation (7.1).

7.2 The Numerical Inverse Fourier Transformation

In Chapter 4, we introduced the Fourier transform of the transverse spatial x, y coordinates to the spectral k_x, k_y wavenumber domain (Equations (4.2), (4.3)) to obtain the electromagnetic field in a planar stratified medium in closed form. In Chapter 6, we exploited the analytical field expressions in the spectral domain to perform the z, z' dependent parts of the reaction integrals also in closed form. The analytical possibilities in the spectral domain have now been exhausted, and we need to return to the space domain by evaluating the inverse Fourier transform of Equation (4.3).

7.2.1 The Mathematical Point of View

By the investigation of Section 5.4 of Chapter 5 and thanks to the hybrid field formulation of Chapter 6, the inverse Fourier transform only consists of evaluating the one-dimensional Fourier-Bessel integrals

$$\begin{aligned} G(\rho, z, z') &= \mathfrak{F}^{-1}\left\{\widetilde{G}(k_\rho, z, z')\right\} = S_0\left\{\widetilde{G}(k_\rho, z, z')\right\} \\ &= \frac{1}{2\pi}\int_0^{+\infty} \widetilde{G}(k_\rho, z, z') J_0(\rho k_\rho)\; k_\rho \mathrm{d}k_\rho \end{aligned} \tag{7.1}$$

which in general has to be evaluated at least partially numerically. The function $\widetilde{G}(k_\rho, z, z')$ is not necessarily the Green's function excited by a "point" source exci-

tation, but can also be integrated over extended "observation" and "source" distributions as in Section 6.4 of Chapter 6. In this case, $\widetilde{G}(k_\rho, z, z')$ stands for any of the closed form formulas Equations (6.35), (6.36), (6.37), (6.38), (6.39), (6.40), (6.41), (6.42), (6.43), (6.44) of Section 6.4 and the z, z' notation used above stands for all combinations of z, z' coordinates z_n , z_m, $z_n^{\pm}$, $z_m^{\pm}$ occurring in these formulas. A typical behaviour of the factors in the integrand is sketched in Figure 7.1. From a mathematical point of view, the remaining task is still a formidable one, since the computation of the integral is difficult. The integration interval in principle extends to infinity which creates numerical problems if the function $\widetilde{G}(k_\rho, z, z')$ decays very slowly for large k_ρ. The function $\widetilde{G}(k_\rho, z, z')$ can also exhibit singularities k_0, k_P on or close to the integration path. The Bessel function $J_0(\rho k_\rho)$ becomes highly oscillatory for large ρ (small period in spectral domain), which may create convergence problems. Extensive literature on the evaluation of these integrals for electromagnetic problems can be traced through [219], [270], [271], [272], [273]. Many of the techniques developed in these works are based on the physical background of the problem, by interpreting Equation (7.1) as a cylindrical and plane wave spectrum discussed generally in the next Section 7.2.2. In this work, we use and expand the techniques originally developed by Vandenbosch [11] and Demuynck [14] to handle the more complicated expressions $\widetilde{G}(k_\rho, z, z')$ appearing in this work as discussed in Section 7.2.3.

7.2.2 The Cylindrical Wave Spectrum

The above difficulties with the inverse Fourier transform can to a large extent be alleviated by introducing analytical techniques based on the physical background. To achieve this, the above formula has to be interpreted as a decomposition of the field into a continuous spectrum of cylindrical and plane waves as depicted in Figure 7.4.

Cylindrical and Plane Waves

The cylindrical waves described by the Bessel function $J_0(\rho k_\rho)$ travel parallel to the layers of the medium with wavenumber k_ρ which is also the independent variable of integration. When the integration in Equation 7.1 is performed over the real axis, it remains strictly real. Along the Z axis, the field is described by plane waves. Their propagation constant along the Z axis γ_i depends on the main k_ρ variable and the properties of the medium. It becomes the wavenumber k_{zi}

$$\gamma_i = jk_{zi} = j\sqrt{k_i^2 - k_\rho^2} \tag{7.2}$$

when $k_\rho < k_i$ for propagating waves along Z as depicted Figure 7.4(a), or it becomes a damping constant α_{zi} for evanescent waves with

$$\gamma_i = \alpha_{zi} = \sqrt{k_\rho^2 - k_i^2} \tag{7.3}$$

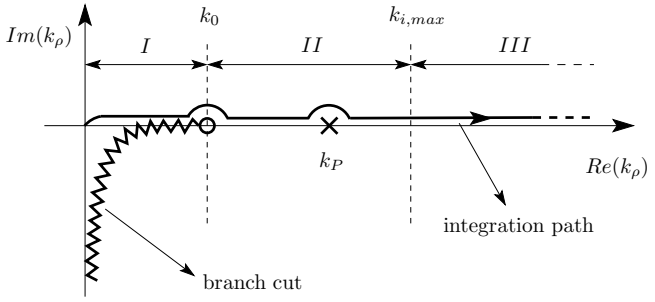

Figure 7.2: Topology of $\widetilde{G}(k_\rho, z, z')$ in the complex k_ρ-plane for a single layered medium backed with a conducting ground plane.

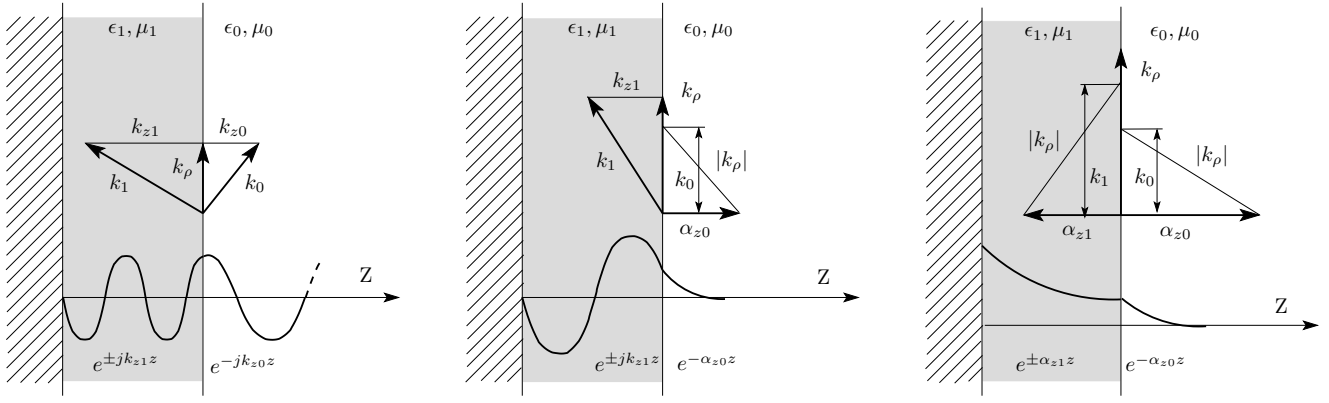

(a) Region I (b) Region II (c) Region III

Figure 7.3: Field behaviour in the Z direction and behaviour of the wavenumbers in the respective media as function of the position along the integration path.

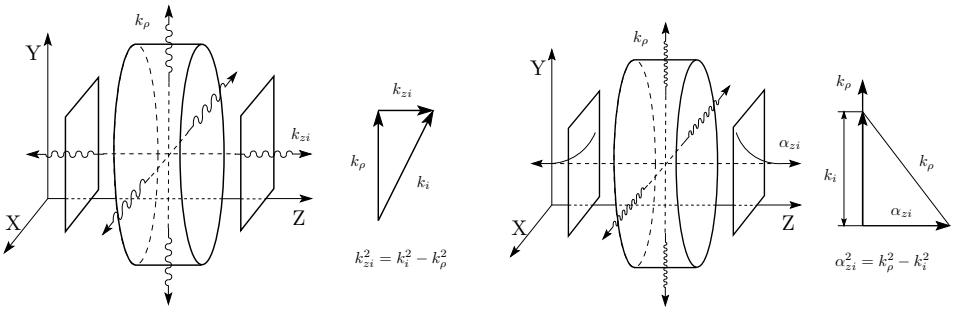

(a) $k_\rho < k_i$ (b) $k_\rho > k_i$

Figure 7.4: Decomposition of the field into a spectrum of cylindrical and plane waves.

when $k_\rho > k_i$ as depicted in Figure 7.4(b). The wavenumber k_ρ can become complex if the integration path is deformed into the complex plane k_ρ-plane as depicted in Figure 7.2. However, the techniques from [11], [14] and worked out further in this work assume only a real axis integration [274].

Topology of $\widetilde{G}(k_\rho, z, z')$ in the complex k_ρ-plane

The behaviour of $\widetilde{G}(k_\rho, z, z')$ along the real axis can be better understood by studying its topology in the complex k_ρ-plane as depicted in Figure 7.2 for the case of a single layered medium above a perfectly conducting ground plane.

In the interval $[0, k_0[$ the spectral wavenumber k_ρ is smaller than the wavenumbers of both media k_1, k_0, such that k_{z1}, k_{z0} are both real. This case is depicted in Figure 7.3(a). Energy is transported in all directions, and this region is thus important to describe the far field radiation pattern. The transition to the next region passes through the branch point singularity k_0. For a more general case, it can be examined that $\widetilde{G}(k_\rho, z, z')$ is an even function of all k_{zi} of layers of limited extend but an odd function of the wavenumber associated with unlimited open regions $i = 0, N+1$. The points $k_\rho = k_i$ with $i = 1, \ldots, N$ are ordinary regular points, while a branch point singularity occurs for $k_\rho = k_0$ and/or $k_\rho = k_{N+1}$. From the branch point, a "branch cut" extends to infinity. It joins the two sheets of the Riemann surface which are associated with the double-valued function $k_{z0} = \sqrt{k_0^2 - k_\rho^2}$. In the next region $]k_0, k_1[$ the spectral wavenumber k_ρ is still smaller than k_1, but already larger than k_0. The wave field thus decays in the open half space with damping constant α_{z0}. This situation is depicted in Figure 7.3(b). The energy can now only be transported in the transverse direction. This is thus the region where surface waves can occur. The surface waves are the eigenmodes of the layer structure and manifest themselves as pole singularities k_P. The exact number and location of the poles depends on

the frequency and the properties of the layers. By extending the reasoning of Figure 7.3(b) to a multilayered medium, we see that the poles can only occur in the interval $max(k_0, k_{N+1}) < k_\rho < max(k_i) = k_{i,max}$. If the media are lossy, the branch point and pole singularities move off the real axis slightly into the fourth quadrant of the complex plane. Finally, in the last region $]k_1, +\infty[$ the spectral wavenumber has become larger than the wavenumbers in both media, such that the field decays along Z everywhere as indicated in Figure 7.3(c). This region is important to describe very rapid field variations in the transverse direction for example in the near field of an imposed current source.

7.2.3 Analytical Extraction for Inverse Fourier Transform

Operations in the Spectral Domain

A purely numerical inverse Fourier transform of a typical function $\widetilde{G}(k_\rho, z, z')$ as depicted in Figure 7.1 is possible only at the cost of excessive computation time. To obtain an accurate value of the spatial function $G(\rho)$ from the unaltered $\widetilde{G}(k_\rho, z, z')$, a very large number of sampling points in the spectral domain has to be taken. The number of sampling points is determined by the upper truncation limit $k_{\rho,max}$ of the numerical integration domain $[0, k_{\rho,max}]$ and the sampling rate within this interval. The slow decay of $\widetilde{G}(k_\rho, z, z')$ neccesitates a very high limit $k_{\rho,max}$. Rapid variations of $\widetilde{G}(k_\rho, z, z')$ require a high sampling rate. Rapid variations of $\widetilde{G}(k_\rho, z, z')$ are typically present at a branch point k_0 and a pole k_P. To avoid such costly purely numerical work, the original function $\widetilde{G}(k_\rho, z, z')$ is transformed into a well behaved smooth and rapidly decaying function $\widetilde{G}_{nu}(k_\rho, z, z')$. To achieve this, each problematic behaviour is extracted in closed form as described below.

Extraction of the Spectral Asymptotes

The behaviour of $\widetilde{G}(k_\rho, z, z')$ in the spectral domain for $k_\rho \to +\infty$ is called the spectral asymptotic behaviour. In Section 5.5.2 of Chapter 5, it was shown that this asymptotic part can be obtained from a multiple reflection computation of the Green's functions in the layer structure under the assumption that k_ρ is much larger then any of the wavenumbers of the layers k_i. By performing the whole computation of the expression for $\widetilde{G}(k_\rho, z, z')$ in series expansion for $k_\rho \to \infty$, we can write write for the asymptotic part

$$\lim_{k_\rho \to \infty} \widetilde{G}(k_\rho, z, z') \approx \widetilde{G}_{as}(k_\rho, z, z') = \sum_{m=1}^{3} \sum_{i=1}^{N_m} C_{as}^{mi} \widetilde{G}_{as}^{m}(k_\rho, \Delta_i). \tag{7.4}$$

The outer summation runs over the order of the asymptotic equivalent functions

$$\widetilde{G}_{as}^{1}(k_\rho, \Delta) = \frac{\left(1 - e^{-k_\rho t}\right)}{k_\rho} e^{-k_\rho \Delta} \tag{7.5}$$

$$\widetilde{G}^2_{as}(k_\rho,\Delta) = \frac{\left(1-e^{-k_\rho t}\right)^2}{k_\rho^2} e^{-k_\rho \Delta} \tag{7.6}$$

$$\widetilde{G}^3_{as}(k_\rho,\Delta) = \frac{\left(1-e^{-k_\rho t}\right)^3}{k_\rho^3} e^{-k_\rho \Delta} \tag{7.7}$$

and for each order m, N_m multiple z,z' distances Δ_i can be taken into account. The factors $\left(1-e^{-k_\rho t}\right)^m$ are convergence factors with $t = 1/k_{i,max}$ and $k_{i,max}$ the maximum wavenumber occurring in the layer structure. These factors do not affect the behaviour for large k_ρ, but force the functions to 0 at the origin of the spectral domain $k_\rho = 0$ such that the inverse Fourier transform converges and can be done analytically (See also Appendix B.4). Compared to the extraction already developed in [14], several improvements have been introduced. First, due to the more complicated nature of the formulas of Section 6.4, the extra order $m = 3$ has been introduced. Second, the computation of the coefficients C^{mi}_{as} is now based on the factorised form of the Green's functions. Thirdly, higher order reflections are now taken into account, which is required when the source and/or observation points are located close to an interface between different layers and the local reflection coefficients Equations (5.83), (5.84) have a considerable amplitude.

Pole Extraction

The presence of a pole in $\widetilde{G}(k_\rho,z,z')$ indicates the propagation of a surface wave in the layer structure. The pole k_P is the propagation constant of the surface wave in the lateral direction. The field pattern of the surface wave is an eigenmode of the entire layer structure [275], [276] and is thus determined by the properties ϵ_i, μ_i and thicknesses d_i of all the layers i and the frequency. The pole occurs at the same value of k_ρ for all possible Green's functions. The extraction procedure first locates all poles close to the real axis. For each pole, a numerical residue computation is performed for one of the current or voltage functions $\widetilde{F}^{S^T}_{ij}(k_\rho,z,z')$. The residues of all current and voltage Green's functions are obtained from reciprocity and the factorised form of these expressions. The evaluation of the Green's functions $\widetilde{G}(k_\rho,z,z')$ in the closed form formulas of Section 6.4 is done by inserting the residues for the current and voltage Green's functions $\widetilde{F}^{S^T}_{ij}(k_\rho,z,z')$ and evaluating all other expressions with $k_\rho = k_P$. Any function can thus be approximated in the neighbourhood of the pole as

$$\lim_{k_\rho \to k_P} \widetilde{G}(k_\rho,z,z') \approx \widetilde{G}_{po}(k_\rho,z,z') = C_{po}(z,z')\left(\frac{2k_P}{(k_\rho-k_P)(k_\rho+k_P)} - \frac{2k_P}{k_\rho^2+k_P^2}\right) \tag{7.8}$$

The coefficient $C_{po}(z,z')$ describes the field pattern of the eigenmode in the Z direction or depends on the fixed integration limits if an analytical integration is performed in the spectral domain. The first term between brackets mimics the singular behaviour of the function $\widetilde{G}(k_\rho,z,z')$ around the pole, while the second term makes the function $\widetilde{G}_{po}(k_\rho,z,z')$ decay fast enough to avoid the introduction of additional spectral asymptotes. In this way, only the behaviour of $\widetilde{G}(k_\rho,z,z')$ around the pole

k_P is seriously affected while the effect on the remainder of the integration domain is minimized.

Branch Point Extraction

The singular behaviour of an arbitrary Green's function around the branch point can generally be written as

$$\begin{aligned}\lim_{k_\rho \to k_0} \widetilde{G}(k_\rho, z, z') &\approx C_{bp}^{-1}(z, z')(\gamma_0)^{-1} + C_{bp}^{0}(z, z')(\gamma_0)^{0} \\ &\quad + C_{bp}^{+1}(z, z')(\gamma_0)^{+1} + C_{bp}^{+2}(z, z')(\gamma_0)^{+2} + \ldots \end{aligned} \tag{7.9}$$

Since $\gamma_0 = \sqrt{k_\rho^2 - k_0^2}$, the first term introduces a real singularity at $k_\rho = k_0$, while the third term generates only an infinite derivative at the same spectral value. The first term only occurs for a homogeneous medium, in which case the branch point actually becomes the "pole" of the "layer" structure. The third term is present for all layer structures with at least one open half space. The coefficients $C_{bp}^{i}(z, z')$ in the above expressions are obtained by a computation "in series expansion". This means that all computations have to be done with the coefficients $C_{bp}^{i}(z, z')$ for all expressions. As compared to the extraction developed in [14], the computations are again based on the factorised form of the Green's functions, while the more complicated form of the closed form expressions of Section 6.4 require to extend the series expansion in Equation (7.9) from power 5 up to power 7. When the coefficients are determined, the problematic behaviour can be isolated as

$$\begin{aligned}\widetilde{G}_{bp}(k_\rho, z, z') &= C_{bp}^{-1}(z, z') \left(\frac{1}{\sqrt{k_\rho^2 - k_0^2}} - \frac{1}{\sqrt{k_\rho^2 + k_0^2}} \right) \\ &\quad + C_{bp}^{+1}(z, z') \left(\sqrt{k_\rho^2 - k_0^2} - k_\rho + \frac{k_0^2}{2} \frac{1}{\sqrt{k_\rho^2 + k_0^2}} \right) \end{aligned} \tag{7.10}$$

As before, the first terms between brackets mimic the behaviour around $k_\rho = k_0$, while the other terms minimize the effect in the remainder of the integration domain. A special extraction as developed in [14] is required in case the pole is located very close to the branch point.

The Numerical and Analytical Part

The problematic behaviour of $\widetilde{G}(k_\rho, z, z')$ can now be extracted such that we obtain a function

$$\begin{aligned}\widetilde{G}_{nu}(k_\rho, z, z') &= \widetilde{G}(k_\rho, z, z') - \left(\widetilde{G}_{as}(k_\rho, z, z') + \widetilde{G}_{po}(k_\rho, z, z') + \widetilde{G}_{bp}(k_\rho, z, z') \right) \\ &= \widetilde{G}(k_\rho, z, z') - \widetilde{G}_{an}(k_\rho, z, z') \end{aligned} \tag{7.11}$$

of which the inverse Fourier transform can be performed numerically with a minimum of effort. The inverse Fourier transform of the extracted part $\widetilde{G}_{an}(k_\rho, z, z') =$

$\widetilde{G}_{as}(k_\rho, z, z') + \widetilde{G}_{po}(k_\rho, z, z') + \widetilde{G}_{bp}(k_\rho, z, z')$ can be done analytically and each part of it can be identified with a characteristic physical field behaviour in the spatial domain.

Operations in the Spatial Domain

When the field in the spatial domain has to be evaluated for large lateral distances, we see from Equation (7.1) and Figure 7.1 that the oscillation of the Bessel function in the spectral domain becomes very rapid. In such a case, only the parts of $\widetilde{G}(k_\rho, z, z')$ where a rapid variation occurs contribute to the integral. Over the smoother level parts, the successive positive and negative parts of the integral cancel each other and such parts thus contribute only very little. The rapid variation of $\widetilde{G}(k_\rho, z, z')$ takes place around the branch point(s) and pole(s). The physical interpretation follows from the analytical inverse Fourier transform of the extracted parts $\widetilde{G}_{bp}(k_\rho, z, z')$ and $\widetilde{G}_{po}(k_\rho, z, z')$.

The Space Wave

From Figure 7.4, it is clear that the spatial counterpart of $\widetilde{G}_{bp}(k_\rho, z, z')$ is a cylindrical field traveling parallel to the layer structure with wavenumber k_0. Its inverse Fourier transform can be obtained analytically using Equations (B.2), (B.3), (B.4) from Appendix B.2 and the results from Table B.1 of Appendix B.4 for $n = 0$, $m = -1$, $\Delta = 0$ to obtain

$$\begin{aligned} G_{bp}(\rho, z, z') \quad = \quad & \frac{1}{2\pi} C_{bp}^{-1}(z, z') \left(\frac{e^{-jk_0\rho}}{\rho} - \frac{e^{-k_0\rho}}{\rho} \right) \\ & + \frac{1}{2\pi} C_{bp}^{+1}(z, z') \left(- \left(jk_0 + \frac{1}{\rho} \right) \frac{e^{-jk_0\rho}}{\rho^2} + \frac{1}{\rho^3} + \frac{k_0^2}{2} \frac{e^{-k_0\rho}}{\rho} \right) \end{aligned} \tag{7.12}$$

which is smooth for small ρ, while for large transverse distances it behaves as

$$\begin{aligned} \lim_{\rho \to +\infty} G_{bp}(\rho, z, z') \quad \approx \quad & \frac{1}{2\pi} C_{bp}^{-1}(z, z') \left(\frac{e^{-jk_0\rho}}{\rho} \right) \\ & + \frac{1}{2\pi} C_{bp}^{+1}(z, z')(-jk_0) \left(\frac{e^{-jk_0\rho}}{\rho^2} \right). \end{aligned} \tag{7.13}$$

For a homogeneous medium, the first term describes the spherical wave front in the lateral direction, while for an open non-homogeneous medium, the second term shows that the field decays very rapidly in the direction parallel to the layers of the medium and produces a zero in the far field radiation pattern.

The Surface Wave

The cylindrical wave front associated with the inverse Fourier transform of $\widetilde{G}_{po}(k_\rho, z, z')$ is done analytically using Equations (B.5), (B.6) from Appendix B.3 to obtain

$$G_{po}(\rho, z, z') = \frac{1}{2\pi} C_{po}(z, z')\ 2k_P \ \left(-j \frac{\pi}{2} H_0^{(2)}(k_P\rho) - K_0(k_P\rho) \right) \tag{7.14}$$

with $H_0^{(2)}$ the Hankel function and K_0 the modified Bessel function, both of the 2^{th} kind and of order 0. By using the small argument expansions of these functions, we see that the expression is well behaved at the origin $\rho \to 0$. By using the large argument expansion of $H_0^{(2)}$, we obtain for large transverse distances

$$\lim_{\rho \to +\infty} G_{po}(\rho, z, z') \approx \frac{1}{2\pi} C_{po}(z, z')\ 2k_P\ \left(-j\frac{\pi}{2}\right)\ e^{j\frac{\pi}{4}} \sqrt{\frac{\pi}{2}}\ \frac{e^{-jk_P\rho}}{\sqrt{k_P\rho}}. \tag{7.15}$$

We thus recover the characteristic behaviour of a cylindrical wavefront propagating with wavenumber k_P.

The Quasi-Static Field

When the field is evaluated for small transverse distances ρ, the period of the Bessel function is very large, such that the inverse Fourier transform is almost entirely determined by the slowly decaying part of $\widetilde{G}(k_\rho, z, z')$. This part has been extracted with $\widetilde{G}_{as}(k_\rho, z, z')$, where we assumed k_ρ much larger than any wavenumber $k_i = \omega\sqrt{\mu_i \epsilon_i}$. Since this assumption is equivalent with $\omega \to 0$, we obtain the quasi-static field constituents described by

$$G_{as}(\rho, z, z') = \sum_{m=1}^{3} \sum_{i=1}^{N_m} C_{as}^{mi} G_{as}^{m}(\rho, \Delta_i) \tag{7.16}$$

where the spatial counterparts of the spectral asymptotes are given in Table B.2 of Appendix B.4. Upon examining these expressions, we see that these functions are smooth for large z, z' separation Δ, but become almost singular when this distance tends to zero. In these cases, only the convergence factor $t = 1/k_{i,max}$ limits their amplitude for $\rho = 0$.

The Regular and Singular Parts

The inverse Fourier transform is thus done partly numerically and partly analytically. The total "Green's function" in the space domain

$$\begin{aligned} G(\rho, z, z') &= G_{nu}(\rho, z, z') + (G_{po}(\rho, z, z') + G_{bp}(\rho, z, z') + G_{as}(\rho, z, z')) \\ &= G_{nu}(\rho, z, z') + G_{an}(\rho, z, z') \end{aligned} \tag{7.17}$$

consist of the purely numerical result $G_{nu}(\rho, z, z')$ and the analytical part $G_{an}(\rho, z, z')$ $= G_{po}(\rho, z, z') + G_{bp}(\rho, z, z') + G_{as}(\rho, z, z')$. The numerical part $G_{nu}(\rho, z, z')$ thus contains the field constituents that could not be extracted analytically, and usually only gives a small contribution, typically still important for the field at intermediate distance. The dominant field behaviour for large transverse distance has been extracted analytically and is composed of the space wave field $G_{bp}(\rho, z, z')$ and the surface wave field $G_{po}(\rho, z, z')$. The dominant field contribution for small transverse distance is extracted as the quasi-static field contributions $G_{as}(\rho, z, z')$. However, for further use in the space domain, we rearrange these contributions into a regular part $G_R(\rho, z, z')$

and a singular part $G_S(\rho, z, z')$

$$\begin{aligned} G(\rho, z, z') &= (G_{nu}(\rho, z, z') + G_{po}(\rho, z, z') + G_{bp}(\rho, z, z')) + G_{as}(\rho, z, z') \\ &= G_R(\rho, z, z') + G_S(\rho, z, z') \end{aligned} \quad (7.18)$$

The regular part $G_R(\rho, z, z')$ should behave smoothly everywhere, including the pathological case $\rho \to 0$, such that it can always be integrated numerically very easily. From the previous section, it thus follows to combine the numerical part with the space and surface wave constituents of the field into $G_R(\rho, z, z') = G_{nu}(\rho, z, z') + G_{po}(\rho, z, z') + G_{bp}(\rho, z, z')$. A numerical integration is not possible in an efficient manner for a function with singular or almost singular behaviour. Such behaviour occurs typically for small spatial separation. Luckily however, the singular and quasi singular field behaviour has been isolated in closed form in $G_{as}(\rho, z, z')$ and these contributions will also be integrated further analytically such that $G_S(\rho, z, z') = G_{as}(\rho, z, z')$.

7.3 Space Domain Evaluation of Reaction Integrals

The z, z' dependent part of all reaction integrals was done analytically in the spectral domain in Section 6.4 of Chapter 6. All information regarding spatial separation in the Z direction and the type of testing and expansion function used in z, z' coordinates is thus incorporated already in the "Green's function" in the spectral domain, for which we keep the terminology "Green's function", although it is to be understood that they are no longer the field components excited by point-like excitations. After the inverse Fourier transform described above in Section 7.2, we obtain expressions of the form $G(\rho)$. The remaining evaluation of the reaction integrals takes place in the space domain and involves only the transverse x, y, x', y' or ρ, ϕ coordinates.

7.3.1 Types of Reaction Integrals in Space Domain

The remaining types of integrals that have to be done in the spatial domain can be grouped as surface-surface and line-line integrals of vector and scalar quantities

$$\int_{S_m} \vec{\Delta}_m(x, y) . \int_{S_n} G(\rho) \vec{\Delta}_n(x', y') \, \mathrm{d}S' \mathrm{d}S \quad (7.19)$$

$$\int_{S_m} \Pi_m(x, y) \int_{S_n} G(\rho) \Pi_n(x', y') \, \mathrm{d}S' \mathrm{d}S \quad (7.21)$$

$$\int_{l_m} \vec{\Delta}_m(x, y) . \int_{l_n} G(\rho) \vec{\Delta}_n(x', y') \, \mathrm{d}l' \mathrm{d}l \quad (7.20)$$

$$\int_{l_m} \Pi_m(x, y) \int_{l_n} G(\rho) \Pi_n(x', y') \, \mathrm{d}l' \mathrm{d}l \quad (7.22)$$

and combined surface-line or line-surface integrals of vector and scalar quantities

$$\int_{S_m} \vec{\Delta}_m(x,y).\int_{l_n} G(\rho)\vec{\Delta}_n(x',y')\ \mathrm{d}l'\mathrm{d}S \quad (7.23) \qquad \int_{S_m} \Pi_m(x,y)\int_{l_n} G(\rho)\Pi_n(x',y')\ \mathrm{d}l'\mathrm{d}S \quad (7.25)$$

$$\int_{l_m} \vec{\Delta}_m(x,y).\int_{S_n} G(\rho)\vec{\Delta}_n(x',y')\ \mathrm{d}S'\mathrm{d}l \quad (7.24) \qquad \int_{l_m} \Pi_m(x,y)\int_{S_n} G(\rho)\Pi_n(x',y')\ \mathrm{d}S'\mathrm{d}l \quad (7.26)$$

where

$$\rho = \sqrt{(x-x')^2+(y-y')^2}. \quad (7.27)$$

The possible combinations of integration domains for observation and source coordinates are depicted in Figure 7.5.

The evaluation of the above integrals over the testing functions are simplified as in Equations (3.51), (3.52) in the model evaluation of Section 3.5.1 of Chapter 3, by multiplying their value at the center x_c, y_c of the integration domains with their surface S_m or length l_m

$$S_m\vec{\Delta}_m(x_c,y_c).\int_{S_n} G(\rho')\vec{\Delta}_n(x',y')\ \mathrm{d}S' \quad (7.28) \qquad S_m\Pi_m(x_c,y_c)\int_{S_n} G(\rho')\Pi_n(x',y')\ \mathrm{d}S' \quad (7.30)$$

$$l_m\vec{\Delta}_m(x_c,y_c).\int_{l_n} G(\rho')\vec{\Delta}_n(x',y')\ \mathrm{d}l' \quad (7.29) \qquad l_m\Pi_m(x_c,y_c)\int_{l_n} G(\rho')\Pi_n(x',y')\ \mathrm{d}l' \quad (7.31)$$

$$S_m\vec{\Delta}_m(x_c,y_c).\int_{l_n} G(\rho')\vec{\Delta}_n(x',y')\ \mathrm{d}l' \quad (7.32) \qquad S_m\Pi_m(x_c,y_c)\int_{l_n} G(\rho')\Pi_n(x',y')\ \mathrm{d}l' \quad (7.34)$$

$$l_m\vec{\Delta}_m(x_c,y_c).\int_{S_n} G(\rho')\vec{\Delta}_n(x,',y')\ \mathrm{d}S' \quad (7.33) \qquad l_m\Pi_m(x_c,y_c)\int_{S_n} G(\rho')\Pi_n(x',y')\ \mathrm{d}S' \quad (7.35)$$

with now

$$\rho' = \sqrt{(x_c-x')^2+(y_c-y')^2}. \quad (7.36)$$

A further improvement would be to implement a complete Galerkin evaluation of these integrals also for the transverse $x, y,\ \ x', y'$ coordinates, since the z, z' integrations are already and exactly evaluated in a Galerkin sense. With the above simplifications however, the only remaining integrations over the source domains are

$$\int_{S_n} G(\rho')\vec{\Delta}_n(x',y')\ \mathrm{d}S' \quad (7.37) \qquad \int_{S_n} G(\rho')\Pi_n(x',y')\ \mathrm{d}S' \quad (7.39)$$

$$\int_{l_n} G(\rho')\vec{\Delta}_n(x',y')\ \mathrm{d}l' \quad (7.38) \qquad \int_{l_n} G(\rho')\Pi_n(x',y')\ \mathrm{d}l' \quad (7.40)$$

where the surface integration of a scalar quantity Equation (7.39) and line integrals of vector and scalar quantities Equations (7.38) and (7.40) can in principle be derived from the most complicated surface integral of a vector quantity Equation (7.37).

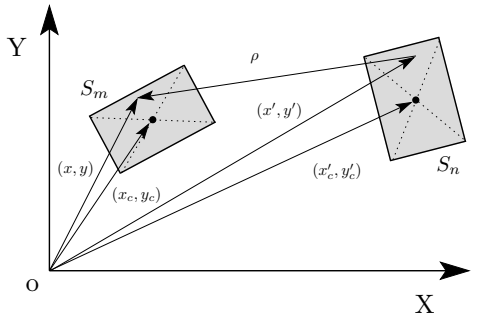

(a) Observation and source surface integrations.

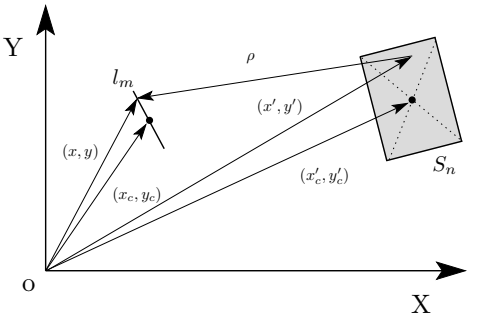

(b) Observation line integral and source surface integration.

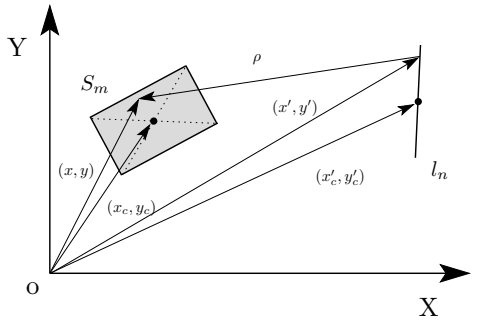

(c) Observation surface and source line integration domains.

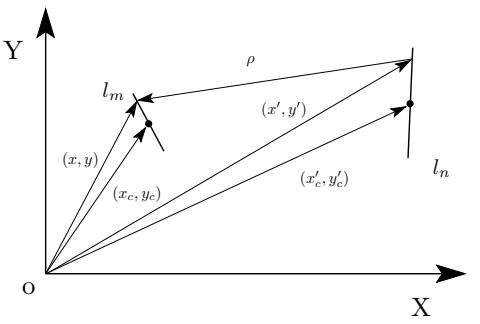

(d) Observation and source line integration domains.

Figure 7.5: Possible combinations of two-dimensional integration domains in the space domain for observation surface S_m or line segment l_m with source surface S_n or line segment l_n.

7.3.2 The Regular and Singular Parts of the Green's functions

Inserting the regular and singular parts of the Green's function Equation (7.18) into Equation (7.37), and obliterating the index n notation, we need to evaluate

$$\int_{S'} G(\rho')\vec{\Delta}(x', y') \, \mathrm{d}S' = \int_{S'} G_R(\rho')\vec{\Delta}(x', y') \, \mathrm{d}S' + \int_{S'} G_S(\rho')\vec{\Delta}(x', y') \, \mathrm{d}S'. \quad (7.41)$$

The regular part is integrated numerically in Section 7.3.3. The singular part can be integrated analytically as explained in Section 7.3.4.

As a last preparation, we note that both the regular and singular parts can be evaluated without additional error at this point by using the value of the constant function

$$\Pi(x', y') \quad = \quad \Pi(x'_c, y'_c) \tag{7.42}$$

and by using the exact expansion for the linear vector function

$$\begin{aligned}\vec{\Delta}(x', y') = \quad & \left[\Delta_x(x'_c, y'_c) + \frac{\partial \Delta_x}{\partial x'}(x'_c, y'_c)(x'-x'_c) + \frac{\partial \Delta_x}{\partial y'}(x'_c, y'_c)(y'-y'_c)\right] \vec{i}_x \\ & + \left[\Delta_y(x'_c, y'_c) + \frac{\partial \Delta_y}{\partial x'}(x'_c, y'_c)(x'-x'_c) + \frac{\partial \Delta_y}{\partial y'}(x'_c, y'_c)(y'-y'_c)\right] \vec{i}_y. \end{aligned} \tag{7.43}$$

7.3.3 Numerical Integration of Regular Part

The regular part of the Green's function $G_R(\rho')$ is not completely available in closed form, but all its contributions are very smooth as a function of ρ', and therefore this part can be safely integrated numerically. Since the discretisation is always chosen such that the size of each integration domain is much smaller then the variation of the field or Green's function in the spatial domain, we can approximate the regular part of the Green's function by the lowest order terms of its series expansion around the center point x'_c, y'_c

$$\begin{aligned} G_R(x', y') \quad \approx \quad & G_R(x'_c, y'_c) + \frac{\partial G_R}{\partial x'}(x'_c, y'_c)(x' - x'_c) + \frac{\partial G_R}{\partial y'}(x'_c, y'_c)(y' - y'_c) \\ & + \frac{1}{2}\frac{\partial^2 G_R}{\partial x'^2}(x'_c, y'_c)(x' - x'_c)^2 + \frac{1}{2}\frac{\partial^2 G_R}{\partial y'^2}(x'_c, y'_c)(y' - y'_c)^2 \\ & + \frac{\partial^2 G_R}{\partial x' \partial y'}(x'_c, y'_c)(x' - x'_c)(y' - y'_c). \end{aligned} \tag{7.44}$$

Line Integrals

Inserting Equations (7.42) and (7.44) into the line integral of a scalar quantity Equation (7.40), and expressing the derivatives of the regular part of the Green's function $G_R(\rho')$ in cylindrical coordinates, we obtain

$$\begin{aligned} & \int_{l'} G_R(\rho')\Pi(x', y')\ \mathrm{d}l' \approx \\ & \Pi(x'_c, y'_c)\left[G_R(\rho'_c)L_{00} + \frac{1}{\rho'^3_c}\frac{\partial G_R}{\partial \rho'}(\rho'_c)\left\{\frac{1}{2}\left(y'^2_c L_{20} + x'^2_c L_{02}\right) - x'_c y'_c L_{11}\right\}\right. \\ & \qquad \left. + \frac{1}{\rho'^2_c}\frac{\partial^2 G_R}{\partial \rho'^2}(\rho'_c)\left\{\frac{1}{2}\left(x'^2_c L_{20} + y'^2_c L_{02}\right) + x'_c y'_c L_{11}\right\}\right] \end{aligned} \tag{7.45}$$

while inserting Equations (7.43) and (7.44) into the line integral of a vector quantity Equation (7.38), neglecting higher order terms and again expressing the derivatives of

the regular Green's function $G_R(\rho')$ in cylindrical coordinates, we obtain the slightly more complicated result

$$\begin{aligned}
&\int_{l'} G_R(\rho')\vec{\Delta}(x',y')\ \mathrm{d}l' \approx \\
&\quad \vec{\Delta}(x'_c,y'_c)\left[G_R(\rho'_c)L_{00} + \frac{1}{\rho'^3_c}\frac{\partial G_R}{\partial \rho'}(\rho'_c)\left\{\frac{1}{2}\left(y'^2_c L_{20} + x'^2_c L_{02}\right) - x'_c y'_c L_{11}\right\}\right. \\
&\qquad\qquad \left. + \frac{1}{\rho'^2_c}\frac{\partial^2 G_R}{\partial \rho'^2}(\rho'_c)\left\{\frac{1}{2}\left(x'^2_c L_{20} + y'^2_c L_{02}\right) + x'_c y'_c L_{11}\right\}\right] \\
&\quad + \frac{\partial \vec{\Delta}}{\partial x'}(x'_c,y'_c)\frac{1}{\rho'_c}\frac{\partial G_R}{\partial \rho'}(\rho'_c)\left[\, x'_c L_{20} + y'_c L_{11}\right] \\
&\quad + \frac{\partial \vec{\Delta}}{\partial y'}(x'_c,y'_c)\frac{1}{\rho'_c}\frac{\partial G_R}{\partial \rho'}(\rho'_c)\left[\, y'_c L_{02} + x'_c L_{11}\right]
\end{aligned} \tag{7.46}$$

where the "line moment" integrals occurring in the above Equations (7.45) and (7.46) are defined as

$$L_{00} = \int_{l'} \mathrm{d}l' \tag{7.47}$$

$$L_{11} = \int_{l'} (x' - x'_c)(y' - y'_c)\ \mathrm{d}l' \tag{7.48}$$

$$L_{20} = \int_{l'} (x' - x'_c)^2\ \mathrm{d}l' \tag{7.49}$$

$$L_{02} = \int_{l'} (y' - y'_c)^2\ \mathrm{d}l' \tag{7.50}$$

and can be easily determined analytically for any line segment l'.

Surface Integrals

Similar formulas are obtained for the surface integrations. Inserting Equations (7.42) and (7.44) into the surface integral of a scalar quantity Equation (7.39), we obtain the formula

$$\begin{aligned}
&\int_{S'} G_R(\rho')\Pi(x',y')\ \mathrm{d}S' \approx \\
&\quad \Pi(x'_c,y'_c)\left[G_R(\rho'_c)S_{00} + \frac{1}{\rho'^3_c}\frac{\partial G_R}{\partial \rho'}(\rho'_c)\left\{\frac{1}{2}\left(y'^2_c S_{20} + x'^2_c S_{02}\right) - x'_c y'_c S_{11}\right\}\right. \\
&\qquad\qquad \left. + \frac{1}{\rho'^2_c}\frac{\partial^2 G_R}{\partial \rho'^2}(\rho'_c)\left\{\frac{1}{2}\left(x'^2_c S_{20} + y'^2_c S_{02}\right) + x'_c y'_c S_{11}\right\}\right]
\end{aligned} \tag{7.51}$$

while inserting Equations (7.43) and (7.44) into the surface integral of the vector quantity Equation (7.37), we obtain the more complicated result

$$\begin{aligned}
&\int_{S'} G_R(\rho')\vec{\Delta}(x',y')\ \mathrm{d}S' \approx \\
&\quad \vec{\Delta}(x'_c,y'_c)\left[G_R(\rho'_c)S_{00} + \frac{1}{\rho'^3_c}\frac{\partial G_R}{\partial \rho'}(\rho'_c)\left\{\frac{1}{2}\left(y'^2_c S_{20} + x'^2_c S_{02}\right) - x'_c y'_c S_{11}\right\}\right.
\end{aligned}$$

$$+\frac{1}{\rho_c'^2}\frac{\partial^2 G_R}{\partial \rho'^2}(\rho_c')\left\{\frac{1}{2}\left(x_c'^2 S_{20}+y_c'^2 S_{02}\right)+x_c' y_c' S_{11}\right\}\Bigg]$$
$$+\frac{\partial \vec{\Delta}}{\partial x'}(x_c',y_c')\frac{1}{\rho_c'}\frac{\partial G_R}{\partial \rho'}(\rho_c')\left[\, x_c' S_{20}+y_c' S_{11}\right]$$
$$+\frac{\partial \vec{\Delta}}{\partial y'}(x_c',y_c')\frac{1}{\rho_c'}\frac{\partial G_R}{\partial \rho'}(\rho_c')\left[\, y_c' S_{02}+x_c' S_{11}\right] \tag{7.52}$$

where the "surface moment" integrals occurring in Equations (7.51) and (7.52) are now defined as

$$S_{00}=\int_{S'} \mathrm{d}S' \tag{7.53}$$
$$S_{11}=\int_{S'} (x'-x_c')(y'-y_c')\ \mathrm{d}S' \tag{7.54}$$
$$S_{20}=\int_{S'} (x'-x_c')^2\ \mathrm{d}S' \tag{7.55}$$
$$S_{02}=\int_{S'} (y'-y_c')^2\ \mathrm{d}S' \tag{7.56}$$

can again be determined analytically for all regular geometrical shapes of the surface S'.

In all the above formulas, the "line moment" integrals L_{00}, L_{10}, L_{01}, L_{22} and the "surface moment" integrals S_{00}, S_{10}, S_{01}, S_{22} are available in closed form. The values of the scalar functions and vector functions $\Pi(x_c',y_c')$, $\vec{\Delta}(x_c',y_c')$ and their derivatives at the center point (x_c',y_c') of the source domain are known analytically. Only the value of the regular Green's function G_R and its derivatives

$$G_R(\rho_c'),\quad \frac{\partial G_R}{\partial \rho'}(\rho_c'),\quad \frac{\partial^2 G_R}{\partial^2 \rho'}(\rho_c') \tag{7.57}$$

have to be evaluated numerically at the transverse distance ρ_c' with

$$\rho_c'=\sqrt{(x_c-x_c')^2+(y_c-y_c')^2}. \tag{7.58}$$

7.3.4 Analytical Integration of Singular Part

The singular nature of the other part of the Green's function $G_S(\rho')$ excludes a numerical treatment, but all contributions to $G_S(\rho')$ are available in closed form and can also be integrated further analytically with some effort as described hereafter. The singular part of the Green's function consists of several contributions that are the spatial counterparts of the asymptotic functions that were extracted in the spectral domain in order to make the numerical inverse Fourier transformation possible. The singular part of the Green's function is written as in Equation (7.16)

$$G_S(\rho',z,z') \;=\; \sum_{m=1}^{3}\sum_{i=1}^{N_m} C_{as}^{mi} G_{as}^{m}(\rho',\Delta_i) \tag{7.59}$$

where the first summation runs over the type $m = 1, 2, 3$ of the extracted function of which the expressions are given in Table B.2 of Appendix B.4, and the second summation i takes into account N_m multiple z, z' distances Δ_i for that type of function.

Line Integrals

Inserting the complete expansion for the scalar quantity Equation (7.42), but retaining the analytical expressions for the singular part of the Greens' function $G_S(\rho')$, we obtain for the line integral of a scalar quantity (7.40)

$$\int_{l'} G_S(\rho')\Pi(x', y') \, \mathrm{d}l' = \Pi(x'_c, y'_c) \int_{l'} G_S(\rho') \, \mathrm{d}l' \tag{7.60}$$

while combining the exact expansion for the vector quantity Equation (7.43) with the analytical expressions for $G_S(\rho')$ for the line integral of a vector Equation (7.38) gives

$$\begin{aligned}\int_{l'} G_S(\rho')\vec{\Delta}(x', y') \, \mathrm{d}l' = \vec{\Delta}(x'_c, y'_c) &\int_{l'} G_S(\rho') \, \mathrm{d}l' \\ &+ \frac{\partial \vec{\Delta}}{\partial x'}(x'_c, y'_c) \left[\int_{l'} x' G_S(\rho') \, \mathrm{d}l' - x'_c \int_{l'} G_S(\rho') \, \mathrm{d}l' \right] \\ &+ \frac{\partial \vec{\Delta}}{\partial y'}(x'_c, y'_c) \left[\int_{l'} y' G_S(\rho') \, \mathrm{d}l' - y'_c \int_{l'} G_S(\rho') \, \mathrm{d}l' \right]. \end{aligned} \tag{7.61}$$

We thus see that the line integrals that have to be evaluated analytically are all of the form

$$\int_{l} \begin{Bmatrix} 1 \\ x \\ y \end{Bmatrix} G_S(\rho, \Delta) \, \mathrm{d}l \tag{7.62}$$

where the integrations run over a straight line segment from the Cartesian coordinates x_u, y_u to x_v, y_v or from the cylindrical coordinates ρ_u, ϕ_u to ρ_v, ϕ_v as depicted in Figure 7.6. Apart from these coordinates, the analytical integration is sometimes facilitated by the introduction of a "rotated" η, ξ coordinate system, such that the ξ axis stands orthogonally to the line segment l. In these coordinates, the line integrals are written as

$$\int_{l} \begin{Bmatrix} 1 \\ x \\ y \end{Bmatrix} G_S(\rho, \Delta) \, \mathrm{d}l = \int_{\phi_u}^{\phi_v} \begin{Bmatrix} 1 \\ \rho\cos\phi \\ \rho\sin\phi \end{Bmatrix} G_S(\rho_l(\phi), \Delta) \sqrt{\rho^2 + \left(\frac{\partial \rho}{\partial \phi}\right)^2} \, \mathrm{d}\phi \tag{7.63}$$

$$= \int_{\eta_u}^{\eta_v} \begin{Bmatrix} 1 \\ L\cos\phi_L + \eta\sin\phi_L \\ L\sin\phi_L - \eta\cos\phi_L \end{Bmatrix} G_S(\sqrt{L^2 + \eta^2}, \Delta) \, \mathrm{d}\eta \tag{7.64}$$

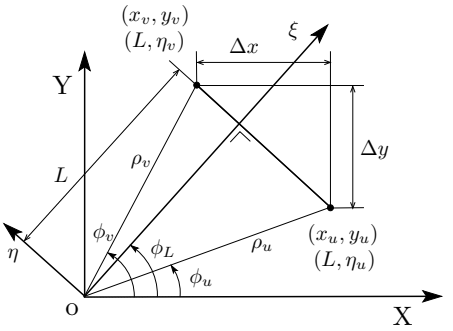

Figure 7.6: Analytical integration over a line segment in a cylindrical ρ, ϕ and in a "rotated" ξ, η coordinate system.

where L is the length on the ξ axis to the line segment, ϕ_L is the angle it substends with the X axis, and $\rho_l(\phi)$ the equation of the line segment itself in cylindrical coordinates

$$\rho_l(\phi) \quad = \quad \frac{L}{\cos(\phi - \phi_L)}. \tag{7.65}$$

The full analytical evaluation of $G_S(\rho)$ involves inserting the summation of Equation (7.59) over the types of extracted functions $G^m_{as}(\rho, \Delta)$, and over the multiple possible z, z' distances Δ_i. From the explicit formulas for the functions $G^m_{as}(\rho, \Delta)$ given in Table B.2 of Appendix B.4, we see that the basic integrals to be evaluated are all of the form

$$\int_l \left\{ \begin{array}{c} 1 \\ x \\ y \end{array} \right\} \frac{1}{\sqrt{\rho^2 + \Delta^2}} \, \mathrm{d}l, \tag{7.66}$$

$$\int_l \left\{ \begin{array}{c} 1 \\ x \\ y \end{array} \right\} \ln\left(\sqrt{\rho^2 + \Delta^2} + \Delta\right) \, \mathrm{d}l, \tag{7.67}$$

$$\int_l \left\{ \begin{array}{c} 1 \\ x \\ y \end{array} \right\} \sqrt{\rho^2 + \Delta^2} \, \mathrm{d}l \tag{7.68}$$

for which the full analytical results are given completely in Appendix C.1.

Surface Integrals

Inserting the complete expansion for the scalar quantity Equation (7.42), but retaining the analytical expressions for the singular part of the Greens' function $G_S(\rho')$, we obtain for the surface integral of a scalar quantity (7.39)

$$\int_{S'} G_S(\rho') \Pi(x', y') \, \mathrm{d}S' = \Pi(x'_c, y'_c) \int_{S'} G_S(\rho') \, \mathrm{d}S' \tag{7.69}$$

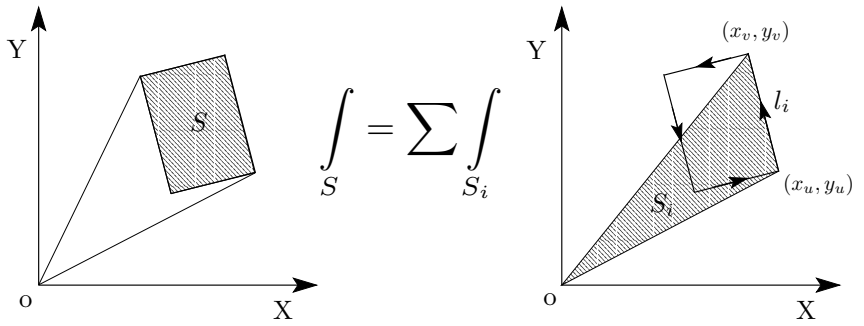

Figure 7.7: Decomposition of the domain S of the surface integration into triangular domains S_i.

while combining the exact expansion for the vector quantity Equation (7.43) with the analytical expressions for $G_S(\rho')$ for the surface integral of a vector Equation (7.37) gives

$$\begin{aligned}\int_{S'} G_S(\rho')\vec{\Delta}(x',y')\ \mathrm{d}S' = \vec{\Delta}(x'_c,y'_c)\int_{S'} G_S(\rho')\ \mathrm{d}S' \\ +\frac{\partial\vec{\Delta}}{\partial x'}(x'_c,y'_c)\left[\int_{S'} x'G_S(\rho')\ \mathrm{d}S' - x'_c\int_{S'} G_S(\rho')\ \mathrm{d}S'\right] \\ +\frac{\partial\vec{\Delta}}{\partial y'}(x'_c,y'_c)\left[\int_{S'} y'G_S(\rho')\ \mathrm{d}S' - y'_c\int_{S'} G_S(\rho')\ \mathrm{d}S'\right]. \quad (7.70)\end{aligned}$$

The analytical solution for the following types of surface integrals

$$\int_S \begin{Bmatrix}1\\x\\y\end{Bmatrix} G_S(\rho,\Delta)\ \mathrm{d}S \quad = \quad \sum_i \int_{S_i} \begin{Bmatrix}1\\x\\y\end{Bmatrix} G_S(\rho,\Delta)\ \mathrm{d}S_i \qquad (7.71)$$

is facilitated by decomposing the integral over the surface S into a sum of surface integrals over the triangular area's S_i, each bounded by the outer edge l_i and the connecting lines of the origin o with the points $x_u, y_u,\ \ x_v, y_v$ as shown in Figure 7.7. These resulting types of surface integrals can again be evaluated as shown in Figure 7.8 in the cylindrical ρ, ϕ coordinate system of Figure 7.8(a) or in the "rotated" ξ, η coordinate system of Figure 7.8(b) as

$$\int_{S_i} \begin{Bmatrix}1\\x\\y\end{Bmatrix} G_S(\rho,\Delta)\ \mathrm{d}S_i = \int_{\phi_u}^{\phi_v}\int_0^{\rho_l(\phi)} \begin{Bmatrix}1\\\rho\cos\phi\\\rho\sin\phi\end{Bmatrix} G_S(\rho,\Delta)\ \rho\mathrm{d}\rho\mathrm{d}\phi \qquad (7.72)$$

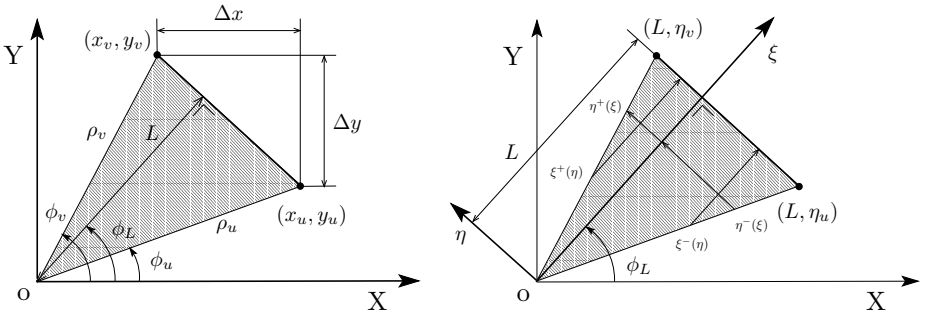

(a) Cylindrical ρ, ϕ coordinate system.

(b) "Rotated" ξ, η coordinate system.

Figure 7.8: Analytical surface integration over a triangular domain.

$$= \int_0^L \int_{\eta^-(\xi)}^{\eta^+(\xi)} \left\{ \begin{array}{c} 1 \\ \xi\cos\phi_L - \eta\sin\phi_L \\ \xi\sin\phi_L + \eta\cos\phi_L \end{array} \right\} G_S(\sqrt{\xi^2+\eta^2}, \Delta)\ \mathrm{d}\eta\mathrm{d}\xi \quad (7.73)$$

$$= \int_{\eta_u}^{0} \int_{\xi^-(\eta)}^{L} + \int_0^{\eta_v} \int_{\xi^+(\eta)}^{L} \left\{ \begin{array}{c} 1 \\ \xi\cos\phi_L - \eta\sin\phi_L \\ \xi\sin\phi_L + \eta\cos\phi_L \end{array} \right\} G_S(\sqrt{\xi^2+\eta^2}, \Delta)\ \mathrm{d}\xi\mathrm{d}\eta \quad (7.74)$$

where the inner integration limit for the cylindrical coordinate system $\rho_l(\phi)$ is Equation (7.65), and for the "rotated" ξ, η coordinate system, the inner integration limits are

$$\eta^+(\xi) = \frac{\eta_v}{L}\xi \quad (7.75) \qquad \xi^+(\eta) = \frac{L}{\eta_v}\eta \quad (7.77)$$

$$\eta^-(\xi) = \frac{\eta_u}{L}\xi \quad (7.76) \qquad \xi^-(\eta) = \frac{L}{\eta_u}\eta. \quad (7.78)$$

The full analytical surface integration also involves inserting an expansion of the type Equation (7.59) and evaluating all the occurring integrals which are ultimately composed of the basic types

$$\int_S \left\{ \begin{array}{c} 1 \\ x \\ y \end{array} \right\} \frac{1}{\sqrt{\rho^2+\Delta^2}}\ \mathrm{d}S, \quad (7.79)$$

$$\int_S \left\{ \begin{array}{c} 1 \\ x \\ y \end{array} \right\} \ln\left(\sqrt{\rho^2+\Delta^2}+\Delta\right)\ \mathrm{d}S, \quad (7.80)$$

$$\int_S \left\{ \begin{array}{c} 1 \\ x \\ y \end{array} \right\} \sqrt{\rho^2 + \Delta^2}\, \mathrm{d}S \tag{7.81}$$

for which the full analytical results are given completely in Appendix C.2.

7.4 Conclusions

This chapter has focused on some techniques applied in the numerical evaluation of the inverse Fourier transform and the remaining space domain evaluation of the reaction integrals for the MoM impedance matrix. The physically decisive behaviour of the electromagnetic field in the space domain can be derived in closed form from the distinctive features of the field in the spectral domain. We can thus extract the space wave, surface wave and quasi-static field components in closed form. The part which cannot be extracted analytically in the spectral domain has to be Fourier transformed numerically to the space domain. For the evaluation of the reaction integrals, the numerical and analytical parts of the field are rearranged into a well behaved regular part and a quasi-singular part. The regular part can be integrated safely numerically, while the quasi-singular terms can again be integrated fully analytically. In this way, it is attempted to reduce any computational expensive purely numerical work to a minimum, while dealing with all important computations in an analytical manner. Now that a fairly complete overview of the implementation of a 3D boundary integral equation solver for planar stratified media has been presented, we can move to the ultimate goal of the work presented, to perform a full wave electromagnetic analysis of typical high frequency problems in a planar stratified surround as presented in the next chapter.

Chapter 8

Applications : "Quasi 3D" Structures in Planar Stratified Media

8.1 Introduction

The integral equation full wave electromagnetic solver MAGMAS3D developed in this work and described in the previous chapters can be applied to analyse a multitude of practical problems. The only requirement is that the physical structure fits in the framework of, or in a first approximation can be simplified into, a "quasi 3D" structure in a planar multilayered environment as described in Section 5.7 in Chapter 5. Due to the technical background of the problem, most of the problems that one first thinks of as being fully three dimensional are upon closer investigation actually covered by the formulation developed in this work.

The validation of the theory and software developed in this work is given in this chapter. It is performed by comparison with known analytical results, published simulated and measured results from open literature, and comparison with commercially available full wave software packages such as the integral equation based Zeland Software IE3D and the present day flag ship EM simulator, the High Frequency Structure Simulator (HFSS) provided by Ansoft Corporation, which uses the Finite Element Method (FEM).

The validation examples given below are dived into three categories of increasing complexity which roughly correspond to the gradual development of the software. The first class of examples are the simplest and are primarily aimed at a first verification

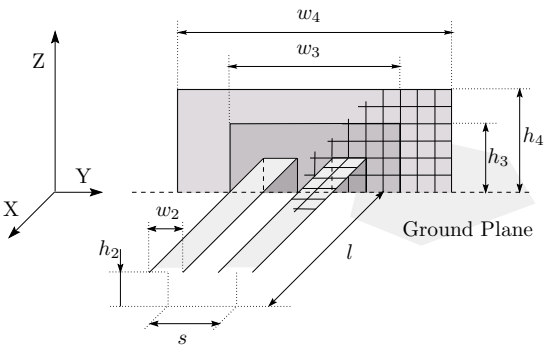

Figure 8.1: From a "circuit-theoretical" to a "field-theoretical" short circuit of a two-conductor transmission line.

of correctness of the software. The typical antenna structures are already more complicated and are grouped in the second category. The circuit oriented examples of the last category are the most complicated and most demanding of the software, but also constitute the potentially biggest area of future growth and application of numerical electromagnetics.

8.2 Basic Test Structures

The examples in this section are rough first time validations of the techniques developed in this work. The first two examples were actually analysed with separate stand alone test software, not integrated within the MAGMAS3D framework. This test software can handle quasi 3D structures as described in Chapter 5, but only for a homogeneous medium, or a half open homogeneous space above an infinite perfectly conducting ground plane. However, the computations are performed as if a general layered medium is present. In this way, the basic principles of the hybrid field formulation and combined spectral space domain approach can be tested based on the simple free space scalar Green's function and without the additional complications that arise in a general multilayered medium. The third example is the first result of the more general MAGMAS3D software, the implementation of which was strongly aided by the experience gained in the development of the test software.

8.2.1 Reflection of Even and Odd Modes on 2-Conductor Line

In this example, we illustrate the difference between a "circuit-theoretical" and a "field-theoretical" short circuit of a transmission line. The geometry is given in Figure 8.1. A two-conductor transmission line is located above an infinite ground plane.

The "circuit-theoretical" short is obtained by connecting the metallic lines of this waveguiding structure straight to the ground plane. A "field-theoretical" short circuit in principle requires an infinitely large perfectly conducting vertical plate. Therefore, progressive better short circuits are obtained with the increasing size of a finite vertical plate as indicated in Figure 8.1. Dimensions for the transmission line are $w_2 = 1cm$, $h_2 = 1.5cm$, $s = 2cm$. We will also compare the reflection for the even mode and odd mode. For the dimensions stated above these modes have characteristic impedances of 90Ω for the even mode and 280Ω for the odd mode. The S-parameter reference plane

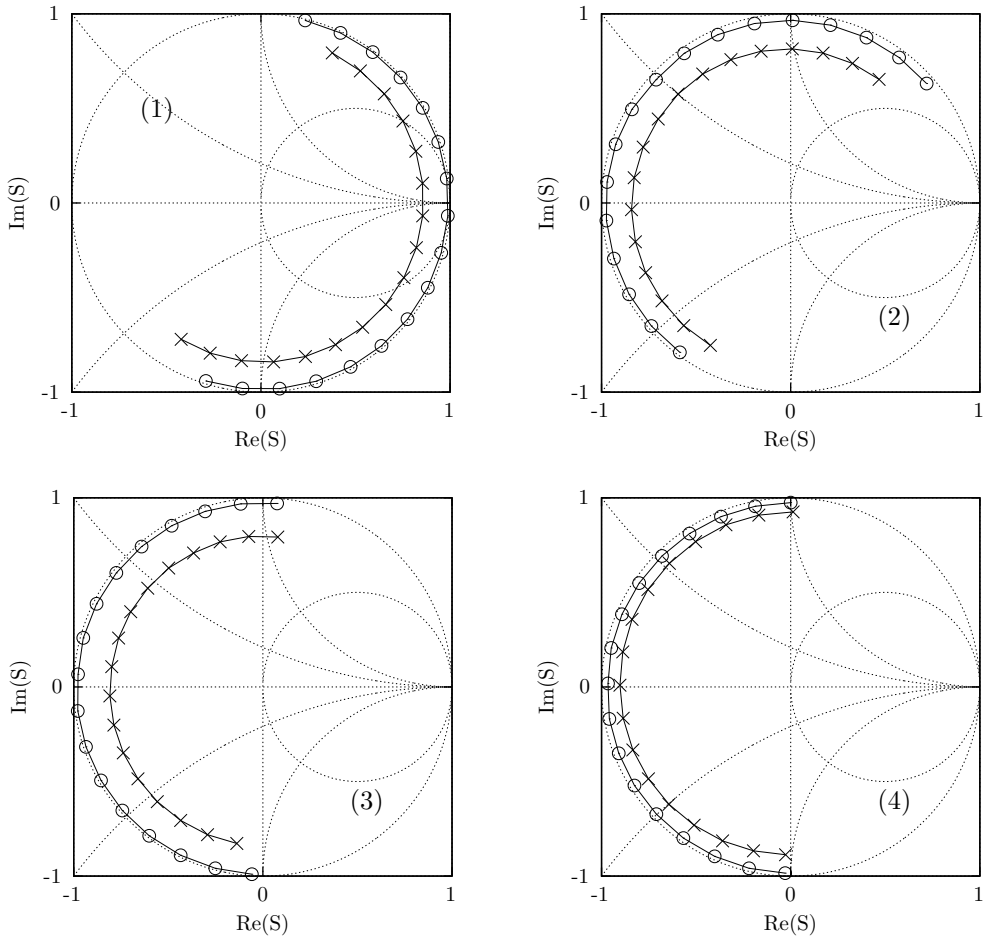

Figure 8.2: Smith chart representation of the reflection coefficient S_{11} on the two conductor transmission line of Figure 8.1 for even (×) and odd mode (○): (1) open, (2) "circuit-theoretical" short circuit by connecting the conductors straight to the ground plane, (3), (4) progressive better "field-theoretical" short circuits with a vertical plate of increasing size, 1.4-1.8 GHz, 17 points.

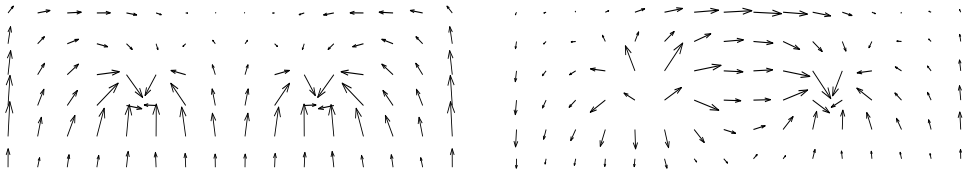

(a) Even mode. (b) Odd mode.

Figure 8.3: Vector current distributions on the vertical plate with size w_4, $h_4$of Figure 8.1 for even and odd mode at the central frequency 1.6 GHz.

is located at one wavelength from the short at 1.6 GHz, at $l = 18.75cm$. The computed S-parameters are given on a Smith chart from 1.4-1.8 GHz in 17 frequency points for even ($\times$) and odd ($\circ$) mode in Figure 8.2. As a reference result, the reflection for an open line is given first in Figure 8.2(1). The "circuit-theoretical" short circuit results of Figure 8.2(2) are compared with the results of a "field-theoretical" short circuit in Figures 8.2(3), 8.2(4) for a vertical rectangular plate of dimensions $w_3 = 8cm$, $h_3 = 3cm$, $w_4 = 12cm$, $h_4 = 4.5cm$. The largest plate has 16×6 subdivisions along Y and Z, while the transmission line conductors have 2×25 subdivisions along Y and X. As expected, the short circuit performs better for the odd mode, as the field distribution is more confined between the conductors. Also notice that the amplitude of the reflection coefficient S_{11} is smaller for the even mode, indicating a larger radiation loss. The resulting vector current distributions on the largest vertical plate with dimensions w_4, h_4 are depicted at the central frequency of 1.6 GHz in Figure 8.3.

8.2.2 Resonance of Closed Rectangular Cavity

Figure 8.4 shows a perfectly conducting rectangular cavity constructed out of horizontal and vertical conducting plates. For such a simple rectangular cavity the resonance frequencies are known analytically. As a verification of the developed software, in this example we attempt to calculate these frequencies in a numerical manner. The numerical approach can also be applied for arbitrarily shaped cavities where no analytical expressions for the resonant frequencies are available.

A first method to compute the resonant frequencies numerically consists of monitoring the numerical stability of the solution of the EFIE. The EFIE has no unique solution for the current on the surface of the cavity at the resonant frequencies (see Section 3.5.1 of Chapter 3). This theoretical fact causes the numerical solution to become unstable in the neighbourhood of a resonance. The resonant frequencies can then be detected by plotting the condition number of the discrete matrix representation of the integral equation as a function of frequency for a fixed geometry, or as a function of

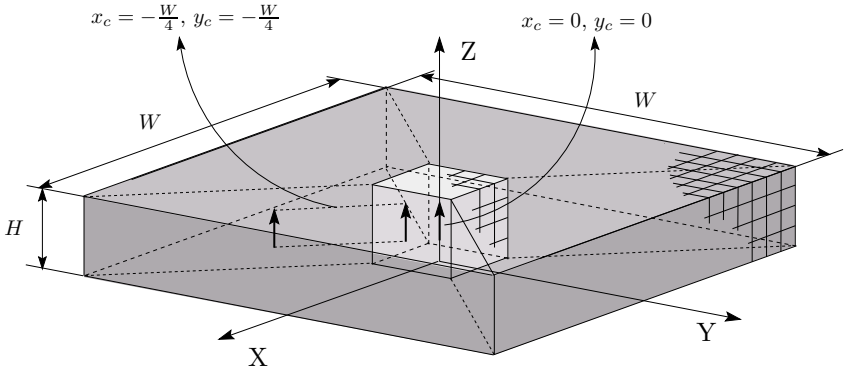

Figure 8.4: Perfectly conducting rectangular cavity with a dipole current source excitation. The frequency is kept fixed while the width w is varied to detect the analytically known resonance frequencies in a numerical manner. The resonances that can be detected in this way depend upon the position x_c, y_c of the excitation within the cavity.

a varying characteristic dimension for a fixed frequency. The first technique has been tested with our software but did not give the desired result with a sufficient degree of accuracy, as the number of unknowns (up to 3300) seems to be too large. Also, with the numerical techniques developed in this work, the numerically intensive computation of the Green's functions has to be redone for each frequency point, which is rather inefficient for this particular test. The second approach in which the frequency is kept fixed was used in [277] for a very simple two dimensional example with a very limited number of unknowns. This approach is also used in our three dimensional example, where we keep the frequency fixed at 1.875 GHz and vary the lateral size W of the rectangular boxes. The Green's functions now have to be computed only once and simply stored for reuse with a series of different lateral dimensions W. The heigh of the cavity is also kept fixed at a small dimension $H = 0.04m$ compared to the wavelength $\lambda = 0.16m$ such that no resonances can be associated with the Z direction. It also limits the numerically intensive computation of Green's functions to a minimum. The structure is excited with a simple vertical dipole current excitation as depicted in Figure 8.4. The widths at which a resonance is expected are now given as

$$W_{m,n} = \sqrt{m^2 + n^2}\frac{\lambda}{2} \tag{8.1}$$

with m, n the modenumbers associated with the field distributions along the X, Y directions. The lowest order resonance situations that we wish to calculate are

$$W_{1,1} = \sqrt{2}\frac{\lambda}{2} = 0.1131m, \tag{8.2}$$

$$W_{1,2} = \sqrt{5}\frac{\lambda}{2} = 0.1789m, \tag{8.3}$$

$$W_{2,2} = \sqrt{8}\frac{\lambda}{2} = 0.2263m. \tag{8.4}$$

The width W was thus varied between $0.04m$ and $0.25m$. The largest box structure has $25 \times 25 \times 4$ subdivisions along X,Y and Z. The technique of [277] again gave insatisfactory results as the condition number depends on the matrix size which varied in our example from 220 to 3300 unknowns, such that the resonances could hardly be distinguished from the monotonic increase with matrix size. Luckily, the resonances can also be detected in a more physical manner by examining the electromagnetic

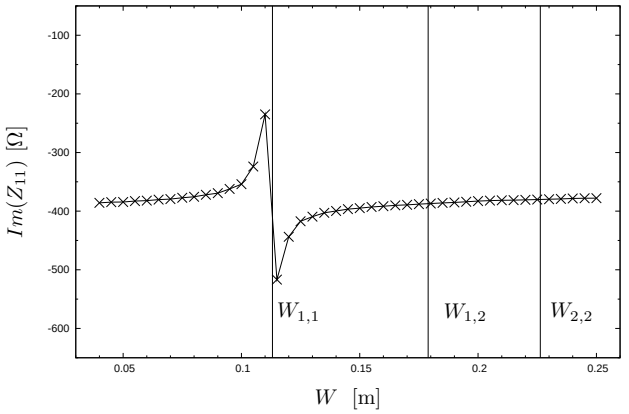

(a) Excitation in middle at $x_c = 0, y_c = 0$

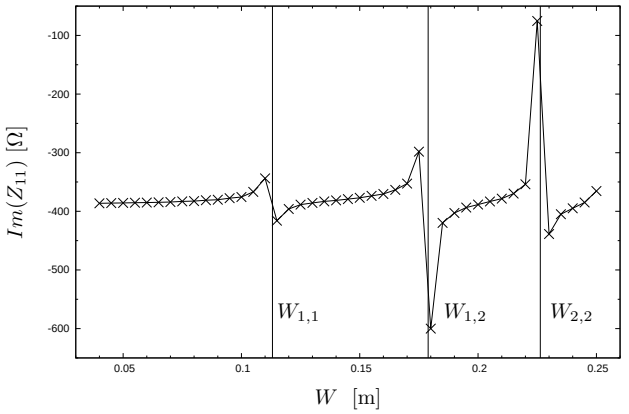

(b) Excitation in corner at $x_c = -W/4$, $y_c = -W/4$.

Figure 8.5: Imaginary part of the self impedance of the imposed current source for 33 cavity widths W between $0.04m$ and $0.25m$. The detection of cavity resonances at widths $W_{m,n}$ depends on the position of the excitation x_c, y_c within the box.

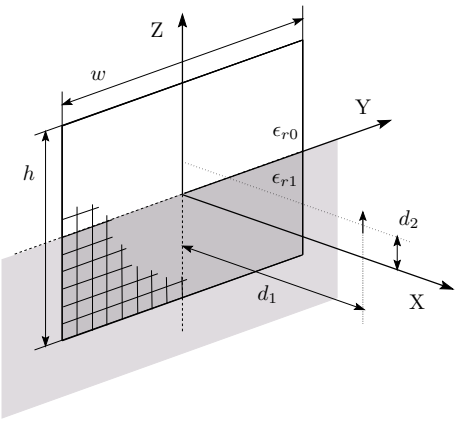

Figure 8.6: A vertical conducting plate penetrating an air-dielectric interface and illuminated by a current dipole source.

self-coupling of the imposed dipole current. The real part of this self impedance is necessarily zero since no radiation can leave the cavity. The reactive imaginary part however undergoes a characteristic jump as we pass through a resonant situation. Figure 8.5(a) plots the imaginary part of the self impedance as a function of 33 cavity widths W between $0.04m$ and $0.25m$, when the excitation is positioned perfectly in the middle of the cavity. Notice that for this case, only the first resonance seems to be detected. This immediately points out the drawback for this approach, since the measure in which a resonant field distribution is excited strongly depends on the location of the excitation. By positioning the current source perfectly in the middle, the higher order asymmetric field distributions of the $m, n = 1, 2$ and $m, n = 2, 2$ modes are not excited at all. Figure 8.5(b) demonstrates that by moving the excitation into the corner of the cavity at $x_c = -W/4$, $y_c = -W/4$, these higher order resonances are also correctly detected.

8.2.3 Current Distribution on Vertical Plate Penetrating a Dielectric Interface

In this example, we verify for a generic test structure that all analytical and numerical work for the discretisation of the BIE in a stratified medium described in the previous chapters translates into the correct behaviour of the current distribution on a macroscopic scale.

The test structure of Fig. 8.6 shows a large vertical conducting surface that penetrates the interface between two infinite media. The upper half space has $\epsilon_{r0} = 1.0$, while the lower half space has $\epsilon_{1r} = 16.0$. The dimensions of the plate are $w = 10.0cm$, $h = 7.5cm$, and the air-dielectric interface is located in the middle of the plate.

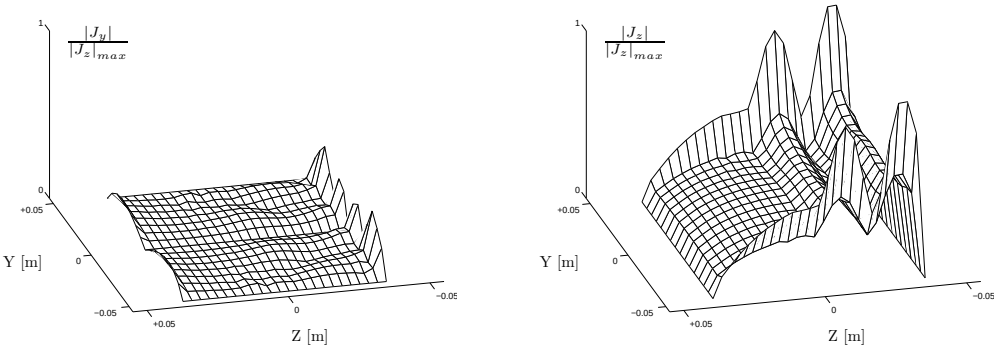

(a) Amplitude of J_y.

(b) Amplitude of J_z.

Figure 8.7: Amplitude of Y, Z current components on the large vertical plate of Figure 8.6.

The computation was done with 16×12 subdivisions along Y and Z. The plate is illuminated with a vertical current dipole located at $d_1 = 10cm$, $d_2 = 1.25cm$ as illustrated in Fig. 8.6. The frequency is 1.875 GHz. At this frequency, the top half of the plate has a vertical dimension which corresponds to a quarter wavelength in air, while in the lower half space, it is a complete wavelength high.

By the direction of the illuminating current source, we expect a dominant J_z component. This is satisfied by comparison of the amplitudes of the Y, Z current components depicted in Figures 8.7(a) and 8.7(b). We also expect the different wavelengths in the upper and lower medium to manifest themselves in the current distribution. This is seen most clearly in Figure 8.7(b).

The behaviour of the J_z current component over the interface at $z = 0$ also needs to be verified. The line of reasoning is similar to the one given in [244]. From the continuity of the H_y field components over the interface close the surface of the plate, it follows that the J_z current components are also continuous at $z = 0$. Continuity of the E_x field across the interface can be related to the charge densities and thus the derivatives of the J_z currents just above and below the interface as

$$\frac{\frac{\partial J_z}{\partial z}(0+)}{\frac{\partial J_z}{\partial z}(0-)} = \frac{\epsilon_{r0}}{\epsilon_{r1}} \tag{8.5}$$

which is also satisfied in Figure 8.7(b).

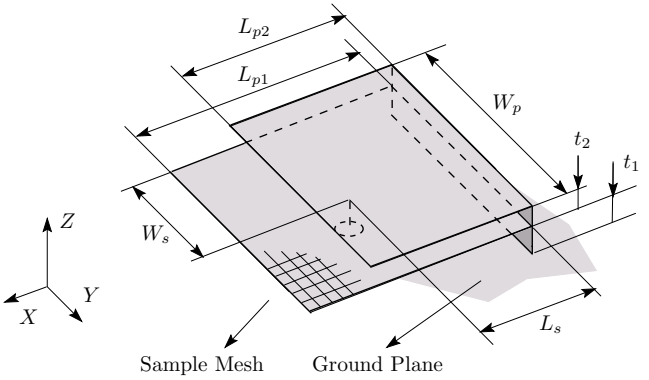

Figure 8.8: Structure of a probe fed stacked quarter wavelength patch antenna with vertical short circuit.

8.3 Antennas

In this section, a number of quasi three dimensional antenna structures are analysed. These three dimensional antennas typically result from efforts to improve the characteristics of traditional printed planar antennas, such as their limited bandwidth and efficiency. A possible technique to improve the bandwidth is to use electrically thicker or multilayer substrates, as in the structure of Section 8.3.3. This has however the disadvantage of increasing the physical size of the antenna and it also enhances the propagation of surface wave modes. At higher frequencies, this can cause a reduction of radiation efficiency, and an increased mutual coupling when multiple antennas are disposed in array configurations. One technique to avoid mutual coupling in arrays is the use of metallic cavities to enclose the radiator as in Section 8.3.4. Surface wave excitation can be suppressed by reducing substrate permittivity up to the point where air filled antennas are considered as in the first example of Section 8.3.1. For present day mobile communications, the physical size of the antenna has to be limited and the stringent design specifications can only be met by leaving the traditional planar antenna structure and using the additional degrees of freedom available in quasi three dimensional antennas as the ones of Sections 8.3.1, 8.3.2, 8.3.3 given below.

8.3.1 The Stacked Quarter Wavelength Patch Antenna

In practical communications systems, one often requires wideband or dual frequency operation, for which it is very attractive to use a single antenna element. Dual frequency operation can be achieved in a single element by adding shorting pins. The bandwidth can be improved by exploiting the effect of mutual coupling between two stacked (placed above eachother) or juxtaposed (placed next to eachother) patches.

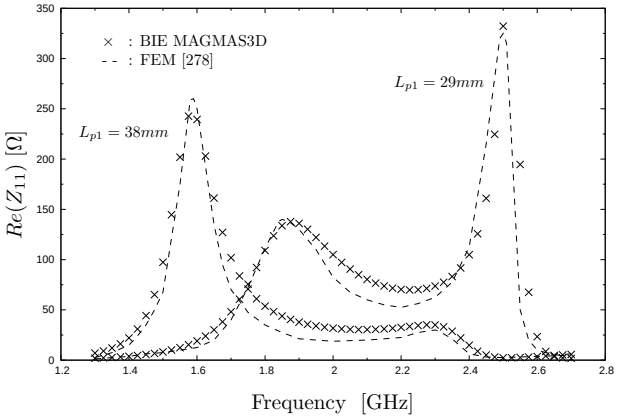

Figure 8.9: Real part of the input impedance of the antenna of Figure 8.8, 1.3-2.7 GHz, 57 points.

In this way, the resonance frequencies of two slightly different sized resonators can be "smeared out" into wideband frequency operation. The juxtaposed configuration however results in a significantly wider structure. In [278], these considerations are combined in the design depicted in Figure 8.8. The antenna consist of two stacked patches, constructed simply in air for which we assume $\epsilon_r = 1.0$. The size of the patches can be reduced from the standard half wavelength to only a quarter wavelength by short circuiting them at the edge with a vertical conducting plate. This vertical short circuit generates a mirror image (although an imperfect one) to simulate the other half of the patches. The position of the two resonance frequencies can be shifted by altering the dimensions of the patches and in this way a dual band antenna (resonance frequencies clearly separated) or a wideband antenna (resonances blurred together) can be obtained. The dimensions in Figure 8.8 are $W_p = 35.0mm$, $L_{p2} = 25.0mm$, $t_1 = 6.8mm$, $t_2 = 4.8mm$, $L_s = 18.0mm$, $W_s = 17.5mm$. Figure 8.9 depicts the real part of the input impedance for two values of the length of the lower patch, $L_{p1} = 29mm$ and $L_{p1} = 38mm$ in the frequency band 1.2-2.7 GHz in 57 points. The upper patch was discretised using 13×16 subdivisions, while the lower patch has 15×16 and 18×16 subdivisions along X and Y for sizes $L_{p1} = 29mm$ and $L_{p1} = 38mm$ respectively. The vertical wall has 16×3 subdivisions along Y and Z between the ground plane and middle patch, and 16×2 subdivisions between the two patches. The results of [278] were obtained with their own Finite Element Method (FEM) and takes into account the finite thickness of the metal sheets ($0.3mm$), assumes a finite ground plane of $100mm \times 100mm$ and employs a special probe model for the feed. Our results assume infinitely thin metal, an infinite ground plane and we use only a constant vertical current to model the probe feed.

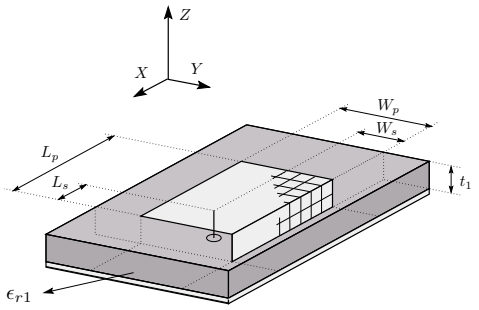

Figure 8.10: Geometry of short circuited probe fed patch antenna fabricated on single layer substrate.

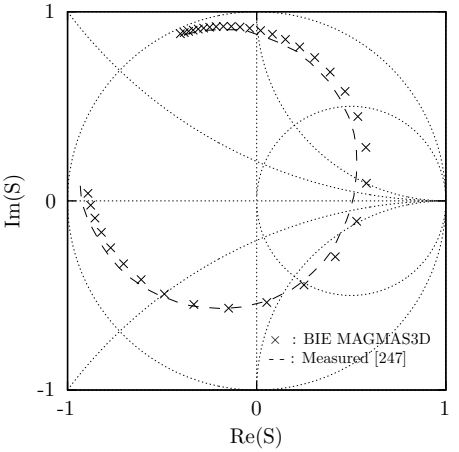

Figure 8.11: Input reflection S_{11} for the antenna of Figure 8.10, 2.6-2.95 GHz, 36 points.

8.3.2 The Short Circuited Patch Antenna

The same principle is applied for the probe fed short circuited patch antenna of Figure 8.10. However, this single patch antenna is fabricated on a single layer Duroid 5870 substrate with $t_1 = 1.57mm$, $\epsilon_{r1} = 2.33$ and loss tangent $\tan\delta = 0.0012$. The dimensions of the patch are $W_p = 30mm$, $L_p = 42mm$. The patch has 30×20 subdivisions along X and Y. The vertical wall has 30×2 subdivisions along X and Z. The probe feed is positioned at $W_s = 9mm$, $L_s = 4.2mm$. Figure 8.11 compares the measured results for the input reflection coefficient S_{11} of this structure from [247], [248], [249] with our computed results in the frequency band 2.6-2.95 GHz in 36 points on a Smith chart. In our simulations, the probe feed was modeled with a constant vertical current and the losses were neglected. Notice that the antenna is not matched to the feed as it was not produced with a specific application in mind, but only to validate theory and numerical computations.

8.3.3 The Patch Antenna with Vertical Metalisation

A more complicated antenna is depicted in Figure 8.12. The antenna is fabricated in a double layer medium. The lower substrate (RO 3003) has $\epsilon_{r1} = 3.00$, $t_1 = 1.54mm$, $\tan\delta = 0.0013$ while the upper layer is the same as in the previous example. The antenna consists of two patches, connected with a vertical metallic wall. Their dimensions are $W_p = 30mm$, $L_p = 40mm$ while the coaxial feed is positioned at $W_s = 11.25mm$, $L_s = 5.00mm$. The two patches both have 30×20 subdivisions along X and Y, and the vertical wall has 30×2 subdivisions along X and Z. Figures 8.13 and 8.14 compare the measurements of S_{11} from [249] with our simulated results in the

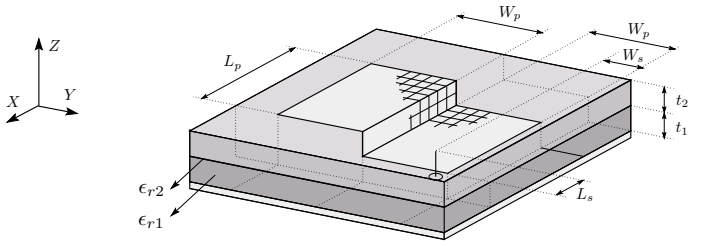

Figure 8.12: A coaxially fed two-level patch antenna with vertical metalisation in a two layer dielectric medium.

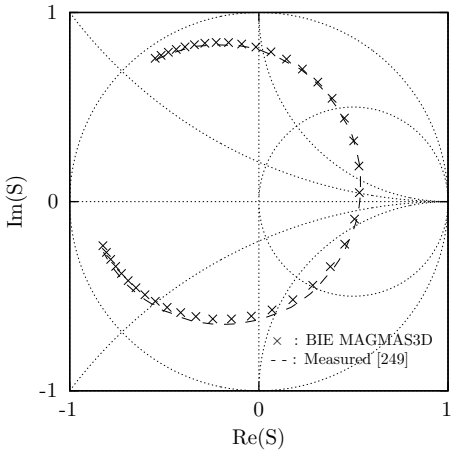

Figure 8.13: Input reflection S_{11} for the antenna of Figure 8.12, 1.9-2.3 GHz, 41 points.

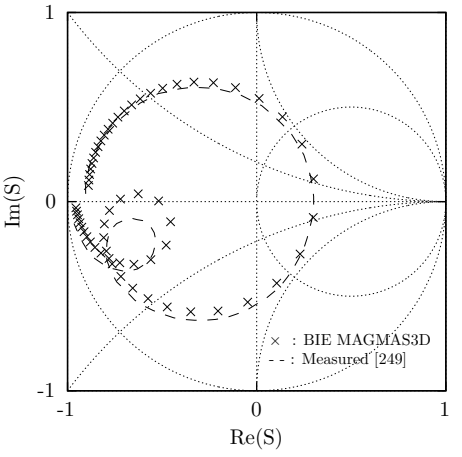

Figure 8.14: Input reflection S_{11} for the antenna of Figure 8.12, 2.4-3.0 GHz, 61 points.

frequency band 1.9-2.3 GHz in 41 points, and 2.4-3.0 GHz in 61 points respectively. Notice that the predictions become less accurate in the higher frequency band.

8.3.4 The Cavity Backed Aperture/Patch Antenna with Dielectric Overlay

In the previous antenna examples, the vertical conductors still have modest size compared to the horizontal parts of the antenna. In the following example, this is no longer the case, as the vertical parts now have the same size as the horizontal parts, of the order of magnitude of the wavelength. Figure 8.15 depicts the cavity-backed antenna that we will analyse. This antenna can be considered as a slot or a patch antenna depending on whether one concentrates on the opening or on the patch in the upper ground plane as the part responsible for generating radiation. Feeding is

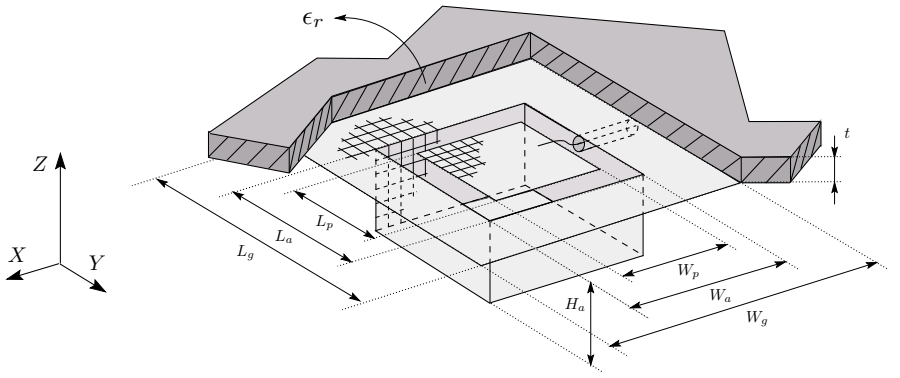

Figure 8.15: Geometry of a coaxially fed cavity-backed aperture or patch antenna covered with a dielectric superstrate.

achieved with a coaxial line of which the inner conductor terminates on the middle of the patch. The structure is backed by a rectangular metallic cavity. The dimensions of the patch are $W_p = L_p = 1.5cm$. The size of the cavity is $W_a = L_a = 1.875cm$, and a depth $H_a = 0.9375cm$. The patch has 9×11 subdivisions along X and Y. The cavity has $10 \times 10 \times 6$ subdivisions along X, Y and Z. The influence of a top cover dielectric layer of thickness $t = 7874mm$ and $\epsilon_r = 2.2$ on the antenna performance is also considered.

This antenna was designed, analysed and measured in [279]. For the theoretical analysis, they short circuited the slot in the upper ground plane and replaced it by equivalent magnetic sheet currents. Expressing continuity of the magnetic field over

.... : $\epsilon_r = 1.00$, BIE [279]

Δ, ∇ : $\epsilon_r = 1.00$, BIE MAGMAS3D

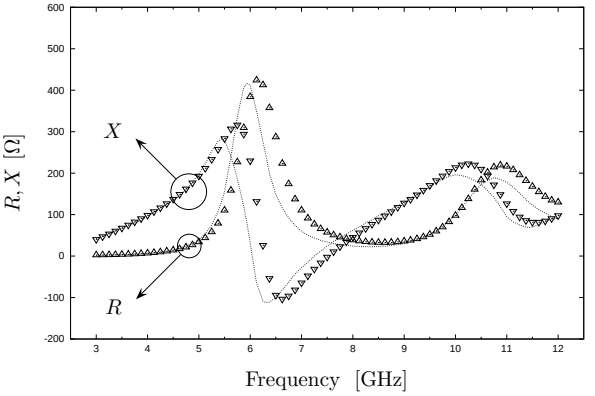

Figure 8.16: Input impedance R+jX of the cavity-backed antenna of Figure 8.15 when no dielectric cover is present, 3.0-12.0 GHz, 73 points.

.... : $\epsilon_r = 1.00$, BIE [279]
- - : $\epsilon_r = 2.22$, BIE [279]
— : $\epsilon_r = 2.22$, Measured [279]

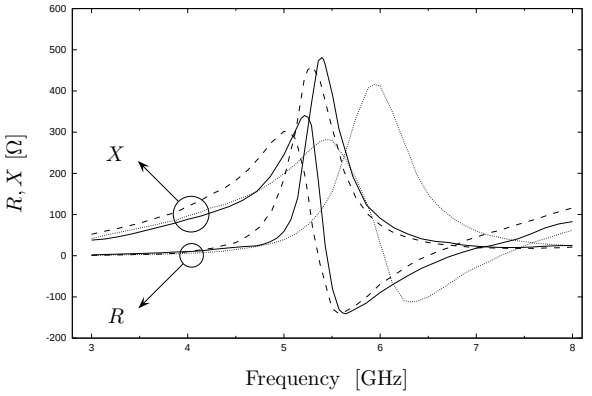

Figure 8.17: Input impedance R+jX of the antenna of Figure 8.15 with and without a dielectric overlay, as computed and measured by [279] in the frequency range 3.0-8.0 GHz.

Δ, ∇ : $\epsilon_r = 1.00$, BIE MAGMAS3D
$\times$, $+$: $\epsilon_r = 2.22$, BIE MAGMAS3D
— : $\epsilon_r = 2.22$, Measured [279]

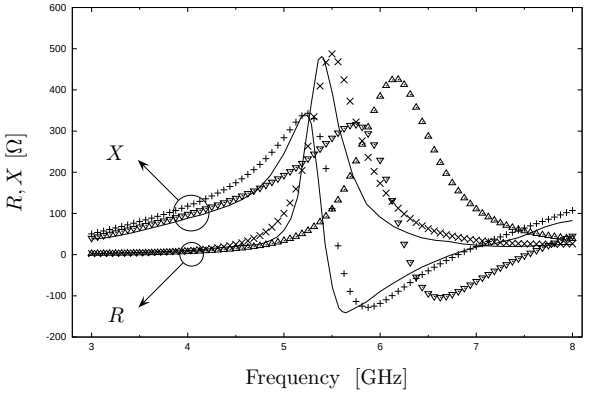

Figure 8.18: Input impedance R+jX of the antenna of Figure 8.15 with and without a dielectric overlay, as computed in the frequency range 3.0-8.0 GHz, in 81 points, and compared with the measurements of [279].

the aperture opening results in an integral equation for this magnetic current. The kernels occurring in this equation are a Green's function for the lower closed air filled rectangular cavity and a Green's function for the upper single layer medium. In [279], a combination of pulse and piece-wise sinusoidal subdomain expansion functions are used to model the magnetic current, and a spectral domain approach to compute the matrix elements was used. The excitation is a delta gap voltage generator in the slot area between patch and ground plane. This is a very efficient approach for this particular example, as only the magnetic current over the small aperture opening has to be modeled. The approach is however limited to perfectly conducting closed rectangular cavities.

To show the validity of our approach, we perform a dual analysis in which all electric

currents are computed. The bottom of the cavity is taken as an infinite ground plane of the layer structure. The current on the cavity side walls, the patch and on the upper ground plane is expanded using rooftop functions. The upper ground plane is thus necessarily finite in our approach with dimensions $W_g = L_g = 48.75mm$ and 26×26 subdivisions along its outer perimeter. Our excitation is a current source connecting the patch to the surrounding upper ground plane. Of course, our analysis is less efficient than the approach of [279] for this particular example. However, our more general approach can handle arbitrarily shaped cavities, with possible openings in the side walls and can take into account the effect of the finite ground plane if desired.

In [279], simulations were done for this antenna without a dielectric cover in the 3.0-12.0 GHz frequency range, while measured results are only available for a dielectric covered antenna in the 3.0-8.0 GHz range. In Figure 8.16, we compare the computations of [279] for the homogeneous case with our own results over the entire frequency range 3.0-12.0 GHz, in 73 points. Fairly good agreement is observed. These results for the homogeneous case are also repeated in Figure 8.17 but only over the frequency range 3.0-8.0 GHz as a reference curve. In this Figure, we also depict the computed and measured results of [279] for the case when the dielectric cover is present. One clearly observes the shift of the resonance frequency as the electrical size of the antenna is slightly increased due to the presence of the dielectric cover. The measured results are also compared with our own simulation results in Figure 8.18 over the 3.0-8.0 GHz range, in 81 frequency points. A slight shift in frequency is present between our own simulations and those of [279] for all cases, with the measured results neutrally in the middle. Deviations may be due to different feed models used, as a further increase of the size of our finite ground plane or a further refinement of the mesh gave no further significant improvement of the results.

8.4 Circuits, Packaging, Interconnections

In this section, the applicability of our full wave field solver to tackle problems from traditional low frequency and higher frequency microwave electronics is demonstrated. In general, the geometry and material composition of a circuit problem creates a more complicated boundary value problem than for a typical antenna structure. The size of the problem domain is also generally smaller compared to the wavelength, while the discretisation of the current still needs to be very dense to model very fine geometrical features. In general, this has created some numerical problems such that it was more difficult to obtain the accurate and stable solutions for the problems presented below.

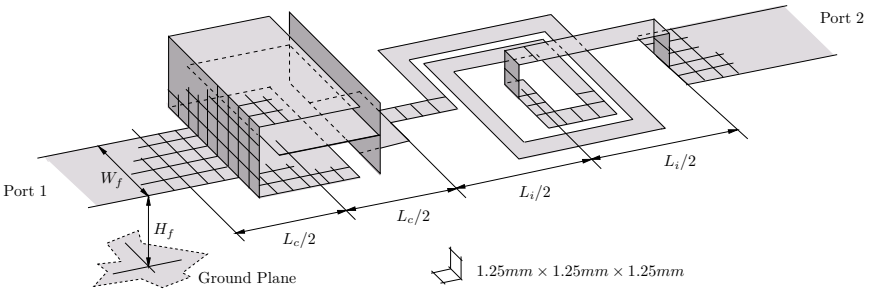

(a) Actual geometry of the problem.

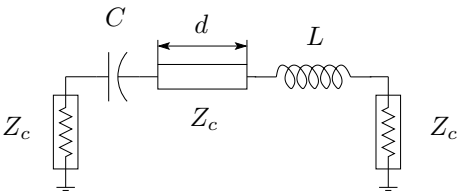

(b) Low frequency equivalent circuit model.

Figure 8.19: Series resonator obtained by connecting a multilayered capacitor and a square spiral inductor with an airbridge in series on a microstrip line.

8.4.1 The Lumped Element Series Resonator

Figure 8.19 shows the physical configuration of a lumped element resonator consisting of a series connection of a multilayered capacitor and a square spiral inductor with an airbridge. The circuit is fed by a simple microstrip line above an infinite ground plane. This example is designed to illustrate the approximate nature of classical lumped element circuit theory and explicitly shows the transition into the frequency range where a complete solution of the boundary value problem is required to take into account the wave nature of the field as discussed in Sections 2.7 and 2.8 of Chapter 2. The medium is assumed to be homogeneous with $\epsilon_{r1} = 1.0$. The characteristic impedance of the microstrip line is then completely determined by its width $W_f = 6.25mm$ and height $H_f = 5mm$ above the ground plane at $Z_c = 115\Omega$. All S-parameters are normalized to this impedance. The main dimensions of the multilayered capacitor and square spiral inductor are $L_c = 16.25mm$ and $L_i = 20.00mm$ respectively. Most of the structure conforms with a regular geometrical grid with unit cell size $1.25mm \times 1.25mm \times 1.25mm$ and the mesh shown in Figure 8.19. Only the spacing between the turns of the spiral inductor is half the unit cell size. The dimensions were explicitly chosen such that the deviation from the lumped element behaviour occurs below 3 GHz. When the lumped elements are small compared to the wavelength,

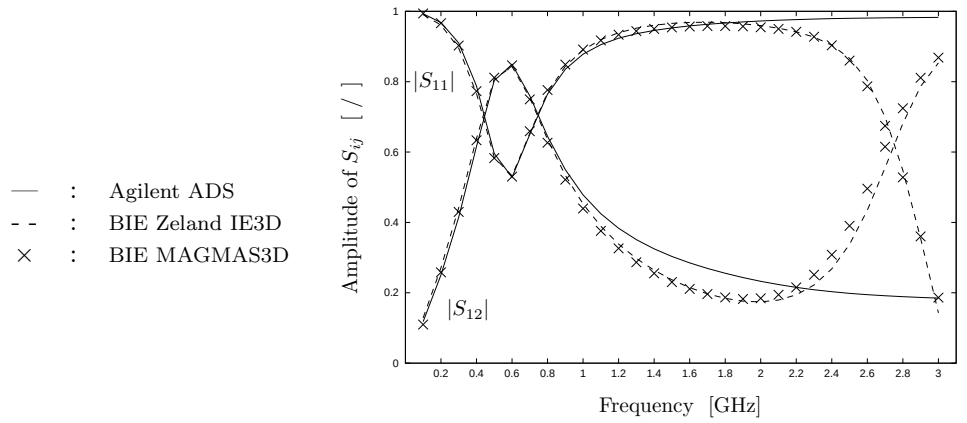

Figure 8.20: S-parameters for the resonator of Figure 8.19(a) obtained from the lumped element equivalent of Figure 8.19(b) and 2 full wave simulations from 0.1-3.0 GHz, 30 points.

their behaviour can still be characterised by a single number. The electrostatic capacitance $C = 0.80pF$, and the quasi-static inductance $L = 50nH$ can be obtained from approximate formulas [280]. A low frequency equivalent circuit is depicted in Figure 8.19(b). Although the individual lumped elements are "small" at 1GHz, their series connection already has a considerable dimension, and a section of transmission line was inserted to model the distributed nature of the circuit to some extent. The length of the section equals the distance between the centers of the components $d = 18.25mm$. The circuit simulation can be performed by paper and pencil or using Agilent ADS and these results are compared with two full wave simulations in Figure 8.20. The first uses the hybrid BIE method implemented within this work, and the second uses the space domain dyadic EFIE formulation implemented within Zeland Software IE3D. The reduced order equivalent circuit model is seen to be only valid in the lower frequency range. The validity of such circuit models can be extended to higher frequencies by adding more discrete elements, up to the point where the number of discrete elements equals the number of expansion functions used in the full wave analysis.

8.4.2 The Packaged Microwave Circuit

Microwave Monolithic Integrated Circuits (MMIC's) are commonly packaged in a metallic box [281], [282] as depicted in Figure 8.21. The effect of the enclosing cavity can often be assumed to be negligible, if proximity effects [283] resulting from electromagnetic coupling with closely located sidewalls can be avoided. This approach has not posed very serious problems because the size of the circuit packages has not been electrically large. As the level of integration and/or operation frequency increases,

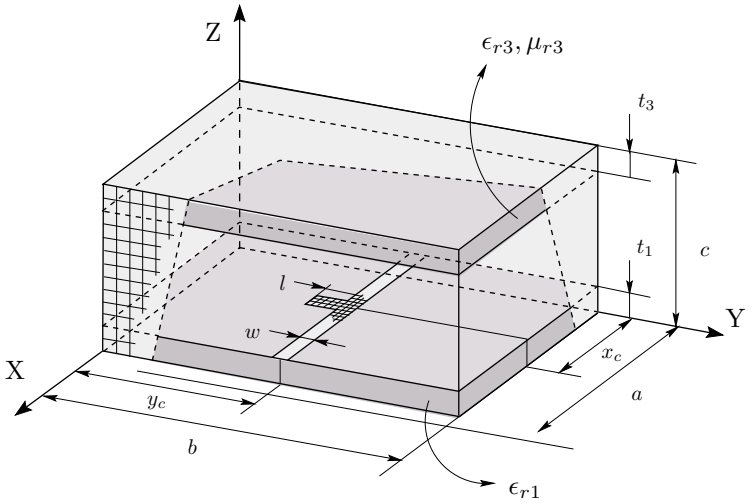

Figure 8.21: Studying the effect of the metallic package and absorbing materials on the circuit behaviour of the MMIC.

the electrical size of the enclosure also increases. If the system operates at frequencies near one of the enclosure resonances, the electromagnetic coupling between different parts of the circuit or the interaction of the circuit with the package can be significantly altered as resonant field distributions within the enclosure can be excited [253], [284]. In this case, the topology of the circuit itself and the location of the circuit within the enclosure can be very important as it determines the measure in which the resonant field distributions are excited [284], [285]. Apart from trying to avoid their excitation by paying attention to geometry, the effect of the resonance can also be damped by introducing absorbing materials or resistive films to reduce the quality factor of the resonant cavity [284], [285], [286]. Nevertheless, there usually remain frequency shifts and other perturbations of the circuit response. These phenomena are displayed in the present example from [285].

A simple microstrip trace with width $w = 1.40mm$ is realised on a lossy substrate with thickness $t_1 = 1.27mm$ and $\epsilon_{r1} = 10.5(1 - j0.0023)$. It has a stop band in the transmission S_{21} at 11.0 GHz due to the shunt stub with the same width and length $l = 1.90mm$ located in the middle of the line. This circuit is then placed at position x_c, y_c in a perfectly conducting metallic box with dimensions $a = 15.00mm$, $b = 24.00mm$, $c = 12.70mm$ as depicted in Figure 8.21. The microstrip circuit is meshed according to a regular grid with unit cell size $w/3$. The box has 15×24 subdivisions along X and Y. In the Z direction, there are 2 subdivisions in the first and third layer, with 9 subdivisions in the middle air "layer" as depicted in Figure 8.21. For an enclosure of this size, there is only one resonant mode in the 9.0-12.0 GHz band, namely the TM_{110} mode at 11.8 GHz. To damp the effect of this mode when excited, a microwave absorbing layer with thickness $t_3 = 1.27mm$ and

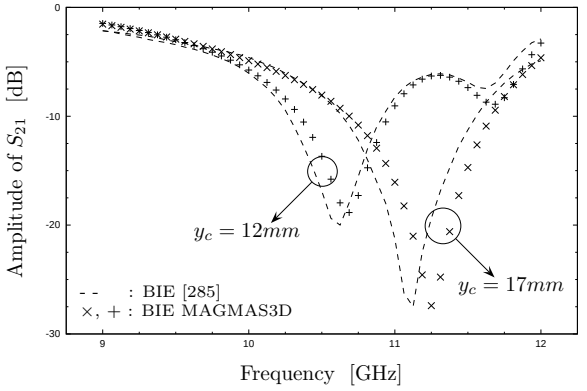

Figure 8.22: Amplitude of S_{21} for the boxed circuit of Figure 8.21 as computed in 49 points in the frequency range 9.0-12.0 GHz. The response is influenced by the location y_c in the box.

$\epsilon_{r3} = 21(1 - j0.02)$, $\mu_{r3} = 1.1(1 - j1.4)$ is attached to the cover of the enclosure.

Figure 8.22 compares the results of [285] with our own computations for the amplitude of S_{21} from 9.0-12.0 GHz in 49 points for two positions y_c of the circuit within the box. When the circuit is positioned off center at $x_c = 7.50mm$, $y_c = 17.00mm$, the circuit behaviour is hardly altered. However, when the circuit is moved to the center of the box at $x_c = 7.50mm$, $y_c = 12.00mm$ the excitation of the box resonance significantly alters the overall behaviour. In [285], a detailed study of the relation between excitation of the resonant field distribution and location and direction of the current components on the line and stub can be found.

The theoretical analysis of [285] was done using a BIE applied on the surface of the microstrip circuit only. The effect of the box is taken into account in the Green's function, such that the current on the box walls does not need to be discretised. A spatial domain approach for the computation of the matrix elements was used. In our analysis, the bottom and top cover of the box are part of the planar layer structure, while the current on the circuit and the vertical box walls is completely expanded using rooftop functions.

8.4.3 The Microstrip Rectangular Spiral Inductor

The following structure may be considered as a typical example of the degree to which physical data has to be simplified in order to make the problem accessible to fruitful numerico-mathematical analysis. It also shows the importance of modelling fine geometrical features if their dimensions are an appreciable fraction of the wavelength.

The example was originally introduced in [287]. They fabricated and measured a

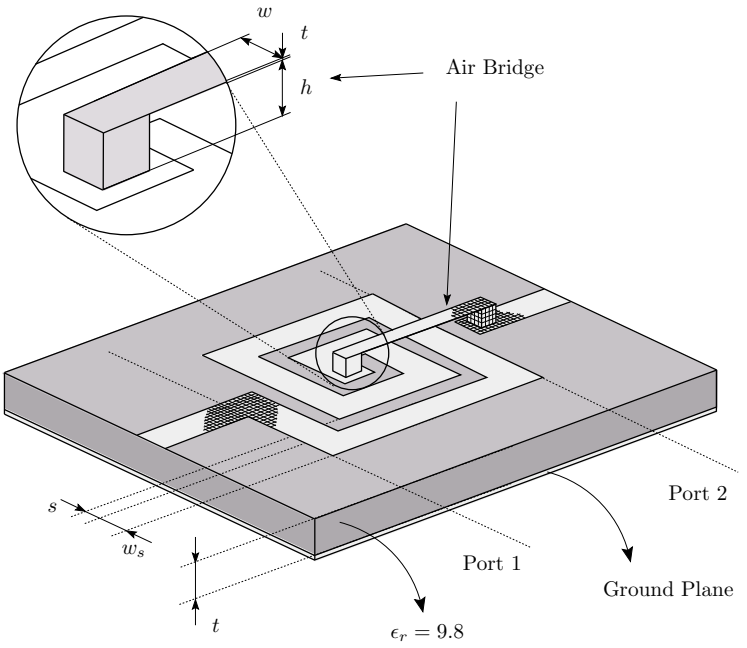

Figure 8.23: Microstrip rectangular spiral inductor with an airbridge of which the upper piece is modeled as a zero thickness flat strip.

square spiral inductor with an airbridge. The dimensions of this inductor were explicitly taken a bit larger than usual, such that all resonant phenomena are in a frequency area that allows practical realisation and verification by measurements. In this distributed inductor, all coupling effects between lines and discontinuities and the transmission properties of the airbridge have to be taken fully into account.

The geometrical models for the numerical analysis are depicted in Figures 8.23 and 8.24 with an impression of the most dense mesh used in the computations. The printed circuit part of the spiral inductor is realised on a single layer Al_2O_3 substrate with thickness $t = 635.0\mu m$ and $\epsilon_r = 9.8$. The feeding microstrip lines of width $w_s = 625.0\mu m$ then have an approximate impedance of 50Ω. The turns of the spiral have the same width and have a spacing $s = 312.5\mu m$ everywhere. This part of the structure can be modeled without introducing any grave approximations. However, the airbridge is realised in practice using a wire with circular cross section of diameter $317.5\mu m$. It is soldered vertically onto the printed circuit and the bended into the horizontal section such that the lower edge is located at a height $h = 317.5\mu m$ above the printed circuit. The real physical problem is thus fully three dimensional. If the circular cross section is approximated as a rectangular one, the problem becomes "quasi 3D" and the numerical analysis is strongly simplified. The width of the vertical studs of the airbridge are taken as $w = 312.5\mu m$ to conform with the mesh on the spiral

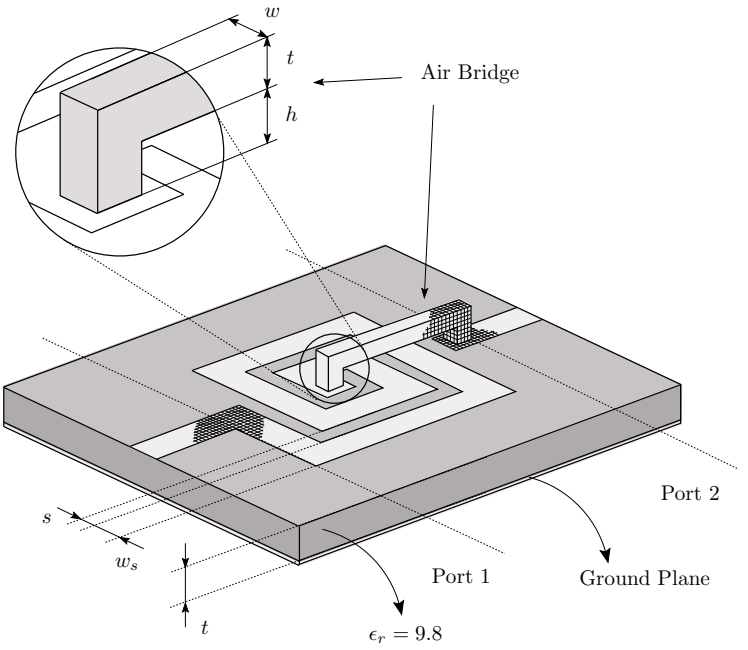

Figure 8.24: Microstrip rectangular spiral inductor with an airbridge of which the finite thickness of the upper piece is modeled as a box.

inductor, while the lower edge of the airbridge is positioned at a height $h = 317.5\mu m$. The upper piece of the airbridge will be modeled either as a flat strip as in Figure 8.23 with zero thickness $t = 000.0\mu m$ or as a rectangular box with thickness $t = 317.5\mu m$ as in Figure 8.24. The mesh on the horizontal parts of the model conform perfectly with a regular geometrical grid with unit cell size $78.125\mu m \times 78.125\mu m$, creating 8 subdivisions along the width w_s of the microstrip line, and 4 along the width w of the airbridge and vertical studs. Along the Z direction, 4 subdivisions were taken over the heights h and t as depicted in Figure 8.24, creating only slight deviations from the horizontal unit cell size.

Apart from the resulting geometrical simplification of cross section and bends at the corners, the numerical models also assume the current to flow on the surface of the wire instead of being distributed over its entire cross section. Any losses are also neglected in the analysis.

We investigate the influence of modelling the finite thickness of the upper piece of the airbridge. The original measurements by [287] were done in the frequency range 0.1-30.0 GHz and supplemented with Finite Difference Time Domain (FDTD) simulations. The finite thickness of the upper piece of the airbridge was not taken into account as it was modeled as a flat strip as depicted in Figure 8.23. A Boundary

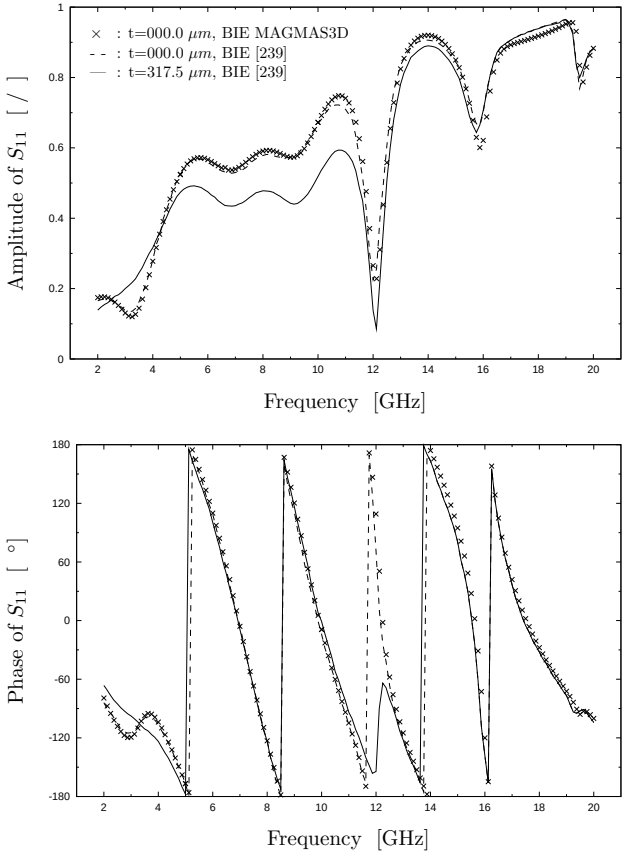

Figure 8.25: Amplitude and phase of S_{11}, 2.0-20.0 GHz, 145 points. Thickness of the upper piece of the airbridge $t = 000.0\mu m$.

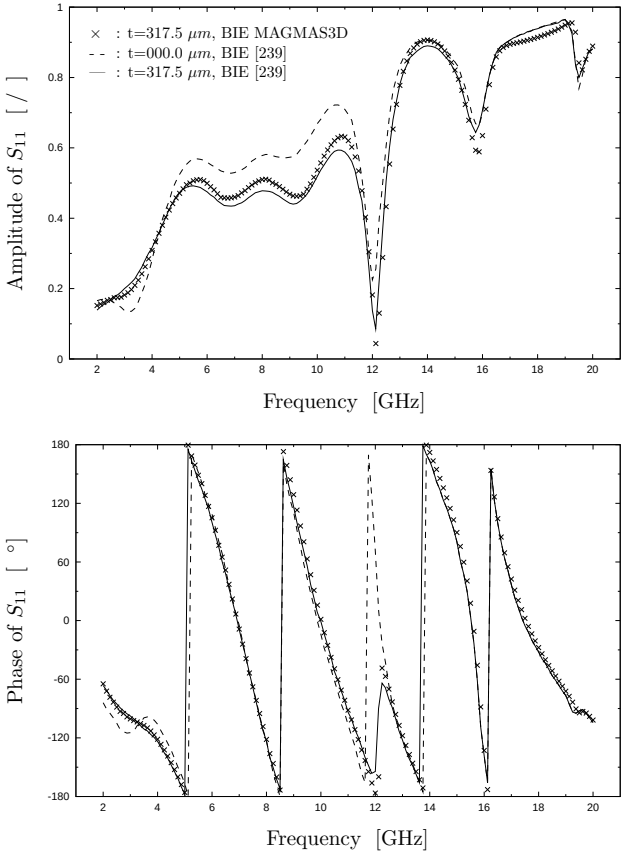

Figure 8.26: Amplitude and phase of S_{11}, 2.0-20.0 GHz, 145 points. Thickness of the upper piece of the airbridge $t = 317.5\mu m$.

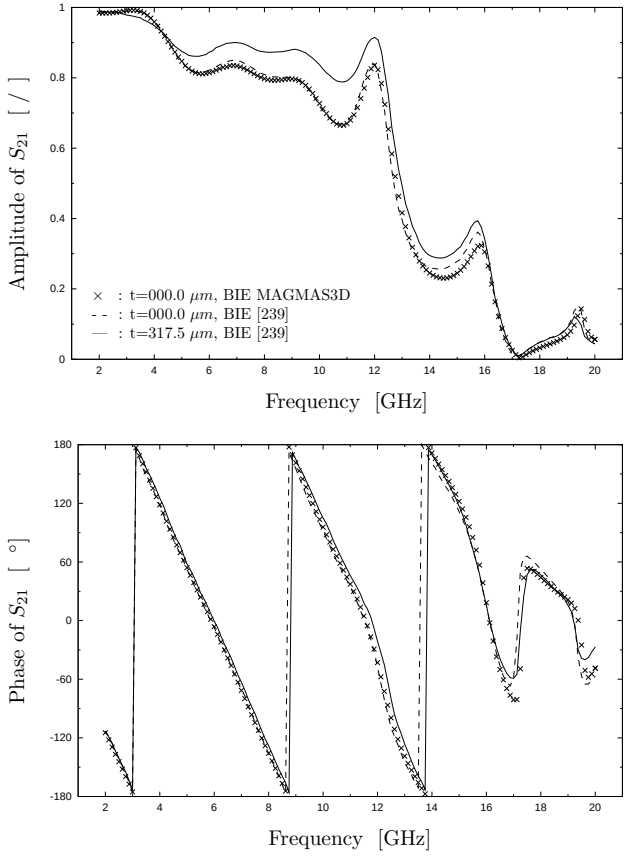

Figure 8.27: Amplitude and phase of S_{21}, 2.0-20.0 GHz, 145 points. Thickness of the upper piece of the airbridge $t = 000.0\mu m$.

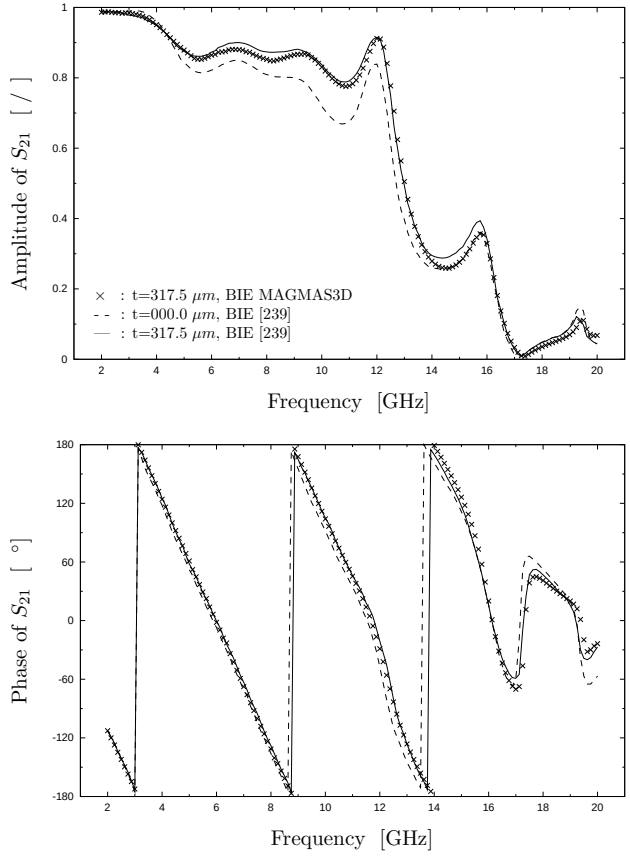

Figure 8.28: Amplitude and phase of S_{21}, 2.0-20.0 GHz, 145 points. Thickness of the upper piece of the airbridge $t = 317.5\mu m$.

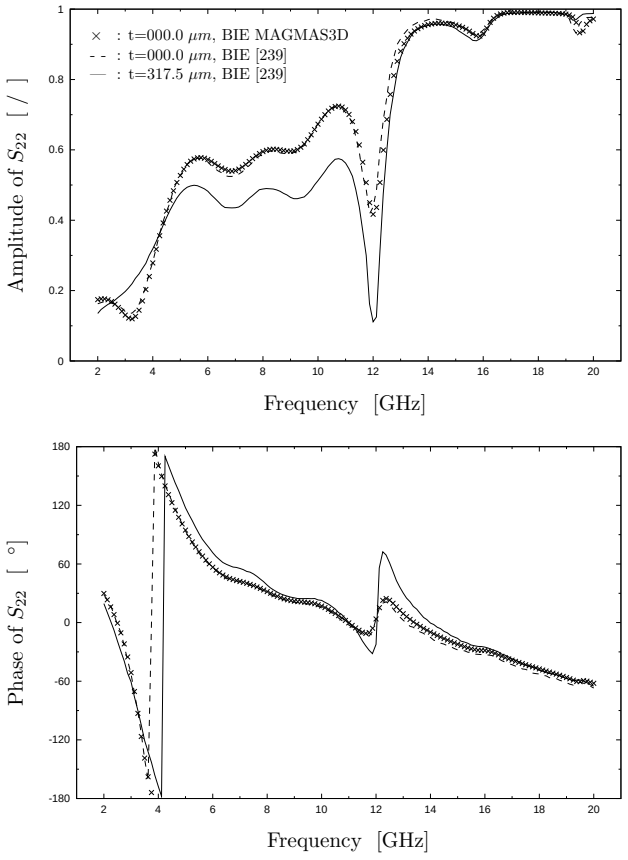

Figure 8.29: Amplitude and phase of S_{22}, 2.0-20.0 GHz, 145 points. Thickness of the upper piece of the airbridge $t = 000.0\mu m$.

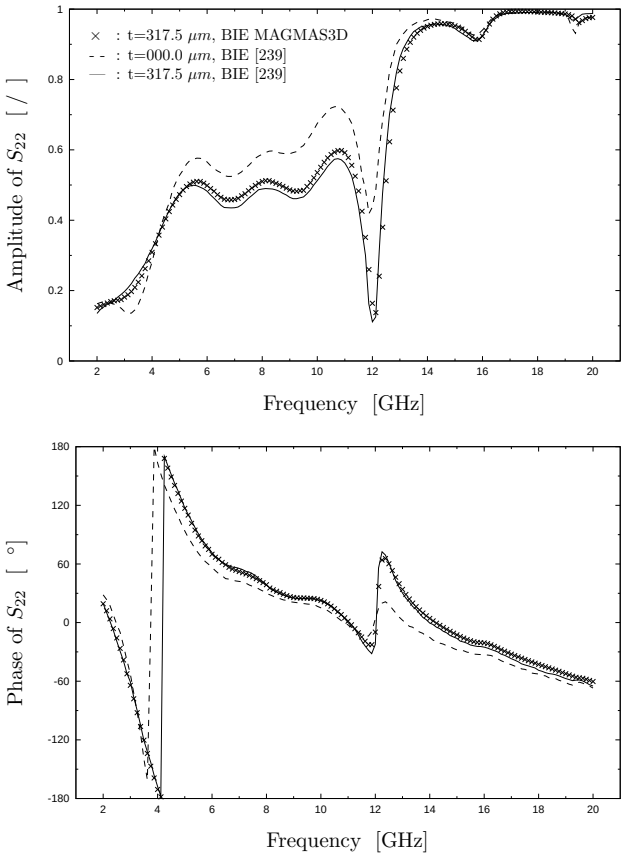

Figure 8.30: Amplitude and phase of S_{22}, 2.0-20.0 GHz, 145 points. Thickness of the upper piece of the airbridge $t = 317.5\mu m$.

Integral Equation (BIE) analysis with a spectral domain approach was done [237]. They also modeled the upper piece as a flat strip and assumed a constant vertical current to model the vertical studs of the airbridge. Both of these results still show an appreciable deviation with the measurements. The improved analysis of [239] investigates the influence of taking into account the finite thickness of the upper piece of the airbridge in the frequency range 0.2-20.0 GHz. They model all current components with a complete space domain three dimensional MPIE approach applied to the "quasi 3D" geometrical model of Figure 8.24. They also performed additional FDTD simulations for both zero and finite thickness to verify their results. The simulated results for finite thickness of [239] correspond better with the original measurements of [287]. The structure has been used further by a number of authors as a reference result, for example in [95], [266], [235], [288], each producing however less accurate numerical results.

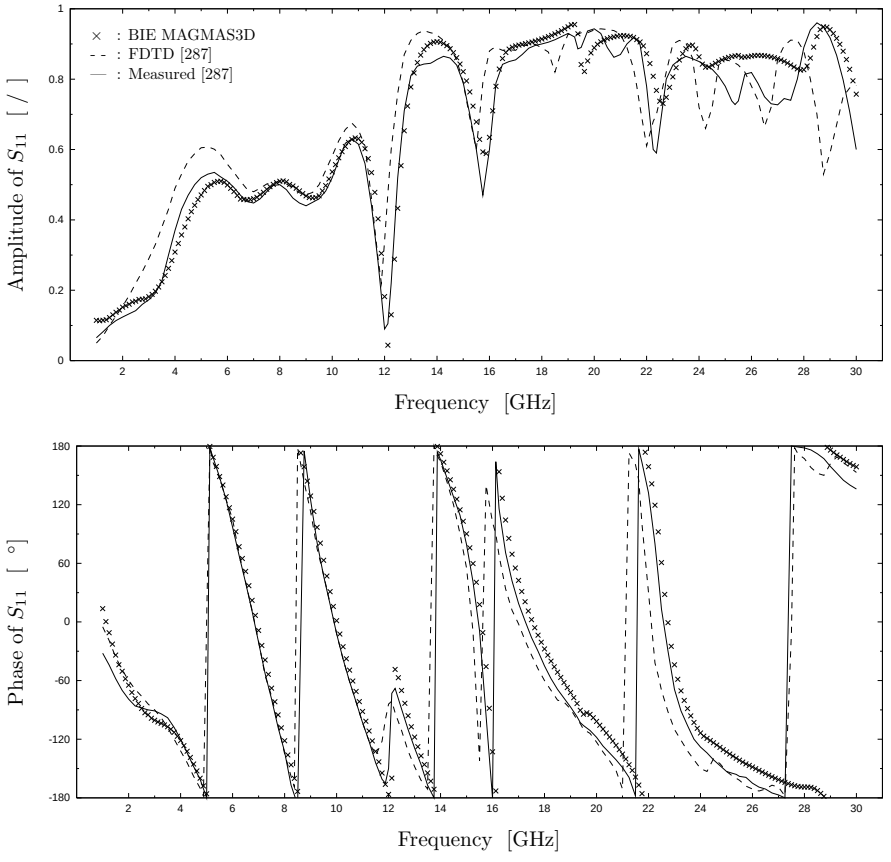

Figure 8.31: Amplitude and Phase of S_{11}, 1.0-30.0 GHz, 233 points. Comparison of MAGMAS3D BIE and FDTD full wave simulations with experimental data.

As a first verification, we compare our simulated results with the simulated MPIE-BIE results of [239] in the frequency range 0.2-20.0 GHz. Here we can assume an identical geometrical model of the structure and a similar mathematical model for the electromagnetic analysis. In these figures, the results of [239] for the thickness of the upper piece of the air bridge $t = 000.0\mu m$ and $t = 317.5\mu m$ are taken as reference curves. Figure 8.25 shows amplitude and phase of S_{11} as we computed for $t = 000.0\mu m$ in the frequency range 0.2-20 GHz, in 145 points. The shift that occurs when the upper piece of the airbridge is modeled as a box is given in the same format in Figure 8.26. Figures 8.27 and 8.28 show the effect on the transmission S_{21}. The corresponding results for S_{22} are given in Figure 8.29 and 8.30 where a bigger effect on the phase data can be discerned.

As a second verification, we compare our simulated results for thickness $t = 317.5\mu m$

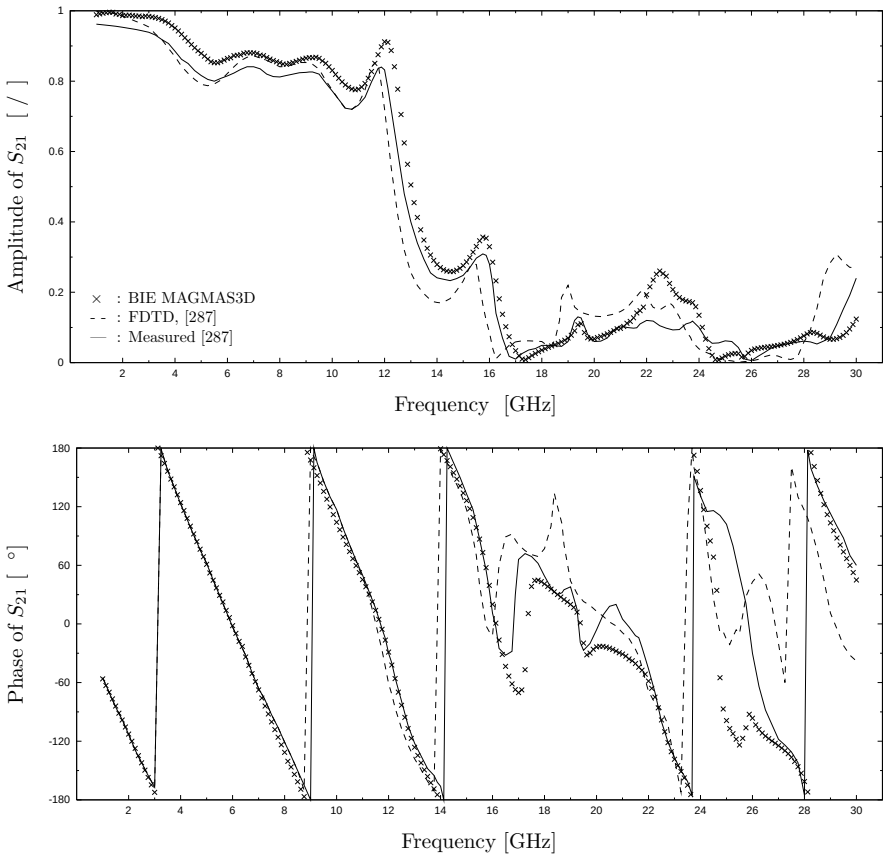

Figure 8.32: Amplitude and Phase of S_{21}, 1.0-30.0 GHz, 233 points. Comparison of MAGMAS3D BIE and FDTD full wave simulations with experimental data.

with the original measurements of [287] over the entire 0.1-30.0 GHz frequency range in Figures 8.31 and 8.32 in 233 points. To better appreciate the degree of difficulty to match full wave simulations to actual measurements, the FDTD simulations of [287] have also been included.

8.4.4 The Surface Mounted Plastic Packaged Integrated Circuit

The following example illustrates the potential of "full wave" electromagnetic field solvers to assist researchers and designers in modelling and designing complicated three dimensional packaging and interconnection problems arising in realistic electronic circuits.

Traditional low cost lead frame surface mounted plastic packages (SOIC8 (Single Outline Integrated Circuit with 8 leads), SSOP8, SSOP24 (Shrink Small Outline Package with 8 or 24 leads)) have been the workhorse of traditional low frequency electronics. The design of such packages has been dictated mainly by mechanical and thermal considerations [289]. In the low frequency range, the electrical effects of the package and interconnections on circuit performance can still be modeled using reduced order lumped element equivalent circuits of the physical discontinuities. Commercial wireless products up to 2.4 GHz have been designed in this manner [290]. However, the inherent low pass characteristics of these packages present a major impediment to operation at higher frequencies. Furthermore, the traditional reduced order lumped element circuit design methodology simply cannot take into account the complicated interaction of the circuit with the package and interconnection structure at these higher frequencies. Nevertheless, if not properly taken into account, these phenomena can seriously degrade the originally intended circuit behaviour. For present day and next generation high performance integrated circuits and packages, the electrical characteristics thus come into the forefront already at the design stage. At this point, "full wave" electromagnetic field solvers can come to the rescue.

Figure 8.33 shows the full physical configuration of the problem that we will study. A generic integrated circuit is packaged with a standard SOIC8 plastic package and surface mounted on a standard Printed Circuit Board (PCB).

The unpackaged circuit is in this case a simple planar microstrip filter realised on a substrate with thickness $0.150mm$ and $\epsilon_{r1} = 4.0$ above an infinite ground plane as depicted in Figure 8.34. The mesh used on this circuit is the same as in Figure 8.35(a). The circuit is intended to have a transmission (S_{21}) stop band around 9.5 GHz as verified by the full wave analysis results of Figure 8.34.

For operation in conjunction with other parts of the total system, the filter is packaged and surface mounted on a PCB as depicted in Figure 8.33. The filter is now embedded in a finite plastic encasing with the same $\epsilon_{r1} = 4.0$. The infinite ground plane is

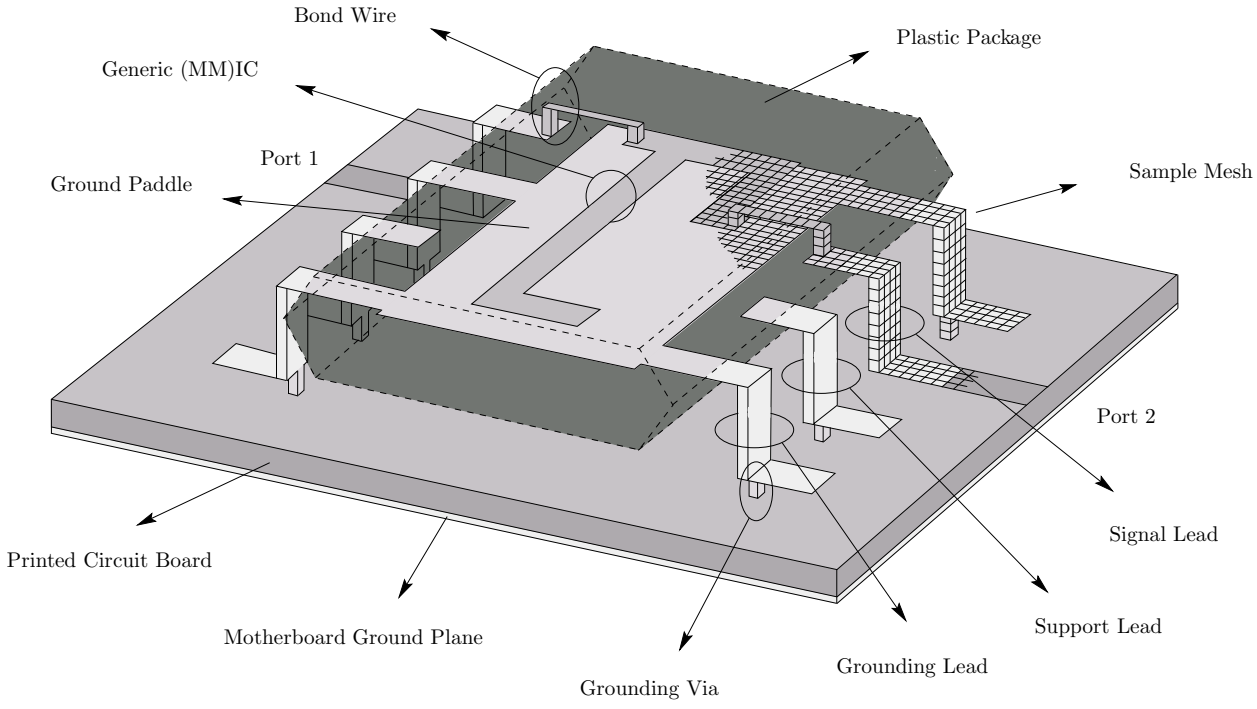

Figure 8.33: Simplified (quasi-) three dimensional geometrical model for the full wave electromagnetic analysis of a SOIC8 (Short Outline Integrated Circuit with 8 leads) packaging and interconnection structure. A generic (MM)IC ((Monolithic Microwave) Integrated Circuit) is packaged in a plastic encasing, and surface mounted on a standard PCB (Printed Circuit Board). The IC is connected with the signal traces of ports 1 and 2 on the PCB using the bond wires and "signal" leads. The elevated ground "paddle" is interconnected with the motherboard ground plane using the "grounding" leads and vias. The "support" leads are only connected with the PCB ground plane.

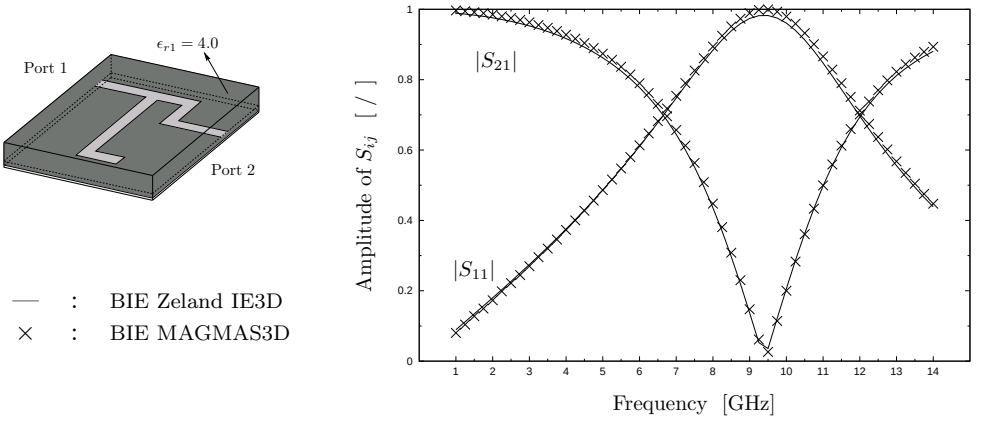

Figure 8.34: Planar geometry and full wave analysis results of the unpackaged microstrip filter circuit. S-parameters computed in frequency range 1.0-14.0 GHz, in 53 points.

replaced by a finite ground elevated "paddle" of dimensions $2.4mm \times 2.4mm$. This structure is supported above the PCB by metal studs called the "leads", leaving an intervening air region between PCB and plastic package of thickness $0.2mm$. Some of the leads are made in one piece with the ground paddle. These "grounding" leads connect the elevated paddle with the real PCB ground plane by vias which penetrate through the PCB dielectric with $\epsilon_{r2} = 10.0$ and thickness $0.25mm$. Other "support" leads are not connected with the paddle but have vias to the PCB ground plane and only serve to support the structure mechanically. Still other "signal" leads are not connected with the paddle nor with the ground plane. These can be used to transfer the useful signal or wave traveling on the PCB signal traces to the package such that it can finally reach the filter by means of wire bonds. One conductor of the wave guiding structure thus consists of the PCB signal traces, "signal" leads, bond wires and printed part of the filter. The second conductor which carries the "return current" is composed of the ground paddle, the grounding leads, vias and PCB ground plane.

The characteristics of this packaged filter are now measured between the signal traces on the PCB. In a low frequency circuit theoretical way of reasoning the effects can be distinguished as follows. The "discontinuities" like trace to lead transition, PCB-air-plastic transition and bond wires disturb the propagation of the useful signal. Electromagnetic capacitive coupling occurs between all closely spaced parts [290], especially between the leads and between leads and PCB ground, and inductive effects can be associated with all parts where the current has to travel along a certain length, like along the paddle and through the bond wires [290]. Finally, the finite elevated ground paddle provides "poor grounding characteristics" for the actual circuit. From an electromagnetic point of view, the effects of the packaging and interconnection are studied by transforming the relatively simple boundary value problem of Figure 8.34 into the considerably more complicated one of Figure 8.33 and comparing their solutions.

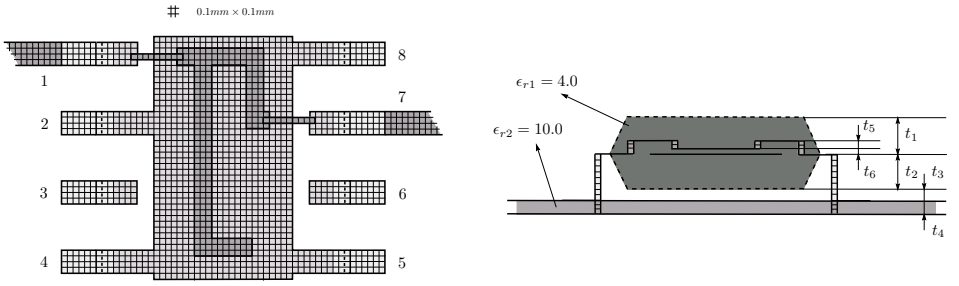

(a) Top View (b) Side/Front View

Figure 8.35: Top and Side View of the mesh on the geometrical model of Figure 8.33.

This SOIC8 example was studied in [290]. Using Sonnet *em* 3D planar BIE software, circuits models were extracted to model the effect of the package and interconnections on circuit behaviour. Results were compared with complete full wave simulations of the total structure. The effects of different grounding topologies were studied. These results will be used further on as reference data. In these BIE analyses, it is assumed that the plastic package extends horizontally to infinity such that the structure can be analysed as a stacked layer structure. The approach was verified further in [291] for the geometrically more complicated SSOP24 structure. Lumped element equivalents were extracted using Sonnet *em* and Finite Element Method HFSS. Measurements were performed on a simplified scale model. The SOIC8 was also analysed in [292] using the FDTD method, such that the finite extent of the plastic encasing can be taken into account. This seems to affect the results slightly starting from 11 GHz. Finally, a complete full wave analysis and design of a SSOP8 package was done in [289] also using Finite Element Method HFSS.

In this work, we focus on the complete full wave simulations of the entire structure. We compare the results of [290] using Sonnet *em* 3D planar BIE software with simulations performed with Zeland Software IE3D fully three dimensional BIE software, our own hybrid BIE 'quasi three dimensional MAGMAS3D software and finally the fully three dimensional Finite Element Method used in Ansoft HFSS. In all of these analyses, including the Finite Element Method, it is assumed that the top plastic encasing extends to infinity horizontally, such that a stacked layer structure can be assumed as a background medium. In this way all computations assume identical geometrical and material parameters such that results can be compared on an equal basis.

A top and side view of the structure of Figure 8.33 is given in Figures 8.35(a) and 8.35(b). The horizontal parts of the structure conform perfectly with a regular geometrical grid with cell size $0.1mm \times 0.1mm$. The thicknesses that determine the vertical dimensions of Figure 8.35(b) are $t_1 = 0.635mm$, $t_2 = 0.635mm$, $t_3 = 0.200mm$, $t_4 = 0.250mm$, $t_5 = 0.100mm$, $t_6 = 0.150mm$, with the mesh in the Z direction also

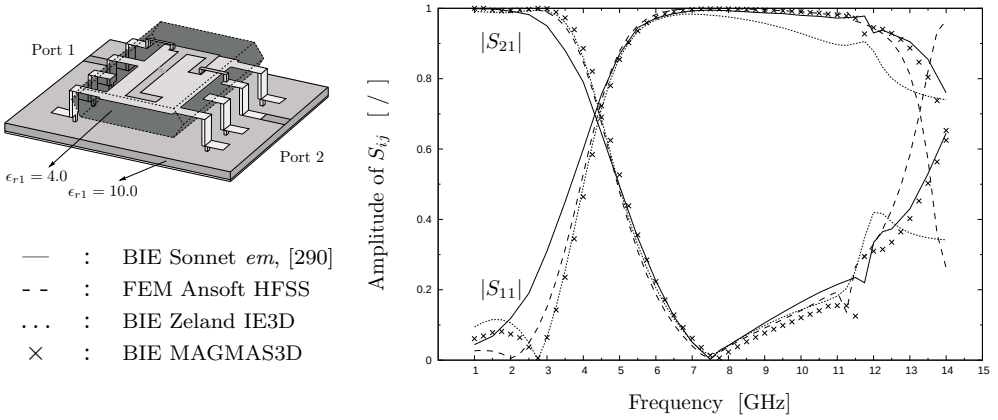

Figure 8.36: (Quasi) 3D geometry and comparison of 4 full wave analysis results for a the completely packaged and interconnected structure of Figure 8.33. S-parameters computed in the frequency range 1.0-14.0 GHz, in 53 points.

depicted. The leads are numbered as indicated in Figure 8.35(a). In this configuration, leads 3 and 6 are "support" leads, while 2,4,5 and 8 are "grounding" leads. The remaining "signal" leads 1 and 7 are connected with the PCB signal traces and thus correspond to ports 1 and 2 of the entire structure.

The main result of the analysis gives the net effect of the entire packaging and interconnection structure on the circuit behaviour. This is best observed by comparing the effect on the amplitude of the S-parameters as depicted in Figure 8.36, which was computed in the frequency range 1-14 GHz, in 27 points and these results are to be compared with the original unpackaged behaviour of Figure 8.34. The packaging and interconnections severely affect circuit performance, as they shift the original transmission zero from 9.5 GHz down to 7.75 GHz. Also notice that with exactly the same physical input parameters, all full wave solvers indeed predict roughly the same qualitative behaviour, but considerable deviations in the quantitative results are still present. Although not particularly a popular topic, robustness and correctness of full wave software certainly merits additional attention. In the low frequency range, the similar results of the 3D solvers Zeland Software IE3D, MAGMAS3D and HFSS are somewhat different from the Sonnet *em* 3D planar solver. This slight difference is believed to be caused by the fact that this last solver does not model the horizontal current components on the vertical pieces, but assumes only truly vertical currents. On the high frequency end, correspondence between Sonnet *em*, MAGMAS3D and HFSS seems to indicate less reliable results from Zeland Software IED3. Unfortunately, experimental verification seems remote as this deviation occurs in the region where the effect of the finite plastic encasing becomes important.

The fairly good agreement between the results of Figure 8.36 was obtained only after some trial and error computations. In particular, it was apparently necessary to model

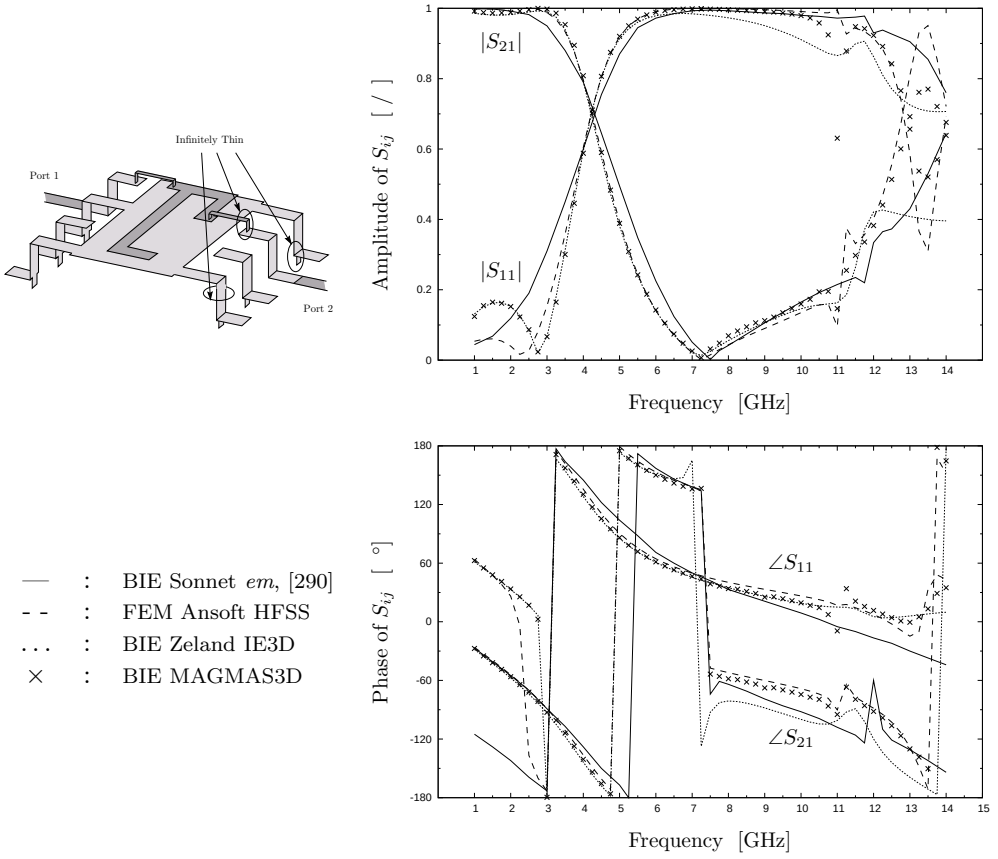

Figure 8.37: Amplitude and phase of the S-parameters obtained from 4 full wave analyses of the geometrical model with infinitely thin conductors everywhere. (The layer structure is still the same as in Figure 8.33.)

the vertical pieces of the bond wires, leads and vias as boxes with finite thickness. Initial exploratory computations assumed infinitely thin conductors everywhere and gives the results of Figures 8.37 for the amplitude and phase of the S-parameters (The layer structure is not depicted but still present in Figure 8.37). Since the reference results of [290] were obtained with Sonnet *em* which uses volumetric vertical currents, it was decided to model the vertical pieces as boxes, giving the improved results of Figures 8.38. Since the BIE methods are surface based, this slight geometrical refinement increased the size of the linear system to be solved from 4070×4070 for the infinitely thin model to 5190×5190 for the finite thickness model. No such comparable increase in computational effort was observed for the Finite Element Method HFSS computations.

In our last test case, we examine the influence of the grounding configuration on the

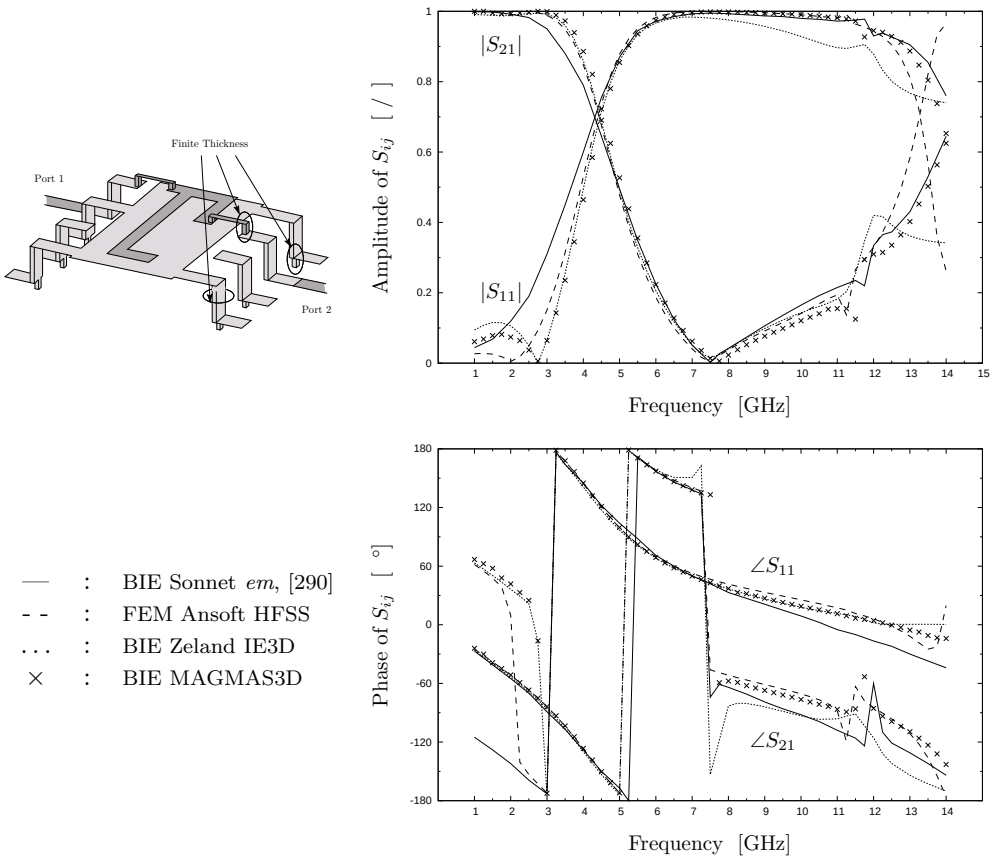

Figure 8.38: Amplitude and phase of the S-parameters obtained from 4 full wave analyses of the geometrical model with finite thickness vertical conductors and infinitely thin horizontal conductors. (The layer structure is still the same as in Figure 8.33.)

circuit behaviour. The following simulations were performed with the finite thickness geometrical model. In the original configuration of Figure 8.33, which we will call grounding configuration A, the leads 2,4,5,8 connect the elevated ground paddle to the motherboard ground plane. This situation is depicted in a simplified manner in Figure 8.39(a). It also shows symbolically the path of the image return current. This return current flows below the filter on the ground paddle and has to find its way back to the PCB motherboard ground plain. It flows as close as possible below the filter on the paddle until it reaches the edge below the bond wire. It then flows essentially along the edge of the paddle until it reaches a grounded lead such that it can descend through the lead and the via to the PCB ground. The S_{21} transmission for this case A is plotted again on a linear scale now in Figure 8.39(b) and compared with the simulations of [290]. In situation B of Figure 8.39(a), we disconnect grounding leads 4,5 such that they become simple support leads. The leads 2,8 continue to provide

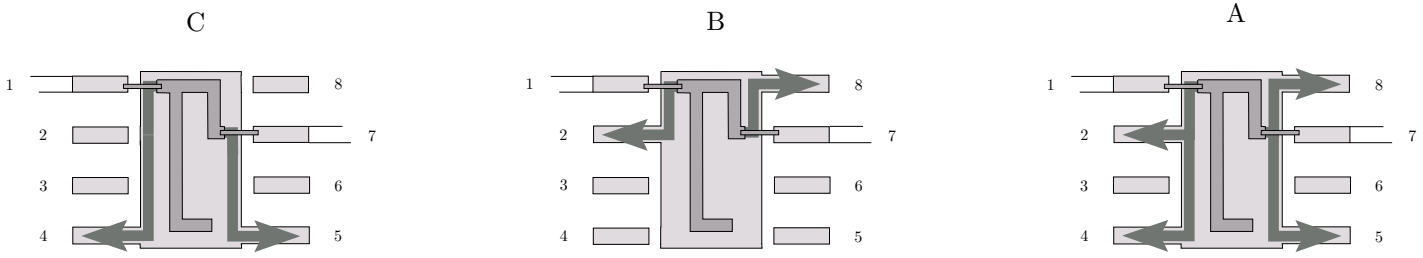

(a) Grounding configurations A : leads 2,4,5,8 grounded, B : leads 2,8 grounded, C : leads 4,5 grounded .

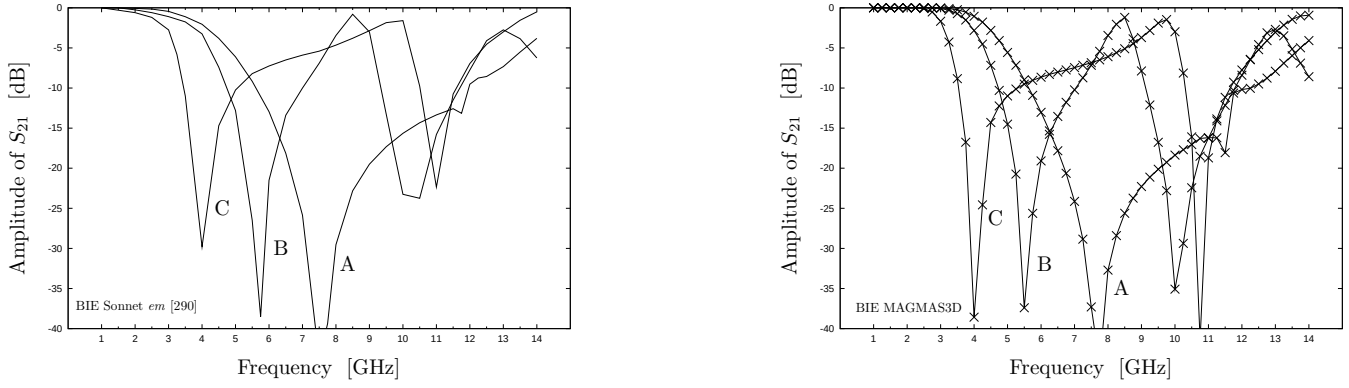

(b) Amplitude of S_{21} for the different grounding configurations A,B,C of Figure 8.39(a). Comparison between results of Sonnet *em* [290] on the left and MAGMAS3D on the right.

Figure 8.39: Influence of the grounding configuration of the elevated ground paddle on overall circuit behaviour. As the quality of the grounding deteriorates from configuration A to C, the first transmission zero of S_{21} originally located at 9.5 GHz for the unpackaged case shifts down progressively.

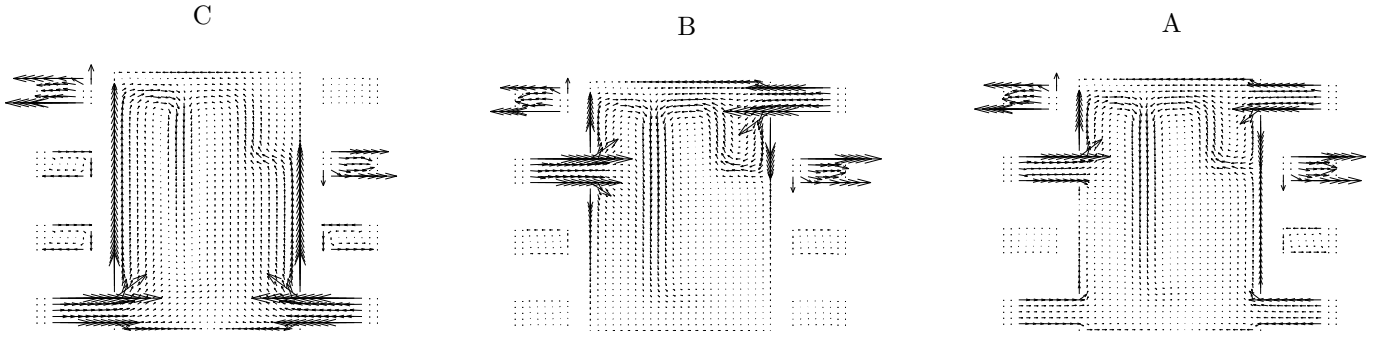

(a) Vector current distribution

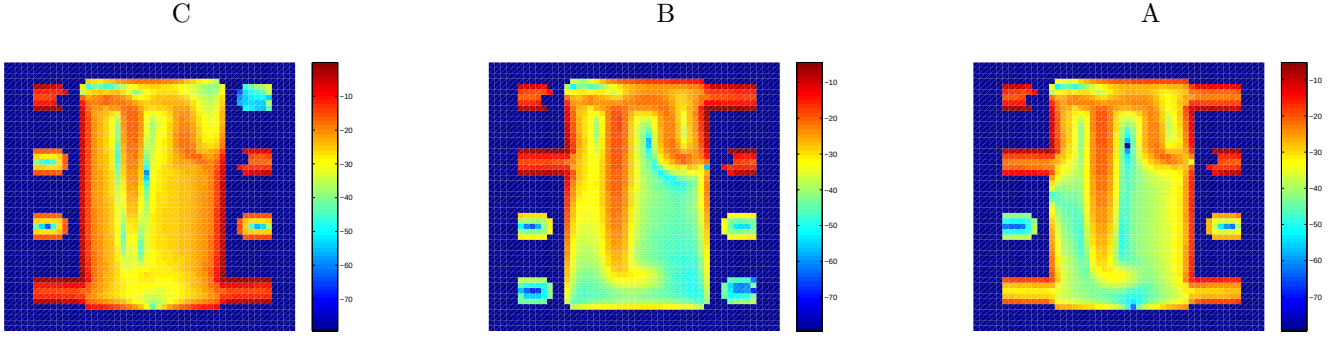

(b) Normalised amplitude current plot

Figure 8.40: Vector and amplitude plot of the current distribution on the elevated ground paddle and leads (part on same height as paddle) of Figure 8.33 for the different grounding configurations of Figure 8.39(a) at a frequency of 3 GHz.

grounding close to the bond wires. The grounding of the paddle now deteriorates as two current return paths are cut of. This can be seen also in Figure 8.39(b) where the transmission zero in S_{21} is now shifted even further down to 5.5 GHz. Finally, in the worst scenario C of Figure 8.39(a), we disconnect the best grounding leads 2,8 and only return the grounding leads 4,5 which are located very far from the bond wires. In this case, the worst shift in transmission zero of S_{21} occurs down to 4 GHz as depicted in Figure 8.39(b).

For this problem, we can clearly relate the macroscopic device behaviour to the fundamental vector current distribution on the conducting surfaces of the structure. Figure 8.40(a) depicts the vector current distribution on the elevated ground paddle and leads (the part on the same height as the paddle) for the three different grounding configurations of Figure 8.39(a) at a frequency of 3 GHz. These plots clearly show that the current indeed flows below the filter, the remaining return path that the current follows, and the singularities of the current along the edges of the conductors. The amplitude of the total current at each point is plotted also in Figure 8.40(b) for the three configurations. For the worst grounding configuration C, we see that the return current has to travel a long distance to reach the bottom grounding leads. In the amplitude plot of Figure 8.40(b), it is seen the current spreads out over the ground plane, thereby creating inductive and capacitive reactive effects that have detrimental effects on the overall device behaviour.

8.5 Conclusions

This chapter has demonstrated the capabilities of the full wave electromagnetic boundary integral equation field solver developed in this work. Any problem which fits the description of a "quasi 3D" dimensional structure embedded within a planar multilayered environment as given in Section 5.7 of Chapter 5 can in principle be analysed. Many electromagnetic boundary value problems arising in practical high frequency electrical engineering which appear fully three dimensional at first sight are actually covered by the formulation presented in this work. Correctness and accuracy of the solver have been validated by comparison with analytical results, simulations and measurements from open literature, and by comparison with results from commercially available full wave solvers. The range of problems covered in this chapter demonstrates that in the near future, full wave field solvers have the potential to become indispensable research and design tools, provided that the electromagnetic modelling community will spend sufficient attention on improving accuracy, correctness, robustness, speed and user-friendliness of the software tools it develops.

Chapter 9

Conclusions

Since the 1960's, the field of electromagnetics has slowly been transformed by the increasing availability of computing resources. Analytical and experimental techniques in electromagnetics have been supplemented with the still rising field of numerical analysis. High frequency full wave electromagnetic field analysis, having its roots in the antenna field, has now drastically increased its capacities in handling complex geometries and material configurations. Today, the full wave analysis of realistic three dimensional electromagnetic engineering problems, the most complicated of which typically arise in electronic circuits, is slowly becoming a reality. The availability of such numerical modelling technology in the form of commercial CAD packages since the 1980's has gradually opened up the potential area of application of computational electromagnetics from the strictly military to the entire commercial field founded upon high frequency and high speed electronic circuitry.

The work performed in this thesis reflects this ongoing evolution. The boundary integral solver MAGMAS, originally dedicated to the analysis of planar patch antenna configurations, has been transformed into the MAGMAS3D tool, capable of analysing a wide range of three dimensional structures embedded within a planar stratified medium. The planar antenna background has provided the two main characteristics of the MAGMAS3D solver. First, the antenna background has, as in the entire electromagnetics field, provided a strong analytical foundation. The upgrade of the planar to the 3D solver described in this work clearly continues within this tradition, with most of the progress again founded upon analytical developments. Secondly, the technical background of the planar antenna with its fabrication on a dielectric substrate has now provided the capacity to analyse three dimensional structures also located in a planar layered medium. The combination of this geometry with this material surrounding arises frequently in other related areas, with applications not remaining restricted to planar and 3D antennas, but extending into the circuit domain of Microwave and Millimeter wave Integrated Circuits (MMIC's),

Micro-Electromechanical Systems (MEMS), RF Printed Circuit boards (PCB's), high frequency interconnect and packaging problems and high speed digital circuits. The work performed to achieve this progress is extensively documented in this dissertation, with the main new developments highlighted below.

Chapter 4 generalises the expression for the electric and magnetic field generated by a dipole current source in the spectral domain from only a transverse current source located at the interface between dielectric layers to a complete three dimensional current source with arbitrary position within the layer structure. A new notation was developed, which clearly expresses all Green's functions as a function of voltages and currents on the equivalent transmission line systems, which is more suited for the analysis of three dimensional structures, and which is at the same time more conform with the ones used in modern literature. A completely new factorised form for any Green's function expression was developed, valid for an arbitrary layer structure. It extracts the often problematic z, z' dependence of the expressions in simple and symmetric form. This factorisation offers numerical and analytical advantages over the standard available expressions found in literature.

In Chapter 5, it was shown for the first time that the several distinct mixed potential formulations for the electric field in the spatial domain are related by the theoretical gauge transformation formalism, applied to the case of a multilayered medium. The study of the relationship of the field formulation with the geometry of the problem has resulted in a new hybrid dyadic mixed potential field formulation, specifically tailored to analyse "quasi 3D" structures. These structures are not fully three dimensional in a strict sense, but can still be used to analyse most problems that one first thinks of as being fully three dimensional. The formulation has the advantage that it avoids typical theoretical and numerical problems that hamper the traditional separate dyadic or mixed potential formulations.

Chapter 6 demonstrates how the geometry of the problem also has a strong influence on how the elements of the discrete matrix representation of the BIE can be computed. Traditional spectral and space domain approaches have been further blended in a combined spectral space domain approach, which is used together with the hybrid field formulation. All z, z' dependent parts of the reaction integrals involve the dyadic parts of the formulation and are done in closed form in the spectral domain. All transverse integrations are done with the space domain mixed potential formalism. The return to the space domain takes place at an optimal intermediate stage of the computation, depending on the directions of fields and currents. The closed form spectral integrations replace traditional purely numerical integrations with an interpolation procedure in the spatial domain to evaluate the z, z' dependent parts. Contrary to other similar work, the closed form formulas are used to model all current components and are valid for an arbitrarily layered medium.

Chapter 7 points out that several numerical and analytical techniques already developed in [11], [14] had to be upgraded as well. Several improvements were made such that the inverse Fourier transform can now act upon the more involved analytical

formulas of Chapter 6. For the space domain evaluation of the reaction integrals, line integrals now also have to be included and combined with the existing surface integrations. The necessary numerical and analytical formulas were developed.

These concepts were developed and tested in two software packages. Initial developments were tested in separate stand alone software, capable of analysing "quasi 3D" structures, but only for the case of a homogeneous medium, possibly located above an infinite ground plane. The more general techniques for a general multilayered medium have been incorporated into the MAGMAS3D framework.

Chapter 8 demonstrates the geometrical and electromagnetic capabilities of the software. The potential area of application is illustrated by a range of examples not only from the traditional antenna field but also from the "high frequency" microwave and more traditional "low frequency" circuit domain. The correctness and accuracy of the software is validated by comparison with known analytical results, measurements and simulations from open literature, and other simulated results obtained from commercially available full wave simulators.

Future work on the MAGMAS3D framework can be divided in two categories. The first type of work is the one required if commercial viability is to be achieved. In this case, the graphical user interface should be improved to accommodate the new geometrical structures. The processing of purely geometrical information like the generation of a suitable mesh should be streamlined. In the core electromagnetic engine, additional attention should be spent on increasing efficiency and speed, for example by applying the DCIM techniques already developed by Soliman [20] to accelerate the numerical inverse Fourier transform. The second category comprises further research activities. Work has already been done to combine planar magnetic current modelling with the three dimensional electric currents, but this has not yet achieved an operational status. On the longer term, work has also started to use the techniques described in this thesis to model limited volumes of dielectric inhomogeneities within the layer structure with a volumetric integral equation approach.

Appendix A

Factorisation of Green's function

A.1 Transfer Functions

When $z > z'$, the transfer functions are

$$V^{>}_{i_{ref},j_{ref}} = \prod_{k=j_{ref}}^{i_{ref}+1} \frac{e^{-\gamma_k d_k} + \Gamma^{>}_k e^{-\gamma_k d_k}}{1 + \Gamma^{>}_k} \quad \text{(A.1)} \qquad I^{>}_{i_{ref},j_{ref}} = \prod_{k=j_{ref}}^{i_{ref}+1} \frac{e^{-\gamma_k d_k} - \Gamma^{>}_k e^{-\gamma_k d_k}}{1 - \Gamma^{>}_k} \quad \text{(A.2)}$$

while for $z < z'$, they are

$$V^{<}_{i_{ref},j_{ref}} = \prod_{k=j_{ref}+1}^{i_{ref}} \frac{1 + \Gamma^{<}_k}{e^{-\gamma_k d_k} + \Gamma^{<}_k e^{-\gamma_k d_k}} \quad \text{(A.3)} \qquad I^{<}_{i_{ref},j_{ref}} = \prod_{k=j_{ref}+1}^{i_{ref}} \frac{1 - \Gamma^{<}_k}{e^{-\gamma_k d_k} - \Gamma^{<}_k e^{-\gamma_k d_k}} \quad \text{(A.4)}$$

A.2 Observation Shift Functions

When the reference interface for observation layer i is on the left side $i_{ref} = i$, we define $Y^{>}_{+} = Y_i + Y^{>}_i$, $Y^{>}_{-} = Y_i - Y^{>}_i$ and $Y^{<}_{+} = Y_i + Y^{<}_i$, $Y^{<}_{-} = Y_i - Y^{<}_i$ for

$$V^{\lessgtr}_{i,i}(z) \quad = \quad \frac{1}{2Y_i} \left(Y^{\lessgtr}_{+} e^{-\gamma_i (z - z_i)} + Y^{\lessgtr}_{-} e^{+\gamma_i (z - z_i)} \right) \qquad \text{(A.5)}$$

$$I^{\lessgtr}_{i,i}(z) = \frac{1}{2Y^{\lessgtr}_i}\left(Y^{\lessgtr}_+ e^{-\gamma_i(z-z_i)} - Y^{\lessgtr}_+ e^{+\gamma_i(z-z_i)}\right). \quad \text{(A.6)}$$

When the reference interface for observation layer i is on the right side $i_{ref} = i-1$, we redefine $Y^{>}_+ = Y_i + Y^{>}_{i-1}$, $Y^{>}_- = Y_i - Y^{>}_{i-1}$ and $Y^{<}_+ = Y_i + Y^{<}_{i-1}$, $Y^{<}_- = Y_i - Y^{<}_{i-1}$ for

$$V^{\lessgtr}_{i,i-1}(z) = \frac{1}{2Y_i}\left(Y^{\lessgtr}_+ e^{-\gamma_i(z_{i-1}-z)} + Y^{\lessgtr}_- e^{+\gamma_i(z_{i-1}-z)}\right) \quad \text{(A.7)}$$

$$I^{\lessgtr}_{i,i-1}(z) = \frac{1}{2Y^{\lessgtr}_{i-1}}\left(Y^{\lessgtr}_+ e^{-\gamma_i(z_{i-1}-z)} - Y^{\lessgtr}_- e^{+\gamma_i(z_{i-1}-z)}\right). \quad \text{(A.8)}$$

A.3 Source Shift Functions

When the refer interference for source layer j is on the left side $j_{ref} = j$, we again define $Y^{<}_+ = Y_j + Y^{<}_j$, $Y^{<}_- = Y_j - Y^{<}_j$ and $Y^{>}_+ = Y_j + Y^{>}_j$, $Y^{>}_- = Y_j - Y^{>}_j$ for

$$V^{V,\lessgtr}_{j,j}(z') = \frac{1}{2}\left(Y^{\gtrless}_+ e^{-\gamma_j(z'-z_j)} - Y^{\gtrless}_- e^{+\gamma_j(z'-z_j)}\right)\frac{1}{Y^{<}_j - Y^{>}_j} \quad \text{(A.9)}$$

$$V^{I,\lessgtr}_{j,j}(z') = \frac{1}{2Y_j}\left(Y^{\gtrless}_+ e^{-\gamma_j(z'-z_j)} + Y^{\gtrless}_- e^{+\gamma_j(z'-z_j)}\right)\frac{1}{Y^{<}_j - Y^{>}_j} \quad \text{(A.10)}$$

$$I^{V,\lessgtr}_{j,j}(z') = \frac{Y^{\lessgtr}_j}{2}\left(Y^{\gtrless}_+ e^{-\gamma_j(z'-z_j)} - Y^{\gtrless}_- e^{+\gamma_j(z'-z_j)}\right)\frac{1}{Y^{<}_j - Y^{>}_j} \quad \text{(A.11)}$$

$$I^{I,\lessgtr}_{j,j}(z') = \frac{Y^{\lessgtr}_j}{2Y_j}\left(Y^{\gtrless}_+ e^{-\gamma_j(z'-z_j)} + Y^{\gtrless}_- e^{+\gamma_j(z'-z_j)}\right)\frac{1}{Y^{<}_j - Y^{>}_j}. \quad \text{(A.12)}$$

When the refer interference for source layer j is on the left side $j_{ref} = j-1$, we redefine $Y^{<}_+ = Y_j + Y^{<}_{j-1}$, $Y^{<}_- = Y_j - Y^{<}_{j-1}$ and $Y^{>}_+ = Y_j + Y^{>}_{j-1}$, $Y^{>}_- = Y_j - Y^{>}_{j-1}$ for

$$V^{V,\lessgtr}_{j-1,j}(z') = \frac{1}{2}\left(Y^{\gtrless}_+ e^{-\gamma_j(z_{j-1}-z')} - Y^{\gtrless}_- e^{+\gamma_j(z_{j-1}-z')}\right)\frac{1}{Y^{<}_{j-1} - Y^{>}_{j-1}} \quad \text{(A.13)}$$

$$V^{I,\lessgtr}_{j-1,j}(z') = \frac{1}{2Y_j}\left(Y^{\gtrless}_+ e^{-\gamma_j(z_{j-1}-z')} + Y^{\gtrless}_- e^{+\gamma_j(z_{j-1}-z')}\right)\frac{1}{Y^{<}_{j-1} - Y^{>}_{j-1}} \quad \text{(A.14)}$$

$$I^{V,\lessgtr}_{j-1,j}(z') = \frac{Y^{\lessgtr}_{j-1}}{2}\left(Y^{\gtrless}_+ e^{-\gamma_j(z_{j-1}-z')} - Y^{\gtrless}_- e^{+\gamma_j(z_{j-1}-z')}\right)\frac{1}{Y^{<}_{j-1} - Y^{>}_{j-1}} \quad \text{(A.15)}$$

$$I^{I,\lessgtr}_{j-1,j}(z') = \frac{Y^{\lessgtr}_{j-1}}{2Y_j}\left(Y^{\gtrless}_+ e^{-\gamma_j(z_{j-1}-z')} + Y^{\gtrless}_- e^{+\gamma_j(z_{j-1}-z')}\right)\frac{1}{Y^{<}_{j-1} - Y^{>}_{j-1}}. \quad \text{(A.16)}$$

Appendix B

Analytical Sommerfeld Integrals

Some characteristic field behaviours in the spatial domain can be studied with Sommerfeld integrals that can be performed analytically.

B.1 The Sommerfeld Identity

The Sommerfeld identity ([36], p. 242, formula 14) decomposes the frequency domain free space scalar Green's function into a continuous spectrum of cylindrical and plane waves

$$\int_0^{+\infty} \frac{e^{-j\sqrt{k_\rho^2 - k_0^2}|z-z'|}}{\sqrt{k_\rho^2 - k_0^2}} \; J_0(\rho k_\rho) \; k_\rho \mathrm{d}k_\rho = \frac{e^{-jk_0 R}}{R} \tag{B.1}$$

with $\rho = \sqrt{(x-x')^2 + (y-y')^2}$, $R = \sqrt{(x-x')^2 + (y-y')^2 + (z-z')^2}$.

B.2 Space Wave Field Components

The extraction of the space wave field components in the spatial domain can be obtained from the Sommerfeld identity above or from ([203], p. 667, formula 6.554.1)

$$\int_0^{+\infty} \frac{1}{\sqrt{k_\rho^2 - k_0^2}} \; J_0(\rho k_\rho) \; k_\rho \mathrm{d}k_\rho \quad = \quad \frac{e^{-jk_0\rho}}{\rho} \tag{B.2}$$

$$\int_0^{+\infty} \frac{1}{\sqrt{k_\rho^2 + k_0^2}}\, J_0(\rho k_\rho)\, k_\rho \mathrm{d}k_\rho \;=\; \frac{e^{-k_0\rho}}{\rho}. \tag{B.3}$$

By partial integration to k_0, we obtain from Equation (B.2)

$$\int_0^{+\infty} \sqrt{k_\rho^2 - k_0^2}\, J_0(\rho k_\rho)\, k_\rho \mathrm{d}k_\rho \;=\; -\left(jk_0 + \frac{1}{\rho}\right) \frac{e^{-jk_0\rho}}{\rho^2}. \tag{B.4}$$

B.3 Surface Wave Field Components

The spatial surface wave components are obtained from ([203], p. 676, formula 6.577.1)

$$\int_0^{+\infty} \frac{1}{k_\rho^2 - k_0^2}\, J_0(\rho k_\rho)\, k_\rho \mathrm{d}k_\rho \;=\; -j\frac{\pi}{2} H_0^{(2)}(k_0\rho) \tag{B.5}$$

$$\int_0^{+\infty} \frac{1}{k_\rho^2 + k_0^2}\, J_0(\rho k_\rho)\, k_\rho \mathrm{d}k_\rho \;=\; K_0(k_0\rho) \tag{B.6}$$

with $H_0^{(2)}$ the Hankel function and K_0 the modified Bessel function, both of the 2^{th} kind and of order 0.

B.4 Quasi Static Field Components

For the near field behaviour in the spatial domain, a number of analytical Sommerfeld integrals can be derived from ([203], p. 692, formula 6.621.4)

$$\int_0^{+\infty} \frac{e^{-k_\rho\Delta}}{k_\rho^m}\, J_n(\rho k_\rho)\, k_\rho \mathrm{d}k_\rho = (-1)^{-m+1} \rho^{-n} \frac{d^{-m+1}}{d\Delta^{-m+1}} \left[\frac{\left(\sqrt{\rho^2 + \Delta^2} - \Delta\right)^n}{\sqrt{\rho^2 + \Delta^2}} \right] \tag{B.7}$$

for which the results are collected in Table B.1.

Although a trend is visible that a faster spectral decay gives a less singular spatial behaviour, the integrals for $m = +2, +3$ still diverge. This is however caused by the behaviour at the origin of the spectral domain and disturbs the anology between spectral asymptotic and spatial singular behaviour. This can be avoided by including a convergence factor $1 - e^{-k_\rho t}$ in the integrandum which forces the function to 0 for

	n=0	n=1	n=2
m=-1	$\frac{2\Delta^2-\rho^2}{\sqrt{\rho^2+\Delta^2}^5}$	$\frac{3\rho\Delta}{\sqrt{\rho^2+\Delta^2}^5}$	$\frac{3\rho^2}{\sqrt{\rho^2+\Delta^2}^5}$
m=0	$\frac{\Delta}{\sqrt{\rho^2+\Delta^2}^3}$	$\frac{\rho}{\sqrt{\rho^2+\Delta^2}^3}$	$\frac{2}{\rho^2}-\frac{\Delta\left(2\Delta^2+3\rho^2\right)}{\rho^2\sqrt{\rho^2+\Delta^2}^3}$
m=+1	$\frac{1}{\sqrt{\rho^2+\Delta^2}}$	$\frac{1}{\rho}\left(1-\frac{\Delta}{\sqrt{\rho^2+\Delta^2}}\right)$	$\frac{\sqrt{\rho^2+\Delta^2}}{\rho^2}\left(1-\frac{\Delta}{\sqrt{\rho^2+\Delta^2}}\right)^2$

Table B.1: Usefull analytical Sommerfeld integrals obtained from Equation (B.7).

$k_\rho \to 0$. It then becomes possible to continue the intuitively expected correspondence by evaluating

$$\int_0^{+\infty} \frac{\left(1-e^{-k_\rho t}\right)^m e^{-k_\rho \Delta}}{k_\rho^m} J_n(\rho k_\rho)\ k_\rho \mathrm{d}k_\rho \tag{B.8}$$

of which we only need the results for $n=0$ summarized in Table B.2

	n=0
m=+1	$\frac{1}{\sqrt{\rho^2+\Delta^2}}-\frac{1}{\sqrt{\rho^2+(\Delta+t^2)^2}}$
m=+2	$\ln\frac{\left(\sqrt{\rho^2+(\Delta+t)^2}+\Delta+t\right)^2}{\left(\sqrt{\rho^2+\Delta^2}+\Delta\right)\left(\sqrt{\rho^2+(\Delta+2t)^2}+\Delta+2t\right)}$
m=+3	$-\ (\Delta+3t)\ln\left(\sqrt{\rho^2+(\Delta+3t)^2}+\Delta+3t\right)+\ \sqrt{\rho^2+(\Delta+3t)^2}$ $+3(\Delta+2t)\ln\left(\sqrt{\rho^2+(\Delta+2t)^2}+\Delta+2t\right)-3\sqrt{\rho^2+(\Delta+2t)^2}$ $-3(\Delta+\ t)\ln\left(\sqrt{\rho^2+(\Delta+\ t)^2}+\Delta+\ t\right)+3\sqrt{\rho^2+(\Delta+\ t)^2}$ $+\ (\Delta\qquad)\ln\left(\sqrt{\rho^2+(\Delta\qquad)^2}+\Delta\qquad\right)-\ \sqrt{\rho^2+(\Delta\qquad)^2}$

Table B.2: Analytical Sommerfeld integrals for Equation (B.8).

Appendix C

Analytical Space Domain Integrals

C.1 Line Integrals

The integrations over a straight line segment l are evaluated in the ρ, ϕ and ξ, η coordinate systems of Figure 7.6 of Chapter 7, where all symbols are defined.

C.1.1 Integrals of the type $\int_l \{1, x, y\} \frac{1}{\sqrt{\rho^2 + \Delta^2}} \, \mathrm{d}l$

$$\int_l \frac{1}{\sqrt{\rho^2 + \Delta^2}} \, \mathrm{d}l = \ln \frac{\sqrt{\rho_v^2 + \Delta^2} + \eta_v}{\sqrt{\rho_u^2 + \Delta^2} + \eta_u} \tag{C.1}$$

$$\int_l \left\{ \begin{matrix} x \\ y \end{matrix} \right\} \frac{1}{\sqrt{\rho^2 + \Delta^2}} \, \mathrm{d}l = + \left\{ \begin{matrix} +\cos\phi_L \\ +\sin\phi_L \end{matrix} \right\} L \int_l \frac{1}{\sqrt{\rho^2 + \Delta^2}} \, \mathrm{d}l + \left\{ \begin{matrix} -\sin\phi_L \\ +\cos\phi_L \end{matrix} \right\} \left(\sqrt{\rho_v^2 + \Delta^2} - \sqrt{\rho_u^2 + \Delta^2} \right) \tag{C.2}$$

C.1.2 Integrals of the type $\int_l \{1, x, y\} \ln\left(\sqrt{\rho^2 + \Delta^2} + \Delta\right) \, \mathrm{d}l$

$$\int_l \ln\left(\sqrt{\rho^2 + \Delta^2} + \Delta\right) \, \mathrm{d}l =$$

$$
\begin{aligned}
&+ \eta_v \ln\left(\sqrt{\rho_v^2+\Delta^2}+\Delta\right) - \eta_u \ln\left(\sqrt{\rho_u^2+\Delta^2}+\Delta\right) \\
&- L\left[+sgn(\eta_v)\left\{\arcsin\frac{L^2+\Delta\left(\sqrt{\rho_v^2+\Delta^2}+\Delta\right)}{\sqrt{L^2+\Delta^2}\left(\sqrt{\rho_v^2+\Delta^2}+\Delta\right)}-\frac{\pi}{2}\right\}\right. \\
&\qquad\left.-sgn(\eta_u)\left\{\arcsin\frac{L^2+\Delta\left(\sqrt{\rho_u^2+\Delta^2}+\Delta\right)}{\sqrt{L^2+\Delta^2}\left(\sqrt{\rho_u^2+\Delta^2}+\Delta\right)}-\frac{\pi}{2}\right\}\right] \\
&- (\eta_v-\eta_u) + \Delta\ln\left|\frac{\eta_v+\sqrt{\rho_v^2+\Delta^2}}{\eta_u+\sqrt{\rho_u^2+\Delta^2}}\right|
\end{aligned}
\tag{C.3}
$$

$$
\begin{aligned}
&\int_l \left\{\begin{matrix} x \\ y \end{matrix}\right\} \ln\left(\sqrt{\rho^2+\Delta^2}+\Delta\right)\,\mathrm{d}l = \\
&\quad + \left\{\begin{matrix} +\cos\phi_L \\ +\sin\phi_L \end{matrix}\right\} L \int_l \ln\left(\sqrt{\rho^2+\Delta^2}+\Delta\right)\,\mathrm{d}l \\
&\quad + \left\{\begin{matrix} -\sin\phi_L \\ +\cos\phi_L \end{matrix}\right\} \left[-\frac{1}{4}\left(\rho_v^2-\rho_u^2\right)+\frac{\Delta}{2}\left(\sqrt{\rho_v^2+\Delta^2}-\sqrt{\rho_u^2+\Delta^2}\right)\right. \\
&\qquad\qquad + \frac{\eta_v^2}{2}\ln\left(\sqrt{\rho_v^2+\Delta^2}+\Delta\right) - \frac{\eta_u^2}{2}\ln\left(\sqrt{\rho_u^2+\Delta^2}+\Delta\right) \\
&\qquad\qquad \left. + \frac{L^2}{2}\ln\frac{\sqrt{\rho_v^2+\Delta^2}+\Delta}{\sqrt{\rho_u^2+\Delta^2}+\Delta}\right]
\end{aligned}
\tag{C.4}
$$

C.1.3 Integrals of the type $\int_l \{1,x,y\}\sqrt{\rho^2+\Delta^2}\,\mathrm{d}l$

$$
\begin{aligned}
\int_l \sqrt{\rho^2+\Delta^2}\,\mathrm{d}l &= +\frac{\eta_v}{2}\sqrt{\rho_v^2+\Delta^2} - \frac{\eta_u}{2}\sqrt{\rho_y^2+\Delta^2} \\
&\quad + \frac{L^2+\Delta^2}{2}\ln\left|\frac{\eta_v+\sqrt{\rho_v^2+\Delta^2}}{\eta_u+\sqrt{\rho_u^2+\Delta^2}}\right|
\end{aligned}
\tag{C.5}
$$

$$
\begin{aligned}
\int_l \left\{\begin{matrix} x \\ y \end{matrix}\right\} \sqrt{\rho^2+\Delta^2}\,\mathrm{d}l &= + \left\{\begin{matrix} +\cos\phi_L \\ +\sin\phi_L \end{matrix}\right\} L \int_l \sqrt{\rho^2+\Delta^2}\,\mathrm{d}l \\
&\quad + \left\{\begin{matrix} -\sin\phi_L \\ +\cos\phi_L \end{matrix}\right\} \frac{1}{3}\left[\sqrt{\rho_v^2+\Delta^2}^3 - \sqrt{\rho_u^2+\Delta^2}^3\right]
\end{aligned}
\tag{C.6}
$$

C.2 Surface Integrals

The surface integrations over a rectangular area S are made in the ρ, ϕ coordinate system of Figure 7.8(a) and the ξ, η coordinates of Figure 7.8(b) of Chapter 7.

C.2.1 Integrals of the type $\int\limits_S \{1, x, y\} \dfrac{1}{\sqrt{\rho^2 + \Delta^2}}\ \mathrm{d}S$

$$\int\limits_S \frac{1}{\sqrt{\rho^2+\Delta^2}}\ \mathrm{d}S = -\Delta\left(\phi_v - \phi_u\right) - L\ \ln\left(\frac{\sqrt{\rho_v^2+\Delta^2}-\eta_v}{\sqrt{\rho_u^2+\Delta^2}-\eta_u}\right)$$
$$+\Delta\left[+\arcsin\frac{\Delta\sin\left(\phi_v-\phi_L\right)}{\sqrt{L^2+\Delta^2}} - \arcsin\frac{\Delta\sin\left(\phi_u-\phi_L\right)}{\sqrt{L^2+\Delta^2}}\right] \qquad \text{(C.7)}$$

$$\int\limits_S \left\{\begin{array}{c} x \\ y \end{array}\right\} \frac{1}{\sqrt{\rho^2+\Delta^2}}\ \mathrm{d}S =$$
$$+\left\{\begin{array}{c} +\cos\phi_L \\ +\sin\phi_L \end{array}\right\}\left[+\frac{L^2+\Delta^2}{2}\ln\frac{\sqrt{\rho_v^2+\Delta^2}+\eta_v}{\sqrt{\rho_u^2+\Delta^2}+\eta_u}\right.$$
$$\left.-\frac{\Delta^2}{2}\left\{+\frac{\eta_v}{\rho_v}\ln\frac{\sqrt{\rho_v^2+\Delta^2}+\rho_v}{\Delta} - \frac{\eta_u}{\rho_u}\ln\frac{\sqrt{\rho_u^2+\Delta^2}+\rho_u}{\Delta}\right\}\right]$$
$$+\left\{\begin{array}{c} -\sin\phi_L \\ +\cos\phi_L \end{array}\right\}\left[+\frac{L}{2}\left\{\sqrt{\rho_v^2+\Delta^2}-\sqrt{\rho_u^2+\Delta^2}\right\}\right.$$
$$\left.-\frac{L\Delta^2}{2}\left\{+\frac{1}{\rho_v}\ln\frac{\sqrt{\rho_v^2+\Delta^2}+\rho_v}{\Delta} - \frac{1}{\rho_u}\ln\frac{\sqrt{\rho_u^2+\Delta^2}+\rho_u}{\Delta}\right\}\right] \qquad \text{(C.8)}$$

C.2.2 Integrals of the type $\int\limits_S \{1, x, y\} \ln\left(\sqrt{\rho^2+\Delta^2}+\Delta\right)\ \mathrm{d}S$

$$\int\limits_S \ln\left(\sqrt{\rho^2+\Delta^2}+\Delta\right)\ \mathrm{d}S =$$
$$-\frac{L}{4}\left(\eta_v-\eta_u\right) - \frac{\Delta^2}{2}\left(\phi_v-\phi_u\right) - \frac{L\Delta}{2}\ln\frac{\sqrt{\rho_v^2+\Delta^2}-\eta_v}{\sqrt{\rho_u^2+\Delta^2}-\eta_u}$$
$$+sgn(\eta_v)\frac{L}{2}\left[|\eta_v|\left\{\ln\left(\sqrt{\rho_v^2+\Delta^2}+\Delta\right)-1\right\} + \Delta\ln\frac{\sqrt{\rho_v^2+\Delta^2}+|\eta_v|}{\sqrt{L^2+\Delta^2}}\right.$$
$$\left.-L\left\{\arcsin\frac{L^2+\Delta\left(\sqrt{\rho_v^2+\Delta^2}+\Delta\right)}{\sqrt{L^2+\Delta^2}\left(\sqrt{\rho_v^2+\Delta^2}+\Delta\right)} - \frac{\pi}{2}\right\}\right]$$

$$
\begin{aligned}
&-sgn(\eta_u)\frac{L}{2}\left[|\eta_u|\left\{\ln\left(\sqrt{\rho_u^2+\Delta^2}+\Delta\right)-1\right\}+\Delta\ln\frac{\sqrt{\rho_u^2+\Delta^2}+|\eta_u|}{\sqrt{L^2+\Delta^2}}\right.\\
&\qquad\left.-L\left\{\arcsin\frac{L^2+\Delta\left(\sqrt{\rho_u^2+\Delta^2}+\Delta\right)}{\sqrt{L^2+\Delta^2}\left(\sqrt{\rho_u^2+\Delta^2}+\Delta\right)}-\frac{\pi}{2}\right\}\right]\\
&+\frac{\Delta^2}{2}\left[\arcsin\frac{\Delta\sin\left(\phi_v-\phi_L\right)}{\sqrt{L^2+\Delta^2}}-\arcsin\frac{\Delta\sin\left(\phi_u-\phi_L\right)}{\sqrt{L^2+\Delta^2}}\right]
\end{aligned}
\tag{C.9}
$$

$$
\begin{aligned}
&\int_S\left\{\begin{array}{c}x\\y\end{array}\right\}\ln\left(\sqrt{\rho^2+\Delta^2}+\Delta\right)\,\mathrm{d}S=\\
&\quad+\left\{\begin{array}{c}+\cos\phi_L\\+\sin\phi_L\end{array}\right\}\left[-\frac{L^2}{2}\left(\eta_v-\eta_u\right)+\frac{\Delta^3}{6}\ln\Delta\left(\frac{\eta_v}{\rho_v}-\frac{\eta_u}{\rho_u}\right)\right.\\
&\qquad-\frac{1}{18}\left(\eta_v^3-\eta_u^3\right)+\frac{1}{18}\left(\eta_v\rho_v^2-\eta_u\rho_u^2\right)\\
&\qquad+\frac{L^2}{3}\left\{\eta_v\ln\left(\sqrt{\rho_v^2+\Delta^2}+\Delta\right)-\eta_u\ln\left(\sqrt{\rho_u^2+\Delta^2}+\Delta\right)\right\}\\
&\qquad+\frac{\Delta^3}{6}\left\{\frac{\eta_v}{\rho_v}\ln\left(\sqrt{\rho_v^2+\Delta^2}+\rho_v\right)-\frac{\eta_u}{\rho_u}\ln\left(\sqrt{\rho_u^2+\Delta^2}+\rho_u\right)\right\}\\
&\qquad+sgn(\eta_v)\left\{+\frac{\Delta}{2}\left(\frac{L^2}{2}+\frac{\Delta^2}{3}\right)\ln\frac{\sqrt{\rho_v^2+\Delta^2}+|\eta_v|}{\sqrt{L^2+\Delta^2}}\right.\\
&\qquad\qquad\left.-\frac{L}{3}\left(\arcsin\frac{L^2+\Delta\left(\sqrt{\rho_v^2+\Delta^2}+\Delta\right)}{\sqrt{L^2+\Delta^2}\left(\sqrt{\rho_v^2+\Delta^2}+\Delta\right)}-\frac{\pi}{2}\right)\right\}\\
&\qquad-sgn(\eta_u)\left\{+\frac{\Delta}{2}\left(\frac{L^2}{2}+\frac{\Delta^2}{3}\right)\ln\frac{\sqrt{\rho_u^2+\Delta^2}+|\eta_u|}{\sqrt{L^2+\Delta^2}}\right.\\
&\qquad\qquad\left.\left.-\frac{L}{3}\left(\arcsin\frac{L^2+\Delta\left(\sqrt{\rho_u^2+\Delta^2}+\Delta\right)}{\sqrt{L^2+\Delta^2}\left(\sqrt{\rho_u^2+\Delta^2}+\Delta\right)}-\frac{\pi}{2}\right)\right\}\right]\\
&\quad+\left\{\begin{array}{c}-\sin\phi_L\\+\cos\phi_L\end{array}\right\}\left[-\frac{L}{12}\left(\eta_v^2-\eta_u^2\right)-\frac{L}{18}\left(\rho_v^2-\rho_u^2\right)\right.\\
&\qquad+\frac{L}{6}\left\{\rho_v^2\ln\left(\sqrt{\rho_v^2+\Delta^2}+\rho_v\right)-\rho_u^2\ln\left(\sqrt{\rho_u^2+\Delta^2}+\rho_u\right)\right\}\\
&\qquad+\frac{\Delta^3L}{6}\ln\Delta\left(\frac{1}{\rho_v}-\frac{1}{\rho_u}\right)+\frac{\Delta L}{3}\left(\sqrt{\rho_v^2+\Delta^2}-\sqrt{\rho_u^2+\Delta^2}\right)\\
&\qquad\left.+\frac{\Delta^3L}{6}\left\{\frac{1}{\rho_v}\ln\left(\sqrt{\rho_v^2+\Delta^2}+\rho_v\right)-\frac{1}{\rho_v}\ln\left(\sqrt{\rho_v^2+\Delta^2}+\rho_v\right)\right\}\right]
\end{aligned}
\tag{C.10}
$$

C.2.3 Integrals of the type $\int\limits_S \{1, x, y\}\sqrt{\rho^2+\Delta^2}\ \mathrm{d}S$

$$\begin{aligned}\int\limits_S \sqrt{\rho^2+\Delta^2}\ \mathrm{d}S = &+\frac{L}{6}\left[|\eta_v|\sqrt{\rho_v^2+\Delta^2}-|\eta_u|\sqrt{\rho_u^2+\Delta^2}\right]-\frac{\Delta^3}{3}\left(\phi_v-\phi_u\right)\\ &+\frac{L}{2}\left(\frac{L^2}{3}+\Delta^2\right)\ln\frac{\sqrt{\rho_v^2+\Delta^2}+|\eta_v|}{\sqrt{\rho_u^2+\Delta^2}+|\eta_u|}\\ &+\frac{\Delta^3}{3}\left[\arcsin\frac{\Delta|\eta_v|}{L\sqrt{\rho_v^2+\Delta^2}}-\arcsin\frac{\Delta|\eta_u|}{L\sqrt{\rho_u^2+\Delta^2}}\right]\end{aligned}\tag{C.11}$$

$$\begin{aligned}&\int\limits_S \left\{\begin{array}{c}x\\y\end{array}\right\}\sqrt{\rho^2+\Delta^2}\ \mathrm{d}S =\\ &\quad+\left\{\begin{array}{c}+\cos\phi_L\\+\sin\phi_L\end{array}\right\}\left[+\frac{L^2}{8}\left(\eta_v\sqrt{\rho_v^2+\Delta^2}-\eta_u\sqrt{\rho_u^2+\Delta^2}\right)\right.\\ &\qquad\qquad+\frac{\left(L^2+\Delta^2\right)^2}{8}\left\{\ln\left(\sqrt{\rho_v^2+\Delta^2}+\eta_v\right)-\ln\left(\sqrt{\rho_v^2+\Delta^2}+\eta_v\right)\right\}\\ &\qquad\qquad\left.-\frac{\Delta^4}{8}\left\{\frac{\eta_v}{\rho_v}\ln\frac{\sqrt{\rho_v^2+\Delta^2}+\rho_v}{\Delta}-\frac{\eta_v}{\rho_v}\ln\frac{\sqrt{\rho_v^2+\Delta^2}+\rho_v}{\Delta}\right\}\right]\\ &\quad+\left\{\begin{array}{c}-\sin\phi_L\\+\cos\phi_L\end{array}\right\}\left[+\frac{L}{12}\left\{\sqrt{\rho_v^2+\Delta^2}^3-\sqrt{\rho_u^2+\Delta^2}^3\right\}\right.\\ &\qquad\qquad+\frac{L\Delta^2}{8}\left\{\sqrt{\rho_v^2+\Delta^2}-\sqrt{\rho_u^2+\Delta^2}\right\}\\ &\qquad\qquad\left.+\frac{L\Delta^4}{8}\left\{\frac{1}{\rho_v}\ln\frac{\sqrt{\rho_v^2+\Delta^2}+\rho_v}{\Delta}-\frac{1}{\rho_u}\ln\frac{\sqrt{\rho_u^2+\Delta^2}+\rho_u}{\Delta}\right\}\right]\end{aligned}\tag{C.12}$$

Bibliography

[1] A.A. Oliner, "Historical perspectives on microwave field theory," *IEEE Trans. Microwave Theory Tech.*, vol. MTT-32, pp. 1022–1045, Sep. 1984.

[2] K.C. Gupta, T. Itoh, and A.A. Oliner, "Microwave and RF education - past, present, and future," *IEEE Trans. Microwave Theory Tech.*, vol. MTT-50, pp. 1006–1013, Mar. 2002.

[3] E.C. Niehenke, R.A. Pucel, and I.J. Bahl, "Microwave and millimeter-wave integrated circuits," *IEEE Trans. Microwave Theory Tech.*, vol. MTT-50, pp. 846–857, Mar. 2002.

[4] A. Taflove, "Why study electromagnetics: the first unit in an undergraduate electromagnetics course," *IEEE Antennas Propagat. Mag.*, vol. 44, pp. 132–139, Apr. 2002.

[5] Z.J. Cendes, "Unlocking the magic of Maxwell's equations," *IEEE Spectrum*, pp. 29–34, Apr. 1989.

[6] Z.J. Cendes, "EM simulators = CAE tools," *IEEE Spectrum*, pp. 73–93, Nov. 1990.

[7] M.B. Steer, J.W. Bandler, and C.M. Snowden, "Computer-aided design of RF and microwave circuits and systems," *IEEE Trans. Microwave Theory Tech.*, vol. MTT-50, pp. 996–1005, Mar. 2002.

[8] E. Rejman, "Circuit designers : an endangered species ?," *Microwave Journal*, pp. 150–167, Nov. 2001.

[9] J.W. Bandler, "Guest editorial on special issue on automated circuit design using electromagnetic simulators," *IEEE Trans. Microwave Theory Tech.*, vol. MTT-45, pp. 709–710, May 1997.

[10] S.M. El-Ghazaly, R. Sorrentino, and M.B. Steer, "Guest editorial on special issue on global modelling of millimeter wave circuits and devices," *IEEE Trans. Microwave Theory Tech.*, vol. MTT-47, pp. 813–814, Jun. 1999.

[11] G.A.E. Vandenbosch, *The analysis of coaxially fed microstrip patch configurations in stratified dielectric media*, Ph.D. Dissertation, Katholieke Universiteit Leuven, Leuven, Belgium, May 1991.

[12] G.A.E. Vandenbosch and A.R. Van de Capelle, "A highly accurate feed model for microstrip, dual patch microstrip and microstrip backfire antenna," *Radio Sci.*, vol. 26, pp. 571–577, Mar.-Apr. 1991.

[13] G.A.E. Vandenbosch and A.R. Van de Capelle, "Mixed-potential integral expression formulation of the electric field in a stratified dielectric medium - application to the case of a probe current source," *IEEE Trans. Antennas Propagat.*, vol. AP-40, pp. 806–817, Jul. 1992.

[14] F.J. Demuynck, *The expansion wave concept : A new way to model mutual coupling in microstrip arrays applied in combination with a transmission line model*, Ph.D. Dissertation, Katholieke Universiteit Leuven, Leuven, Belgium, March 1995.

[15] F.J. Demuynck and G.A.E. Vandenbosch, "The expansion wave concept - part II : a new way to model mutual coupling in microstrip arrays," *IEEE Trans. Antennas Propagat.*, vol. AP-46, pp. 407–413, Mar. 1998.

[16] F.J. Demuynck, G.A.E. Vandenbosch, and A.R. Van de Capelle, "Analytical treatment of the Green's function singularities in a stratified dielectric medium," 23^{th} European Microwave Conference (EuMC), 1993, pp. 1000–1001.

[17] F.J. Demuynck, G.A.E. Vandenbosch, and A.R. Van de Capelle, "The expansion wave concept - part I : efficient calculation of spatial Green's functions in a stratified dielectric medium," *IEEE Trans. Antennas Propagat.*, vol. AP-46, pp. 397–406, Mar. 1998.

[18] V. Volski and G.A.E. Vandenbosch, "Radiation patterns of sources placed near the truncation of a semi-infinite dielectric structure: the demonstration case of a magnetic line current," *IEEE Trans. Antennas Propagat.*, vol. AP-48, pp. 240–245, Feb. 2000.

[19] A.Y. Svezhentsev, "Mixed-potential Green's functions for sheet electric current over metal-dielectric cylindrical structure," *J. Electromagn. Waves Appl.*, vol. 16, pp. 813–835, 2002.

[20] E.A. Soliman, *Planar microwave structures in layered media: full-wave analysis, design and characterization*, Ph.D. Dissertation, Katholieke Universiteit Leuven, Leuven, Belgium, Feb. 2000.

[21] E.A. Soliman, S. Brebels, E. Beyne, and G.A.E. Vandenbosch, "2x2 and 4x4 arrays of annular slot antennas in MCM-D technology fed be coplanar CPW networks," *IEE Proc. Pt. H., Microwaves Antennas Propagat.*, vol. 146, pp. 335–338, Oct. 1999.

[22] E.A. Soliman, P. Pieters, and E. Beyne, "Numerically efficient spatial-domain moment method for multislot transmission lines in layered media - application to multislot lines in MCM-D technology," *IEEE Trans. Microwave Theory Tech.*, vol. MTT-47, pp. 1782–1787, Sep. 1999.

[23] B.L.A. Van Thielen and G.A.E. Vandenbosch, "Method for the calculation of mutual coupling between discontinuities in planar circuits," *IEEE Trans. Microwave Theory Tech.*, vol. MTT-50, pp. 155–164, Jan. 2002.

[24] E. Whittaker, *A History of the Theories of Aether and Electricity, vol I : The classical theories*, Humanities press New York, N.Y., 1973, 434 pages, ISBN 0-391-00274-0.

[25] A. O'Rahilly, *Electromagnetics, a Critical Examination of Fundamentals*, Longmans, Green and Co., 1938, 884 pages.

[26] A.K. Torres Assis, *Weber's Electrodynamics*, Kluwer Academic Publishers, 1962, 274 pages, ISBN 0-7923-3137-0.

[27] J.C. Maxwell, *A Treatise on Electricity and Magnetism*, Dover Publications Inc., New York, 1954.

[28] J.C. Maxwell, "A dynamical theory of the electromagnetic field," *Philosophical Transactions of the Royal Society of London*, pp. 459–512, 1865.

[29] H. Hertz, "Über elektrodynamische wellen im luftraum und deren reflexion," *Annalen der Physik*, vol. 34, pp. 609–623, 1888.

[30] H. Hertz, "Die kräfte electrischer schwingungen, behandelt nach der Maxwell'schen theorie," *Annalen der Physik*, vol. 36, pp. 1–22, 1889.

[31] O. Darrigol, *Electrodynamics from Ampere to Einstein*, Oxford University Press, 2000, 552 pages, ISBN 0-198-50594-9.

[32] C.-T. Tai, "On the presentation of Maxwell's theory," *Proceedings of the IEEE*, pp. 936–945, Aug. 1972.

[33] G. Green, *An Essay of the Application of Mathematical Analysis to the Theories of Electricity and Magnetism*, Nottingham, 1828.

[34] R.E. Collin, *Field Theory of Guided Waves*, IEEE Press, Piscataway (N.J.), 1991, 852 pages, ISBN 0-87942-237-8.

[35] C.-T. Tai, *Dyadic Green's Functions in Electromagnetic Theory*, Intext monograph series in electrical engineering. Intext Educational Publ. Scranton, 1971, 246 pages, ISBN 0-7002-2345-2.

[36] A. Sommerfeld and E.G. Strauss, *Partial Differential Equations of Physics*, vol. VI of *Lectures on Theoretical Physics*, Academic Press New York, N.Y., 1966, 335 pages.

[37] J.A. Stratton, *Electromagnetic Theory*, International series in Pure and Applied Physics. MacGraw-Hill, New York, 1941, 615 pages, ISBN 0-07-062150-0.

[38] R. Mittra, Ed., *Computer Techniques for Electromagnetics*, vol. 7 of *International Series of Monographs in Electrical Engineering*, Pergamon Oxford, 1973, Chapter 4 : "Integral Equation Solutions of Three-dimensional Scattering Problems" by A.J. Poggio, E.K. Miller, 403 pages, ISBN 0-08-016888-4.

[39] A. Liénard, "Champ électrique et magnétique produit par une charge électrique concentrée en un point et animée d'un movement quelconque," *L' Éclairage Électrique*, pp. 5–14, 53–59,106–112, Jul. 1898.

[40] E. Wiechert, "Elektrodynamische elementargesetze," *Archives Néerlandaises*, pp. 549–73, 1900.

[41] R.P. Feynman, R.B. Leighton, and M. Sands, *The Feynman Lectures on Physics, Volume II: Electromagnetism and Matter*, Addison-Wesley Publishing Company, Inc., 1964, ISBN 0-201-02117-X.

[42] G.S. Smith, *An Introduction to Classical Electromagnetic Radiation*, Cambridge University Press, Cambridge, 1997, 653 pages, ISBN 0-521-58698-4.

[43] E.K. Miller and J.A. Landt, "Direct time-domain techniques for transient radiation and scattering from wires," *Proceedings of the IEEE*, pp. 1396–1423, Nov. 1980.

[44] E.K. Miller, "An exploration of radiation physics in electromagnetics," Montreal, Canada, 1997, IEEE International Symposium on Antennas and Propagation Digest, pp. 048–2051.

[45] J.G. Maloney, G.S. Smith, and W.R. Scott, "Accurate computation of the radiation from simple antennas using the finite-difference time-domain method," *IEEE Trans. Antennas Propagat.*, pp. 1059–1068, Jul. 1990.

[46] G.S. Smith, "On the interpretation for radiation from simple current distributions," *IEEE Antennas Propagat. Mag.*, pp. 39–44, Aug. 1998.

[47] G.S. Smith and T.W. Herschel, "On the transient radiation of energy from simple current distributions and linear antennas," *IEEE Antennas Propagat. Mag.*, pp. 49–62, Jun. 2001.

[48] C.C. Bantin, "Radiation from a pulse-excited thin wire monopole," *IEEE Antennas Propagat. Mag.*, pp. 64–69, Jun. 2001.

[49] M.A. Heald, "Electric fields and charges in elementary circuits," *American Journal of Physics*, pp. 522–526, Jun. 1984.

[50] C.S. Lai, "Alternative choice for the energy flow vector of the electromagnetic field," *American Journal of Physics*, pp. 841–842, Sep. 1981.

[51] U. Backhaus and K. Schäfer, "On the uniqueness of the vector for energy flow density in electromagnetic fields," *American Journal of Physics*, pp. 279–280, Mar. 1986.

[52] A. Sommerfeld and E.G. Ramberg, *Electrodynamics*, vol. III of *Lectures on Theoretical Physics*, Academic Press New York, N.Y., 1964, 371 pages.

[53] A. Deutsch, "When are transmission-line effects important for on-chip interconnects ?," *IEEE Trans. Microwave Theory Tech.*, vol. MTT-45, pp. 1836–1846, Oct. 1997.

[54] V.H. Rumsey, "Reaction concept in electromagnetic theory," *Phys. Rev.*, pp. 1483–1491, Jun. 1954.

[55] R.F. Harrington, *Time Harmonic Electromagnetic Fields*, McGraw-Hill Electrical and Electronic Engineering Series. McGraw-Hill, 1961, 480 pages, ISBN 07-026745-6.

[56] R.F. Harrington, *Field Computation by Moment Methods*, Mac Millan Series in Electrical Science. Mac Millan, New York, 1968, 229 pages.

[57] J. Sercu, N. Faché, and D. De Zutter, "Characterisation of TEM and non-TEM planar transmission lines with a full-wave 3D field analysis technique," Montreal, Canada, 1993, 23^{th} European Microwave Conference, pp. 328–329.

[58] M.N. Abdulla and M.B. Steer, "Extraction of network parameters in the electromagnetic analysis of planar structures using the method of moments," *IEEE Trans. Microwave Theory Tech.*, vol. MTT-49, pp. 94–103, Jan. 2001.

[59] W.J.R. Hoefer, "Time domain electromagnetic simulation for microwave CAD applications," *IEEE Trans. Microwave Theory Tech.*, vol. MTT-40, pp. 1517–1527, Jul. 1992.

[60] O.C. Zienckiewicz, *The Finite Element Method in Engineering Science*, McGraw-Hill, 1971.

[61] P. Silvester, "Finite element solution of homogenuous waveguide solutions," *Alta Frequenza*, vol. 38, pp. 313–317, 1969.

[62] D. Sun, J. Manges, X. Yuan, and Z. Cendes, "Spurious modes in finite-element methods," *IEEE Trans. Antennas Propagat.*, vol. AP-37, pp. 12–24, Oct. 1995.

[63] J.L. Volakis, A. Chatterjee, and L.C. Kempel, *Finite Elements for Electromagnetics*, IEEE/OUP Series on Electromagnitic Wave Theory. IEEE Press - Oxford University Press, 1998, 344 pages, ISBN 0-7803-3425-6.

[64] A.F. Peterson, S.L. Ray, and R. Mittra, *Computational Methods for Electromagnetics*, IEEE Press Series on Electromagnetic Waves. IEEE Press - Oxford University Press, 1998, 564 pages, ISBN 0-7803-1122-1.

[65] Z.J. Cendes, "Vector finite elements for electromagnetic field computation," *IEEE Transactions on Magnetics*, vol. MAG-27, pp. 3958–3966, Sep. 1991.

[66] H. Whitney, *Geometric Integration Theory*, Princeton University Press, NJ., 1957.

[67] J.C. Nedelec, "Mixed finite elements in R^3," *Numer. Math.*, vol. 35, pp. 315–341, 1980.

[68] G. Mur, "Edge elements, their advantages and their disadvantages," IEEE Trans. Magnetics, vol. MAG-30, pp. 3552–3557, Sept. 1994.

[69] K.D. Paulsen, D.R. Lynch, and J.W. Strohbehn, "Three-dimensional finite, boundary, and hybrid element solutions of the Maxwell equations for lossy dielectric media," *IEEE Trans. Microwave Theory Tech.*, vol. MTT-36, pp. 682–693, Apr. 1988.

[70] X.-Q. Sheng, J.-M. Jin, J. Song, C.-C. Lu, and W.C. Chew, "On the formulation of hybrid finite-element and boundary integral methods for 3-D scattering," *IEEE Trans. Antennas Propagat.*, vol. AP-46, pp. 303–311, Mar. 1998.

[71] E. Bayliss and E. Turkel, "Radiation boundary conditions for wave-like equations," *Comm. Pure Appl. Math.*, vol. 33, pp. 707–725, 1980.

[72] A.F. Peterson, "Absorbing boundary conditions for the vector wave equation," *Microwave Opt. Tech. Lett.*, vol. 1, pp. 62–64, Apr. 1988.

[73] J.P. Webb and V.N. Kanellopoulos, "Absorbing boundary condtions for finite element solution of the vector wave equation," *Microwave Opt. Tech. Lett.*, vol. 1, pp. 370–372, Oct. 1989.

[74] A. Chatterjee and J.L. Volakis, "Conformal absorbing boundary conditions for the vector wave equation," *Microwave Opt. Tech. Lett.*, vol. 6, pp. 886–888, 1993.

[75] A. Chatterjee, J. Jin, and J.L. Volakis, "Edge-based finite elements and vector ABC's applied to 3-D scattering," *IEEE Trans. Antennas Propagat.*, vol. AP-41, pp. 221–226, Feb. 1993.

[76] S.R. Legault, T.B.A. Senior, and J.L. Volakis, "Design of planar absorbing layers for domain truncation in FEM applications," *Electromagnetics*, vol. 16, pp. 451–464, Jul.-Aug. 1996.

[77] T. Özdemir and J.L. Volakis, "A comparative study of an absorber boundary condition and an artificial absorber for truncating finite element meshes," *Radio Sci.*, vol. 29, pp. 1255–1263, Sep.-Oct. 1994.

[78] J.P. Bérenger, "A perfectly matched layer for the absorption of electromagnetic waves," *Journal of computational physics*, vol. 114, pp. 185–200, 1994.

[79] R.D. Graglia, D.R. Wilton, and A.F. Peterson, "Higher order interpolatory vector bases for computational electromagnetics," *IEEE Trans. Antennas Propagat.*, vol. AP-45, pp. 329–342, Mar. 1997.

[80] A.F. Peterson and K.R. Aberegg, "Parametric mapping of vector basis functions for surface integral equation formulations," *Appl. Computat. Electromagnet. Soc. (ACES) J.*, vol. 10, pp. 107–115, Nov. 1995.

[81] A.F. Peterson, "Error in the finite element discretization of the scalar Helmholtz equation over electrically large regions," *IEEE Microwave Guided Wave Lett.*, vol. 1, pp. 219–222, Aug. 1991.

[82] Jr. W.R. Scott, "Errors due to spatial discretization and numerical precision in the finite element method," *IEEE Trans. Antennas Propagat.*, vol. AP-42, pp. 1565–1570, Nov. 1994.

[83] R.L. Lee, "A study of discretization error in the finite element approximation of wave solutions," *IEEE Trans. Antennas Propagat.*, vol. AP-40, pp. 542–549, May 1992.

[84] K.W. Morton and D.F. Mayers, *Numerical Solution of Partial Differential Equations*, Cambridge University Press, 1994, 227 pages, ISBN 0-521-42922-6.

[85] K.S. Yee, "Numerical solution of initial boundary value problems involving Maxwell's equations in isotropic media," *IEEE Trans. Antennas Propagat.*, vol. AP-14, pp. 302–307, May 1966.

[86] D.M. Sheen, S.M. Ali, M.D. Abouzahra, and J.A. Kong, "Application of the three-dimensional finite-difference time-domain method to the analysis of planar microstrip circuits," *IEEE Trans. Microwave Theory Tech.*, vol. MTT-38, pp. 849–857, Jul. 1990.

[87] R. Courant, K.O. Friedrichs, and H. Lewy, "Über die partiellen differenzengleichungen der mathematischen physik," *Math. Ann.*, vol. 100, pp. 32, 1928.

[88] M. Mrozowski, "Stability condition for the explicit algorithms of the time domain analysis of Maxwell's equations," *IEEE Microwave Guided Wave Lett.*, vol. 4, pp. 279–281, Aug. 1994.

[89] T. Namiki, "3-D ADI-FDTD method- unconditionally stable time-domain algorithm for solving full vector Maxwell's equations," *IEEE Trans. Microwave Theory Tech.*, vol. MTT-48, pp. 1743–1748, Oct. 2000.

[90] A. Taflove, *Computational Electrodynamics : the Finite Difference Time Domain Method*, Artech House, Inc., 1997, 599 pages, ISBN 0-89006-792-9.

[91] J. De Moerloose and D. De Zutter, "Surface integral representation radiation boundary condition for the FDTD method," *IEEE Trans. Antennas Propagat.*, vol. AP-41, pp. 890–896, July 1993.

[92] H. Rogier, F. Olyslager, and D. De Zutter, "A new hybrid FDTD-BIE approach to model electromagnetic scattering problems," *IEEE Microwave Guided Wave Lett.*, vol. 8, pp. 138–140, Mar. 1998.

[93] G. Mur, "Absorbing boundary conditions for the finite-difference approximation of the time-domain electromagnetic-field equations," *IEEE Trans. Electromagn. Compat.*, vol. EMC-23, pp. 377–382, Nov. 1981.

[94] B. Engquist and A. Majda, "Absorbing boundary conditions for the numerical simulation of waves," *J. Math. Comp.*, vol. 31, pp. 629–651, Jul. 1977.

[95] C.J. Railton, E.M. Daniel, D.-L. Paul, and J.P. McGeehan, "Optimized absorbing boundary conditions for the analysis of planar circuits using the finite difference time domain method," *IEEE Trans. Microwave Theory Tech.*, vol. MTT-41, pp. 290–297, Feb. 1993.

[96] D.S. Katz, E.T. Thiele, and A. Taflove, "Validation and extension to three dimensions of the berenger PML absorbing boundary conditions for FD-TD meshes," *IEEE Microwave Guided Wave Lett.*, vol. 4, pp. 268–270, Aug. 1994.

[97] J.P. Bérenger, "Improved PML for the FDTD solution of wave-structure interaction problems," *IEEE Trans. Antennas Propagat.*, vol. AP-45, pp. 466–473, Mar. 1997.

[98] R. Mittra and U. Pekel, "A new look at the Perfectly Matched Layer (PML) concept for the reflectionless absorption of electromagnetic waves," *IEEE Microwave Guided Wave Lett.*, vol. 5, pp. 84–86, Mar. 1995.

[99] A.C. Cangellaris and D.B. Wright, "Analysis of the numerical error caused by the stair-stepped approximation of a conducting boundary in FDTD simulations of electromagnetic phenomena," *IEEE Trans. Antennas Propagat.*, vol. AP-39, pp. 1518–1525, 1993.

[100] K.S. Kunz and L. Simpson, "A technique for increasing the resolution of finite-difference solutions of Maxwell's equations," *IEEE Trans. Electromagn. Compat.*, vol. EMC-23, pp. 419–422, Apr. 1981.

[101] S.S. Zivanovic, K.S. Yee, and K.K. Mei, "A subgridding algorithm for the time-domain finite-difference method to solve Maxwell's equations," *IEEE Trans. Microwave Theory Tech.*, vol. MTT-38, pp. 471–479, Mar. 1991.

[102] M. Okoniewski, E. Okoniewska, and M.A. Stuchly, "A three-dimensional subgridding algorithm for FDTD," *IEEE Trans. Microwave Theory Tech.*, vol. MTT-45, pp. 422–428, Mar. 1997.

[103] R. Holland, "Finite difference solutions of Maxwell's equations in generalized nonorthogonal coordinates," *IEEE Trans. Nucl. Sci.*, pp. 4598–4591, Dec. 1983.

[104] M. Fusco, "FDTD algorithm in curvilinear coordinates," *IEEE Trans. Antennas Propagat.*, vol. AP-38, pp. 76–89, Jan. 1990.

[105] N. Madsen and R. Ziolkowski, "A modified finite volume technique for Maxwell's equations," *Electromagnetics*, vol. 10, pp. 127–145, Jan. 1990.

[106] N. Madsen, "Divergence preserving discrete surface integral methods for Maxwell's equations using nonorthogonal unstructured grids," *J. Comput. Physics*, vol. 119, pp. 34–35, Jan. 1995.

[107] S.D. Gedney, F.S. Lansing, and D.L. Rascoe, "Full wave analysis of microwave monolithic circuit devices using a generalized Yee-algorithm based on an unstructured grid," *IEEE Trans. Microwave Theory Tech.*, vol. MTT-44, pp. 1393, Aug. 1996.

[108] R.F. Harrington, "Matrix methods for field problems," *IEEE Trans. Antennas Propagat.*, vol. AP-55, no. 2, pp. 136–149, Feb. 1967.

[109] D.R. Wilton and C.M. Butler, "Effective methods for solving integral and integro-differential equations," *Electromagnetics*, vol. 1, pp. 289–308, 1981.

[110] M.M. Ney, "Method of moments as applied to electromagnetic problems," *IEEE Trans. Antennas Propagat.*, vol. MTT-33, pp. 972–980, Oct. 1985.

[111] D.R. Wilton, "Review of current status and trends in the use of integral equations in computational electromagnetics," *Electromagnetics*, vol. 12, pp. 287–341, 1992.

[112] T.K. Sarkar, A.R. Djodjević, and E. Arvas, "On the choice of expansion and weighting functions in the numerical solution of operator equations," *IEEE Trans. Antennas Propagat.*, vol. AP-33, pp. 988–996, Sept. 1985.

[113] D.R. Wilton and S. Govind, "Incorporation of edge conditions in moment method solutions," *IEEE Trans. Antennas Propagat.*, vol. AP-25, pp. 845–850, Nov. 1977.

[114] T.K. Sarkar, "A note on the choice of weighting functions in the method of moments," *IEEE Trans. Antennas Propagat.*, vol. AP-33, pp. 436–441, Apr. 1985.

[115] R. Mittra, Ed., *Numerical and Asymptotic Techniques in Electromagnetics*, vol. 3 of *Topics in Applied Physics*, Springer-Verlag, Berlin, Heidelberg, New York, 1975, Chapter 5 : Stability and Convergence of Moment Method Solutions, R. Mittra, C.A. Klein.

[116] A.W. Glisson and D.R. Wilton, "Simple and efficient numerical methods for problems of electromagnetic radiation and scattering from surfaces," *IEEE Trans. Antennas Propagat.*, vol. AP-28, pp. 593–603, 1980.

[117] S.M. Rao, D.R. Wilton, and A.W. Glisson, "Electromagnetic scattering by surfaces of arbitrary shape," *IEEE Trans. Antennas Propagat.*, vol. AP-30, no. 3, pp. 409–418, May 1982.

[118] R.E. Hodges and Y. Rahmat-Samii, "The evaluation of MFIE integrals with the use of vector triangle basis functions," *Microwave Opt. Tech. Lett.*, vol. 14, pp. 9–14, Jan. 1997.

[119] J.M. Rius, E. Úbeda, and J. Parrón, "On the testing of the magnetic field integral equation with RWG basis functions in method of moments," *IEEE Trans. Antennas Propagat.*, vol. AP-49, pp. 1550–1553, Nov. 2001.

[120] S.W. Lee, J. Boersma, C.L. Law, and G.A. Deschamps, "Singularity in Green's function and its numerical evaluation," *IEEE Trans. Antennas Propagat.*, vol. AP-28, pp. 311–317, 1980.

[121] D.B. Miron, "The singular integral problem in surfaces," *IEEE Trans. Antennas Propagat.*, vol. AP-31, pp. 507–509, May 1983.

[122] D.R. Wilton et *al.*, "Potential integrals for uniform and linear source distributions on polygonal and polyhedral domains," *IEEE Trans. Antennas Propagat.*, vol. AP-32, pp. 276–281, Mar. 1984.

[123] J.K. Skwirzynski, Ed., *Theoretical Methods for Determining the Interaction of Electromagnetic Waves with Structures*, Sijthoff & Noordhoff International Publishers B.V., Alphen aan den Rijn, The Netherlands, 1981, Part I, Chapter 3, "Surface Integral Equations for Conducting and Dielectric Bodies," R.F. Harrington and J.R. Mautz, 913 pages, ISBN 90-286-2161-X.

[124] A.F. Peterson, "The 'interior' resonance problem associated with surface integral equations of electromagnetics," *Electromagnetics*, vol. 10, pp. 293–312, 1990.

[125] R.F. Harrington and J.R. Mautz, "H-field, E-field, and combined-field solutions for conducting bodies of revolution," *Arch. Elek. Ubertragungstech. (AEU)*, vol. 32, pp. 157–164, Apr. 1978.

[126] R.F. Harrington and J.R. Mautz, "A combined-source solution for radiation and scattering from a perfectly conduction body," *IEEE Trans. Antennas Propagat.*, vol. AP-27, pp. 445–454, Jul. 1979.

[127] R. Mittra, Y. Rahmat-Samii, D.V. Jamnejad, and W.A. Davis, "A new look at the thin plate scattering problem," *Radio Sci.*, vol. 8, pp. 869–875, 1973.

[128] A.J. Poggio G.J. Burke, "Numerical electromagnetics code (NEC) - method of moments," *Technical document 116*, Jul. 1977, Naval Ocean Systems Center, San Diego, Calif.

[129] D.R. Wilton and A.W. Glisson, "On improving the stability of the electric field integral equation at low frequency," Los Angeles, CA, 1981, IEEE AP-S Int. Symposium, p. 24.

[130] J.-S. Zhao and W.C. Chew, "Integral equation solution of Maxwell's equations from zero to microwave frequencies," *IEEE Trans. Antennas Propagat.*, vol. AP-48, pp. 1635–1645, October 2000.

[131] J.R. Mautz and R.F. Harrington, "An E-field solution for a conducting surface small or comparable to the wavelength," *IEEE Trans. Antennas Propagat.*, vol. AP-32, pp. 330–339, April 1994.

[132] E. Arvas, R.F. Harrington, and J.R. Mautz, "Radiation and scattering from electrically small conducting bodies of arbitrary shape," *IEEE Trans. Antennas Propagat.*, vol. AP-34, pp. 66–77, January 1986.

[133] D.R. Wilton, "Topological considerations in surface patch and volume cell modeling of electromagnetic scatterers," Santiago de Compostela, Spain, 1983, URSI Int. Symp. Electromagn. Theory, pp. 65–68.

[134] G. Vechhi, "Loop-star decomposition of basis functions in the discretization of the EFIE," *IEEE Trans. Antennas Propagat.*, vol. AP-47, pp. 339–346, February 1999.

[135] S.M. Rao and D.R. Wilton, "Transient scattering by conducting surfaces of arbitrary shape," *IEEE Trans. Antennas Propagat.*, vol. AP-39, pp. 56–61, Jan. 1991.

[136] M.J. Bluck and S.P. Walker, "Time domain BIE analysis of large three-dimensional electromagnetic scattering problems," *IEEE Trans. Antennas Propagat.*, vol. AP-45, pp. 894–901, May 1997.

[137] A.A. Ergin, B. Shanker, and E. Michielssen, "The plane wave time domain algorithm for the fast analysis of transient wave phenomena," *IEEE Antennas Propagat. Mag.*, vol. 41, pp. 39–52, Aug. 1999.

[138] B. Shanker, A.A. Ergin, K. Aygün, and E. Michielssen, "Analysis of transient electromagnetic scattering phenomena using a two-level plane wave time-domain algorithm," *IEEE Trans. Antennas Propagat.*, vol. AP-48, pp. 510–523, Apr. 2000.

[139] B.P. Rynne, "Instabilities in time marching algorithms for scattering problems," *Electromagnetics*, vol. 6, pp. 129–144, 1986.

[140] P.J. Davies, "Stability of time-marching numerical shemes for the electric field integral equation," *J. Electromagn. Waves Appl.*, vol. 8, pp. 85–114, 1994.

[141] G. Manara, A. Monorchio, and R. Reggiannini, "A space-time discretization criterion for a stable time-marching solution of the electric field integral equation," *IEEE Trans. Antennas Propagat.*, vol. AP-45, pp. 527–532, Mar. 1997.

[142] S. Dodson, S.P. Walker, and M.J. Bluck, "Implicitness and stability of time domain integral equation scattering analysis," *Appl. Comp. Electromagn. Soc. J.*, vol. 13, pp. 291–301, 1998.

[143] B. Shanker, A.A. Ergin, K. Augün, and E. Michielssen, "Analysis of transient electromagnetic scattering from closed surfaces using a combined field integral equation," *IEEE Trans. Antennas Propagat.*, vol. AP-48, pp. 1064–1074, Jul. 2000.

[144] N. Hersovici, "New considerations in the design of microstrip antennas," *IEEE Trans. Antennas Propagat.*, vol. AP-46, pp. 807–812, Jun. 1998.

[145] M. Farina and T. Rozzi, "A 3-D integral equation-based approach to the analysis of real-life MMICs-application to microelectromechanical systems," *IEEE Trans. Microwave Theory Tech.*, vol. MTT-49, pp. 2235–2240, Dec. 2001.

[146] L.P.B. Katehi, J.F. Harvey, and E. Brown, "MEMS and Si micromachined circuits for high frequency applications," *IEEE Trans. Microwave Theory Tech.*, vol. MTT-50, pp. 858–865, Mar. 2002.

[147] C. Schuster, "Parasitic modes on printed circuit boards and their effects on EMC and signal integrity," *IEEE Trans. Electromagn. Compat.*, vol. EMC-43, pp. 416–425, Nov. 2001.

[148] M. R. Abdul-Gaffoor, H.K. Smith, A.A. Kishk, and A.W. Glisson, "Simple and efficient full-wave modeling of electromagnetic coupling in realistic RF multilayer PCB layouts," *IEEE Trans. Microwave Theory Tech.*, vol. MTT-50, pp. 1445–1457, Jun. 2002.

[149] M. Piket-May, A. Taflove, and J. Baron, "FD-TD modeling of digital signal propagation in 3D circuits with passive and active loads," *IEEE Trans. Microwave Theory Tech.*, vol. MTT-42, pp. 1514–1523, Aug. 1994.

[150] B.K. Gilbert and G.-W. Pan, "MCM packaging for present- and next-generation high clock-rate digital- and mixed-signal electronic systems: areas for development," *IEEE Trans. Microwave Theory Tech.*, vol. MTT-45, pp. 1819–1835, Oct. 1987.

[151] W.D. Becker, P.H. Harms, and R. Mittra, "Time-domain electromagnetic analysis of interconnects in a computer chip package," *IEEE Trans. Microwave Theory Tech.*, vol. MTT-40, pp. 2155–2163, Dec. 1992.

[152] J.-G. Yook, N.I. Dib, and L.P.B. Katehi, "Characterization of high frequency interconnects using finite difference time domain and finite element methods," *IEEE Trans. Microwave Theory Tech.*, vol. MTT-42, pp. 1727–1736, Sep. 1994.

[153] J.-G. Yook, L.P.B. Katehi, K.A. Sakallah, R.S. Martin, L. Huang, and T.A. Schreyer, "Application of system-level EM modeling to high-speed digital IC packages and PCB's," *IEEE Trans. Microwave Theory Tech.*, vol. MTT-45, pp. 1847–1855, Oct. 1987.

[154] S. Sercu and L. Martens, "High-frequency circuit modeling of large pin count packages," *IEEE Trans. Microwave Theory Tech.*, vol. MTT-45, pp. 1897–1903, Oct. 1997.

[155] Y. Chen, P. Harms, R. Mittra, and W.T. Beyene, "An FDTD-Touchstone hybrid technique for equivalent circuit modeling of SOP electronic packages," *IEEE Trans. Microwave Theory Tech.*, vol. MTT-45, pp. 1911–1917, Oct. 1997.

[156] T.-S. Horng, S.-M. Wu, H.-S. Huang, C.-T. Chiu, and C.-P. Hung, "Modeling of lead-frame plastic CSPs for accurate prediction of their low-pass filter effects on RFICs," *IEEE Trans. Microwave Theory Tech.*, vol. MTT-49, pp. 1538–1545, Sep. 2001.

[157] J. DeLap, "Planar EM simulation of multi-chip modules and BGA packages," *Microwave Journal*, pp. 140–148, Nov. 2001.

[158] A. Sommerfeld, "Über die ausbreitung der wellen in der drahtlosen telegraphie," *Ann. der Physik*, vol. 28, pp. 665–736, Mar. 1909.

[159] J.R. Wait, "Propagation of radiowaves over a stratified ground," *Geophysics*, vol. 18, pp. 416–422, 1953.

[160] C. Tang, "Electromagnetic fields due to dipole antennas embedded in stratified anisotropic media," *IEEE Trans. Antennas Propagat.*, vol. AP-27, pp. 665–670, Sep. 1979.

[161] S.M. Ali and S.F. Massoud, "Electromagnetic fields of buried sources in stratified anisotropic media," *IEEE Trans. Antennas Propagat.*, vol. AP-27, pp. 671–678, Sep. 1979.

[162] J.A. Kong, "Electromagnetic fields due to dipole antennas over stratified anisotropic media," *Geophysics*, vol. 37, pp. 958–966, Dec. 1972.

[163] T. Sphicopoulos, V. Teodoris, and F.E. Gardiol, "Tractable form of the dyadic Green's function for application to multilayered isotropic media," *Electron. Lett.*, vol. 19, pp. 1055–1057, 1983.

[164] T. Itoh and R. Mittra, "Spectral domain approach for calculating the dispersion characteristics of microstrip lines," *IEEE Trans. Microwave Theory Tech.*, vol. MTT-21, pp. 496–499, 1973.

[165] J.B. Davies and D. Mirshekar-Syahkal, "Spectral domain solution of arbitrary coplanar transmission line with multilayer substrates," *IEEE Trans. Microwave Theory Tech.*, vol. MTT-25, pp. 143–146, Feb. 1977.

[166] R. Mittra and T. Itoh, "A new technique for the analysis of the dispersion characteristics of microstrip lines," *IEEE Trans. Microwave Theory Tech.*, vol. MTT-19, pp. 47–56, Jan. 1971.

[167] T. Itoh and R. Mittra, "A technique for computing dispersion characteristics of shielded microstrip lines," *IEEE Trans. Microwave Theory Tech.*, vol. MTT-22, pp. 896–898, Oct. 1974.

[168] Y. Rahmat-Samii, T. Itoh, and R. Mittra, "A spectral domain analysis for solving microstrip discontinuity problems," *IEEE Trans. Microwave Theory Tech.*, vol. MTT-22, pp. 372–378, Apr. 1974.

[169] T. Itoh, "Generalized spectral domain method for multiconductor printed lines an its application to turnable suspended microstrip," *IEEE Trans. Microwave Theory Tech.*, vol. MTT-26, pp. 983–987, Dec. 1978.

[170] T. Itoh, "Spectral domain immittance approach for dispersion characteristics of generalized printed transmission lines," *IEEE Trans. Microwave Theory Tech.*, vol. MTT-28, pp. 733–736, Jul. 1980.

[171] R.H. Jansen, "The spectral-domain approach for microwave integrated circuits," *IEEE Trans. Microwave Theory Tech.*, vol. MTT-33, pp. 1043–1056, Oct. 1985.

[172] J. Wang, "General method for the computation of radiation in stratified media," *IEE Proc. Pt. H., Microwaves Antennas Propagat.*, vol. 132, pp. 379–387, Feb. 1985.

[173] N.K. Das and D.M. Pozar, "A generalized spectral-domain Green's function for multilayer dielectric substrates with application to multilayer transmission lines," *IEEE Trans. Microwave Theory Tech.*, vol. MTT-35, pp. 326–335, Mar. 1987.

[174] G.P.S. Cavalcante, D.A. Rogers, and A.J. Gariola, "Analysis of electromagnetic wave propagation in multilayered media using dyadic Green's functions," *Radio Sci.*, vol. 17, pp. 503–508, 1982.

[175] T. Sphicopoulos, V. Theodoris, and F. Gardiol, "Dyadic Green function for the electromagnetic field in multilayered isotropic media: an operator approach," *IEE Proc. Pt. H., Microwaves Antennas Propagat.*, vol. 132, pp. 329–334, Aug. 1985.

[176] J.K. Lee and J.A. Kong, "Dyadic Green's functions for layered anistropic medium," *Electromagnetics*, vol. 3, pp. 111–130, 1983.

[177] J.S. Bagby, "Dyadic Green's functions for integrated electronic and optical circuits," *IEEE Trans. Microwave Theory Tech.*, vol. MTT-35, pp. 206–210, Feb. 1987.

[178] L. Vegni, R. Cichetti, and P. Capece, "Spectral dyadic Green's function formulation for planar integrated structures," *IEEE Trans. Antennas Propagat.*, vol. AP-36, pp. 1075–1065, Aug. 1988.

[179] M.S. Viola and D.P. Nyquist, "An observation on the Sommerfeld-integral representation of the electric dyadic Green's function for layered media," *IEEE Trans. Microwave Theory Tech.*, vol. MTT-36, pp. 1289–1292, August 1988.

[180] S. Barkeshli and P.H. Pathak, "On the dyadic Green's function for a planar multilayered dielectric/magnetic media," *IEEE Trans. Antennas Propagat.*, vol. AP-40, pp. 128–142, Jan. 1992.

[181] P. Bernardi, "Dyadic Green's functions for conductor-backed layered structures excited by arbitrary tridimensional sources," *IEEE Trans. Antennas Propagat.*, vol. AP-42, pp. 1474–1483, Aug. 1994.

[182] S.-G. Pan and I. Wolff, "Scalarization of dyadic spectral Green's functions and network formalism for three-dimensional full-wave analysis of planar lines and antennas," *IEEE Trans. Microwave Theory Tech.*, vol. MTT-42, pp. 2118–2127, Nov. 1994.

[183] K.A. Michalski and J.R. Mosig, "Multilayered media Green's functions in integral equation formulations," *IEEE Trans. Antennas Propagat.*, vol. AP-45, pp. 508–519, March 1997.

[184] T.M. Gregorczyk, *Integrated 3D antennas for millimeter-wave applications: theoretical study and technological realization*, Ph.D. Dissertation, École Polytechnique Fédérale de Lausanne, Lausanne, Switzerland, 2000, Thèse EPFL No. 2299.

[185] K.A. Michalski, "Missing boundary conditions of electromagnetics," *Electron. Lett.*, vol. 22, pp. 921–922, August 1986.

[186] R. Kastner, E. Heymann, and A. Sabban, "Spectral domain iterative analysis of single- and double-layered microstrip antennas using the conjugate gradient algorithm," *IEEE Trans. Antennas Propagat.*, vol. 36, pp. 1204–1212, Sept. 1988.

[187] R. Kastner, "On the singularity of the full spectral Green's dyad," *IEEE Trans. Antennas Propagat.*, vol. AP-35, pp. 1303–1305, Nov. 1997.

[188] H.C. Pocklington, "Electrical oscillations in wires," *Cambridge Philos. Soc. Proc.*, vol. 9, pp. 324–332, 1897.

[189] E. Hallén, "Theoretical investigations into the transmitting and receiving qualities of antennae," *Nova Acta Regiae Societatis Scientiarium Upsaliensis (Sweden)*, vol. IV, no. 4, pp. 1–44, 1938.

[190] J.R. Mosig, "Arbitrarily shaped microstrip structures and their analysis with a mixed potential integral equation," *IEEE Trans. Microwave Theory Tech.*, vol. MTT-36, pp. 314–323, February 1988.

[191] K.A. Michalski and D. Zheng, "Electromagnetic scattering and radiation by surfaces of arbitrary shape in layered media, part I: theory," *IEEE Trans. Antennas Propagat.*, vol. AP-38, pp. 335–334, March 1990.

[192] A.D. Yaghjian, "Electric dyadic Green's function in the source region," *Proceedings of the IEEE*, vol. 68, pp. 248–263, Feb. 1980.

[193] J.J.H. Wang, "A unified and consistent view on the singularities of the electric dyadic Green's function in the source region," *IEEE Trans. Antennas Propagat.*, vol. AP-30, pp. 463–468, May 1982.

[194] M. Silberstein, "Application of a generalized Leibniz rule for calculating electromagnetic fields within continuous source regions," *Radio Sci.*, vol. 26, pp. 183–190, Jan.-Feb. 1991.

[195] J. Chen, A.A. Kishk, and A.W. Glisson, "Application of a new MPIE formulation to the analysis of a dielectric resonator embedded in a multilayered medium coupled to a microstrip circuit," *IEEE Trans. Microwave Theory Tech.*, vol. MTT-49, pp. 263–279, Feb. 1991.

[196] J. Chen, A.A. Kishk, and A.W. Glisson, "MPIE for conducting sheets penetrating a multilayer medium," Seattle, WA, 1994, Dig. IEEE AP-S Int. Symp., pp. 1346–1349.

[197] W.A. Johnson, "Analysis of vertical tubular cylinder which penetrates an air-dielectric interface and which is excited by an azimuthally symmetric source," *Radio Sci.*, vol. 18, pp. 1273–1281, Nov.-Dec. 1983.

[198] K.A. Michalski and C.E. Smith, "Analysis of parallel monopole antennas residing in contiguous media," in *Nat. Radio Sc. Meet. Dig.*, Boulder, CO, 1986, p. 230.

[199] K.A. Michalski and D. Zheng, "Analysis of wire antennas of arbitrary shape residing in contiguous half-spaces," York, UK, 1987, 5^{th} Int. Conf. Antennas Propagat. (ICAP 87), pp. 507–511.

[200] J.R. Mosig and F.E. Gardiol, *A Dynamical Radiation Model for Microstrip Structures*, vol. 59 of *Advances in Electronics and Electron Physics*, Editor P. Hawkes, Academic Press, New York, 1982, pp. 139-237.

[201] K.A. Michalski, "The mixed-potential electric field integral equation for objects in layered media," *Arch. Elek. Ubertragungstech. (AEU)*, vol. 39, pp. 317–322, Sep.-Oct. 1985.

[202] K.A. Michalski, C.E. Smith, and C.M. Butler, "Analysis of horizontal two-element array antenna above a dielectric halfspace," *IEE Proc. Pt. H., Microwaves Antennas Propagat.*, vol. 132, pp. 335–338, Aug. 1985.

[203] I.S. Gradshteyn and I.M. Ryzhik, *Table of Integrals, Series, and Products*, Academic Press, 6^{th} edition, 2000, 1163 pages, ISBN 0-12-294757-6.

[204] N. Faché and D. De Zutter, "Rigorous full-wave space-domain solution for dispersive microstrip lines," *IEEE Trans. Microwave Theory Tech.*, vol. MTT-36, pp. 731–737, Apr. 1988.

[205] L. Beyne and D. De Zutter, "Green's function for layered lossy media with special applications to microstrip antennas," *IEEE Trans. Microwave Theory Tech.*, vol. MTT-36, pp. 875–881, May 1988.

[206] N. Faché, J. Van Hese, and D. De Zutter, "Generalized space domain Green's dyadic for multilayered media with special applications to microwave interconnections," *J. Electromagn. Waves Appl.*, vol. 3, pp. 651–669, 1992.

[207] J. Sercu, N. Faché, F. Librecht, and D. De Zutter, "Full-wave space-domain analysis of open microstrip discontinuities including the singular current-edge behavior," *IEEE Trans. Microwave Theory Tech.*, vol. MTT-41, pp. 1581–1588, Sep. 1993.

[208] A. Erteza and B.K. Park, "Nonuniqueness of resolution of Hertz vector in presence of a boundary, and the horizontal dipole problem," *IEEE Trans. Antennas Propagat.*, vol. AP-17, pp. 376–378, May 1969.

[209] K.A. Michalski, "On the scalar potential of a point charge associated with a time-dependent harmonic dipole in a layered medium," *IEEE Trans. Antennas Propagat.*, vol. AP-35, pp. 1299–1301, Nov. 1987.

[210] D. Zheng and K.A. Michalski, "Analysis of arbitrarily shaped coax-fed microstrip antennas - a hybrid mixed-potential integral equation approach," *Microwave Opt. Tech. Lett.*, vol. 3, pp. 200–203, Jun. 1990.

[211] H.Hertz, "The forces of electrical oscillations, treated by Maxwell's theory," *Ann. der Physik*, vol. 36, pp. 1, 1888.

[212] A. Bãnos, *Dipole Radiation in the Presence of a Conducting Half-Space*, Pergamon, New York, 1966.

[213] R.W. Jackson and D.M. Pozar, "Full-wave analysis of microstrip open-end and gap discontinuities," *IEEE Trans. Microwave Theory Tech.*, vol. MTT-33, pp. 1036–1042, Oct. 1985.

[214] M.-J. Tsai, F. De Flaviis, O. Fordham, and N.G. Alexopoulos, "Modeling planar arbitrarily shaped microstrip elements in multilayered media," *IEEE Trans. Microwave Theory Tech.*, vol. MTT-45, pp. 330–337, Mar. 1997.

[215] R.-C. Hsieh and J.-T. Kuo, "Fast full-wave analysis of planar microstrip circuit elements in stratified media," *IEEE Trans. Microwave Theory Tech.*, vol. MTT-46, pp. 1291–1297, Sep. 1998.

[216] L. Barlatey, J.R. Mosig, and T. Sphicopoulos, "Analysis of stacked microstrip patches with a mixed potential integral equation," *IEEE Trans. Antennas Propagat.*, vol. AP-38, pp. 608–615, May 1990.

[217] P.B. Katehi and N.G. Alexopoulos, "Frequency-dependent characteristics of microstrip discontinuities in millimeter-wave integrated circuits," *IEEE Trans. Microwave Theory Tech.*, vol. MTT-33, pp. 1029–1035, Oct. 1985.

[218] G. Coen, N. Faché, and D. De Zutter, "Comparison between two sets of basis functions for the current modeling in the Galerkin spectral domain solution for microstrips," *IEEE Trans. Microwave Theory Tech.*, vol. MTT-42, pp. 505–513, Mar. 1994.

[219] J.R. Mosig and F.E. Gardiol, "Analytical and numerical techniques in the Green's function treatment of microstrip antennas and scatterers," *IEE Proc. Pt. H., Microwaves Antennas Propagat.*, vol. 130, pp. 175–182, Mar. 1983.

[220] J.R. Mosig and F.E. Gardiol, "General integral equation formulation for microstrip antennas and scatterers," *IEE Proc. Pt. H., Microwaves Antennas Propagat.*, vol. 132, pp. 424–432, Dec. 1985.

[221] P. Pichon, J.R. Mosig, and A. Papiernik, "Input impedance of arbitrarily shaped microstrip antennas," *Electron. Lett.*, vol. 24, pp. 1214–1215, Sep 1988.

[222] T.K. Sarkar, P. Midya, Z.A. Maricevic, M. Kahrizi, S.M. Rao, and A. R. Djordevic, "Analysis of arbitrarily shaped microstrip patch antennas using the Sommerfeld formulation," *Int. J. Microwave Millimeter-Wave Comput.-Aided Eng.*, vol. 2, pp. 168–178, 1992.

[223] D.C. Chang and J.X. Zheng, "Electromagnetic modeling of passive circuit elements in MMIC," *IEEE Trans. Microwave Theory Tech.*, vol. MTT-40, pp. 1741–1747, Sep. 1992.

[224] F. Alonso-Monferrer, A.A. Kiskh, and A.W. Glisson, "Green's function analysis of planar circuits in a two-layer grounded medium," *IEEE Trans. Antennas Propagat.*, vol. AP-40, pp. 690–696, Jun. 1992.

[225] J. Sercu, N. Faché, F. Libbrecht, and P. Lagasse, "Mixed potential integral equation technique for hybrid microstrip-slotline multilayered circuits using a mixed rectangular-triangular mesh," *IEEE Trans. Microwave Theory Tech.*, vol. MTT-43, pp. 1162–1172, May 1995.

[226] W.C. Chi and N.G. Alexopoulos, "Radiation by a probe through a substrate," *IEEE Trans. Antennas Propagat.*, vol. AP-29, pp. 1080–1091, Sep. 1986.

[227] S. Pinhas and S. Shtrikman, "Vertical currents in microstrip antennas," *IEEE Trans. Antennas Propagat.*, vol. AP-35, pp. 1285–1289, Nov. 1987.

[228] R.C. Hall and J.R. Mosig, "The analysis of coaxially fed microstrip antennas with electrically thick substrates," *Electromagnetics*, vol. 9, pp. 367–384, 1989.

[229] R.C. Hall and J.R. Mosig, "Rigorous feed model for coaxially fed microstrip antenna," *Electron. Lett.*, vol. 26, pp. 64–66, 1990.

[230] D. Zheng and K.A. Michalski, "Analysis of arbitrarily shaped coax-fed microstrip antennas with thick substrates," *Electron. Lett.*, vol. 26, pp. 794–795, 1990.

[231] H. Legay, R. Gillard, J. Citerne, and G. Piton, "Via-hole effects on radiation characteristics of a patch microstrip antenna coaxially fed through a ground plane," Ann. Telecommun., vol. 46, pp. 367–381, 1991.

[232] D. Zheng and K.A. Michalski, "Analysis of coaxially fed microstrip antennas of arbitrary shape with thick substrates," *J. Electromagn. Waves Appl.*, vol. 5, pp. 1303–1327, 1991.

[233] S. Maeda, T. kashiwa, and I. Fukai, "Full wave analysis of propagation characteristics of a through hole using the finite-difference time-domain method," *IEEE Trans. Microwave Theory Tech.*, vol. MTT-39, pp. 2154–2159, Dec. 1991.

[234] A.G. Yang and M.A. Tassoudji, "Modeling and analysis of vias in multilayered circuits," *IEEE Trans. Microwave Theory Tech.*, vol. MTT-41, pp. 206–214, 1993.

[235] M.-J. Tsai, C. Chen, N.G. Alexopoulos, and T.-S. Horng, "Multiple arbitrary shape via-hole and air-bridge transitions in multilayered structures," *IEEE Trans. Microwave Theory Tech.*, vol. MTT-44, pp. 2504–2511, Dec. 1996.

[236] T. Becks and I. Wolff, "Calculation of three-dimensional passive structures including bond-wires, via-holes and air-bridges using the spectral domain analysis method," 21^th European Microwave Conference, 1991, pp. 571–576.

[237] T. Becks and I. Wolff, "Analysis of 3-D metallization structures by a full-wave spectral domain technique," *IEEE Trans. Antennas Propagat.*, vol. AP-40, pp. 2219–2227, Dec. 1992.

[238] T.-S. Horng, "A rigorous study of microstrip crossovers and their possible improvement," *IEEE Trans. Microwave Theory Tech.*, vol. MTT-42, pp. 1802–1806, Sep. 1994.

[239] R. Bunger and F. Arndt, "Efficient MPIE approach for the analysis of three-dimensional microstrip structures in layered media," *IEEE Trans. Antennas Propagat.*, vol. AP-45, pp. 1141–1153, Aug. 1997.

[240] N. Kinayman and M.I. Aksun, "Efficient use of closed form Green's functions for the analysis of planar geometries with vertical connections," *IEEE Trans. Microwave Theory Tech.*, vol. MTT-45, pp. 593–603, May 1997.

[241] T. Vaupel and V. Hansen, "Electrodynamic analysis of combined microstrip and coplanar/slotline structures with 3-D components based on surface/volume integral-equation approach," *IEEE Trans. Microwave Theory Tech.*, vol. MTT-47, pp. 1788–1800, Sep. 1999.

[242] K.A. Michalski, "Mixed-potential integral equation (MPIE) formulation for nonplanar microstrip structures of arbitrary shape in multilayered uniaxial media," *Int. J. Microwave Millimeter-Wave Comput.-Aided Eng.*, vol. 3, pp. 420–431, 1993.

[243] K.A. Michalski, "Formulation of mixed-potential integral equations for arbitrarily shaped microstrip structures with uniaxial substrates," *J. Electromagn. Waves Appl.*, vol. 7, pp. 899–917, 1993.

[244] G.J. Burke and E.K. Miller, "Modeling antennas near to and penetrating a lossy interface," *IEEE Trans. Antennas Propagat.*, vol. AP-32, pp. 1040–1049, Oct. 1984.

[245] K.A. Michalski and D. Zheng, "Electromagnetic scattering and radiation by surfaces of arbitrary shape in layered media, part II: implementation and results for contiguous half-spaces," *IEEE Trans. Antennas Propagat.*, vol. AP-38, pp. 345–352, Mar. 1990.

[246] Ph. Gay-Balmaz, *Structures 3-D planaires en milieux stratifiés: fonctions de Green et application à des antennes incluant des parois verticales*, Ph.D. Dissertation, École Polytechnique Fédérale de Lausanne, 1996, Thèse EPFL No. 1569.

[247] Ph. Gay-Balmaz and J.R. Mosig, "Structures rayonnantes 3-D planaires en milieu stratifié," Nice, France, 1996, Journeés internationales de Nice sur les Antennes (JINA '96), pp. 127–130.

[248] Ph. Gay-Balmaz, J.R. Mosig, and A.K. Skrivervik, "3-D planar antennas and arrays in stratified media," ESTEC, Noordwijk, Netherlands, 1996, COST245 -ESA workshop on active antennas, pp. 31–43.

[249] Ph. Gay-Balmaz and J.R. Mosig, "Three-dimensional planar radiating structures in stratified media," *Int. J. Microwave Millimeter-Wave Comput.-Aided Eng.*, vol. 7, pp. 330–343, Sep. 1997.

[250] T.M. Gregorczyk, A.K. Skrivervik, and J.R. Mosig, "A full-wave treatment of microstrip antennas containing vertical metalizations," Davos, Switzerland, 2000, AP 2000 Millenium conference on Antennas and Propagation, pp. 280–284.

[251] N.K. Uzunoglu, N.G. Alexopoulos, and J.G. Fikioris, "Radiation properties of microstrip dipoles," *IEEE Trans. Antennas Propagat.*, vol. AP-27, pp. 853–858, Nov. 1979.

[252] D.M. Pozar, "Input impedance and mutual coupling of rectangular microstrip antennas," *IEEE Trans. Antennas Propagat.*, vol. AP-30, pp. 1191–1196, Nov. 1982.

[253] W. Wertgen and R.H. Hansen, "Efficient direct and iterative electrodynamic analysis of geometrically complex MIC and MMIC structures," *Int. J. of Numerical Modeling*, vol. 2, pp. 153–186, 1989.

[254] B. Houshmand, W.C. Chew, and S.W. Lee, "Fourier transform of a linear distribution with triangular support and its applications in electromagnetics," *IEEE Trans. Antennas Propagat.*, vol. AP-39, pp. 252–254, Feb. 1991.

[255] K. McInturff and P.S. Simon, "The fourier transform of linearly varying functions with polygonal support," *IEEE Trans. Antennas Propagat.*, vol. AP-39, pp. 1441–1443, Sep. 1991.

[256] H.-Y. Yang, A. Nakatani, and J.A. Castañeda, "Efficient evaluation of spectral integrals in the moment method solution of microstrip antennas and circuits," *IEEE Trans. Antennas Propagat.*, vol. AP-38, pp. 1127–1130, Jul. 1990.

[257] T.-S. Horng, W.E. McKinzie, and N.G. Alexopoulos, "Full-wave spectral-domain analysis of compensation of microstrip discontinuities using triangular subdomain functions," *IEEE Trans. Microwave Theory Tech.*, vol. MTT-40, pp. 2137–2147, Dec. 1992.

[258] T. Vaupel and V. Hansen, "Effective spectral domain analysis of planar circuits with different kinds of expansion functions on rectangular subdomains," *Int. J. Microwave Millimeter-Wave Comput.-Aided Eng.*, vol. 7, pp. 455–467, Nov. 1997.

[259] M.I. Aksun and R. Mittra, "Choices of expansion and testing functions for the method of moments apllied to a class of electromagnetic problems," *IEEE Trans. Microwave Theory Tech.*, vol. MTT-41, pp. 503–509, Mar. 1993.

[260] S.-O. Park and C.A. Balanis, "Analytical technique to evaluate the asymptotic part of the impedance matrix of Sommerfeld-type integrals," *IEEE Trans. Antennas Propagat.*, vol. AP-45, pp. 798–805, May 1997.

[261] S.-O. Park, A. Balanis, and C.R. Birtcher, "Analaytical evaluation of the asymptotic impedance matrix of a grounded dielectric slab with roof-top functions," *IEEE Trans. Antennas Propagat.*, vol. AP-46, pp. 251–258, Feb. 1998.

[262] I.E. Rana and N.G. Alexopoulos, "Current distribution and input impedance of printed dipoles," *IEEE Trans. Antennas Propagat.*, vol. AP-29, pp. 99–105, Jan. 1981.

[263] N.G. Alexopoulos and I.E. Rana, "Mutual impedance between printed dipoles," *IEEE Trans. Antennas Propagat.*, vol. AP-29, pp. 106–111, Jan. 1981.

[264] J. Sercu, *Stroomdiscretisatie en interactiematrix berekening bij de momentenmethode modellering van hoogfrequente planaire structuren*, Ph.D. Dissertation, Universiteit Gent, 1994.

[265] K.A. Michalski and D. Zheng, "Analysis of planar microstrip structures of arbitrary shape : - to be, or not to be in the spectral domain ?," Winnipeg, Canada, 1990, Symp. Antennas Tech. Applicat. Electromagn., pp. 240–245.

[266] J.-X. Zheng, "Three-dimensional electromagnetic simulations of electronic circuits of general shape," *Int. J. Microwave Millimeter-Wave Comput.-Aided Eng.*, vol. 4, pp. 384–395, 1994.

[267] W. Cai, T. Yu, and Y. Yu, "High-order mixed RWG basis functions for electromagnetic applications," *IEEE Trans. Microwave Theory Tech.*, vol. 49, pp. 1295–1303, Jul. 2001.

[268] F. Ling, J. Liu, and J.-M. Jin, "Efficient electromagnetic modeling of three-dimensional multilayer microstrip antennas and circuits," *IEEE Trans. Microwave Theory Tech.*, vol. 50, pp. 1628–1635, Jun. 2002.

[269] A. John and R.H. Jansen, "A simple new technique for the implementation of vertical currents into the SDA," *Microwave Opt. Tech. Lett.*, vol. 7, pp. 389–392, Jun. 1994.

[270] A. Mohsen, "On the evaluation of Sommerfeld integrals," *IEE Proc. Pt. H., Microwaves Antennas Propagat.*, vol. 129, pp. 177–182, Aug. 1982.

[271] K.A. Michalski, "On the efficient evaluation of integrals arising in the Sommerfeld halfspace problem," *IEE Proc. Pt. H., Microwaves Antennas Propagat.*, vol. 132, pp. 312–318, Aug. 1985.

[272] K.A. Michalski and C.M. Butler, "Evaluation of Sommerfeld integrals arising in the ground stake antenna problem," *IEE Proc. Pt. H., Microwaves Antennas Propagat.*, vol. 134, pp. 93–97, Feb. 1987.

[273] K.A. Michalski, "Extrapolation methods for Sommerfeld integral tails," *IEEE Trans. Antennas Propagat.*, vol. AP-46, pp. 1405–1418, Oct. 1998.

[274] P.B. Katehi and N.G. Alexopoulos, "Real axis integration of Sommerfeld integrals with applications to printed circuit antennas," *Journal of Mathematical Physics*, vol. 24, pp. 527–533, Mar. 1983.

[275] T.-S. Horng, S.-C. Wu, H.-Y. Yang, and N.G. Alexopoulos, "A generalized method for distinguishing between radiation and surface-wave losses in microstrip discontinuities," *IEEE Trans. Microwave Theory Tech.*, vol. MTT-38, pp. 1800–1807, Dec. 1990.

[276] A.K. Bhattacharyya, "Characteristics of space and surface waves in a multilayered structure," *IEEE Trans. Antennas Propagat.*, vol. AP-38, pp. 1231–1238, Aug. 1990.

[277] R. Mittra and C.A. Klein, Eds., *Numerical and Asymptotic Techniques in Electromagnetics*, vol. 3 of *Topics in applied physics*, Springer-Verlag, Berlin-Heidelberg-New York, 1976, Chapter 5 : "Stability and Convergence of Moment Method Solutions".

[278] L. Zaïd, G. Kossiavas, J.-Y. Dauvignac, J. Cazajous, and A. Papiernik, "Dual-frequency and broad-band antennas with stacked quarter wavelength elements," *IEEE Trans. Antennas Propagat.*, vol. AP-47, pp. 654–659, Apr. 1999.

[279] J.-Y. Lee, T.-S. Horng, and N.G. Alexopoulos, "Analysis of cavity-backed aperture antennas with a dielectric overlay," *IEEE Trans. Antennas Propagat.*, vol. AP-42, pp. 1556–1562, Nov. 1994.

[280] A.D. Daly, S.P. Knight, M. Caulton, and R. Eholdt, "Lumped elements in microwave integrated circuits," *IEEE Trans. Microwave Theory Tech.*, vol. MTT-15, pp. 713–721, 1967.

[281] J.C. Rautio and R.F. Harrington, "An electromagnetic time-harmonic analysis of shielded microstrip circuits," *IEEE Trans. Microwave Theory Tech.*, vol. MTT-35, pp. 726–730, Aug. 1987.

[282] S. Hashemi-Yeganeh, "On the summation of double infinite series field computations inside rectangular cavities," *IEEE Trans. Microwave Theory Tech.*, vol. MTT-43, pp. 641–646, Mar. 1995.

[283] R.W. Jackson, "The use of side wall images to compute package effects in MoM analysis of MMIC circuits," *IEEE Trans. Microwave Theory Tech.*, vol. MTT-41, pp. 406–414, Mar. 1995.

[284] P. Mezzanote, M.Mongiardo, L. Roselli, R. Sorrentino, and W. Heinrich, "Analysis of packaged microwave integrated circuits by FDTD," *IEEE Trans. Microwave Theory Tech.*, vol. MTT-42, pp. 1796–1801, Sep. 1994.

[285] J.J. Burke and R.W. Jackson, "Reduction of parasitic coupling in packaged MMIC's," .

[286] R. Faraji-Dana and Y.L. Chow, "Accurate and efficient CAD tool for the design of optimum packaging for (M)MICs," *IEE Proc. Pt. H., Microwaves Antennas Propagat.*, vol. 142, pp. 81–88, Apr. 1995.

[287] M. Rittweger and I. Wolff, "Analysis of complex passive (M)MIC-components using the finite difference time domain method," Dallas, 1990, IEEE MTT-S Int. Microwave Symp. Dig., pp. 1147–1150.

[288] G.-W. Pan, J. Tan, and B.K. Gilbert, "Full wave edge element based analysis of 3D metal-dielectric structures for high clock rate digital and microwave applications," *IEE Proc. Pt. H., Microwaves Antennas Propagat.*, vol. 147, Oct. 2000.

[289] D. Jessie and L. Jolla, "Design techniques for improved microwave performance of small outline packages," Seattle, Washington, 2002, IEEE MTT-S Int. Microwave Symp. Dig, pp. 297–300.

[290] R.W. Jackson, "A circuit topology for microwave modeling of plastic surface mount packages," *IEEE Trans. Microwave Theory Tech.*, vol. MTT-44, pp. 1140–1146, Jul. 1996.

[291] R.W. Jackson and S. Rakshit, "Microwave-circuit modeling of high lead-count plastic packages," *IEEE Trans. Microwave Theory Tech.*, vol. MTT-45, pp. 1926–1933, Oct. 1997.

[292] M. Righi, G. Tardioli, L. Cascio, and W.J.R. hoefer, "Time-domain characterization of packaging effects via segmentation technique," *IEEE Trans. Microwave Theory Tech.*, vol. MTT-45, pp. 1905–1910, Oct. 1997.